IMPACT DAMAGE EVOLUTION OF PLAIN WEAVE COMPOSITES: MULTISCALE MODELING AND EXPERIMENTS

by

Christopher Scott Meyer

A dissertation submitted to the Faculty of the University of Delaware in partial fulfillment of the requirements for the degree of Doctor of Philosophy in Mechanical Engineering

Winter 2022

IMPACT DAMAGE EVOLUTION OF PLAIN WEAVE COMPOSITES:

MULTISCALE MODELING AND EXPERIMENTS

by

Christopher Scott Meyer

Approved: ____
Ajay Prasad, Ph.D.
Chair of the Department of Mechanical Engineering

Approved: ____
Levi T. Thompson, Ph.D.
Dean of the College of Engineering

Approved: ____
Louis F. Rossi, Ph.D.
Vice Provost for Graduate and Professional Education and
Dean of the Graduate College

I certify that I have read this dissertation and that in my opinion it meets the academic and professional standard required by the University as a dissertation for the degree of Doctor of Philosophy.

Signed: ____

John W. Gillespie Jr., Ph.D.
Professor in charge of dissertation

I certify that I have read this dissertation and that in my opinion it meets the academic and professional standard required by the University as a dissertation for the degree of Doctor of Philosophy.

Signed: ____

Bazle Z. Haque, Ph.D.
Member of dissertation committee

I certify that I have read this dissertation and that in my opinion it meets the academic and professional standard required by the University as a dissertation for the degree of Doctor of Philosophy.

Signed: ____

M. Zubaer Hossain, Ph.D.
Member of dissertation committee

I certify that I have read this dissertation and that in my opinion it meets the academic and professional standard required by the University as a dissertation for the degree of Doctor of Philosophy.

Signed: ____

Harry Shenton III, Ph.D.
Member of dissertation committee

ACKNOWLEDGMENTS

First, I am grateful to my advisors Dr. John Gillespie Jr. and Dr. Bazle (Gama) Haque. Thanks to Dr. Gillespie for being challenging and encouraging, patient and supportive, and always educational. In the beginning, I came to him as a practicing engineer with application in mind, and he taught me to consider the science. Thanks to Dr. Haque for many philosophically enlightening discussions about life, the universe, and everything. Thanks also for so much insight, troubleshooting, and assistance with modeling efforts that this work would not have been possible otherwise. Thanks especially for mentoring me and for many energetic discussions about the penetration mechanics of composites. I am also grateful to my dissertation committee for their service and insights, Dr. Zubaer Hossain, Dr. Tripp Shenton, and Dr. Danny O'Brien.

My pursuit of this dissertation would not have been possible without support from the Army Research Laboratory. Thanks to Danny O'Brien for overseeing the ballistic impact experiments, and Joe Lee for running the experiments. Thanks to Mike Thompson for his exceptional skill in manufacturing composites. I am also grateful to my supervisors for allowing me to step away from my duties so that I could pursue this dissertation. Thanks to the SMART Scholarship and ARL for funding me during this time. Finally, thanks to the Materials in Extreme Dynamic Environments program for providing me the research topic for this dissertation.

I am also extremely grateful to Chris Key for invaluable assistance developing the plain weave finite element model. His script started me on the path to studying composites at the mesoscale.

Special thanks to the mechanical engineering department staff and faculty for assistance, guidance, and mentoring through my time at UD. Thanks to Lisa Katzmire and Missy Arenz for their support. Thanks to Dr. Zubaer Hossain and Dr. Michael Santare for encouragement and helpful and stimulating coursework.

Many thanks go to the staff and students of the Center for Composite Materials. Thanks to Raja Ganesh, Mani Sockalingam, Taka Kubota, Brandon Chen, Navid Kermani, Min-young Yun, Molla Ali, Ahmad Abu Obaid, Sagar Doshi, and Albraa Jaber for friendship, conversations, and help with various aspects of lab work and research. Albraa Jaber was also like a brother, and I would not have gotten through the program without him. Special thanks to Molla Ali who worked tirelessly to help with experiments and composites manufacturing. Thanks to Robin Mack, Kristen Scully, Corinne Hamed, and Therese Stratton for administrative support. Special thanks to Johnny Thiravong for lab support. I also am grateful to have had the opportunity to mentor Tam Nguyen, Abir Quabili, and Isabel Catugas.

Finally, my family deserves tremendous thanks for their patience and understanding during this long process. Thanks to my parents, sister, and in-laws for encouragement. I owe a lot to my wife for putting up with me and often putting up without me during this time. Regardless, she was always by my side in good times and bad. My children lost a lot of time with their dad, and I hope to make it up to them soon. I hope my perseverance throughout this process shows them that they can do anything. And thanks to God who was and is and will be with me.

TABLE OF CONTENTS

Appendix

LIST OF TABLES

LIST OF FIGURES

ABSTRACT

Recent developments in plain weave glass/epoxy composites have led to their increasing dual use as a structural and protective material in light armored vehicles. As such, understanding the evolution of damage due to ballistic impact is critical for improving the survivability of these materials. Ballistic impact experiments are often conducted, but post-test inspection of experimental specimens provides a picture of the end-state of damage. Diagnostic tools such as high-speed cameras have limited resolution in space and time, so often only provide insight into a part of the overall damage evolution. Thus, the spatial and temporal evolution of damage in plain weave (PW) composites following ballistic impact is not well understood. So, we turn to modeling to elaborate our understanding of this damage evolution.

At the earliest timescale following projectile impact on woven composites, a stress wave propagates from the impact area through the composite thickness. At longer time scales, a transverse deformation cone forms around the projectile, and primary tows are loaded in tension, which spreads through shear to secondary tows. At the mesoscale—the length scale of a tow cross section—projectile impact causes damage including transverse cracks, tow-tow delamination cracks, tow tension and fiber failure.

Projectile impact experiments were conducted, and the mesoscale damage mode tow-tow delamination was found to be a maximum near the ballistic limit velocity. These experiments were simulated with a state-of-the-art continuum model. The model predicted the projectile residual velocity reasonably well, but demonstrated

a need for improved predictive capability, particularly regarding the ballistic limit velocity. Therefore, this work developed a mesoscale model, which incorporated discrete fabric architecture and showed improvement over the continuum model. However, this model was missing rate-dependent material behavior and the important mesoscale damage mode of tow-tow delamination.

Simulating tow-tow delamination with the cohesive zone modeling approach required rate-dependent traction-separation laws (TSLs). These TSLs were derived using a multi-scale embedded cell modeling approach. A microscale model of fiber-matrix microstructure was embedded within a mesoscale continuum. Model inputs included rate-dependent matrix plasticity and failure and rate-dependent fiber-matrix interfacial debonding. Models were exercised in mode I and mode II to produce tension and shear cracking in the microstructure. The J-integral method was used to bridge the crack energy from the microscale to the mesoscale. The J-integral data were differentiated to derive the mode I and mode II TSLs. Bridging was demonstrated by comparing the load-displacement response of the microstructure to a mesoscale continuum cohesive crack modeled with the TSLs derived from the microscale.

These TSLs were then used in a highly-resolved model of a PW representative volume element (RVE). The RVE was used to model the effects of through-thickness stress wave propagation at the earliest timescale. The damage evolution during this timescale was investigated for a range of impact velocities. It was found that tensile spall due to stress wave propagation can initiate tow-tow delamination (TTD) cracking for lower impact velocities, but higher velocity crushes the material. Delamination cracking at the projectile annulus initiates during this timescale during formation of the deformation cone and facilitates primary tow tensile loading.

Single-layer ballistic perforation experiments were conducted. The PW RVE was repeated in space to build a full-scale model of the impact experiments. In these mesoscale models, TTD was modeled with the TSLs determined from the microscale. The experiments and modeling focused on the ballistic limit velocity (VBL). The mesoscale model provides more realistic deformation than the continuum model, which allowed ranking of energy absorbing mechanisms. The mesoscale model indicated two phases of penetration for impact velocities near VBL. The first phase is dominated by momentum transfer, and the second by tow-tension and pullout. The mesoscale model was used to partition energy dissipation and investigate the damage evolution during perforation. It was found that the development of TTD cracking is important for releasing the constraint on primary tows and enabling tow-elongation and frictional sliding, which dissipate additional energy.

Finally, the multiscale modeling approaches developed in this work form a framework in which a materials-by-design evaluation of novel materials can be used at the lower length scales to derive properties used at higher length scales for evaluating and enhancing understanding of ballistic performance of plain weave composites.

Chapter 1

INTRODUCTION

1.1 Motivation

A composite can be defined as the chemical bonding of two or more dissimilar constituent materials. Composite materials are often designed with the goal of enhancing the mechanical behavior of the constituents. Fiber reinforced polymer composites (FRPCs) have become widespread over the last century. This type of composite is desirable for applications where high strength, stiffness, and damage tolerance is needed along with low weight. These FRPCs have found application in many industries including automotive, aerospace, and protection. Protective composite materials include body armor and vehicle armor. In vehicles, composites can be used in both structural and protective roles. A composite commonly used in structural and protective applications consists of high-strength glass fibers and epoxy matrix. Many thousands of glass fibers are assembled without twist into bundles known as tows. These tows can be woven together to produce plain weave fabric. Plain weave is a common weave with a simple over-under pattern. The plain weave fabric is layered and infused with matrix such as epoxy. Plain weave glass fiber reinforced epoxy matrix composites are a common material for protective applications.

Protection materials are subjected to dynamic events such as ballistic impact. Under ballistic impact, the dynamic behavior of the plain weave glass/epoxy composites is of interest. Dynamic behavior of materials involves high strains, high strain rates, and high pressures. This is the subject of various studies on materials in extreme dynamic environments. Improving material protective response under dynamic loading can involve a materials-by-design approach. This approach uses advanced materials characterization to provide input to computational models and validates these models with experimental data. Such computational models operate in various length and time scales. Length scales include the macroscale—the scale of the experiment or structure; the mesoscale—the scale of the composite woven architecture; the microscale—the scale of constituent fibers and matrix; and the nanoscale—the scale of fiber-matrix interphase. Ultimately, these models help to identify important material behavior or deformation and damage mechanisms that can be optimized to enhance performance.

In a materials-by-design context, this work develops multiscale models including realistic geometry and rate-dependent material behavior. These models bridge length scales from the microscale to the mesoscale and from the mesoscale to the structural length scale. A microscale model of fracture informs a mesoscale model of ballistic perforation. The mesoscale model response is validated by experimental perforation experiments. The validated model is used to partition energy dissipation, to investigate important deformation and damage mechanisms, and to identify areas for optimizing material, design, or processing for enhanced penetration resistance.

1.2 Objectives of the Research

The overarching goal of this research was to enhance understanding of mesoscale damage evolution in space and time and the contributions of that damage to energy dissipation in ballistic perforation of thin composites. Currently available experimental observation techniques lack the spatial or temporal resolution to study ballistic impact damage at the mesoscale. This led to the development of finite element models for this study. These models are also useful in a materials-by-design approach for improving composite penetration resistance.

Single-layer plain weave composite perforation experiments revealed important damage modes occurring at the length scale of composite tows, the mesoscale. It was found that these damage modes are maximum near the ballistic limit velocity. Because they did not include mesoscale damage, continuum models were shown to be inadequate for predicting the ballistic limit velocity. Due to the complexity of mesoscale geometry and the size of ballistic test specimens, mesoscale modeling of ballistic impact on composites has typically used a coarse mesh, rough geometry, and limited rate-dependent material behaviors. Thus, high-fidelity, geometrically realistic, mesoscale models were developed that incorporate extensive rate-dependent material models and parameters.

Experiments showed that the tow-tow delamination mesoscale damage mode plays an important role in energy absorption near the ballistic limit. Mesoscale modeling has so far either neglected this damage mode, made unrealistic assumptions, or used higher length scale constitutive behavior to model this lower length scale damage. With currently available techniques, it is not possible to study this damage mode experimentally. Therefore, this work developed models to study this damage at the microscale with embedded cell models of realistic microstructure. Microscale crack initiation and propagation was modeled at the mesoscale with the cohesive zone model, with microscale constitutive behavior bridged to the mesoscale with the J-integral method.

The evolution of damage at the earliest timescale was investigated with a highly resolved mesoscale model. This model studied the through-thickness stress wave propagation and the early time deformation wave formation. The evolution of damage was studied under and around the projectile impact location. The model was used to predict damage evolution as a function of impact velocity.

Additional ballistic impact experiments were conducted. The mesoscale modelling approach was validated against these experiments. The mesoscale model was shown to accurately predict the ballistic limit velocity and the impact versus residual velocity response of the projectile-target pair. The validated model was used to partition energy dissipation. Finally, the model was used to provide insight into ways of improving woven composite ballistic penetration resistance.

1.3 Outline of the Dissertation

Chapter 2 begins by defining the length and time scales of interest. Preliminary single-layer perforation experiments and results are presented. From these results, important mesoscale damage modes are identified and quantified. Continuum modeling of the experimental impact vs. residual velocity results shows the need for improvement. Preliminary mesoscale modeling shows the need to incorporate mesoscale tow-tow delamination with appropriate length scale constitutive behavior and higher fidelity rate-dependent constitutive behavior.

In Chapter 3 the preliminary mesoscale model is improved to include realistic geometry and tow-tow delamination. The model is validated with the preliminary single-layer experimental data, but more fidelity is needed to predict ballistic limit velocity. The material constitutive behavior used lacks strain-rate dependence. This work reveals the need for additional fidelity of constitutive behavior, particularly the tow-tow delamination properties.

Tow-tow delamination is modeled in the mesoscale model with the cohesive zone model. The focus of Chapter 4 is on determining the needed tow-tow delamination properties. An embedded cell microscale model with resolved fiber-matrix microstructure is developed. Rate-dependent material behavior is used, and microscale cracks are evolved. The microscale is bridged up to the mesoscale using the J-integral method.

With the tow-tow delamination properties derived from the lower length scale, Chapter 5 implements tow-tow delamination in a highly-resolved model of projectile impact. The model is used to investigate damage evolution during the earliest timescale after projectile impact. Through-thickness stress wave propagation, damage, and tow-tow delamination is studied under and around the projectile impact location.

In Chapter 6, new single-layer plain weave glass/epoxy ballistic perforation experiments are conducted. A mesoscale model is developed to simulate these experiments. The model is validated using the experimental impact and residual velocity results. Then the validated model is used to partition energy dissipation. Finally, the model is used to identify important energy dissipation mechanisms that can be optimized for improvements to penetration resistance.

In Chapter 7, the conclusions from the work are reviewed and future work is proposed for the continuation and extension of the subject research. Future work includes extending the validated model from the previous chapter by simulating multilayer impact experiments. The experiments are from the literature. The mesoscale model developed in this work is shown to predict the impact and residual velocity response of a 22-layer composite with reasonable accuracy, highlighting the potential for future work in application of the mesoscale modeling approach developed in this dissertation.

1.4 Unique Contributions of this Dissertation

1. This work is the first to demonstrate the importance of mesoscale damage near the ballistic limit velocity. Emphasis is placed on tow-tow delamination, which was first identified in this work and is typically neglected in the literature.

2. This work is the first to use the embedded cell modeling approach with rate-dependent matrix and fiber-matrix debonding, apply the approach to mode I and mode II fracture in [90/90] and [0/90] unidirectional composites, and use the J-integral method to bridge from the microscale to the mesoscale to determine strain-rate dependent traction-separation laws.

3. Global mode II loading in 90° unidirectional fiber-matrix microstructure was simulated at the microscale for the first time. This work shows that, under global mode II loading, cracks open locally in mode I, which is in agreement with experimental results from the literature.

4. This work developed the first high-fidelity mesoscale ballistic impact models of plain weave composites with a highly-resolved mesh, realistic geometry, rate-dependent constitutive behavior, and included rate-dependent tow-tow delamination.

5. This work is the first to study the effects of early-time, through-thickness stress wave propagation on damage and delamination in a plain weave composite. This work studied the evolution of damage under and around the projectile at the earliest

timescale as functions of the through-thickness stress wave and formation of the transverse deformation cone wave.

6. The mesoscale model developed in this work was used to partition the energy dissipation at the mesoscale in ballistic perforation of a plain weave composite. The model was used to identify mechanisms to optimize for improving ballistic penetration resistance in plain weave composites.

7. This work used higher-fidelity mesoscale models of multilayer woven composite penetration than have been published in the literature.

8. This work has enhanced the transverse impact community's body of knowledge with a more complete picture of plain weave composite impact damage evolution in time and space through studies of the effects of mechanisms at different length and time scales.

Chapter 2

BACKGROUND, PRELIMINARY EXPERIMENTS AND MODELING

Considerable research has been published on modeling ballistic impact on fabrics and fabric composites. The goals of these works are varied, but generally move toward understanding penetration and perforation mechanisms and enhancing penetration resistance. These computational works are often validated experimentally or analytically. Often, a continuum modeling approach is used. This approach is favored for its computational efficiency. Recent developments in supercomputing can better manage the computational cost and have expanded the accessibility of high-performance computing. This advent has spurred the development of models with lower length scale resolution. These models give new insights into penetration mechanics not available with state-of-the-art continuum models.

2.1 Length and Time Scales

Computational solid mechanics modeling makes extensive use of continuum mechanics. This work presumes the reader understands continuum mechanics. Solid materials, such as metals, ceramics, polymers, and their composites, are composed of atoms and empty space, but the material is assumed to be continuous. The continuum theory of matter attempts to describe relationships between phenomena, while neglecting the structure of material on a smaller scale.[1] Finite element analysis (FEA) discretizes this continuum into elements. These elements have nodes at their corners, and the FEA software solves for nodal accelerations from applied forces.

Accelerations are integrated twice to get nodal displacements and the change in displacement over time steps gives strain and strain rate. From average strain and stiffness, stress is solved for at the centroid of the elements. Thus, the continuum assumption applied to complex lower length scale structures is used to model the higher length scale stress-strain behavior. To gain new understanding of the dynamic behavior of composites, this work makes extensive use of FEA and the continuum assumption at various length scales.

The macroscale or structural length scale includes macroscopic (large scale) system-level behavior. For example, the vehicle in figure 2.1 is a macroscale system of mechanical components and composite armor, which can be subjected to ballistic impact. The macroscale can be defined as >1 cm; that is, any detail smaller than about one centimeter is assumed to be represented by a continuum. For example, the detail of the woven fabric composite armor plate in figure 2.1 is assumed a continuum. But the plate is actually composed of interwoven yarns or tows,[1] as seen in figure 2.1.

Lower length scale models include resolved constituents at length scales that are shorter than the continuum scale. Hence, the mesoscale[2] here is defined as ~1–10 mm.[3] That is, any detail smaller than about the millimeter scale is assumed a

---

[1] "Yarn" typically refers to a *twisted* bundle of fibers, usually glass fiber, which can be continuous or not. "Tow" typically refers to an *untwisted* bundle of *continuous* fibers, usually, but not always, carbon fiber. Here we use tow to describe an untwisted bundle of continuous glass fibers. The literature often uses "yarn" to describe bundles of glass fiber, regardless of twist. Yarn is used instead of tow if used in works cited.

[2] "Mesoscale" simply means a middle length scale, so varies widely and requires definition based on the lower and higher length scales that surround it.

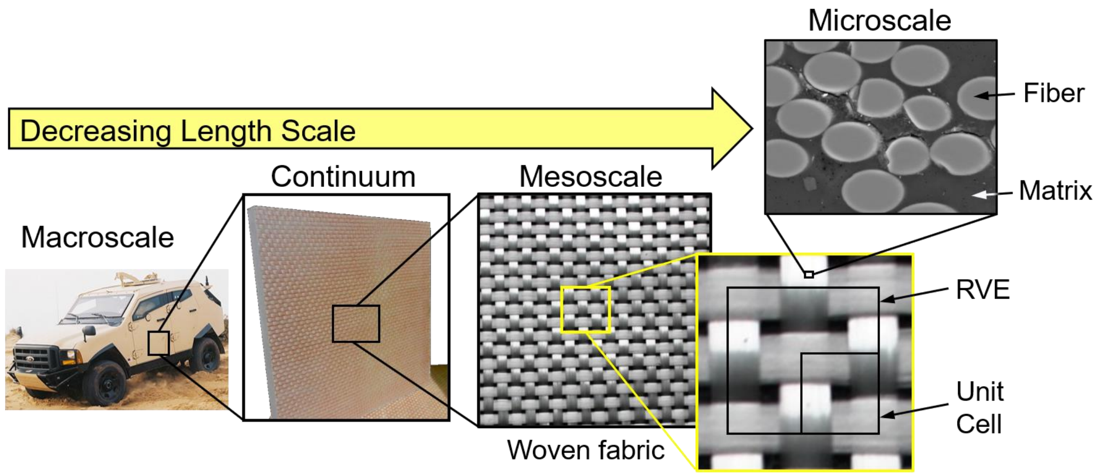

Figure 2.1: Multiple length scales involved in plain weave composite armor panels.

continuum. As shown in figure 2.1, woven fabric composites are made up of symmetrical units called representative or repeating volume elements (RVEs), which can be subdivided into the simplest unit cell. It is reasonable to assume that RVEs are statistically the same across the whole composite. Therefore, mesoscale models can tile these RVEs in space to make a large panel or can use an RVE with symmetric boundary conditions to represent the composite. Mesoscale models of woven fabric composites are resolved to the length scale of a tow cross section, such as shown in figure 2.2. The fibers and matrix within the tows are assumed a continuum. The next lower length scale is the microscale, defined as ~1–10 μm. At the microscale, discrete fibers and matrix are resolved, such as seen in figure 2.2. The diameter of a typical glass fiber is ~10 μm. Lower length scales can include the atomic length scale, which

---

[3] The *tilde* symbol is used here to indicate the order of magnitude. So, "~1–10 mm" should be read as "on the order of 1 to 10 millimeters."

is the scale of the fiber-matrix interphase, ~1-10 nm, and the angstrom length scale, which is used to describe the atomic structure of fiber, interphase, and matrix, ~0.05-0.1 nm. The lowest length scale considered in this work is the microscale with fiber-matrix interphase and atomic structures modeled as a continuum.

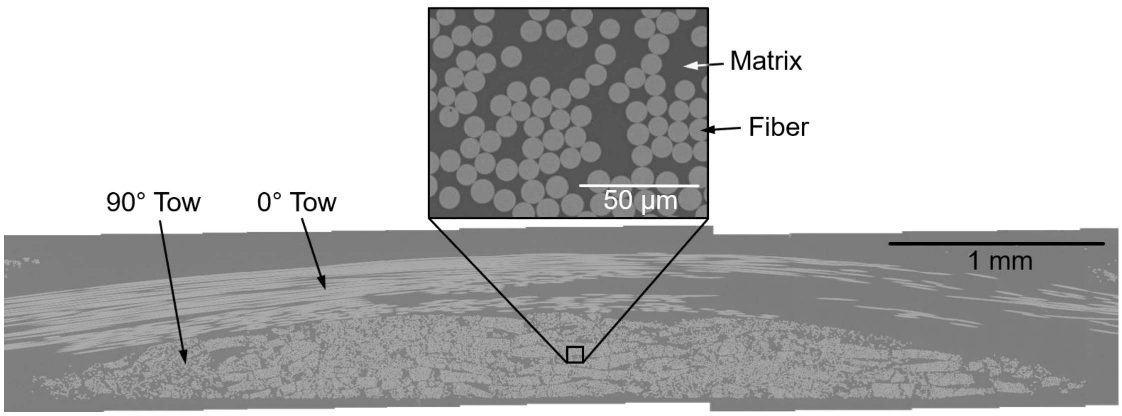

Figure 2.2: Scanning electron micrographs of the cross section of a plain weave glass/epoxy composite.

Time scale depends on the rate of loading. For low-rate or quasi-static loading, the time to failure is long, ~1-10 min. For dynamic loading, such as in ballistic impact, the time to failure is much shorter, ~1-1000 μs.

This work is concerned with the microscale, mesoscale, and macroscale and the dynamic loading timescale.

2.2 Penetration Mechanics of Plain Weave Composites

It is well known that projectile impact on a woven composite target sends stress waves propagating outward from the point of impact (e.g., [2], [3]). Projectile impact on a single-layer plain weave composite is shown schematically in figure 2.3.

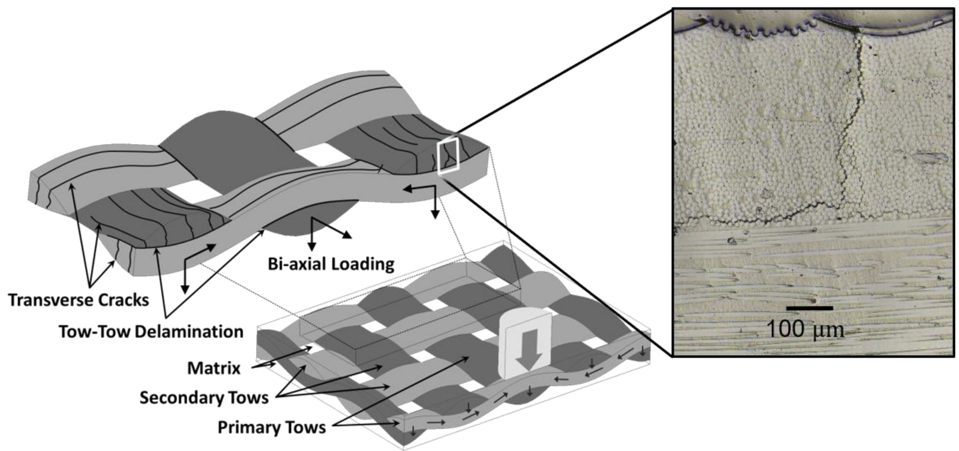

Figure 2.3: Schematic of mesoscale plain weave architecture illustrating impact on primary tows, tension and tow-tow delamination. Inset is a micrograph of mesoscale damage in a single-layer woven composite following impact by a cylindrical projectile.

The earliest timescale (i.e., target thickness divided by target sound speed) involves the projectile contacting the target (see Figure 2.4). This contact leads to through-thickness stress wave propagation and damage under the projectile, depending on the nose shape. At the next timescale (i.e., target diameter divided by target sound speed), in-plane stress waves propagate radially outward from the projectile-target contact. As these waves interact with interfaces, stress concentrations may lead to delamination in multi-layered composites [4]. At a later timescale, a transverse deformation wave propagates out from the impact location [5]. This deformation wave is conical in isotropic materials and pyramidal in plain weave materials. As momentum transfers from projectile to target and the deformation wave expands in a plain weave composite, primary tows are loaded in tension, and secondary tows are loaded by shear spreading of the tensile load [6]–[8]. This primary tow tension leads to tow-tow delamination cracking (e.g., [9], [10]), which may have initiated at earlier timescales. In later timescales, punch-shear, deformation wave growth, and tensile tow failure lead to projectile perforation. Damage initiates, propagates, and evolves across length and timescales due to these various loading conditions, but the damage relative to the earliest timescale is often overlooked in favor of longer timescale deformation.

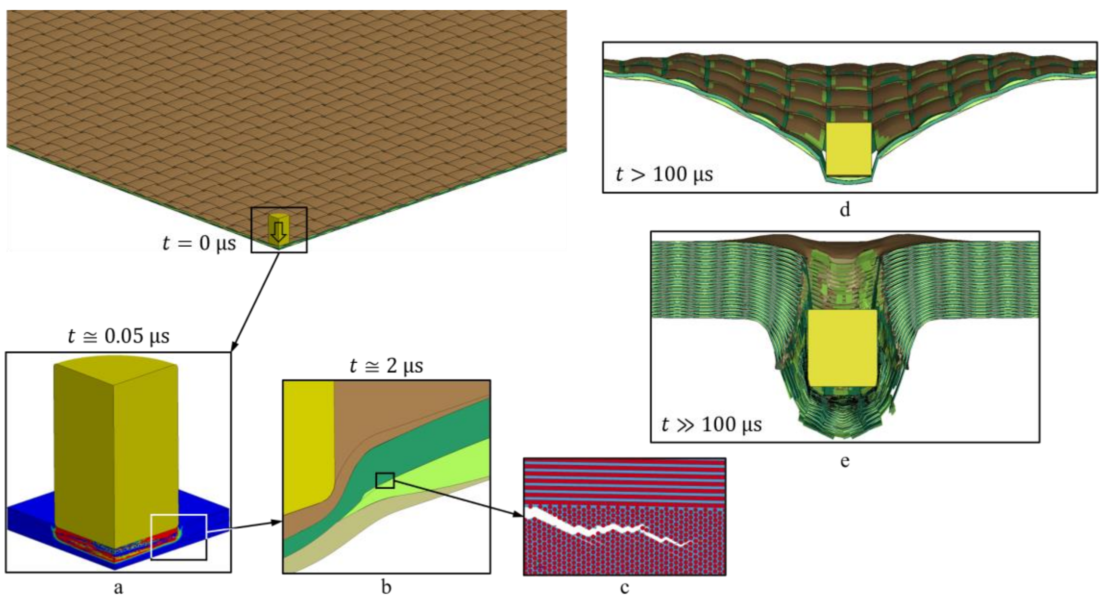

Figure 2.4: Illustration of damage evolution across time scales. (a) Earliest timescale: through-thickness stress wave and damage under projectile. (b) Second timescale: radial stress wave propagation, delamination initiation, transverse deformation wave formation. (c) Microscale tow-tow delamination cracking propagates. (d) In later timescales, momentum transfer, primary tow tension, tow-tow delamination and eventually (e) punch-shear and tow/fiber tensile failure.

2.3 Single-layer Perforation Experiments, Part I

It is understood that multi-layered fabric composite penetration response depends on strike face crush and back face perforation. The initial layers undergo punch-shear deformation, through-thickness compression, and in-plane tension. Multi-layered fabric composite impact also depends on the perforation response of individual layers on the back face. Therefore, the study of composite material penetration mechanics can be decoupled based on the location and function of the layers through the thickness.[11] Experimental studies of single-layer woven composites are also beneficial for reducing sources of error associated with ply interaction, including tow nesting and layer interpenetration.[12]

Ballistic perforation experiments were conducted on single-layer composites to improve understanding of the ballistic response of composite systems.[7] Composites were made from plain weave S-2 glass fabric (5 × 5 tows/inch (2 × 2 tows/cm) areal density 24 oz/yd^2 (744 g/m^2), AGY 463-AA-250, 30 ends), infused with SC-15 toughened epoxy (Kaneka Aerospace, LLC) using vacuum-assisted resin transfer molding.

Single-layer test specimens were 300 × 300 mm (12 × 12 inch) and 0.9 mm thick. Composite density was 1.8 g/cm^3. Specimens were clamped in aluminum plates with 200 mm (8 inch) diameter hole (i.e., clamped boundary conditions). Projectiles were shot from a gas gun and impact and residual velocities were measured with high-speed cameras. Additional details of these experiments may be found in this reference.[9]

Composites were impacted by a 5.6 mm (0.22 caliber) diameter, right circular cylindrical (RCC) blunt-nosed steel projectile. Primary tows are defined as the tows directly under the projectile during an impact.[6] Depending on the size of the projectile, there could be multiple primary tows. Secondary tows are not directly under the projectile. This projectile diameter (5.6 mm) is about the same size as a single tow width (5.0 mm). Hence, the penetration involves mesoscale mechanisms.

At the mesoscale, woven architecture provides additional energy dissipation mechanisms compared with unidirectional composites. Mechanisms include transverse tow matrix cracking, primary tow tension, tension-shear and compression-shear tow failure, secondary tow deformation, tow-tow and tow-matrix delamination, and coupled tension and bending and additional delamination resistance due to tow undulation.[6], [9], [12]–[14] Mesoscale damage is made up of microscale mechanisms such as matrix cracking, fiber-matrix interface debonding, and fiber fracture.

2.3.1 Experimental V_I–V_R Results

Experimental results of impact velocity, V_I, and residual velocity, V_R, after perforation are provided in figure 2.5. The ballistic limit velocity, V_{50}, was determined in accordance with MIL-STD-662F from the three lowest velocity complete perforations and the three highest velocity non-perforations. For all data, V_{50} = 175 m/s. The Lambert-Jonas [15] equation, $V_R = 0.99(V_I^{2.6} - 170^{2.6})^{\frac{1}{2.6}}$ was used to fit the data in figure 2.5.

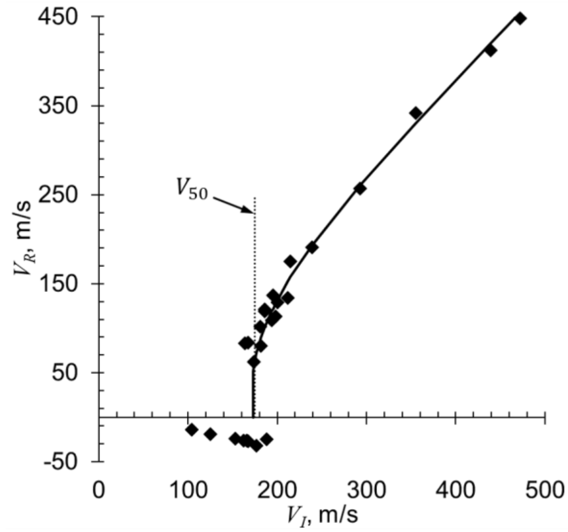

Figure 2.5: Single-layer, plain weave S-2 glass/SC-15 epoxy composite perforation experimental results with residual velocity, V_R, as a function of impact velocity, V_I. Ballistic limit velocity, V_{50} = 175 m/s, is indicated.

2.3.2 Mesoscale Damage

High resolution images were captured of the impacted specimens.[8] The thin composite panels were backlit to reveal poorly understood damage modes that occur at the mesoscale. The local area surrounding the location of projectile perforation is shown in figure 2.6. Punch-shear damage is at the location where the projectile perforated the target. Tow-tow delamination was identified as delaminated interfaces between orthogonal tows within the layer. At the microscale, tow-tow delamination is similar to delamination between 0° and 90° unidirectional composite layers. Tow-tow delamination occurs predominantly in primary tows. Transverse cracking is matrix cracks that develop transverse to the direction of primary tensile loading. Transverse cracks occur predominantly in secondary tows. With sufficient impact energy, primary tows can delaminate from secondary tows and pull out and deform as the projectile perforates the target.

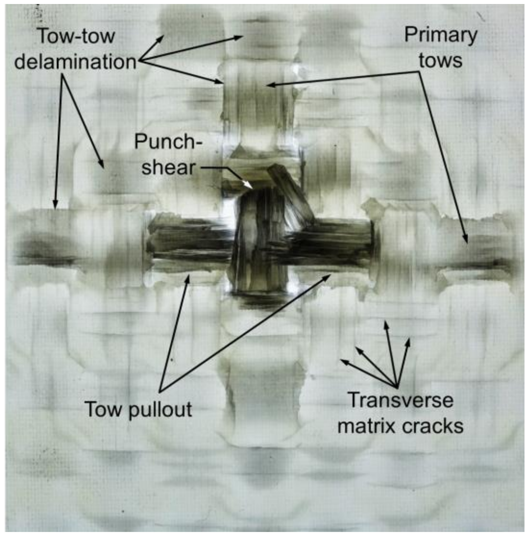

Figure 2.6: Mesoscale damage modes indicated on backlit, high-resolution image of perforated specimen. V_I = 239 m/s, V_R = 191 m/s.

Damaged test specimens were sectioned, mounted, and polished and examined with optical, confocal, and electron microscopy. The confocal cross-section of a tow-tow overlap is shown in figure 2.7. Transverse cracking and tow-tow delamination cracking are indicated in figure 2.7. At the microscale, transverse cracks propagate within the 90° tow, and tow-tow delamination cracks evolves between 0° and 90° tows. However, the tow-tow delamination crack propagates within the 90° tow or through the matrix between 0° and 90° tows. The tow-tow delamination crack in figure 2.7 is examined by scanning electron microscopy in figure 2.8. Figure 2.8 shows that, at the microscale, these cracks evolve as fiber-matrix interface debonding and matrix microcracks.

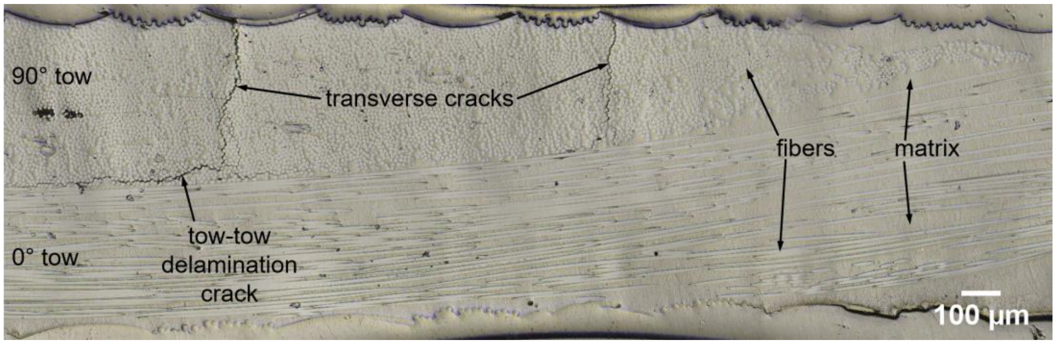

Figure 2.7: Confocal microscopy of a cross-section through a damaged tow-tow overlap after an impact experiment. V_I = 152 m/s, non-perforation.

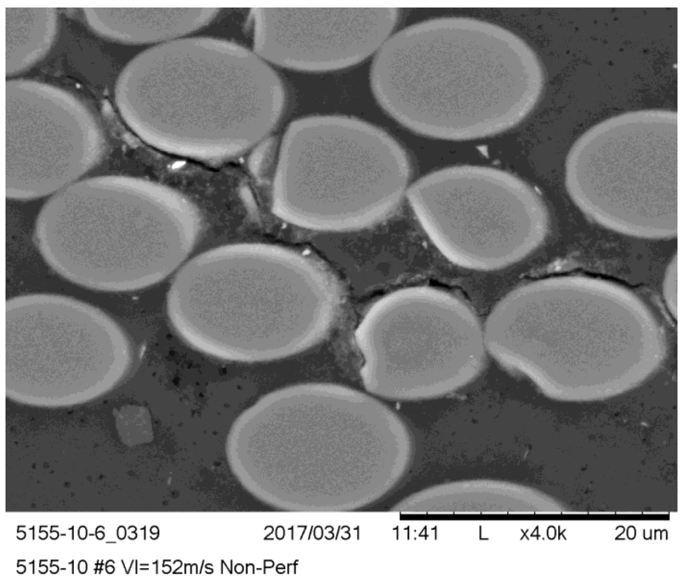

Figure 2.8: Highly magnified (4,000x) scanning electron micrograph of the cross-section through a damaged tow-tow overlap after an impact experiment. V_I = 152 m/s, non-perforation.

The high-resolution images were processed to identify and quantify these mesoscale damage mechanisms.[8], [16], [17] The mesoscale tow-tow delamination is presented in damage maps in figure 2.9. These damage maps show the entire strike face of the experimental specimens with each square representing a single unit cell of tow-tow crossover. Primary tows are outlined in red. The darker the shade in the unit cell, the greater the percent of the unit cell area that is delaminated (c.f., figure 2.6). The damage maps are presented in figure 2.9 with increasing impact velocity from (a) to (f). Recall V_{50} is 175 m/s, so the image in (c) is very near the ballistic limit velocity. Comparing the damage maps, it is clear that tow-tow delamination damage is a maximum at the ballistic limit and decreases with increasing velocity over V_{50}. The quantity of tow-tow delamination damage is plotted as a function of impact velocity in figure 2.10. Figure 2.10 clearly shows a spike in damage at the ballistic limit. Mesoscale damage such as tow-tow delamination and transverse cracks are maximum near the ballistic limit. This is related to primary tow tensile elongation and the formation of a transverse deformation wave, which will be discussed later. As velocity increases beyond V_{50}, there is less time for the development of the deformation wave and damage localizes and becomes dominated by punch-shear.

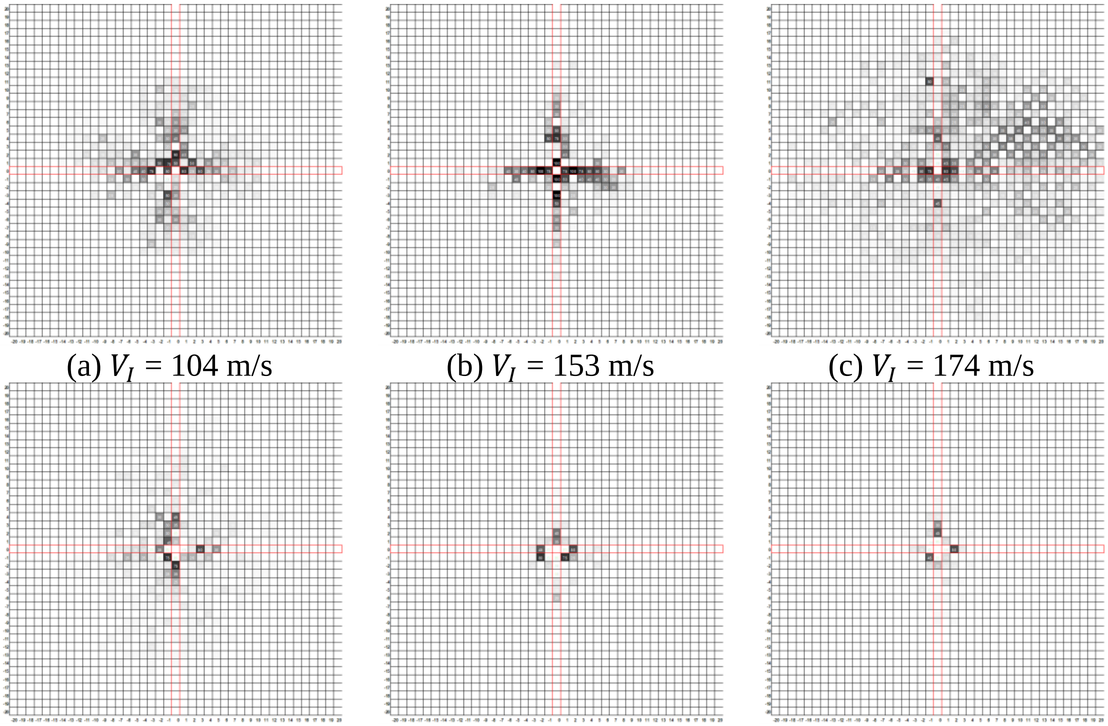

(a) V_I = 104 m/s (b) V_I = 153 m/s (c) V_I = 174 m/s

(d) V_I = 198 m/s (e) V_I = 282 m/s (f) V_I = 472 m/s

Figure 2.9: Damage maps of tow-tow delamination damage illustrating the extent of damage as a function of impact velocity, V_I. Shading indicates extent of damage, and red lines highlight primary tows.

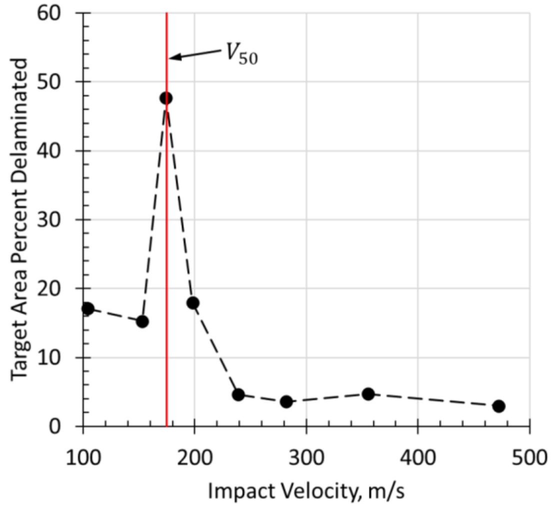

Figure 2.10: Extent of tow-tow delamination damage as a function of impact velocity. Extent of damage is indicated by total delaminated target area. Maximum energy is absorbed by the panel at the V_{50}, corresponding to the maximum in damage extent.

2.4 Continuum Modeling

Ballistic impact experiments are typically conducted on macroscale test specimens. Lower length scale simulations require considerable geometric complexity. The size of test specimens makes simulations with lower length scale resolution computationally expensive. Therefore, composite impact is often simulated with continuum models.[18] Haque and Gillespie [19] used the LS-DYNA [20] explicit, dynamic finite element software to simulate ballistic penetration and perforation of thick-section, multi-layered plain weave S-2 glass/SC-15 epoxy composites. Their continuum models included the rate-dependent, progressive damage and failure constitutive model for composites by Yen [21].

Simple simulations were performed with the plain weave composite modeled as a continuum. The continuum model used effective plain weave properties. The progressive damage, constitutive composite model [21] is discussed in Appendix A. Effective plain weave properties are included in Appendix A. The continuum model results are compared with experimental results in figure 2.11. The continuum model can reasonably predict the perforation behavior for velocities greater than the ballistic limit, but is unable to adequately predict the ballistic limit velocity for this thin composite. As seen in figure 2.11, the continuum model predicts V_{BL} = 104 m/s, which is 41% error compared with experiment. This discrepancy is the motivation for a mesoscale modeling approach.

The mesoscale damage modes were shown to be maximum near the ballistic limit velocity. The continuum model neglects mesoscale architecture and therefore does not include the additional energy dissipation due to mesoscale damage modes. Modeling these damage modes requires a mesoscale model.

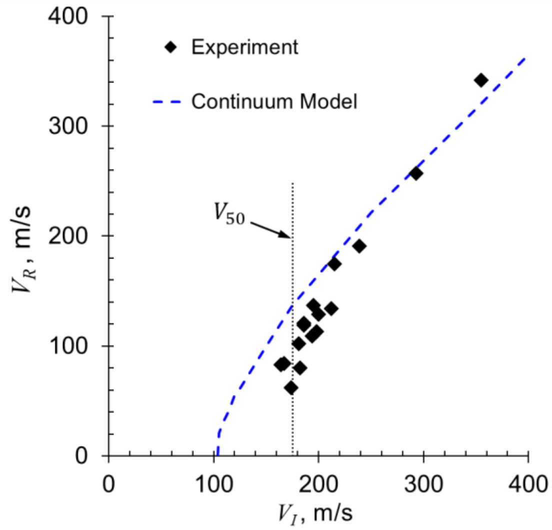

Figure 2.11: Continuum simulation results compared with experimental results. V_{50} = 175 m/s. Continuum V_{BL} = 104 m/s (41% error).

2.5 Preliminary Mesoscale Modeling

Mesostructural architecture in a plain weave composite is composed of interwoven tows and matrix, shown schematically in figure 2.12. The schematic in figure 2.12 has idealized geometry, with no variability in tow shape, angle, or spacing. Olave et al. [22] made measurements of two woven composites' internal mesoscale yarn cross sectional geometry, and studied the effect of mesoscale geometrical variability on macroscale (quasi-static) stiffness using multiscale modeling. They found that mesoscale geometrical variation provides only a small contribution to the experimentally observed stiffness variability, though they did not consider nesting. Their results suggest experimental variability, such as in preparation, setup, and test conditions, has more effect on stiffness than variability in mesostructure. This implies that a mesoscale model using a repeated RVE without variation in geometry, which is the approach taken in the present work, can produce an acceptable macroscale response.

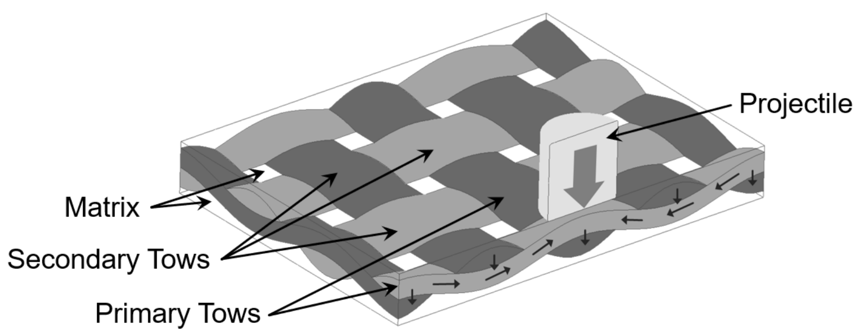

Figure 2.12: Schematic of plain weave fabric composite under projectile impact.

There are a number of methods for discretizing a plain weave RVE. Doitrand et al. [23] compared a voxel mesh (think "Minecraft") to a consistent mesh, which is where the finite element mesh smoothly follows the geometry. They found the voxel approach is inferior to a consistent mesh for simulations in which local stress concentrations are important, such as damage initiation and propagation. They used tetrahedral elements to discretize their RVE. It is much easier to use a tetrahedral mesh than a hexahedral mesh because of the complexity of the mesostructural geometry. However, they state that hexahedral elements are more precise in determining local stress fields.

Hexahedral elements are used in the present work. The mesh is generated with CUBIT [24] based on a script by Key and Alexander [25], [26]. This script uses the geometric equations first proposed analytically by Chou and Ito [27], and later used in finite element analysis by Barbero et al. [28]. These equations are used to generate the RVE geometry shown in figure 2.13 from the parameters indicated in figure 2.13a. These parameters can be determined from micrographs of the composite. Additional detail on the finite element model development will be discussed later.

Most mesoscale modeling of plain weave composites in the literature is focused on predicting stiffness and stiffness degradation and damage evolution due to quasi-static insults (e.g., [22], [23], [28]–[34]). Karkkainan modeled the response of a single plain weave RVE to dynamic loading [13], [14]. Others have applied a mesoscale modeling approach to different fabric composite architectures including twill weave, satin weave, and triaxially braided (e.g., [34]–[41]). Some have used mesoscale modeling to investigate low-velocity impact on woven composites (e.g., [42]–[44]). Mesoscale modeling has been shown to be an effective tool for modeling high-velocity, ballistic impact on plain weave fabric without matrix (e.g., [39], [40], [44]–[51]).

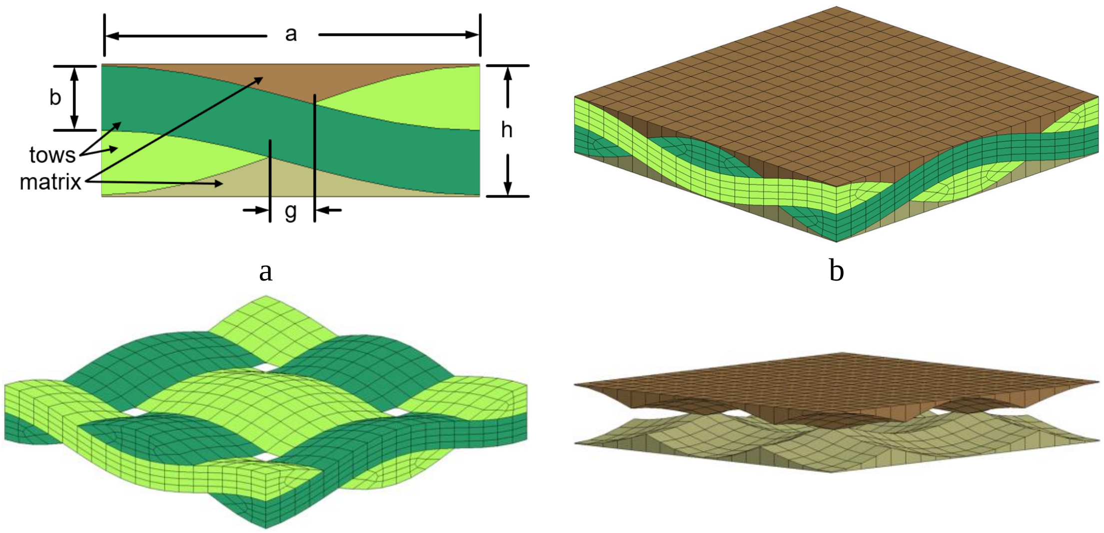

a b

c d

Figure 2.13: Schematic of idealized plain weave composite geometry with (a) parameters used in the generation of a (b) representative volume element, which includes (c) tows and (d) matrix.

However, mesoscale modeling of plain weave fabric composites under high-velocity impact involves complex geometry and rate-dependent material behavior and so can have a high computational cost. One option to reduce computational cost is to minimize the number of elements. Carpenter et al. [52], [53] used a coarse mesh, and got good results compared to mechanical testing, but did not investigate perforation results compared to experiments. Chocron et al. [54] compared multi-layered woven composite impact to experiments, but their mesostructural architecture used a mosaic approach (i.e., block-like, rectangular cross-sectional, straight-edged yarns with no curvature) and was coarsely meshed. A coarse mesh can induce unrealistic stress concentrations at element boundaries and may not properly simulate perforation behavior.

A mesoscale model was developed that included discrete plain weave architecture as shown in figure 2.13. Initially, the dimensions of the unit cell were estimated based on the reported dimensions of the fabric manufacturer and macroscopic composite thickness measurements. The mesoscale model results are compared with experimental and continuum model results in figure 2.14. Simply incorporating mesoscale architecture improved ballistic limit velocity prediction over continuum modeling. Comparing predicted V_{BL} to experimental V_{50} (175 m/s), the respective errors are 41% for the continuum model (104 m/s) and 26% for the mesoscale model (130 m/s). But figure 2.14 and 26% error suggest the mesoscale model is missing additional energy dissipation. This mesoscale model included the plain weave architecture, but rate-dependent matrix plasticity and failure and rate-dependent tow-tow delamination cracking were not included. This preliminary study suggests that incorporating these additional mechanisms will improve limit velocity prediction.

With mesoscale architecture, this model includes some of the energy dissipating mesoscale mechanisms discussed earlier, but not others. Identifying important mesoscale mechanisms and accurately modeling them can provide new understanding of composite penetration mechanics, and opportunity for a materials-by-design approach to improving penetration resistance.

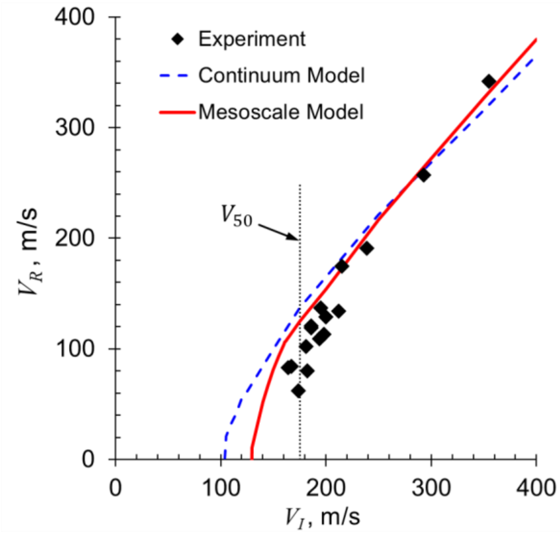

Figure 2.14: Mesoscale and continuum simulation results compared with experimental results. V_{50} = 175 m/s.

2.6 Conclusions

This chapter presented single-layer perforation experiments on plain weave glass/epoxy composites. Backlit, high-resolution photographic study of the post-test damage state revealed mesoscale damage modes including tow-tow delamination. Quantification of the damage as a function of impact velocity showed that this mesoscale damage mode is maximum near the ballistic limit velocity. Continuum modeling was shown to be inadequate for predicting this limit velocity because it does not include mesoscale damage. A preliminary mesoscale model was developed with assumed geometry, limited rate-dependent properties available from the literature, and no tow-tow delamination. This preliminary modeling effort shows that the mesoscale modeling approach can be improved with high-fidelity, realistic geometry, rate-dependent material constitutive behavior, and rate-dependent tow-tow delamination. The next two chapters discuss these improvements.

Chapter 3

MESOSCALE MODEL DEVELOPMENT

3.1 Plain Weave Composite Mesostructure

The mesoscale modeling approach usually involves assumptions about the dimensions of the tow cross sections (e.g., [13], [14], [25], [26], [52]). For example, the plain weave *fabric* used in the present work is specified by the manufacturer as 2 x 2 tows/cm, so it is common to assume the *composite* tow width is 0.5 cm. Mesoscale modeling also typically uses a very coarse mesh (e.g., [52], [54]), a non-consistent mesh that does not follow realistic tow undulation and geometry (e.g., [23], [52], [54]), and unrealistic assumptions about fiber volume fraction (e.g., [13], [14], [52]).

To develop a more realistic mesostructural model of the glass/epoxy plain weave composite, a number of specimens were sectioned, mounted, and polished for microscopic examination. A typical repeating volume element (RVE) cross section is presented in figure 3.1. This image was created with a Keyence VHX-6000 microscope. Similar images were acquired for thirteen RVE cross sections.

Built-in functionality in the Keyence VHX-6000 microscope was used to measure cross-sectional tow dimensions, tow-tow gaps, and RVE dimensions. The RVE model-creation dimensions are reproduced in figure 3.2. These dimensions, determined from measuring thirteen RVE cross sections, are provided in table 3.1. The composite thickness was measured macroscopically with calipers from test specimens since it includes variations in tow compaction, matrix, and undulation over a larger area. Fifteen test specimens were measured to get average thickness.

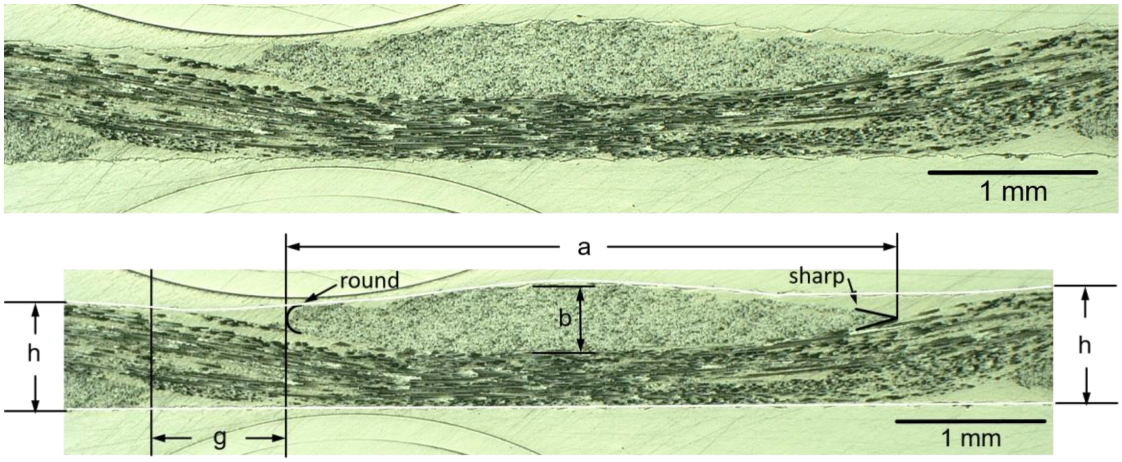

Figure 3.1: Typical plain weave glass/epoxy RVE cross section and with dimensions.

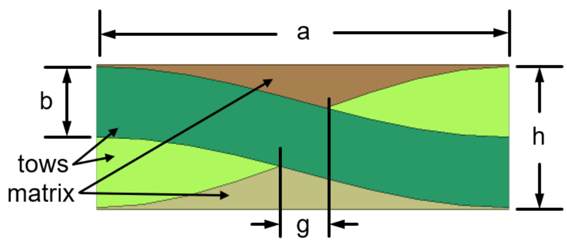

Figure 3.2: Plain weave unit cell dimensions. Unit cell shown is ¼ of an RVE. See reference [28] for equations.

Table 3.1: Plain weave unit cell dimensions measured microscopically from 13 cross sections. Composite thickness measured macroscopically from 15 test specimens.

Description	Parameter	mm
unit cell width	a	4.54 ± 0.23
tow thickness	b	0.46 ± 0.05
tow-tow gap	g	0.36 ± 0.32
composite thickness	h	0.89 ± 0.02

The mesostructural architecture is complex with interwoven, undulating tows and matrix filling space between and around tows. Hence, one of the most difficult aspects of mesoscale modeling fabric composites is generating the mesh.[23] Developing the geometry of the thin ends of the tow cross section is particularly challenging, and several approaches are used in the literature. Some mesoscale models use round ends.[13], [14], [32] Some use truncated ends.[41], [43], [50]–[52], [54] And some use sharp ends.[25], [26], [28] As can be seen in figure 3.1, examples of both round ends and sharp ends can be found in microscopic images of RVEs. While both are valid, examination of the thirteen RVE cross sections suggests the sharp ends are more prevalent. The equations by Ito and Chou [27] and by Barbero et al. [28] generate sharp ends, as in figure 3.2.

As briefly described earlier, a CUBIT [24] script was used to generate a plain weave composite RVE mesh from input of the dimensions in table 3.1.[25], [26] The script allows for the specification of number of elements through the thickness of a tow, through the thickness of a matrix layer, across the width of a tow, and across the width of the tow-tow gap. Because of the sharp-end tow geometry, the number of elements through the tow thickness must be even. The minimum tow through-thickness mesh refinement is two elements, and four was selected to provide high mesh refinement while maintaining manageable computational cost. Typically one or two elements through the tow thickness is used in the literature (e.g., [32], [41], [43], [50]–[52], [54]). There can be one or more elements through matrix thickness, but the matrix is very thin in places, so one is best to avoid driving down the timestep. The gap width and tow width elements were selected to provide a square mesh on the top and bottom RVE surfaces. The RVE mesh is shown in figure 3.3.

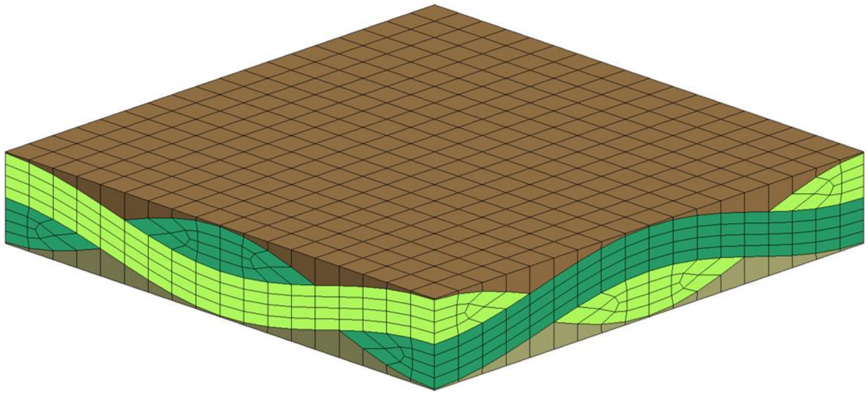

Figure 3.3: Plain weave RVE mesh. (Thickness exaggerated to show detail.)

Multi-layered plain weave composites are generally modeled with flat-top, flat-bottom RVEs similar to figure 3.3. The RVEs are tiled in space both laterally and vertically to build the desired length, width, and thickness of composite target.

Because of the flat matrix geometry shown in figure 3.3, mesoscale models typically must make assumptions about the FVF. Mesoscale models usually neglect the matrix within tows (e.g., [52], [54]). This implies an unrealistically large FVF locally within tows or a lower global FVF than what is found in real composites.[13], [14], [37]

The single-layer experiments discussed earlier have a top surface that follows the tow undulation, as seen in figure 3.1 Burn out was conducted on 20 samples of the plain weave glass/epoxy composites per ASTM D 3171-99. The global fiber volume fraction (FVF) was found to be 45%. Therefore, the RVE geometry in figure 3.3 was made more realistic by adjusting the top and bottom matrix volumes to be more like figure 3.1. The modified RVE is shown in figure 3.4. The single-layer mesoscale model built from this RVE has 45% global FVF (assuming 60% local FVF in tows), which matches the burn-out measurement of the real composite. The local FVF in tows was investigated with electron and optical microscopy, and the average local FVF was found to be 62 ± 0.06%.

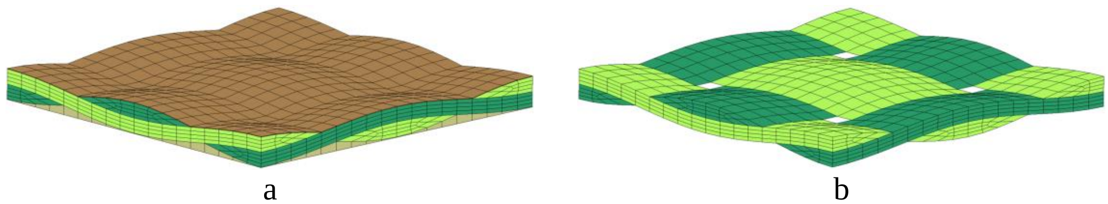

Figure 3.4: Plain weave RVE with matrix layers modified to follow tow undulation and ensure proper global fiber volume fraction. (a) RVE with matrix layers and (b) tows only.

The RVE in figure 3.4 was tiled in space to model the single-layer 300 x 300 mm test specimens described earlier.

3.2 Preliminary Model Validation

The modified mesoscale model was used to simulate the single-layer perforation experiments discussed earlier.[9] In addition to the geometric modifications, this model added rate-dependent matrix and tow-tow delamination.

3.2.1 Unidirectional Composite Tows

The unidirectional composite tows were simulated (both here and earlier) with the progressive damage composite material constitutive model known as MAT_162 in LS-DYNA, which is discussed in Appendix A. For convenience, the parameters used in the model are reproduced here in table 3.2. These parameters are based on those reported in the literature [55] for unidirectional glass/epoxy composite. Initially, the composite tows were modeled as rate-independent. Later work will incorporate strain-rate dependence.

Table 3.2: Unidirectional glass/epoxy parameters for MAT_162 [55].

Miscellaneous Properties	Fiber Volume Fraction 60%	Density, ρ, g/cm^3 1.85		
Elastic Modulus	E_{11}, GPa 64.0	E_{22}, GPa 11.8	E_{33}, GPa 11.8	
Poisson's Ratio	ν_{21} 0.05	ν_{31} 0.05	ν_{32} 0.45	
Shear Modulus	G_{12}, GPa 4.3	G_{23}, GPa 3.7	G_{31}, GPa 4.3	
Tensile Strength	X_{1T}, MPa 1380	X_{2T}, MPa 45	X_{3T}, MPa 45	
Compressive Strength	X_{1C}, MPa 770	X_{2C}, MPa 137		
Shear Strength	S_{12}, MPa 76	S_{23}, MPa 38	S_{31}, MPa 76	
Fiber Mode Strength	S_{FC}, MPa 850	S_{FS}, MPa 250		
Erosion Criteria	Axial Erosion Strain 4.5	Expansion Erosion 4.5	Compression Erosion 0.001	
Rate Effects	X_{1T}, X_{1C}, X_{2T}, X_{2C}, S_{FC}, S_{FS} 0.00	E_{11}, E_{22} 0.00	G_{12}, G_{23}, G_{31} 0.00	E_{33} 0.00

The model and properties are transversely isotropic. Strength and stiffness are greatest in the fiber direction (e.g., X_1 and E_{11} in table 3.2), and significantly less so transverse to the fibers. To accurately simulate the fiber direction in the undulating, interwoven composite tows, each finite element had an orientation assigned to it. This aligned the fiber direction properties with the geometry of the tows. This alignment is illustrated by figure 3.5.

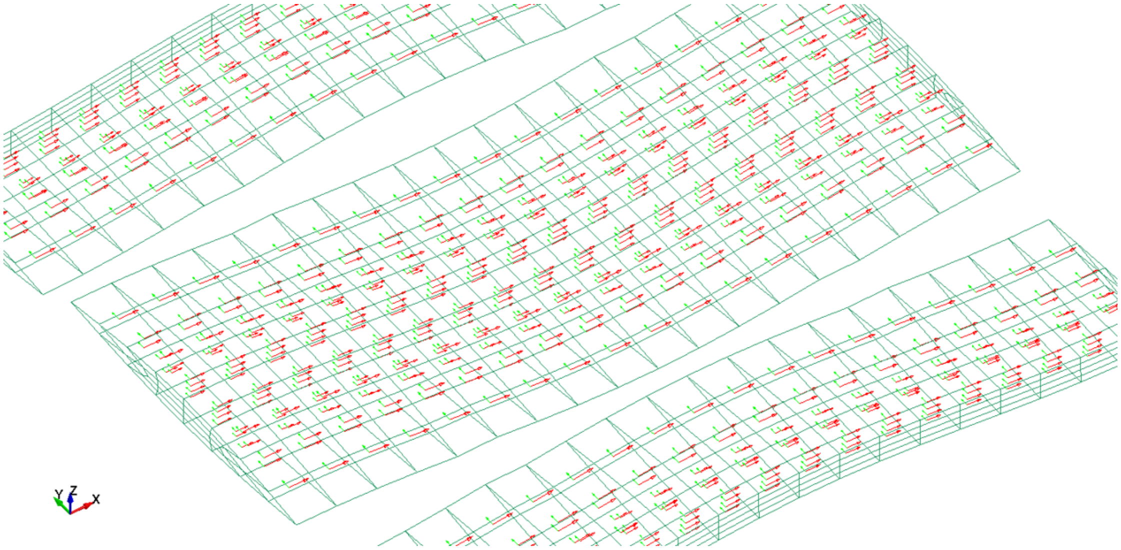

a

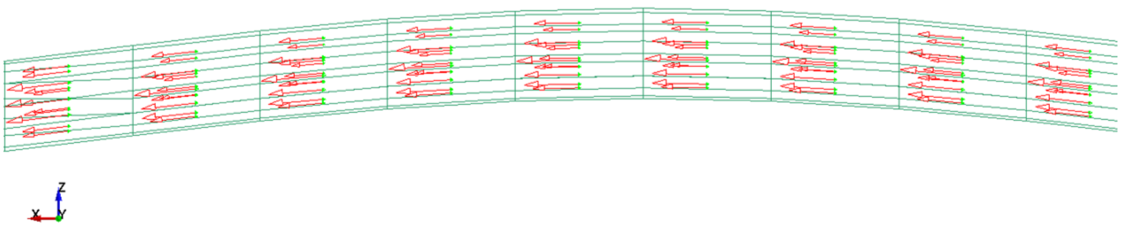

b

Figure 3.5: Finite element model property orientations following the fiber direction tow geometry. Red arrows indicate fiber direction, and green indicate transverse direction in (a) RVE warp tows and (b) warp tow cross section.

3.2.2 Rate-dependent Matrix

The epoxy matrix in these experiments [9] was simulated based on material properties from the literature.[56], [57] In LS-DYNA simulations, MAT_003 was used, which is also known as *MAT_PLASTIC_KINEMATIC. This model accounts for strain rate with a Cowper-Symonds [58] power law, strain hardening constitutive relation as in equation (3.1). [59] Here, yield stress, σ_0, is scaled by a function of strain rate, $\dot{\varepsilon}$, and two material constants, C and p. These material constants were determined by Pankow et al. [56] for SC-15 epoxy and are provided in table 3.3, along with other relevant material properties .

$$\sigma(\dot{\varepsilon}) = \sigma_0 + \sigma_0 \left(\frac{\dot{\varepsilon}}{C}\right)^{\frac{1}{p}} \tag{3.1}$$

Table 3.3: Matrix properties for SC-15. [56], [57]

Density	1.14 g/cm^3
Modulus	2.48 GPa
Poisson's ratio	0.36
Yield stress, σ_0	48.3 MPa
C	4880
p	2.883

3.2.3 Preliminary Tow-tow Delamination

Tow-tow delamination is modeled with the cohesive zone model approach, which is detailed in the next chapter. This approach is incorporated into the mesoscale model as a tiebreak contact between overlapping tows. Refer to the LS-DYNA manual [59] for additional information about tiebreak contact. This model used *CONTACT_AUTOMATIC_ONE_WAY_SURFACE_TO_SURFACE_TIEBREAK, option 9, which follows from the MAT_138 (*MAT_COHESIVE_MIXED_MODE) cohesive element formulation. The tiebreak contact approach was chosen over cohesive elements because of the size and complexity of the geometric interfaces.

This formulation is rate-independent and assumes a mixed-mode bilinear traction-separation law. The bilinear law involves linear stiffness as load increases to a peak traction, followed by a linear softening until the maximum opening displacement is reached. The bilinear traction-separation laws for mode I tension and mode II shear are described by equations (3.2), which are illustrated by figure 3.6. Here, EN is normal (tensile) stiffness, ES is shear stiffness, T_I and T_{II} are tensile and shear tractions, G_{Ic} and G_{IIc} are tensile and shear energy release rates, and δ_I and δ_{II} are tensile and shear separation.

$$G_{Ic} = \frac{1}{2} T_I \delta_I$$
$$G_{IIc} = \frac{1}{2} T_{II} \delta_{II} \tag{3.2}$$

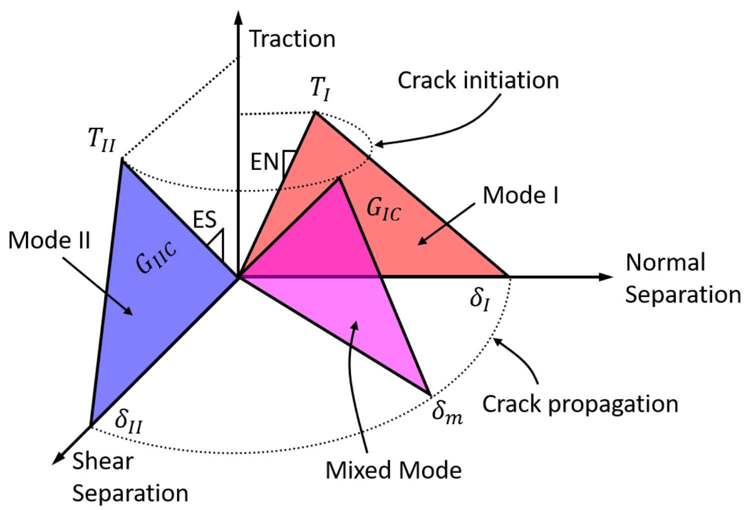

Figure 3.6: Schematic of mixed-mode bilinear traction-separation law.

Mixed mode displacement, δ_m, is given by $\delta_m = \sqrt{\delta_I^2 + \delta_{II}^2}$. The maximum mixed-mode opening displacement at interfacial failure is given by equation (3.3).

$$\delta^{failure} = \frac{2(1+\beta^2)}{\delta^0}\left[\left(\frac{EN}{G_{Ic}}\right) + \left(\frac{ET \times \beta^2}{G_{IIc}}\right)\right]^{-1} \tag{3.3}$$

where $\delta^0 = \delta_I^0 \delta_{II}^0 \sqrt{\frac{1+\beta^2}{(\delta_{II}^0)^2 + (\beta\delta_I^0)^2}}$ is the onset of softening determined from the displacements at peak tractions (i.e., $\delta_I^0 = T_I/EN$ and $\delta_{II}^0 = T_{II}/ES$) and the mode mixity, $\beta = \delta_{II}/\delta_I$.

Carpenter et al. [52] assumed a maximum opening displacement of 0.0001 mm (0.1 μm) for the $\delta^{failure}$ for the yarn/matrix interface. Then they calibrated the peak tractions using finite element models of torsion and delamination experiments. They note that their traction law may be relevant only to their rough, right-angle-dominated plain weave geometry, because it includes the stress concentrations due to this geometry. The present work uses a more consistent and realistic plain weave geometry as discussed earlier. Additionally, note that this traction-separation law (TSL) is reported as between yarn and matrix, not yarn and yarn, which is where tow-tow delamination occurs. Hence, it is anticipated that additional fidelity of TSLs will be needed. Nonetheless, the TSL by Carpenter et al. is provided in table 3.4. Carpenter et al. reported a quasi-static TSL as well, but table 3.4 includes only the medium-rate TSL, which is for $\dot{\varepsilon} = 1\ \mathrm{s}^{-1}$.

Table 3.4: Traction-separation law used initially for tow-tow delamination.[52]

$\dot{\varepsilon}$	$1\ \mathrm{s}^{-1}$
EN	520,000 MPa/mm
ES	1,000,000 MPa/mm
T_I	52 MPa
T_{II}	100 MPa
G_{Ic}	0.0026 MPa-mm
G_{IIc}	0.0050 MPa-mm

3.2.4 Preliminary Results

Recall that this data is from single-layer, plain weave, S-2 glass, SC-15 epoxy perforation experiments.[9] Targets were impacted by 5.6 mm diameter, right circular cylindrical steel projectiles. Test specimens were 300 x 300 mm with clamped boundary conditions outside of a 200 mm diameter hole. Figure 3.7a shows a photograph of a test specimen clamped in the test fixture. Figure 3.7b shows the mesoscale model. The experiments were simulated with a full three-dimensional model using LS-DYNA. Figure 3.8 shows a cross-section through the center of the mesoscale model.

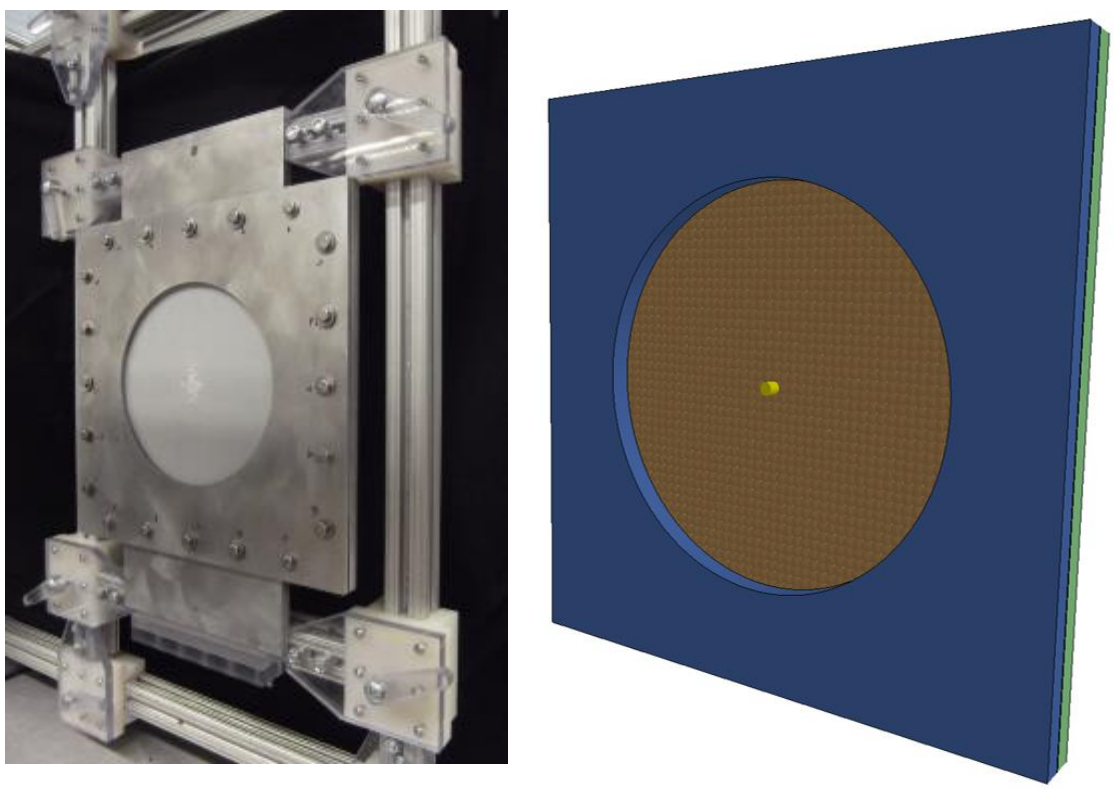

a b

Figure 3.7: (a) Experiment test setup with clamped boundary conditions. (b) Mesoscale model with clamped boundary conditions.

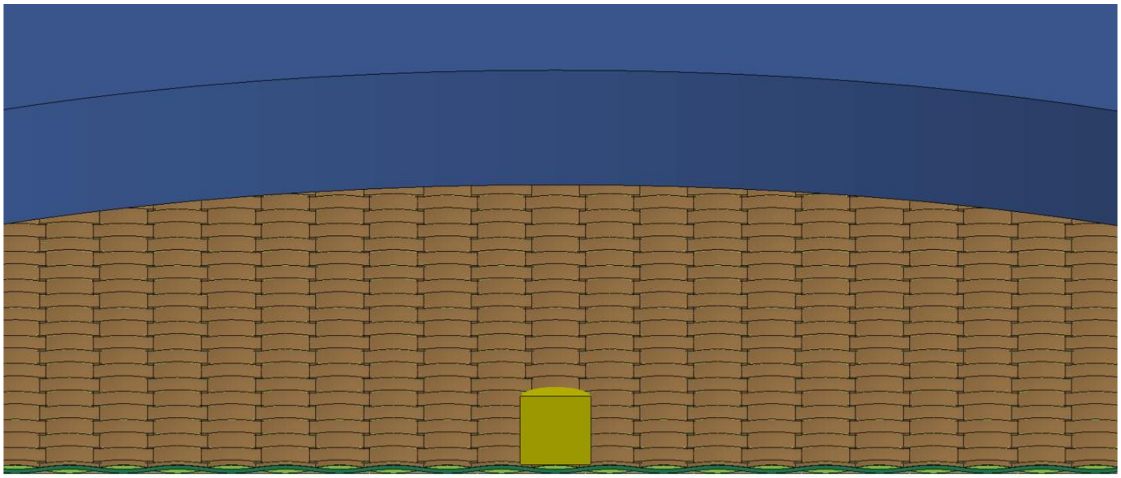

Figure 3.8: Cross section through center of mesoscale model showing clamped boundaries, projectile, and mesoscale architecture.

The predictions by the continuum model, initial mesoscale model, and modified mesoscale model are compared with the experimental data in figure 3.9. All models adequately predict the residual velocity for impact velocities that are much greater than the ballistic limit velocity, V_{50} = 175 m/s. The continuum model predicts V_{BL} with 41% error (104 m/s). Simply adding mesoscale architecture improved V_{BL} prediction to 26% error (130 m/s). The addition of realistic geometry, rate-dependent matrix, and tow-tow delamination increased the accuracy of the mesoscale model predictions near the ballistic limit velocity. With these additions, V_{BL} prediction improved to 7% error (163 m/s).

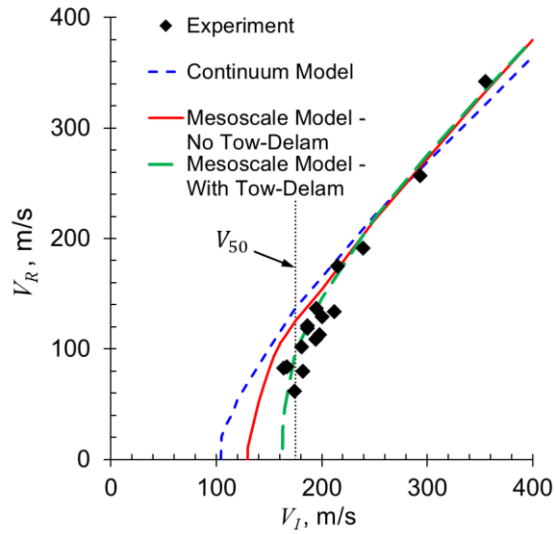

Figure 3.9: Comparison of experimental results with continuum model and mesoscale models without and with tow-tow delamination.

3.3 Conclusions

In this chapter, fidelity was added to the mesoscale model. First, real composite test specimen geometry and fiber volume fraction were investigated. Then the mesoscale model was modified to more realistically reproduce this geometry and FVF. Next, rate-dependent matrix behavior was added to the model. Finally, tow-tow delamination was added to the model.

The prediction of V_{50} was improved, but more improvement is needed to develop a predictive model that can be used to investigate mesoscale damage and partition energy dissipation. Three areas were improved in this chapter: geometry, matrix, and tow-tow delamination. These three areas significantly enhanced the model, which suggests they could be considered for further development. First, improvements in geometry can be made by incorporating more realistic or stochastic tow cross-sectional shapes and stochastic material properties, which vary along the tow length as fiber volume fraction varies. However, such stochastic improvements are beyond the scope of the present work and are recommended for future model development. Second, the matrix was modeled in this chapter with a simple elastic-plastic material model with strain-rate dependent hardening. Incorporating a more advanced rate-dependent model and properties could also improve the model. Finally, the tow-tow delamination was modeled based on assumption of maximum opening displacement and without rate-dependence. Therefore, developing rate-dependent traction-separation laws for governing tow-tow delamination is the focus of the next chapter.

Chapter 4

RATE-DEPENDENT TRACTION-SEPARATION LAW PREDICTIONS

Material damage mechanisms occur at characteristic length scales, which are determined by the inhomogeneities in the material.[60] At the microscale, fracture in polymer composites occurs relative to the fiber reinforcement. Cracks generally propagate through matrix and around fibers as seen in figure 4.1.

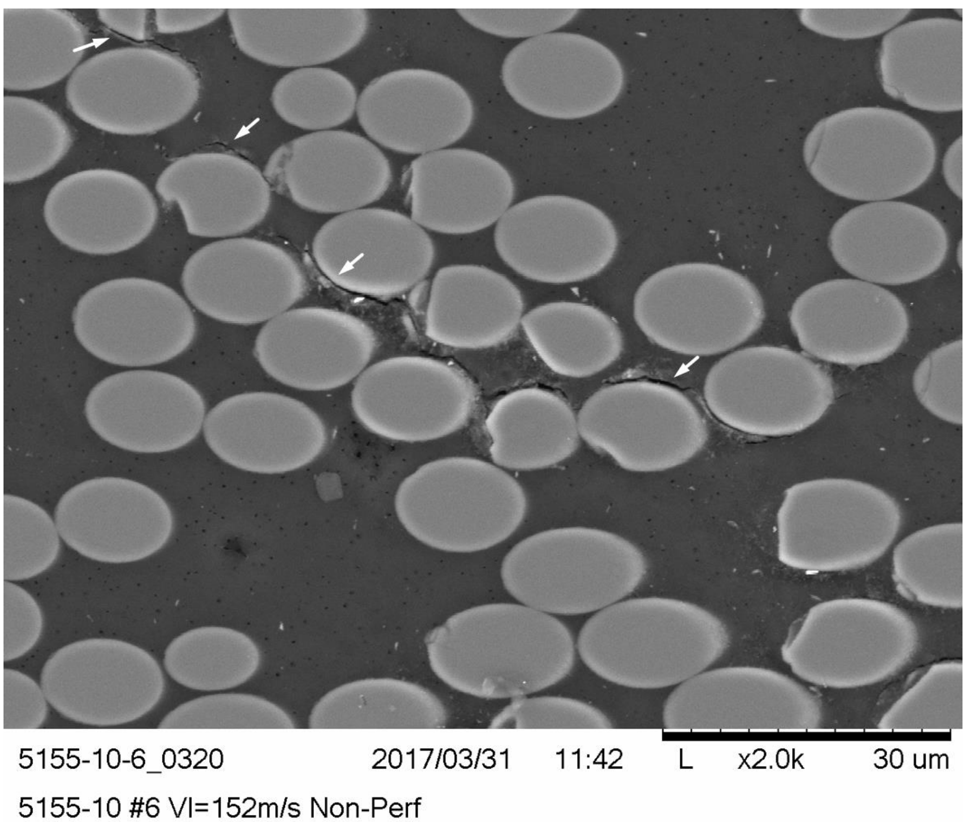

Figure 4.1: Scanning electron micrograph of ballistically impacted plain weave glass/epoxy composite. Crack path is indicated by white arrows.

At the microscale in figure 4.1, the important damage mechanisms involved in this crack include rate-dependent matrix plasticity, rate-dependent matrix failure, and rate-dependent fiber-matrix interfacial failure. In this chapter, these damage mechanisms are incorporated into a model of fiber-matrix microstructure embedded into a mesoscale continuum. Matrix plasticity and failure and fiber-matrix interfacial failure are based on rate-dependent experiments and modeling work from the literature. The J-integral method is used to bridge from the microscale to the mesoscale to determine mesoscale traction-separation laws from microscale fracture models. This work makes heavy use of the cohesive zone model, which is discussed next.

4.1 Cohesive Zone Model

Fracture involves material discontinuity, so it is a challenge to model with Lagrangian finite element methods, such as in LS-DYNA, which generally assume continuity. Nonetheless, there are a number of options for modeling crack growth in finite element models (FEMs). These options include element erosion, release of constrained or merged nodes, element enrichment, or cohesive elements placed along a crack front.[61] In general, some sort of failure criteria governs all of these approaches. There are benefits and drawbacks to each approach. For example, element erosion affects the mass and energy of a finite element analysis, which can affect the evolution of an analysis over time. Cohesive zones typically require *a priori* knowledge of where a crack will occur, which the analyst may not know for complex geometries. The present work makes use of both element erosion and the cohesive zone model (CZM) for the simulation of fracture.

First proposed by Dugdale [62] and Barenblatt [63], CZM has been used to model delamination and fracture in composites (e.g., [64]–[73], etc.). Carpenter et al. [52] used CZM to model cracking between tows and matrix in a plain weave mesoscale model, but they did not consider delamination between interwoven, orthogonal tows. This section provides a brief overview of CZM, but a more detailed discussion is found in these reviews.[74]–[77]

Fracture under remote loading involves the gradual separation of material within a fracture process zone (FPZ). This FPZ is shown schematically in figure 4.2a. Here crack opening within the FPZ involves fibers and matrix. The CZM is a phenomenological model. It approximates the FPZ ahead of a growing crack as a continuum, as shown schematically in figure 4.2b. Because of the continuum assumption, discrete microstructure, such as fibers and matrix, is not required to model the crack opening.

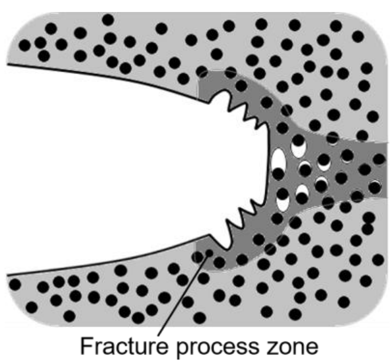

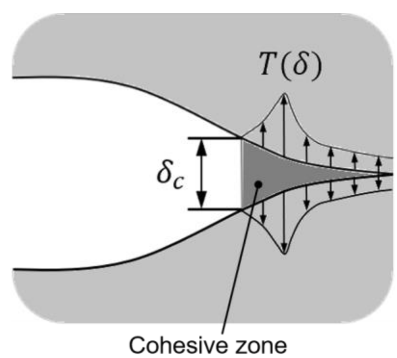

Figure 4.2: (a) Schematic of the fracture process zone ahead of a growing crack, with discrete fibers and matrix. (b) The cohesive zone, a continuum approximation of the fracture process zone.

CZM assumes that the tractions, T, which resist crack opening, are uniquely related to crack opening displacements, δ, such that the critical energy release rate, G_c, necessary for crack growth is given by equation (4.1).

$$G_c = \int_0^{\delta_c} T(\delta)\, d\delta \tag{4.1}$$

Identifying the material constitutive relationship described by equation (4.1) is a significant challenge of the CZM.[74] This constitutive relationship is known as the cohesive law or the traction-separation law (TSL). The TSL governs the tractions that resist cohesive zone separation, T, the critical separation when the cohesive crack propagates, δ_c, and the energy dissipated by this process, G_c.

Many shapes have been investigated for TSLs including linear, bi-linear, tri-linear (or trapezoidal), and exponential. Examples of these TSL shapes are in figure 4.3. The most commonly used shape is bi-linear. Other more complicated shapes have been proposed. The present work uses bi-linear or tri-linear since these are commonly used for modeling delamination.

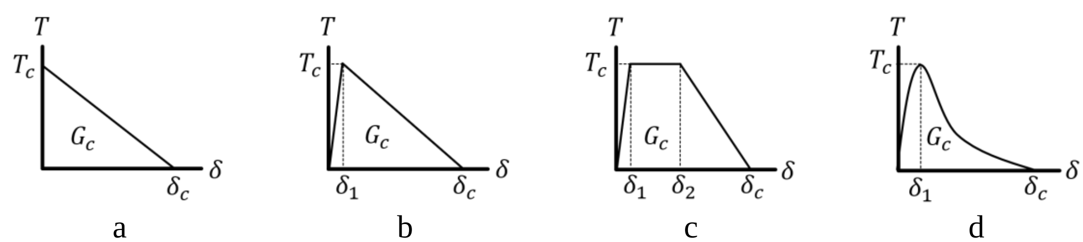

Figure 4.3 Schematic of cohesive traction-separation law shapes including (a) linear, (b) bi-linear, (c) tri-linear or trapezoidal, (d) exponential.

Requirements for TSLs include defining a cohesive strength, work of separation, and tension-shear coupling.[78] A schematic mixed-mode TSL is shown in figure 4.4. The cohesive strengths are the peak mode I (tension) and mode II (shear) tractions, when cracking initiates. The maximum displacement occurs when the crack propagates, and is determined from the work of separation, which is the area under the curves. It has been suggested that the cohesive strength, T, and the cohesive energy, G_c, have more effect on behavior than crack displacement, δ.[79] Needleman [78] states the shape does not significantly affect results if the cohesive zone length is much smaller than the relevant geometric length. Research suggests some TSLs fit particular material behavior better than others, particularly ductile, brittle, and quasi-brittle behavior.[74], [80]–[82] In finite element modeling, an initially rigid or infinite slope (i.e., figure 4.3a) can cause numerical instability, so this shape is generally not used in FEM.[83]

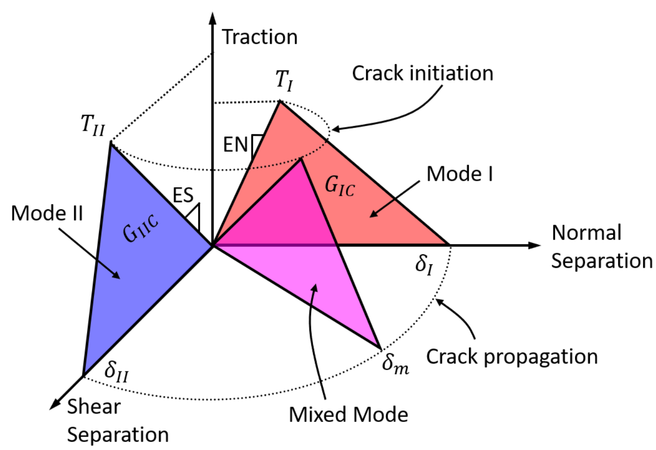

Figure 4.4: Schematic of a mixed-mode, bi-linear, traction-separation law.

Traction-separation laws have been determined experimentally, by molecular dynamics, by finite element analysis, or by some combination of these.[78], [84]–[86] In this work, we use finite element analysis to determine TSLs for use in modeling mesoscale damage.

4.2 J-integral Method

The J-integral method was introduced by Li et al. [86] in 1987. It evaluates the J-integral [87] over a closed contour, Γ, around the fracture process zone (FPZ). In this case, the J-integral specializes to

$$J(\delta) = \int_{\Gamma} T(\delta)\, d\delta \tag{4.2}$$

Then differentiation of equation (4.2) yields the traction-separation law, equation (4.3).

$$T(\delta) = \frac{\partial J(\delta)}{\partial \delta} \tag{4.3}$$

The TSL is determined from the J-integral as a function of crack opening displacement. But determining a TSL for microscale fracture involves very small-scale experiments and observations, requires specialized equipment and techniques, and so may not be practical or possible. The present work uses finite element analysis (FEA) to characterize the TSL while including important microscale deformation and damage mechanisms.

The J-integral is a contour integral, which is not practical in FEA. A domain integral is needed. Shih et al. [88], [89] derived the energy domain integral from the contour J-integral. A detailed derivation is reviewed in Appendix B. Numerical computation of the J-integral uses the energy domain integral. This domain J-integral can be applied to various loading conditions and material behavior, and is mesh insensitive for domains defined sufficiently far from the crack tip.[61]

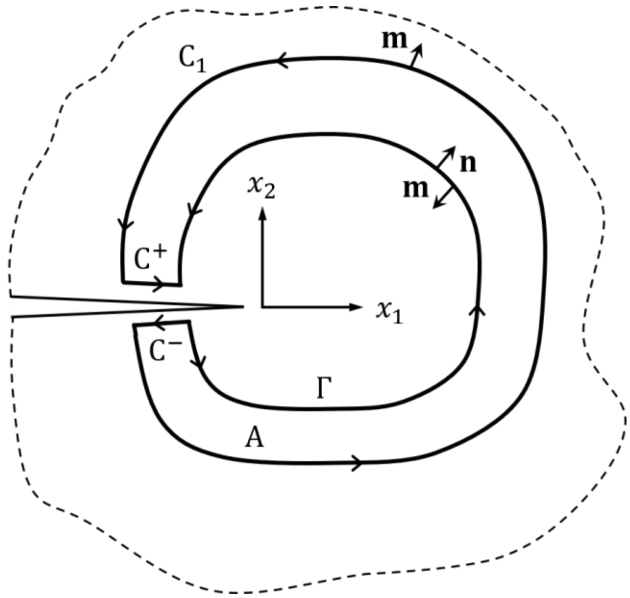

Figure 4.5: Schematic of the energy domain J-integral taken around a crack tip.

Consider figure 4.5. The closed contour $C = C_1 + C^- + C^+ - \Gamma$ has an outward normal unit vector, **m**. The area enclosed by C is A. The crack grows in the x_1 direction. The arbitrary contour Γ begins and ends on the crack line, and has an outward normal **n**. It can be shown [90] that the energy domain integral can be written as

$$J = \int_A \left(\sigma_{ij} \frac{\partial u_i}{\partial x_1} \frac{\partial \tilde{q}}{\partial x_j} - \mathcal{W} \frac{\partial \tilde{q}}{\partial x_1} \right) dA \qquad (4.4)$$

where $\tilde{q}(x_1, x_2)$ is any sufficiently smooth function such that $\tilde{q} = 1$ on Γ and $\tilde{q} = 0$ on C_1.

To compute this energy domain integral from a finite element model, the in-plane stress, strain, and displacement are output for each element k in the domain over time t. Then the J-integral is computed according to

$$J^k(t) = \int_{A^k} \left(\sigma_{ij}^k \frac{\partial u_i^k}{\partial x_1} \frac{\partial \tilde{q}^k}{\partial x_j} - \mathcal{W}^k \frac{\partial \tilde{q}^k}{\partial x_1} \right) dA^k \tag{4.5}$$

where for each element k, A^k is the in-plane area, σ_{ij}^k are the stresses at the integration point, u_i^k are the displacements averaged from the nodes, $\mathcal{W}^k$ are the strain energy densities. Strain energy density is computed from the stresses at element integration points and strains averaged from element nodes according to

$$\mathcal{W}^k = \int_0^{\varepsilon_{ij}^k} \sigma_{ij}^k d\varepsilon_{ij} \tag{4.6}$$

Crack opening displacement is output from the FEM as a function of time, $\delta(t)$. The $\tilde{q}^k$ is a function where $\tilde{q}^k = 1$ at the nodes closest to the crack tip and $\tilde{q}^k = 0$ at the nodes furthest from the crack tip for each element. Typically, the arbitrary function $\tilde{q}$ is defined using the shape functions of the finite elements such that

$$\tilde{q} = \sum_{i=1}^{n} N_i \tilde{q}_i \tag{4.7}$$

where the N_i are the shape functions and $\tilde{q}_i$ are the values of $\tilde{q}$ at nodes $i = 1, \dots, n$. Then $\tilde{q} = 1$ on the inner nodes and $\tilde{q} = 0$ on the outer nodes, relative to the crack tip.

For two-dimensional (2D) rectangular elements in the YZ plane, element shape functions are given by

$$N_1 = \frac{1}{4ab}(Y-a)(Z-b); N_2 = -\frac{1}{4ab}(Y+a)(Z-b);$$
$$N_3 = \frac{1}{4ab}(Y+a)(Z+b); N_4 = -\frac{1}{4ab}(Y-a)(Z+b) \tag{4.8}$$

where $2a$ is the element Y-dimension and $2b$ is the element Z-dimension, and the nodes are numbered counterclockwise. The J-integral can be computed using equations (4.5) to (4.8) from a ring of 2D (or 3D with plain strain boundary conditions) finite elements surrounding a crack tip.

4.3 Embedded Cell Modeling Approach

4.3.1 Background

A J-integral tool has been implemented in LS-DYNA [91] and in ABAQUS [92]. These tools compute the J-integral as a function of time for a contour of finite elements surrounding the crack tip. The J-integral tool involves inputting the number of contours desired. Then the tool computes the J-integral for that number of contours beginning with the elements touching the crack tip and expanding away from the crack tip. In this way, the J-integral has been shown to converge to a consistent value with sufficient distance from the crack tip.[93], [94]

However, Brocks and Scheider [93], [94] demonstrated that discretization error can lead to domain dependence in FEM computation of the J-integral. They also discussed that plastic deformation causes some domain dependence. This is because the existence of the strain energy density potential in equation (4.6) presumes small strain and the deformation theory of plasticity. Discretization error can be reduced by mesh refinement in the FPZ. Error associated with large deformation can be reduced by considering far-field behavior for contours in the elastic region outside the FPZ. Additionally, the contour cannot touch the boundary or any stress concentration. Finally, numerical evaluations of the J-integral should have consistent loading conditions with no unloading or recovery.[93], [94]

Sarrado et al. [92] used the ABAQUS tool to compute mode-decomposed energy release rates for a (macroscale) continuum composite FEM of mixed-mode bending. Sarrado et al. showed that thermodynamically consistent cohesive formulations can provide accurate energy dissipation under mixed-mode loading. Since the contour must be continuous, material discontinuities such as fiber-matrix interfacial failure can cause the built-in J-integral tools to fail, requiring manual calculation of J. The work by Sarrado et al. considered a continuum, which did not include microscale damage mechanisms.

A microscale representative volume element (RVE) of a ceramic fiber metal matrix composite was modeled in an FEA by Scheider [95]. He used this model to derive a TSL, and considered ductile matrix damage and fiber-matrix interface debonding. Scheider suggested that the stress-displacement of the microscale RVE could be directly used as a mesoscale TSL. However, his model considered fibers oriented in three principal directions and embedded in a simple cuboid geometry. Since RVEs typically use periodic boundary conditions, it is not clear if this approach effectively models microscale behavior when bridged up to a structural length scale model.

The embedded cell modeling approach was first used by Canal et al.[96] In this approach, a small region with resolved microstructure is embedded in a larger continuum. The microstructure is assumed to be homogenized into the continuum.

Canal et al. showed this approach is very accurate for predicting damage development ahead of the growing crack tip and for modeling the macroscopic response.

The embedded cell method was also used by Montenegro et al. [97] to model a single-edge notched beam experiment. They included microstructural resolution in the FPZ, and a linear elastic, transversely isotropic continuum composite outside of the FPZ. They modeled isotropic, linear elastic glass fibers, matrix plasticity and damage, and bi-linear cohesive fiber-matrix interfaces. However, neither their matrix constitutive behavior nor their fiber-matrix interface debonding were rate-dependent.

It has been shown that cohesive traction, energy, and traction law shape are strain rate dependent.[98] Montenegro et al. [97] computed the J-integral in the continuum region of their embedded cell model. They used load-line displacement for δ. They showed that the embedded cell approach produces similar results to experiments. But their work did not consider strain rate dependence.

Liu et al. [99] also used the embedded cell and J-integral approach proposed by Montenegro et al.[97] Liu et al. included rate-dependent matrix behavior and a dynamic J-integral formulation (in implicit calculations), but they did not include rate-dependent fiber-matrix debonding. Also, Liu et al. studied crack speed and energy decomposition rather than deriving a traction-separation law.

The present work uses the embedded cell and J-integral approach with rate-dependent matrix and rate-dependent fiber-matrix interface debonding, and uses this approach to derive a traction-separation law. The J-integral is used to bridge from the microscale embedded cell fracture behavior to mesoscale traction-separation laws.

4.3.2 Embedded Cell Model Development

The embedded cell methodology consists of a small-scale finite element model embedded within a large-scale finite element model. In the present work, the small scale involves a microstructure of fibers and matrix, and the large scale involves a mesoscale continuum.

4.3.2.1 Fiber-matrix Microstructure

As discussed earlier, microscopy of tow cross sections showed the average in-tow FVF is about 60%. This work seeks to bridge length scales from discrete fiber-matrix microstructure to the mesoscale in which the fibers and matrix are homogenized into a continuum. Thus, it is important to maintain 60% FVF and locally dense fiber-matrix packing.

A single-fiber unit cell with 60% FVF was developed, and is shown in figure 4.6. This unit cell has the fiber centered. To introduce stochasticity into the microstructure while maintaining 60% FVF throughout, the fiber position within this unit cell was perturbed in one of 16 degrees of freedom (DOF). These 16 DOF were produced by moving the fiber along each of 8 axes by either 1/3 or 2/3 of the distance to the edge of the unit cell. This is exemplified by figure 4.7, which shows the 8 axes and resulting unit cells for the fiber moved 2/3 of the distance to the edge (in the picture they appear to touch the boundary, but they do not). The maximum of 2/3 distance was selected to ensure fibers did not get close to the boundary resulting in very small finite elements, which could reduce the timestep or result in severe element distortion. These 16 perturbations plus the centered baseline unit cell made seventeen realizations.

Crack periodicity results from using repeating microstructure, such as in the work by Liu et al.[99] A MATLAB script was developed that randomly selected from among these unit cell realizations and assembled the microstructure. This approach eliminates crack periodicity and results in a more realistic microstructure.

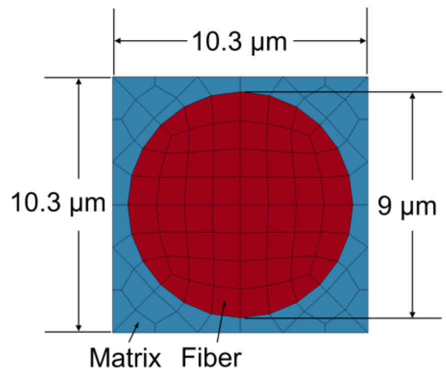

Figure 4.6: Centered, single-fiber unit cell with 60% fiber volume fraction.

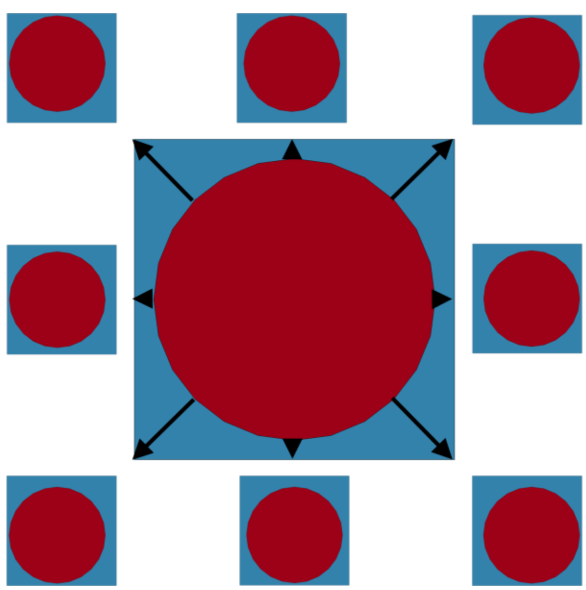

Figure 4.7: Eight of the 16 realizations derived from moving the centered fiber 2/3 of the distance in each direction.

Microscopic examination of impact-damaged plain weave glass/epoxy composites shows that, at the microscale, the cracks are related to a 0° unidirectional composite and a 90° unidirectional composite, as seen in figure 4.8. Thus, the fracture can be represented by delamination cracking within a [0/90] composite and cracking within a [90/90] composite. Seen at the microscale, the mesoscale damage mode of tow-tow delamination is represented by [0/90] delamination cracking, and the mesoscale damage mode of transverse cracking is represented by [90/90] fracture.

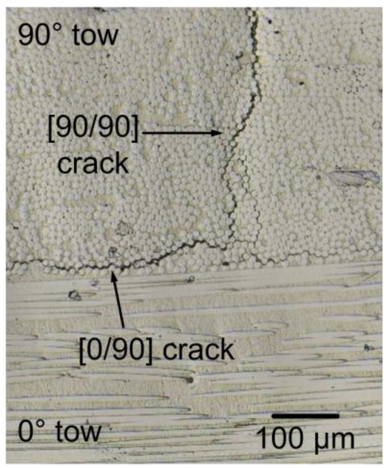

Figure 4.8: Centered, single-fiber unit cell with 60% fiber volume fraction.

Two microstructures were developed, a [90/90] microstructure and a [0/90] microstructure, which are shown in figure 4.9 and 4.10 respectively. The full embedded cells are shown with a magnified crack tip inset. The microstructure can be seen to have an approximately hexagonal packing, but with some fibers close together, some further apart. Microstructurally, the crack will chose the path of greatest stress, which is dominated by stress concentrations formed between close fibers.[100], [101]

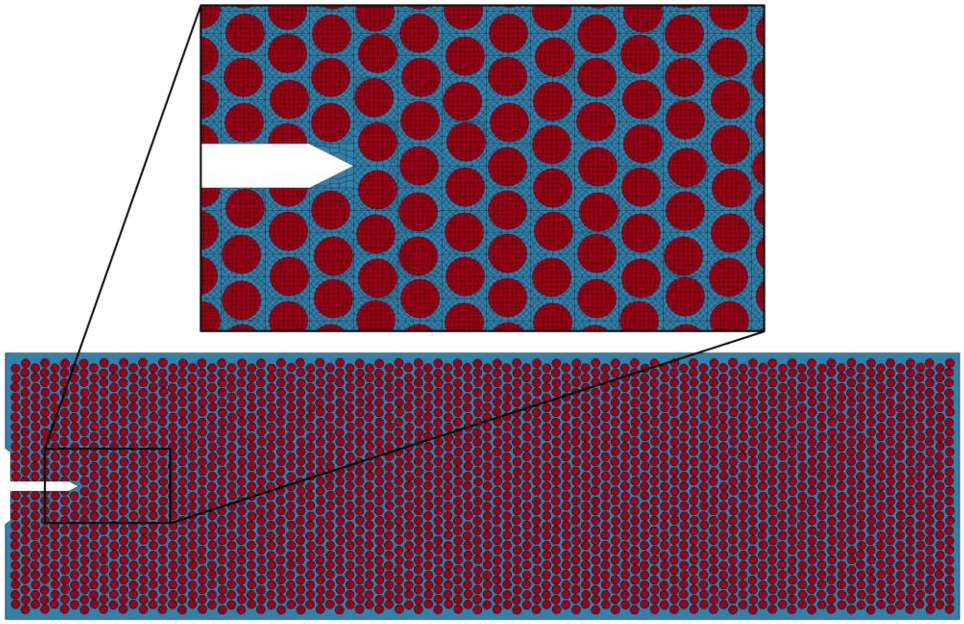

Figure 4.9: Embedded cell microstructure for modeling [90/90] cracking.

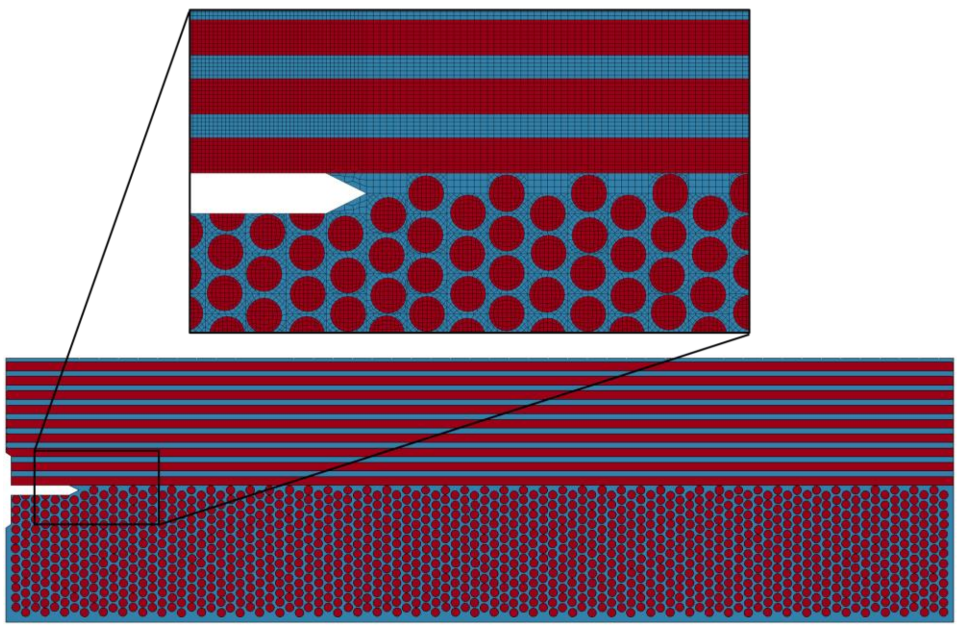

Figure 4.10: Embedded cell microstructure for modeling [0/90] cracking.

The boundary conditions used for these models is plain strain so that crack propagation is essentially two-dimensional in the embedded cells. This is not strictly correct for the [0/90] microstructure since the boundary conditions imply that the fibers in the 0° composite layer are semi-infinite in one of the transverse directions. However, microscopic observation of [0/90] cracking, for example in figure 4.8 (and others), shows that the [0/90] crack does not penetrate into the 0° layer. These cracks propagate transverse to the fiber direction and along the length of the fiber, but cannot cross into the orthogonal layer. It is not energetically favorable for the crack to cross into the 0° layer because to do so requires fiber fracture, which requires much more energy than matrix fracture and fiber-matrix interface debonding. Therefore, the 2D plain strain model is reasonable for [0/90] cracking as well as [90/90] cracking.

4.3.2.2 Mesoscale Continuum

A compact tension (CT) specimen [102] model was developed for simulating mode I tensile fracture. The CT specimen dimensions are shown in figure 4.11. Recall that the mesoscale is defined in this work as the scale of a fiber tow cross section, which is about 0.5 mm thick and 4.5 mm wide. The CT model in figure 4.11 is 2.4 mm by 2.5 mm with a 1 mm embedded cell. Thus, within the embedded cell, the cracking occurs at the microscale, but the J-integral is taken at the mesoscale.

An Arcan-like specimen model was developed for simulating mode II shear fracture. The Arcan specimen dimensions are shown in figure 4.12. Similar to the CT model, this model includes a microscale embedded cell within a mesoscale continuum.

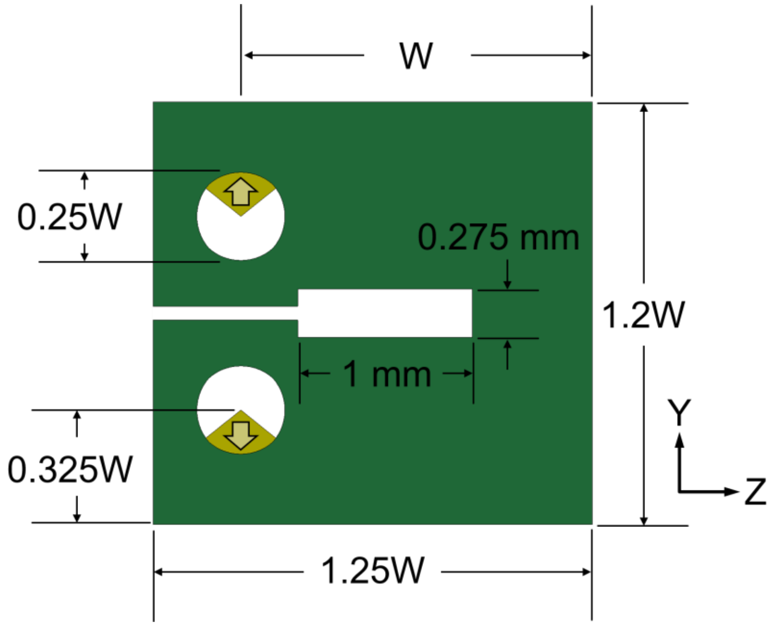

Figure 4.11: Mesoscale continuum compact tension specimen [102] (W = 2 mm) with empty space where microstructure is to be embedded. Arrows indicate direction of loading.

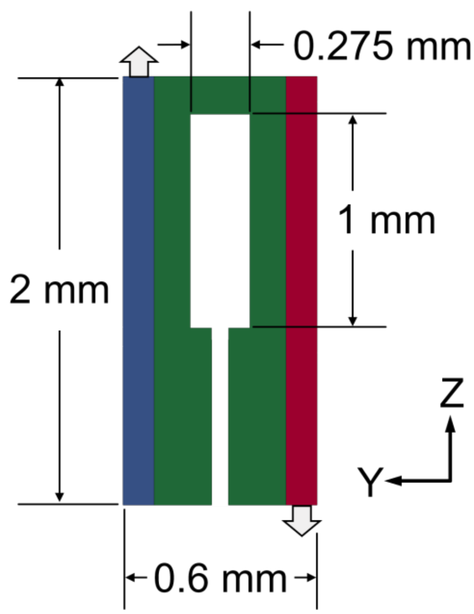

Figure 4.12: Mesoscale continuum Arcan specimen with empty space where microstructure is to be embedded. Arrows indicate direction of loading.

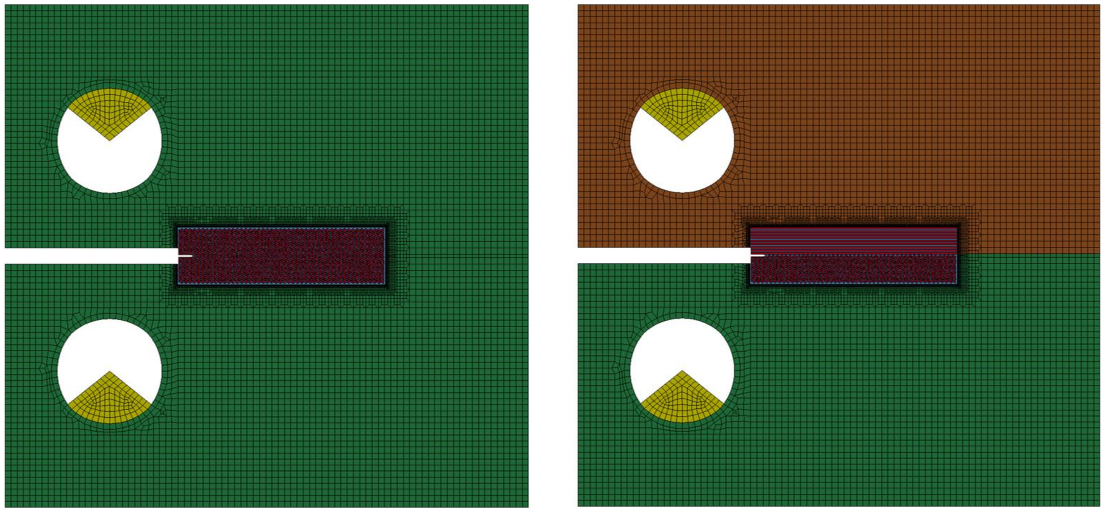

a b

Figure 4.13: Full compact tension model with microstructure embedded in continuum for mode I (a) [90/90] and (b) [0/90] cracking.

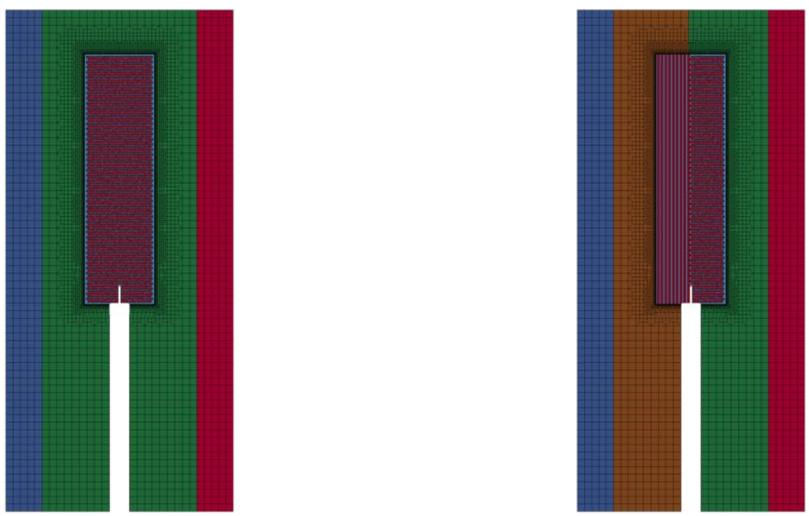

a b

Figure 4.14: Full Arcan shear model with microstructure embedded in continuum for mode II (a) [90/90] and (b) [0/90] cracking.

The finite elements within the microstructure average ~1 μm in size (e.g., figures 4.6, 4.9, 4.10). The finite elements in the mesoscale region are 30 μm square. Figure 4.13 shows the full CT models and figure 4.14 shows the full Arcan models for [0/90] and [90/90] cracking. The mesh in the embedded cell must be coupled to the mesh in the continuum, so there is a region of transitional continuum mesh surrounding the embedded cell. The transitional mesh grows the average finite element size from ~1 μm to 30 μm. To facilitate this coupling, and to ensure no partial fibers are on the embedded cell boundary, a region of neat matrix surrounds the embedded cell (see figures 4.9 and 4.10). Fibers, being stiffer than matrix or continuum composite, would cause stress concentrations at the microscale to mesoscale boundary, and so fibers are not allowed on the boundary.

The path of the domain integral is taken far from the crack tip, near (but not on) the boundary of the specimens. Since the path is far from the crack tip, it can be assumed that linear elasticity holds and so the strain energy density is satisfied by equation (4.6).

To properly model microstructural fracture requires inclusion of the important microscale mechanisms. These mechanisms include rate-dependent matrix behavior and rate-dependent fiber-matrix interfacial debonding.

4.3.2.3 Rate-dependent Matrix

Strain-rate dependent, non-linear epoxy stress-strain behavior was measured by Tamrakar et al.[103], [104]. These properties are for DER353 epoxy, which is an aliphatic glycidyl ether modified bisphenol A/F resin (Olin Epoxy, Haddonfield, NJ). Tamrakar et al. experimentally determined the stress-strain response at quasi-static average strain rates (ASR) of 0.001, 0.01, and 0.1 per second and dynamic strain rates of 2300, 5000, and 12000 per second. These data are shown in figure 4.15. Average strain rates of 100, 1000, 10000, and 100000 per second are extracted from a finite element model (FEM) based on the experimental data. To do this, a unit cube FEM is modeled with experimental data in a tabular material model, MAT_24 in LS-DYNA, and the FEM is loaded at the indicated strain rates and the stress-strain data extracted from the FE model. These extra FE-based curves fill in missing strain rates in the experimental data.

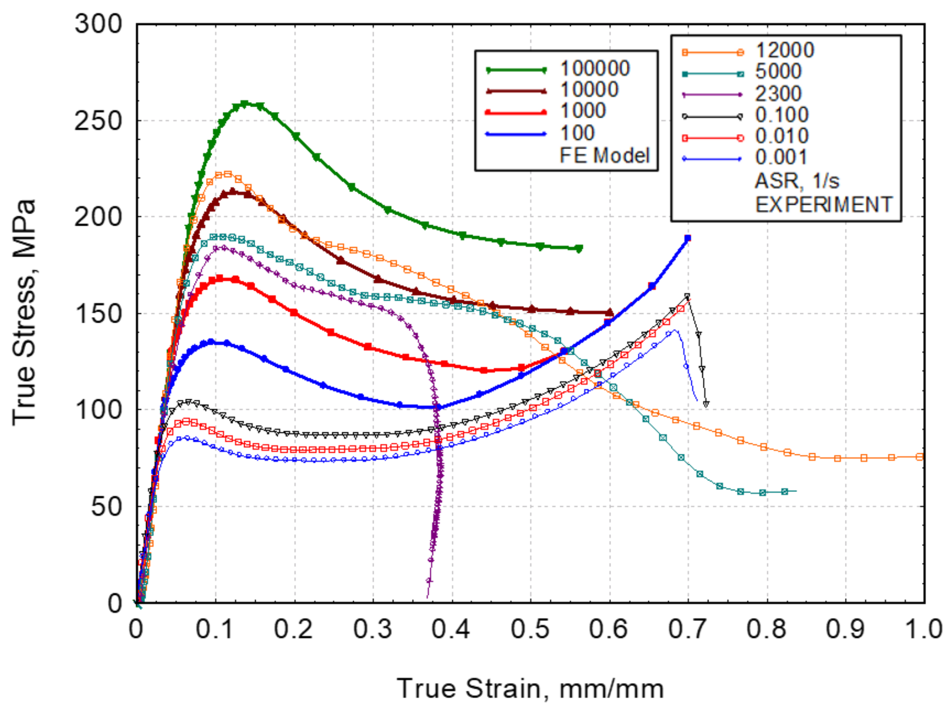

Figure 4.15: Strain-rate dependent DER353 epoxy stress-strain behavior from Tamrakar et al. [103], [104] for average strain rates (ASR).

The stress-strain curves in figure 4.15 are all included in the tabular material model, *MAT_PIECEWISE_LINEAR_PLASTICITY (MAT_24) in LS-DYNA to simulate the rate-dependent behavior of the matrix. LS-DYNA determines the average strain rate within a given matrix element and calls the appropriate tabulated stress strain behavior. The experimental results include thermal softening, but this is not explicitly modeled (post-peak softening is not included in model stress-strain curves).

The non-linear matrix response is governed by MAT_24 and the data in figure 4.15, but matrix failure is governed by element erosion (*MAT_ADD_EROSION). The erosion criteria is based on a failure strain. The quasi-static failure strain in figure 4.15 is about 0.7, and the dynamic failure strain is about 0.2. The dynamic failure strain of 0.2 was chosen because thermal softening dominates the stress-strain behavior beyond about 0.2 strain.

A logarithmic line is fit between two points, quasi-static (10^{-4} s^{-1}, 0.7 mm/mm) and dynamic (10^{6} s^{-1}, 0.2 mm/mm). The equation of this line gives epoxy erosion strain, ε_e, as a function of average strain rate (ASR), and is used by LS-DYNA to compute erosion strain depending on the ASR within each matrix element under load. The equation for this line is $\varepsilon_e = 0.510 - 0.051\log_{10}(\text{ASR})$. This line is shown in figure 4.16. Strain rates less than 10^{-4} have 0.7 erosion strain, or greater than 10^{6} have 0.2 erosion strain, as shown in figure 4.16.

Failure of matrix elements is governed by this erosion criteria. Cracking propagates through matrix by erosion. The matrix elements are eroded (discarded) when they reach a sufficient strain under load, but they can deform significantly before being eroded. Erosion of failed matrix elements prevents numerical instability due to large deformation.

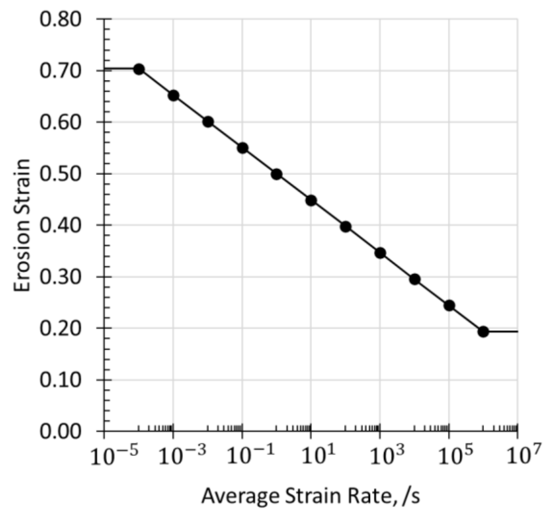

Figure 4.16: Strain-rate dependent DER353 epoxy failure (erosion) strain.

4.3.2.4 Rate-dependent Fiber-matrix Interface

There is a strain-rate dependent cohesive model implemented in LS-DYNA called *MAT_COHESIVE_MIXED_MODE_ELASTOPLASTIC_RATE (MAT_240). This model is based on the work of Martzi et al.[105], [106]. This model requires rate-dependent peak traction and rate-dependent fracture energy data under mode I and mode II loading conditions.

Tamrakar et al. determined rate-dependent mode II (shear) traction-separation law data.[107], [108] This work involved the microdroplet test in which a microscale droplet of epoxy matrix is bonded to a single glass fiber and loaded under mode II up to interfacial failure. The data is provided in table 4.1.

Rate-dependent mode I (tension) parameters are not readily available for glass fiber, epoxy matrix interfacial failure. Ogihara and Koyangi [109] found that normal (mode I) peak stress for glass-epoxy interfacial debonding is about 2/3 of the shear (mode II) peak stress. Therefore, the present work assumes that mode I is 67% of the mode II properties.

Table 4.1: Rate-dependent mode II fiber-matrix interface, bi-linear traction-separation law data by Tamrakar et al. [107], [108]

Mode II Strain Rate, $\dot{\varepsilon}$ s^{-1}	Peak Traction, T_{II}, MPa	Fracture Energy, G_{IIc} MPa · μm	Peak Separation, δ_{max}, μm
90	65	100	3.1
9000	75	150	4.0
10^8	120	300	5.0

This rate-dependent cohesive model fits equations to the rate-dependent traction and energy data. Mode I traction is T and energy is G_{Ic}. Mode II traction is S and energy is G_{IIc}. Equations (4.9) and (4.10) give mode I traction and energy. Equations (4.11) and (4.12) give mode II traction and energy. In equations (4.9) and (4.11), Macaulay brackets, ⟨⟩, signify that the value inside the brackets cannot be negative, rather it takes the maximum of either zero or the value of the function. In equations (4.9) through (4.12), T_0, T_I, S_0, S_I, G_{I_∞}, G_{I_0}, G_{II_∞}, G_{II_0}, $\dot{\varepsilon}_{min}$, and $\dot{\varepsilon}_G$ are constants determined by fitting these equations to the data in table 4.1.

$$T(\dot{\varepsilon}) = T_0 + T_1 \langle \ln(\dot{\varepsilon}/\dot{\varepsilon}_{min}) \rangle^2 \tag{4.9}$$

$$G_{Ic}(\dot{\varepsilon}) = G_{I_0} + \left(G_{I_\infty} - G_{I_0}\right) exp(-\dot{\varepsilon}_G / \dot{\varepsilon}) \tag{4.10}$$

$$S(\dot{\varepsilon}) = S_0 + S_1 \langle ln(\dot{\varepsilon}/\dot{\varepsilon}_{min}) \rangle^2 \tag{4.11}$$

$$G_{IIc}(\dot{\varepsilon}) = G_{II_0} + \left(G_{II_\infty} - G_{II_0}\right) exp(-\dot{\varepsilon}_G/\ \dot{\varepsilon}\ ) \tag{4.12}$$

The mode II data in table 4.1 was fit with equations (4.11) and (4.12). This fitting is illustrated in figure 4.17a. The constants resulting from fitting these equations are provided in table 4.2. Rate-dependent bilinear traction-separation laws can be extracted from these equations by solving for the traction and energy as a function of strain rate and given constants. Examples of such TSLs are provided in figure 4.17b. The initial stiffness of these curves is assumed to be 0.5 GPa/μm. Table 4.2 also includes mode I parameters for equations (4.9) and (4.10), which are 67% of the mode II parameters.

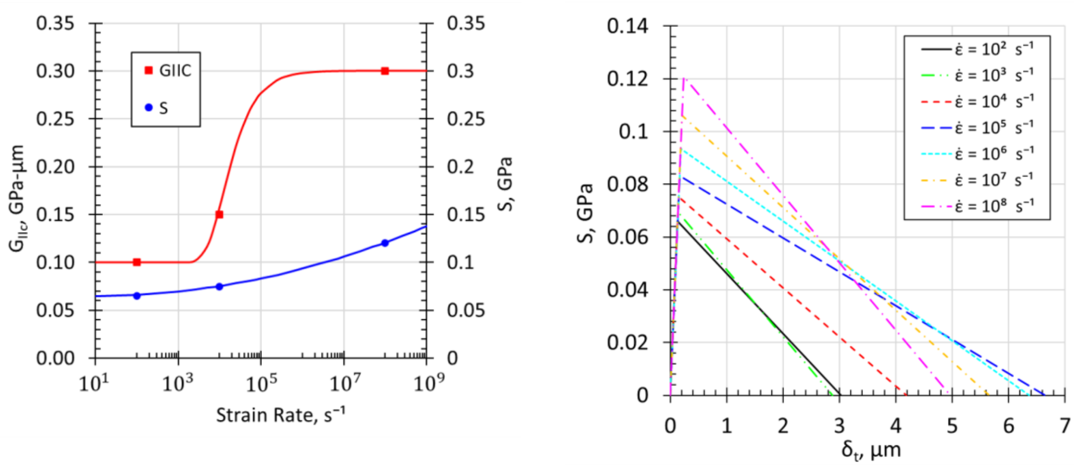

a b

Figure 4.17: (a) Mode II shear traction, S, and fracture energy, G_{IIc}, as a function of strain rate.[106], [108] (b) Example mode II rate-dependent bilinear traction-separation laws for fiber-matrix interfacial debonding.

Table 4.2: Rate-dependent fiber-matrix interface cohesive model parameters.

Mode I			
T_0, MPa	44	G_{I_0}, MPa · μm	67
T_1, MPa	0.144	G_{I_∞}, MPa · μm	201
$\dot{\varepsilon}_{min}$, s^{-1}	10	$\dot{\varepsilon}_G$, s^{-1}	1.25×10^4
Mode II			
S_0, MPa	65	G_{II_0}, MPa · μm	100
S_1, MPa	0.215	G_{II_∞}, MPa · μm	300
$\dot{\varepsilon}_{min}$, s^{-1}	10	$\dot{\varepsilon}_G$, s^{-1}	1.25×10^4

In the finite element model, strain rate is computed from the opening rate divided by the cohesive zone thickness. For zero thickness cohesive zones used in the present work, the separation at the previous time step is used for cohesive zone thickness. This opening strain rate between matrix and fiber elements is used by LS-DYNA to determine the appropriate rate-dependent TSL to govern the fiber-matrix debonding.

4.3.2.5 Elastic and Thermal Properties

Elastic epoxy properties used in the model are provided in table 4.3. Other elastic properties used in this work are also provided in table 4.3 and table 4.4.

Table 4.3: Elastic material properties.

Material	Density, $\mathrm{g/cm^3}$	Elastic Modulus, GPa	Poisson's Ratio	Coefficient of Thermal Expansion, $(°\mathrm{C})^{-1}$	Change in Temperature °C
Steel	7.85	210	0.29	11.0×10^{-6}	130
Glass Fiber	2.49	93.0	0.17	70.0×10^{-6}	
Epoxy	1.15	3.2	0.36	3.4×10^{-6}	
Composite	1.9	see Table 4.4		30.0×10^{-6}	

Table 4.4: Transversely isotropic material properties for glass/epoxy composite.

Elastic Modulus, GPa	$E_{11} = 55.3$	$E_{22} = 11.0$	$E_{33} = 11.0$
Shear Modulus, GPa	$G_{12} = 4.2$	$G_{23} = 3.7$	$G_{31} = 4.2$
Poisson's Ratio	$\nu_{21} = 0.05$	$\nu_{31} = 0.05$	$\nu_{32} = 0.45$

Glass fibers are modeled as elastic since they generally do not fail under cracking transverse to the fiber direction. This can be seen in figure 4.1, which is reproduced here as figure 4.18 for convenience.

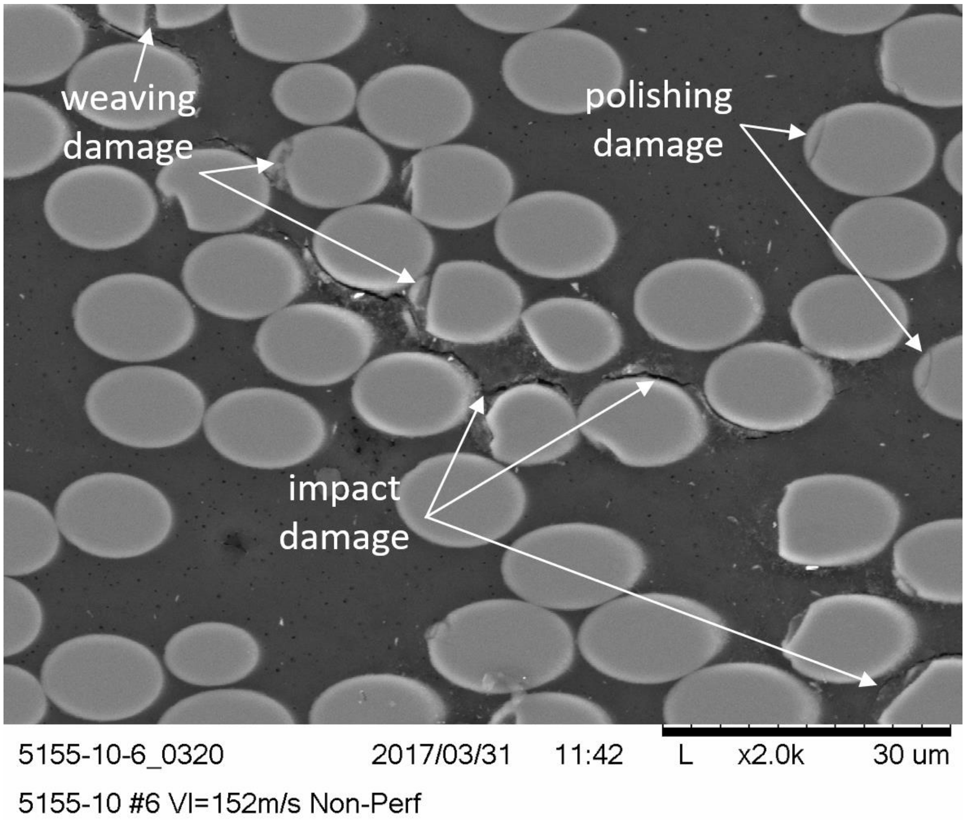

Figure 4.18: Scanning electron micrograph of ballistically impacted plain weave glass/epoxy composite showing sources of glass fiber damage. Here, impact loading is transverse to the fiber direction.

Fiber fracture is generally due to fiber handling and weaving, which is apparent when matrix fills the space between fiber segments, meaning the fiber was damaged before the composite was manufactured (and subsequently ballistically tested). In figure 4.18, the crack may be seen to propagate between broken fiber pieces, but it is clear that it is propagating through the matrix between fiber pieces. In figure 4.18 fiber fracture can also occur due to the sample polishing process, which is evident when the fibers are cracked with no matrix within the crack and the ballistic impact damage is not near these cracked fibers.

4.4 Mesh Sensitivity and Model Validation

Discretization error can lead to domain dependence [93], [95]. A mesh sensitivity study was performed. The CT model in figure 4.13a was developed with a continuum mesh at the crack tip as shown in figure 4.19. In this model, the mesh ahead of the crack was refined by halving the mesh size five times beginning from the 30 μm maximum mesh size of the continuum. Thus, the square mesh ahead of the crack had dimensions 30 μm, 15 μm, 7.5 μm, 3.75 μm, and 1.875 μm. The finest mesh, 1.875 μm, was similar to the mesh size of the fiber-matrix unit cell in figure 4.6. Therefore, the smallest element size is similar to the mesh in the embedded cell model. For the embedded cell microstructure, sensitivity of the number of elements around the circumference of the fiber is beyond the scope of this work and is saved for future study.

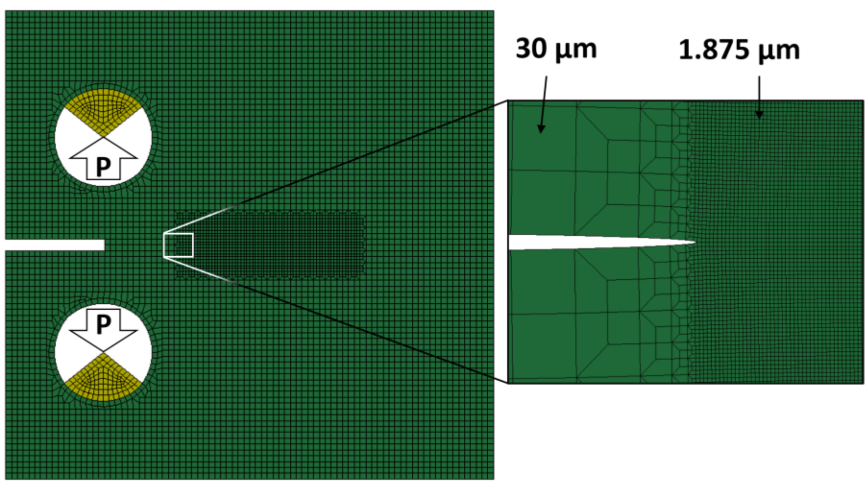

Figure 4.19: Strain-rate dependent DER353 epoxy failure (erosion) strain.

The mesh sensitivity was studied by comparing the model results with mode I stress intensity, K_I, for CT specimens according to ASTM E1820.[110] The K_I is given by equation (4.13), where P is applied load, B is specimen thickness, W is specimen width, and a is initial crack length.

$$K_I = \frac{P}{B\sqrt{W}} \frac{\left(2+\frac{a}{W}\right)\left[0.886+4.64\frac{a}{W}-13.32\left(\frac{a}{W}\right)^2+14.72\left(\frac{a}{W}\right)^3-5.6\left(\frac{a}{W}\right)^4\right]}{\left(1-\frac{a}{W}\right)^{3/2}} \tag{4.13}$$

The specimen has unit thickness with plain strain boundary conditions. The width is 2 mm. Initial crack lengths of 0.4 mm, 0.6 mm, 0.8 mm, and 1.2 mm were studied. This mesh sensitivity study considered linear elastic behavior only, so a is constant and fracture toughness may be converted to J according $J = K_I^2/E'$ where $E' = E/(1-\nu^2)$ for plane strain, isotropic elastic epoxy.

The continuum CT models were each loaded at 10 m/s. The load was applied through steel load noses (yellow in figure 4.19). The maximum principal strain response of the 30 µm model and the 1.875 µm model are compared in figure 4.20. The strain fields in figure 4.20 illustrate that the large element size cannot capture the correct crack tip plastic zone. However, the fine mesh model demonstrates the classic mode I crack tip plastic zone from the plane strain elastic solution.[61] Additionally, figure 4.20b illustrates that the FPZ does not extend outside of the embedded cell region.

Simulations were run for a long enough computation time to ensure the stress state reached equilibrium. The results of the mesh sensitivity study are presented in figure 4.21. The results show convergence as element size decreases with shorter initial crack lengths being generally more accurate. Thus, the initial crack length of 0.4 mm was used in all subsequent analyses.

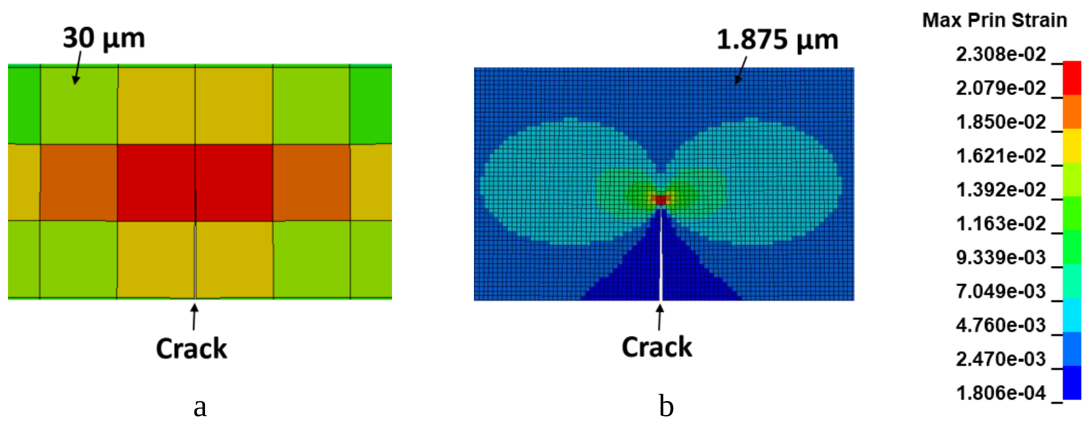

Figure 4.20: (a) Continuum, elastic, plain strain finite element models with (a) 30 µm square mesh and (b) 1.875 µm square mesh. Maximum principal strains are shown at the crack tip with images similarly scaled to mesh refinement. Color bar only applies to (b). Red peak strain in (a) is 0.0026.

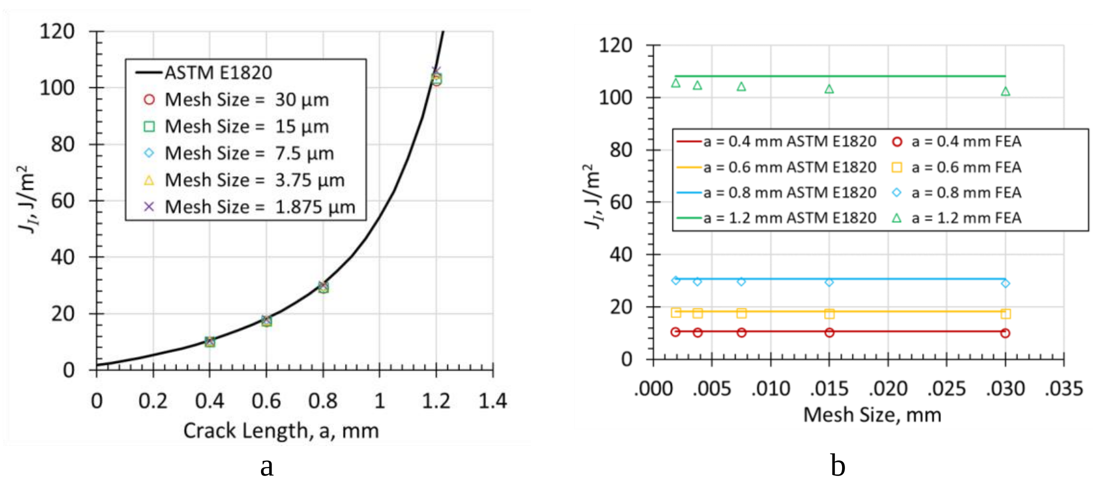

Figure 4.21: Continuum CT model with elastic properties showing mesh sensitivity study results of model prediction compared with ASTM E1820 for (a) increasing crack length and (b) mesh convergence for four crack lengths.

4.5 Residual Stress

An initial thermal cooldown analysis was conducted on the CT and Arcan models to develop the appropriate residual stress within the microstructure. Model temperatures were set to stress free cure temperature 150°C and then cooled to room temperature 20°C. Thus, a change in temperature of $\Delta T = -130°C$. Coefficients of thermal expansion (CTE) and the ΔT were given in table 4.3.

The embedded cell did not apply any residual stress to the continuum, which was stress free. Therefore, the properties used in the microscale and continuum regions were self-consistent and accurate. This was accomplished by grading the CTE of the composite along the element size gradient between the embedded cell and the continuum. However, significant residual stress is present in the embedded cell due to the mismatch in CTE between fiber and matrix. Including residual stress at the microscale is important as it represents a prestress state in the resin and also provides radial compression and friction at the fiber-matrix interphase after debonding.

The implicit thermal cooldown analysis output the model state of stress. This stress state was set as the initial condition of the subsequent explicit analyses. In all simulations, residual stress is present in the microstructural domain due to the mismatch between fiber and matrix thermal expansion coefficients. The magnitude of residual stress was not sufficient to cause matrix yielding or interface debonding.

The CT model thermal cooldown results are presented in figure 4.22. The results in the Arcan microstructure are similar so, to save space, are not shown. Some of the irregularly shaped elements within the continuum mesh size and CTE gradient region have slightly elevated stresses due to the CTE gradient and irregular element shapes. However, these elements are very few and the residual stress in them did not exceed 12 MPa, which is much less than the continuum transverse shear strength of 82

MPa (see table A.3 in Appendix A). Outside the transition region, the entire continuum composite mesh is stress free.

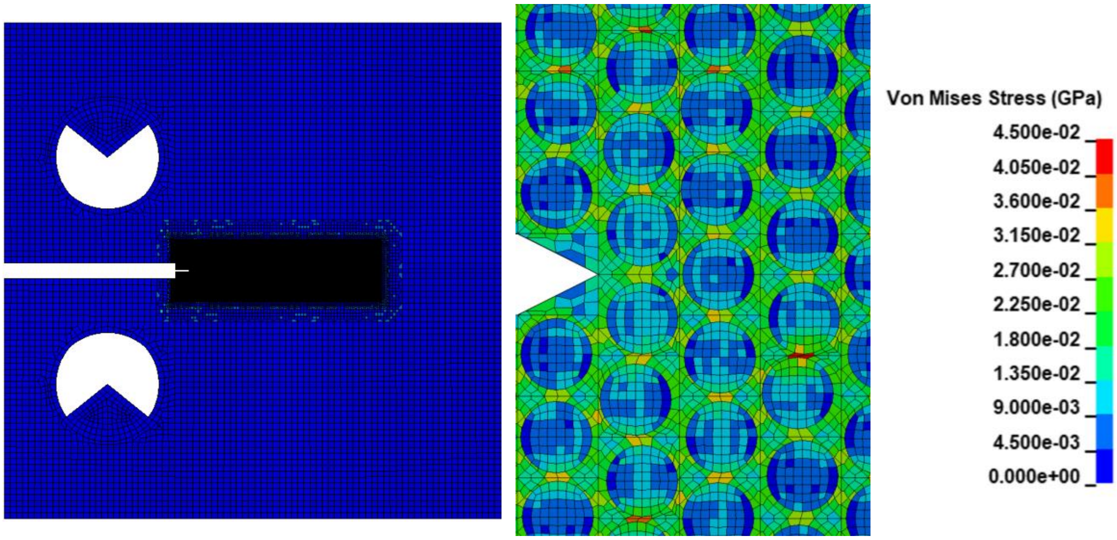

a b

Figure 4.22: Thermal cooldown results showing effective residual stress (von Mises) within the (a) continuum and (b) microstructure.

In the microstructure, maximum Von Mises residual stresses were ~45 MPa within the matrix, and the maximums occurred where fibers were closest packed.

4.6 Mode I Traction-Separation Laws

Tensile mode I load was applied to the embedded cell CT model. Three loading rates were considered: 10 m/s, 1 m/s, and 0.1 m/s. These loading rates corresponded to global strain rates of about 10^3 s^{-1}, 10^2 s^{-1}, 10^1 s^{-1} respectively. The global strain rates were determined using $\dot{\varepsilon} = \dot{\delta}/L$, where $\dot{\delta}$ is the loading rate and L = 2.4 mm is the model size in the loading direction.[14]

In the FPZ, local strain rates can vary and are typically much larger than the global average strain rate. Fiber-matrix interface strain rates were determined from the interface opening rate divided by the opening displacement. Epoxy element strain rate was determined from the derivative of elemental strain over time. Local strain rates for 10 m/s loading were 10^6 to 10^8 s^{-1} for fiber-matrix interfaces, and 10^5 to 10^6 s^{-1} for epoxy elements. Similarly, for 1 m/s loading, 10^5 to 10^6 s^{-1} for fiber-matrix interfaces, and 10^4 to 10^5 s^{-1} for epoxy elements, and for 0.1 m/s loading, 10^4 to 10^5 s^{-1} for fiber-matrix interfaces, and 10^3 to 10^4 s^{-1} for epoxy elements.

Considering figure 4.17a and these local strain rates, fiber-matrix interface G values for 10 m/s loading lie within the upper plateau and so vary little. However, fiber-matrix interface G values for 1 m/s and 0.1 m/s lie within the transition region, and so vary significantly with strain rate. Peak tractions increase quadratically with local strain rate.

The CT model applies load globally in mode I, but locally within the microstructure there can be mixed-mode loading. All models include mixed-mode response with mode I and mode II TSLs. The rate-dependent cohesive model determines the coupling from the normal and tangential relative displacement between interfaces, as described earlier (see figure 4.4).[59]

4.6.1 Mode I [90/90] Transverse Cracks

As loading is applied, the microstructure is deformed, fiber-matrix debonding initiates and matrix fails. This is shown in figure 4.23. Finite element model output was collected while loading increased up to the onset of steady-state crack propagation. Steady-state crack growth occurs when J does not increase with crack extension.[61] Figure 4.23a shows early time crack initiation, which is dominated by matrix plastic deformation and fiber-matrix interface debonding. Figure 4.23b and c show crack propagation, which is dominated by fiber-matrix interface debonding ahead of the crack and matrix plasticity and failure in the growing crack. Figure 4.23d shows the crack upon reaching steady state growth. Crack “branching” appears as fiber-matrix interface debonding in a different direction than primary crack growth.

Evolution of [90/90] transverse cracking under mode I loading at 10 m/s is shown in figure 4.23. Similar crack evolution is shown for [90/90] mode I loading under 1 m/s and 0.1 m/s in figures 4.24 and 4.25 respectively. The more energetic cracking under higher loading rates (e.g., figures 4.23c and d and 4.24c) is illustrated by more crack branching than for lower loading rate. The microstructure is the same for all three loading rates, but different crack morphology evolves for the highest loading rate (figure 4.23d) than lower rates (figures 4.24d and 4.25d). These differences result from the rate-dependent matrix and rate-dependent mixed-mode fiber-matrix interface debonding.

a

b

c

d

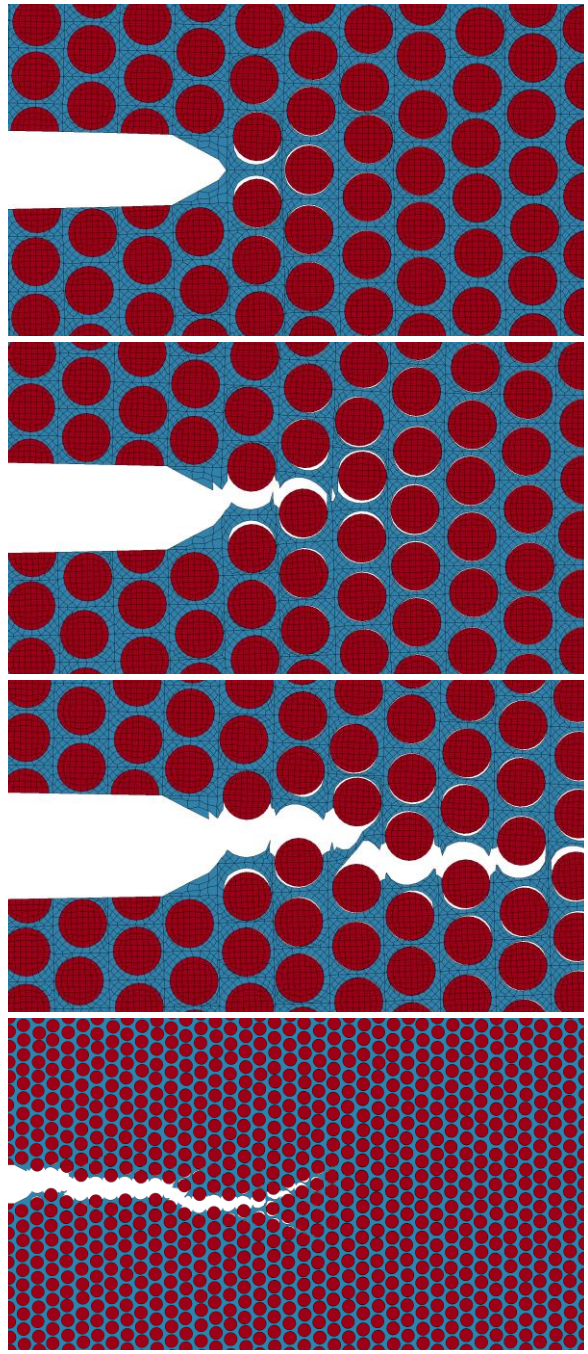

Figure 4.23: Crack growth under 10 m/s mode I loading in [90/90] microstructure with (a) early time initiation and (b) propagation, (c) later time propagation, and (d) crack upon reaching steady-state.

a
b
c
d

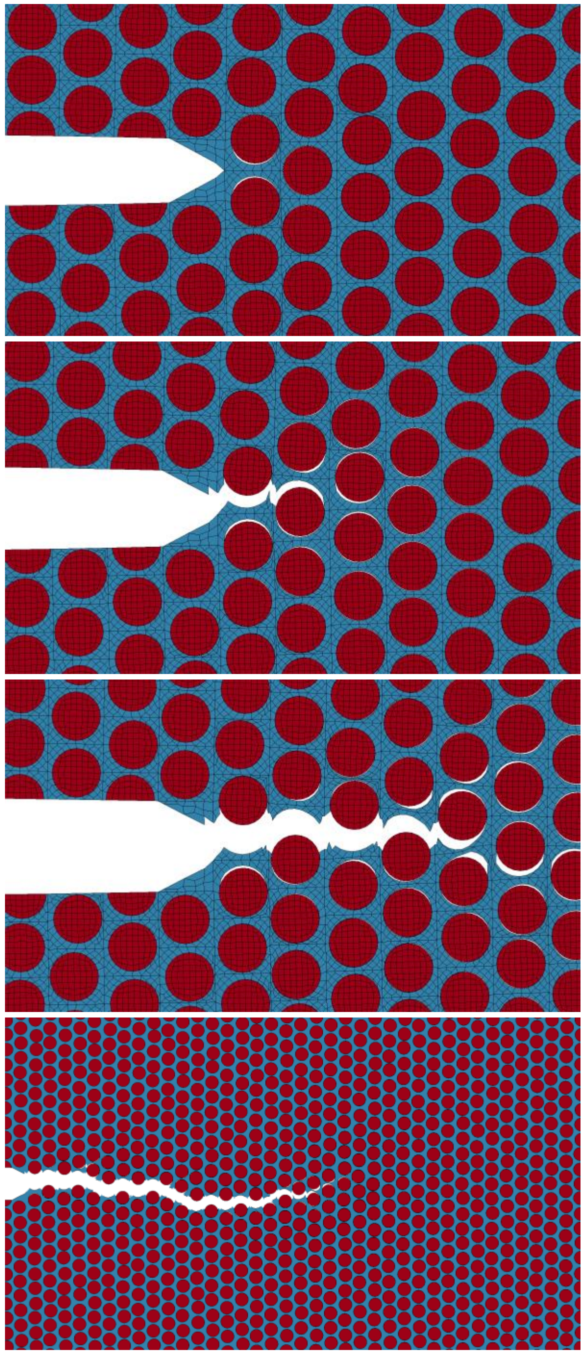

Figure 4.24: Crack growth under 1 m/s mode I loading in [90/90] microstructure with (a) early time initiation and (b) propagation, (c) later time propagation, and (d) crack upon reaching steady-state.

a

b

c

d

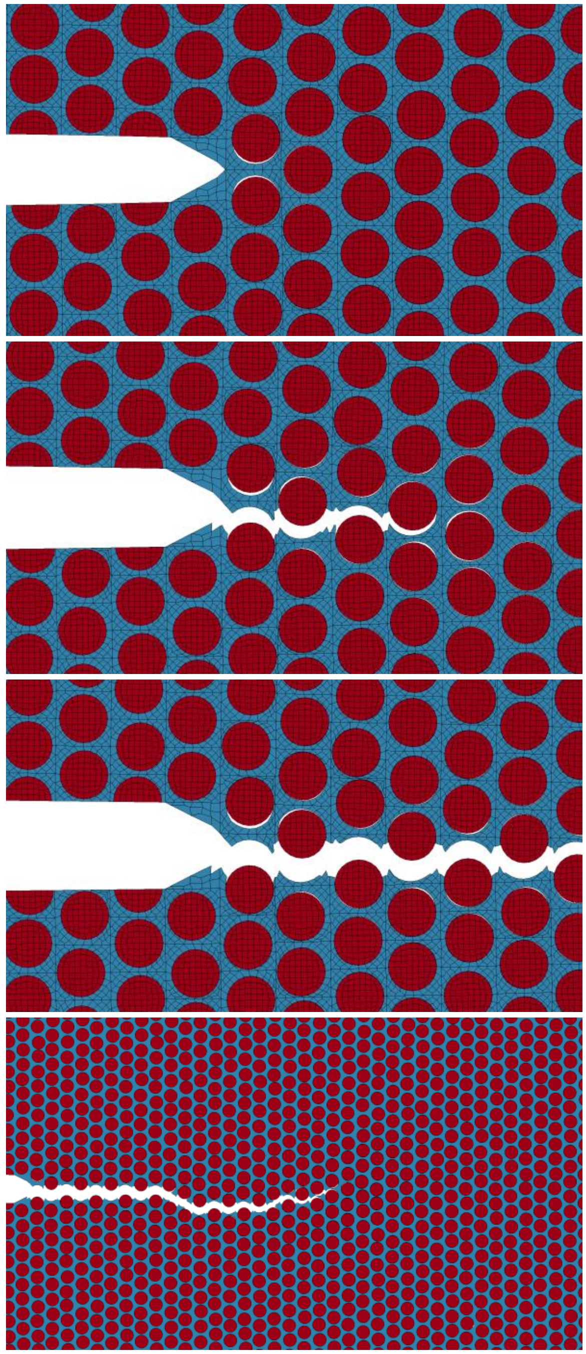

Figure 4.25: Crack growth under 0.1 m/s mode I loading in [90/90] microstructure with (a) early time initiation and (b) propagation, (c) later time propagation, and (d) crack upon reaching steady-state.

4.6.2 Mode I [0/90] Tow-tow Delamination Cracks

As with the [90/90] crack model, the [0/90] crack models were loaded in mode I tension at 10 m/s, 1 m/s, and 0.1 m/s. Evolution of [0/90] transverse cracking under mode I loading at 10 m/s is shown in figure 4.26. Similar crack evolution is shown for [0/90] mode I loading under 1 m/s and 0.1 m/s in figures 4.27 and 4.28 respectively.

Under the applied mode I loading, the microstructure is deformed, fiber-matrix debonding initiates and matrix fails. The cracks in figures 4.26, 4.27, and 4.28 each appear different, which is due to loading rates and the strain-rate dependent behavior in the matrix and fiber-matrix interfaces. Crack branching can be seen in the more energetic crack, figure 4.26.

a

b

c

d

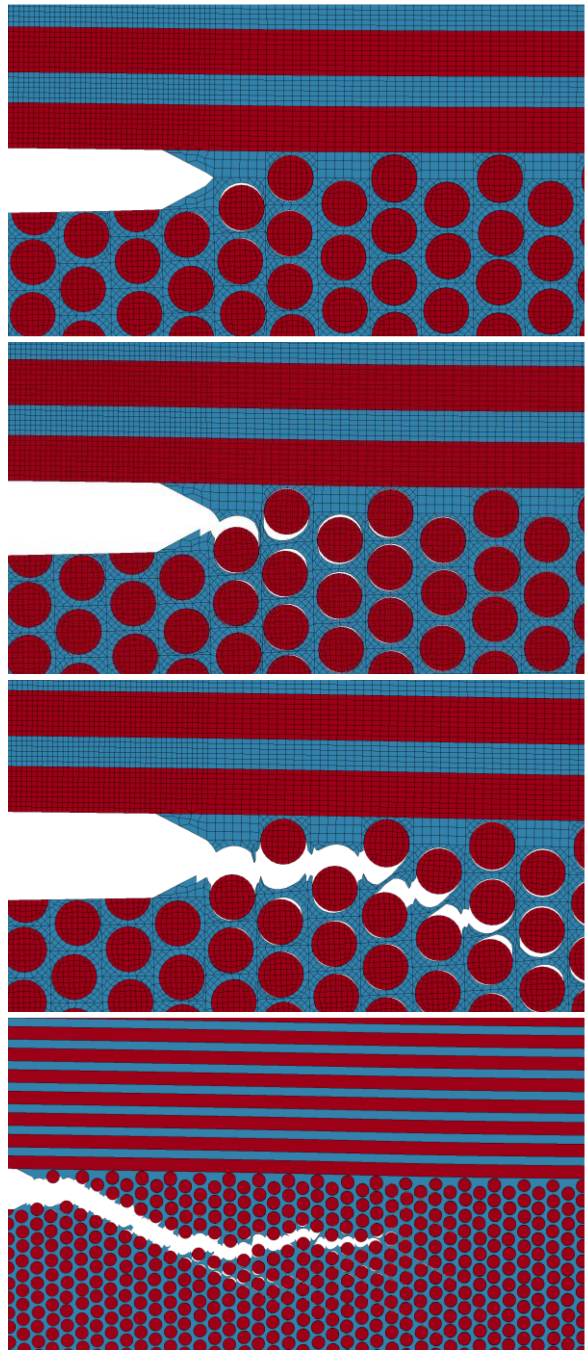

Figure 4.26: Crack growth under 10 m/s mode I loading in [0/90] microstructure with (a) early time initiation and (b) propagation, (c) later time propagation, and (d) crack upon reaching steady-state.

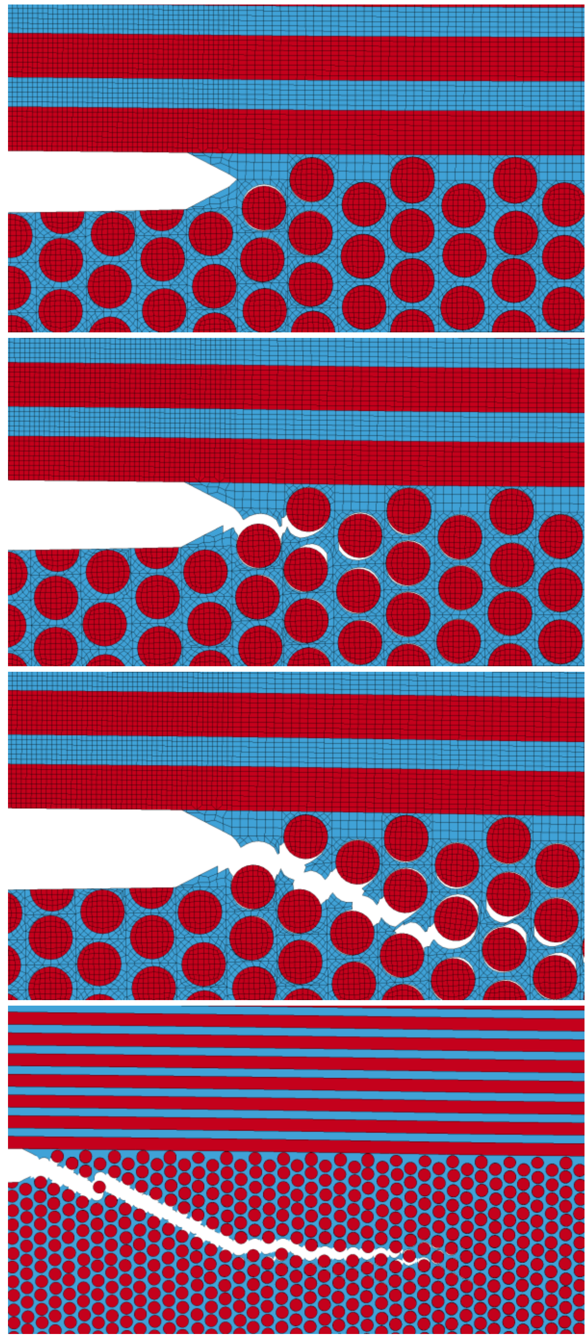

Figure 4.27: Crack growth under 1 m/s mode I loading in [0/90] microstructure with (a) early time initiation and (b) propagation, (c) later time propagation, and (d) crack upon reaching steady-state.

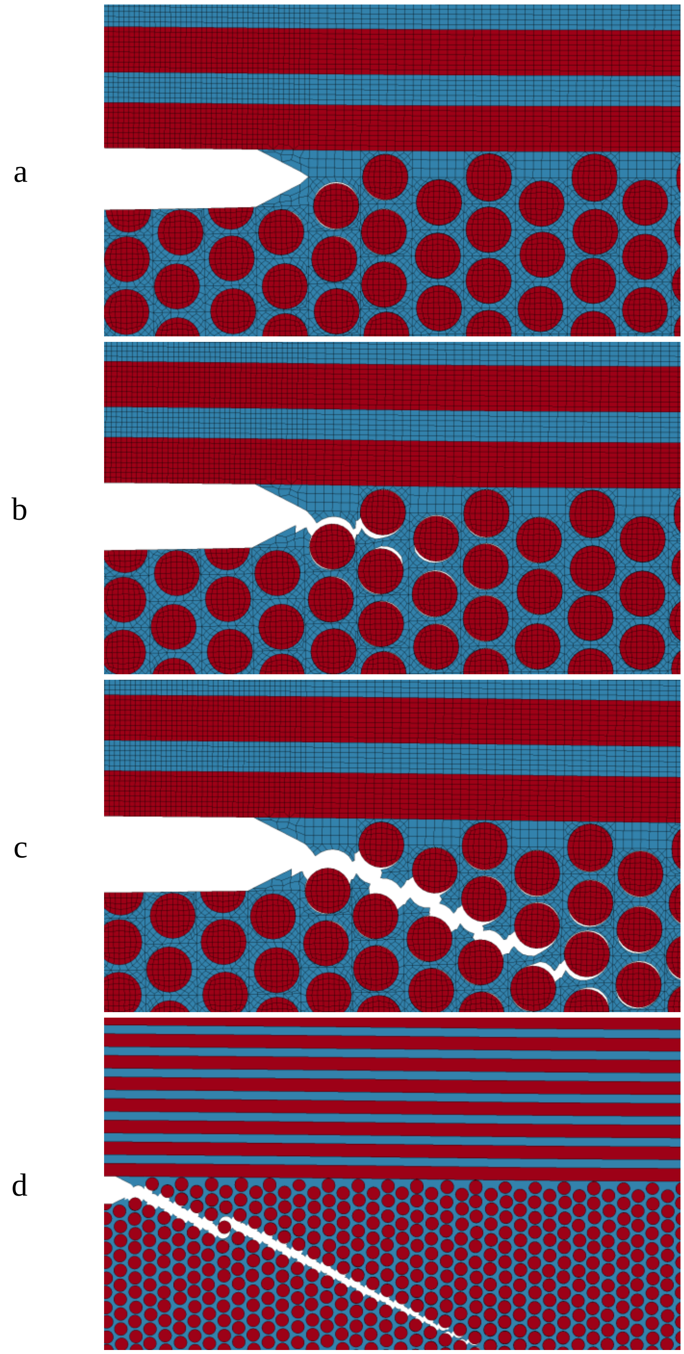

Figure 4.28: Crack growth under 0.1 m/s mode I loading in [0/90] microstructure with (a) early time initiation and (b) propagation, (c) later time propagation, and (d) crack upon reaching steady-state.

4.6.3 Determining Mode I Traction-Separation Laws

Stresses, strains, and displacements were output from the finite element models from a domain in the mesoscale elastic continuum region surrounding the microscale embedded cell. The domain begins and ends on the crack faces and is sufficiently far from the model boundary and load noses to avoid stress concentrations. The model output was then input into a MATLAB program, which computed the J-integral according to equations (4.5) to (4.8). Since stress, strain, and displacement are output as a function of time, the J-integral is computed as a function of time, $J(t)$.

It is difficult to consistently and accurately determine crack length or crack tip opening displacement during propagation in a micromechanical finite element analysis since the model does not have a crack tip, but rather a fracture process zone that encompasses multiple fibers and surrounding matrix.[111] Therefore, the crack mouth opening displacement or load line displacement are often used for δ (e.g., [97], [98], [111], [112]). The present work uses crack mouth opening displacement for δ, and it is output from the model as a function of time, $\delta(t)$.

The $J(t)$ and $\delta(t)$ were correlated to give $J(\delta)$. An S-shaped curve was fit to the $J(\delta)$ data. The equation of the S-shaped curve is (4.14) where α, β, and γ are fitting parameters. The traction-separation law is determined by taking the derivative of the $J(\delta)$ data. The derivative of the S-shaped curve is given by equation (4.15).

$$J(\delta) = \alpha\left(1 - \exp\left\{-\left(\frac{\delta}{\beta}\right)^{\gamma}\right\}\right) \tag{4.14}$$

$$T(\delta) = \frac{\alpha\gamma}{\beta}\left(\frac{\delta}{\beta}\right)^{\gamma-1} \exp\left\{-\left(\frac{\delta}{\beta}\right)^{\gamma}\right\} \tag{4.15}$$

Rate-dependent J-integral data is presented in figure 4.29a for mode I [90/90] transverse cracking. The corresponding rate-dependent traction-separation laws for mode I transverse cracking is presented in figure 4.29b. The curves in figure 4.29b can be fit with a bilinear TSL shape for convenient use in typical cohesive zone modeling. Bilinear TSLs are provided in table 4.5 for each loading rate.

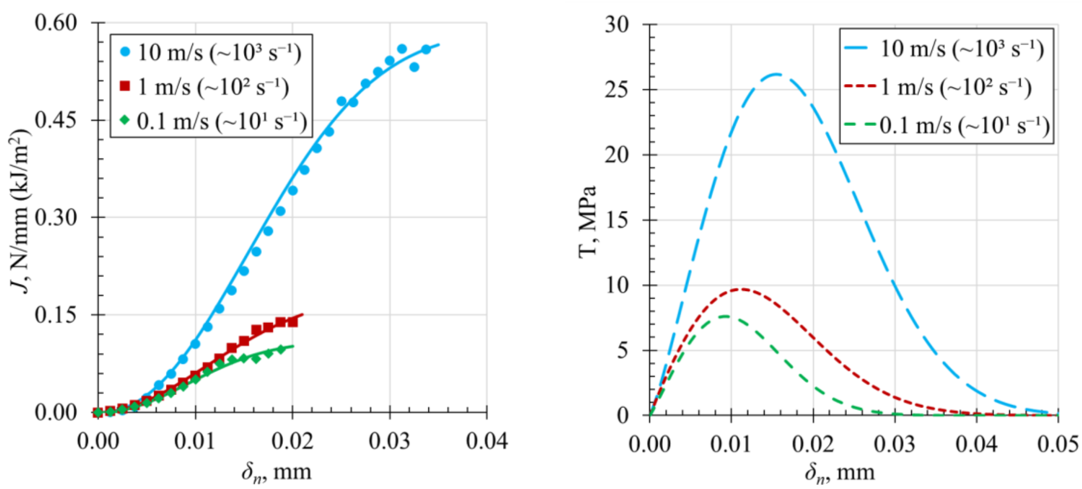

Figure 4.29: (a) Transverse crack [90/90] mode I data and curve fit for J-integral as a function of normal opening displacement and loading rate. (b) Derivative of the fit to J-integral data, which is the traction-separation law for each loading rate.

Table 4.5: Rate-dependent mode I [90/90] transverse crack traction-separation laws.

	$\dot{\delta}$ = 10 m/s	$\dot{\delta}$ = 1 m/s	$\dot{\delta}$ = 0.1 m/s
T_I, MPa	26.2	9.7	7.6
δ_I, mm	0.045	0.038	0.029
G_{Ic}, MPa-mm	0.590	0.185	0.110
E_n, MPa/mm	2275	1385	1169

Rate-dependent J-integral data is presented in figure 4.30a for mode I [0/90] tow-tow delamination cracking. The corresponding rate-dependent traction-separation laws for mode I transverse cracking is presented in figure 4.30b. The curves in figure 4.30b can be fit with a bilinear TSL shape for convenient use in typical cohesive zone modeling. Bilinear TSLs are provided in table 4.6 for each loading rate.

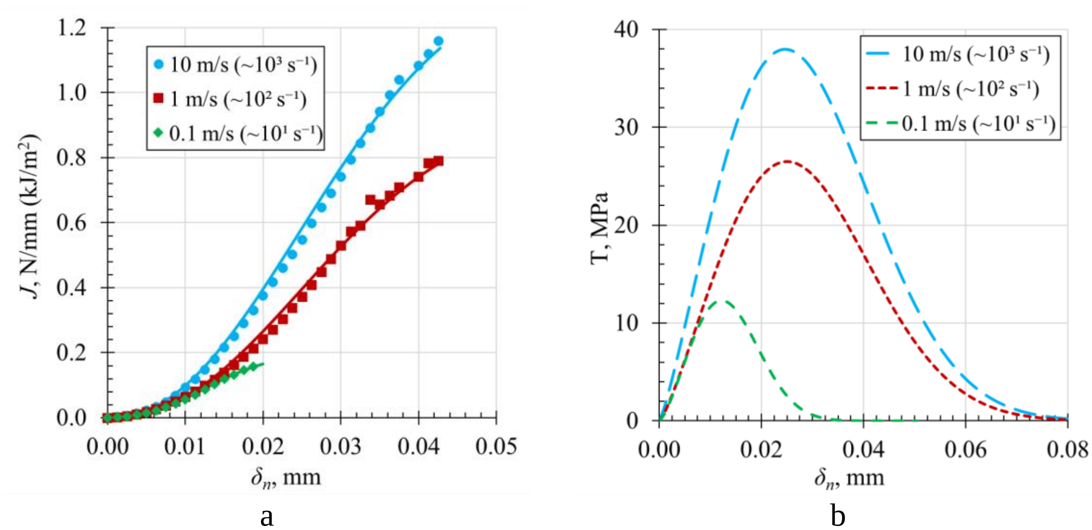

Figure 4.30: (a) Tow-tow delamination crack [0/90] mode I data and curve fit for J-integral as a function of normal opening displacement and loading rate. (b) Derivative of the fit to J-integral data, which is the traction-separation law for each loading rate.

Table 4.6: Rate-dependent mode I [0/90] tow-tow delamination crack traction-separation laws.

	$\dot{\delta} = 10\ \mathrm{m/s}$	$\dot{\delta} = 1\ \mathrm{m/s}$	$\dot{\delta} = 0.1\ \mathrm{m/s}$
T_I, MPa	38.0	26.5	12.3
δ_I, mm	0.085	0.080	0.036
G_{Ic}, MPa-mm	1.360	0.934	0.197
E_n, MPa/mm	2052	1433	1295

4.7 Mode II Traction-Separation Law

Shear mode II load was applied to the embedded cell Arcan model. As with mode I, three loading rates were considered: 10 m/s, 1 m/s, and 0.1 m/s. These loading rates corresponded to global strain rates of about 10^3 s^{-1}, 10^2 s^{-1}, 10^1 s^{-1} respectively. Again, in the FPZ, local strain rates can vary and are typically much larger than the global average strain rate. Local strain rates for 10 m/s loading were 10^6 to 10^9 s^{-1} for fiber-matrix interfaces, and 10^5 to 10^6 s^{-1} for epoxy elements. Similarly, for 1 m/s loading, 10^6 to 10^7 s^{-1} for fiber-matrix interfaces, and 10^4 to 10^5 s^{-1} for epoxy elements, and for 0.1 m/s loading, 10^5 to 10^6 s^{-1} for fiber-matrix interfaces, and 10^3 to 10^4 s^{-1} for epoxy elements.

Similar to mode I loading, considering figure 4.17a and these local strain rates, fiber-matrix interface G values for 10 m/s loading lie within the upper plateau and so do not vary much. However, fiber-matrix interface G values for 1 m/s and 0.1 m/s lie within the transition region, and so vary significantly with strain rate.

The Arcan model applies load globally in mode II, but locally within the microstructure there can be mixed-mode loading. All models include mixed-mode response with mode I and mode II TSLs. The rate-dependent cohesive model determines the coupling from the normal and tangential relative displacement between interfaces, as described earlier (see figure 4.4).[59]

4.7.1 Mode II [90/90] Transverse Cracks

As loading is applied, the microstructure is deformed, fiber-matrix debonding initiates and matrix fails as seen in figure 4.31. Finite element model output was collected while loading increased until the crack approached the boundary. Steady-state crack growth did not occur before the crack reached the boundary. Figure 4.31a shows early time crack initiation, which is dominated by matrix plastic deformation and fiber-matrix interface debonding. Figure 4.31b and c show crack propagation, which is dominated by fiber-matrix interface debonding ahead of the crack and matrix plasticity and failure in the growing crack. Figure 4.31d shows the crack upon reaching the boundary.

Evolution of [90/90] transverse cracking under mode I loading at 10 m/s is shown in figure 4.31. Similar crack evolution is shown for [90/90] mode I loading under 1 m/s and 0.1 m/s in figures 4.32 and 4.33 respectively. Higher loading rates produce more crack branching than lower loading rates. Although the microstructures are the same, different cracks evolve under different loading rates due rate-dependent matrix and fiber-matrix interface debonding.

At the microscale, cracks initiate at the notch and propagate through the microstructure. Cracks grow at an angle relative to the plane of principal normal stress. Under global mode II loading, the cracks propagate locally in mode I. It has been shown that cracks propagate in a direction that minimizes mode II stress intensity.[113] Local mode I opening in composites is consistent with experimental observations by Bradley et al.[114]–[118] They observed microcracking under global mode II loading in cross-ply laminates. Microcracks formed in the 90° layer and opened at roughly 45° to the plane of principal normal stress. These microcracks propagated through the 90° layer until they intersected the adjacent 0° layer. Then the microcracks turned and coalesced into a global mode II crack and delamination between the 0° and 90° layers. The experiments by Bradley et al. demonstrate that under global mode II loading, damage initiates and propagates at the microscale in mode I. [114]–[118] And these experiments are consistent with the mode II simulations of embedded microstructure, which show that in a 90° layer, cracks propagate at an angle in the microstructure.

At the microscale, fracture in fiber reinforced polymer composites usually involves fiber-matrix debonding and matrix deformation.[117] This microscale embedded cell model is the first to predict the initiation and propagation of these damage modes as a function of rate-dependent interphase properties and rate-dependent matrix at this length scale. This explains the appearance of the mode II cracks in figures 4.31, 4.32, and 4.33.

4.7.2 Mode II [0/90] Tow-tow Delamination Cracks

As with the [90/90] crack model, the [0/90] crack models were loaded in mode II shear at 10 m/s, 1 m/s, and 0.1 m/s. Evolution of [0/90] transverse cracking under mode II loading at 10 m/s is shown in figure 4.34. Similar crack evolution is shown for [0/90] mode I loading under 1 m/s and 0.1 m/s in figures 4.35 and 4.36 respectively.

Similar to the [90/90] models, under the applied mode II loading, the microstructure is deformed, fiber-matrix debonding initiates and matrix fails, and cracks appear slightly different due to differences in loading rates and rate-dependent properties.

As was observed for the [90/90] models, under global mode II loading, the [0/90] microstructure cracks propagate at an angle. Again, this is because the cracks are propagating locally in mode I under global mode II loading.

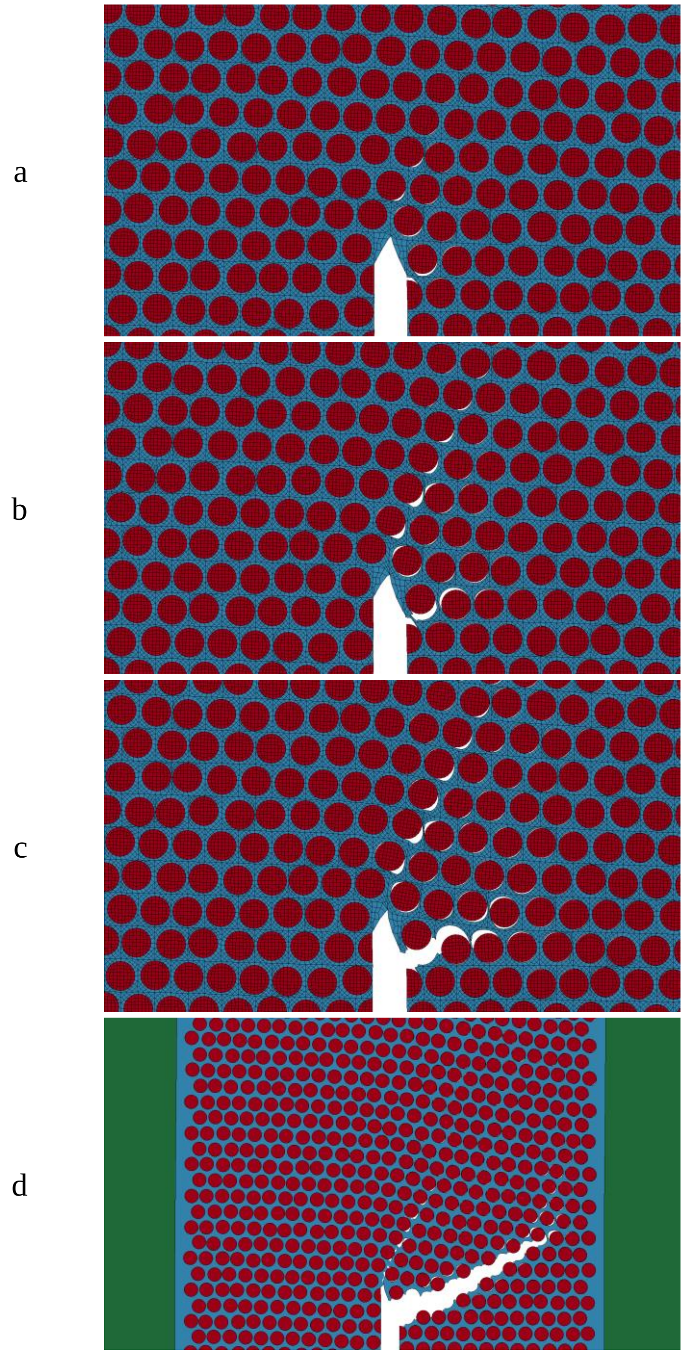

Figure 4.31: Crack growth under 10 m/s mode II loading in [90/90] microstructure with (a) early time initiation and (b) propagation, (c) later time propagation, and (d) crack approaching the embedded cell boundary.

a

b

c

d

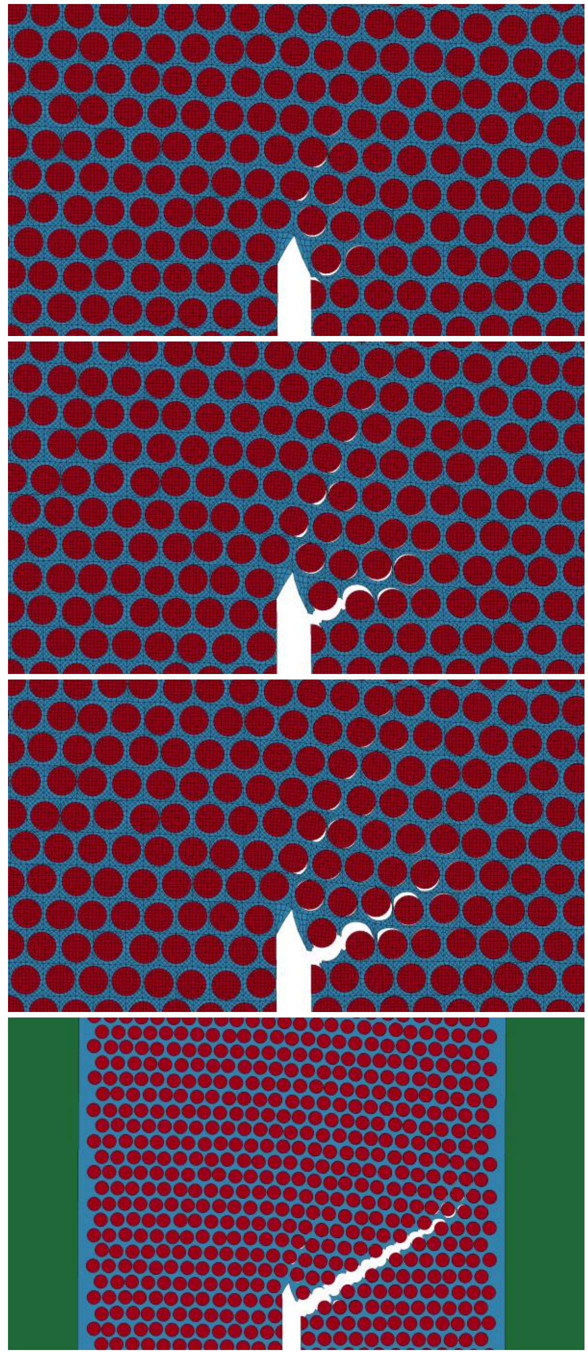

Figure 4.32: Crack growth under 1 m/s mode II loading in [90/90] microstructure with (a) early time initiation and (b) propagation, (c) later time propagation, and (d) crack approaching the embedded cell boundary.

a

b

c

d

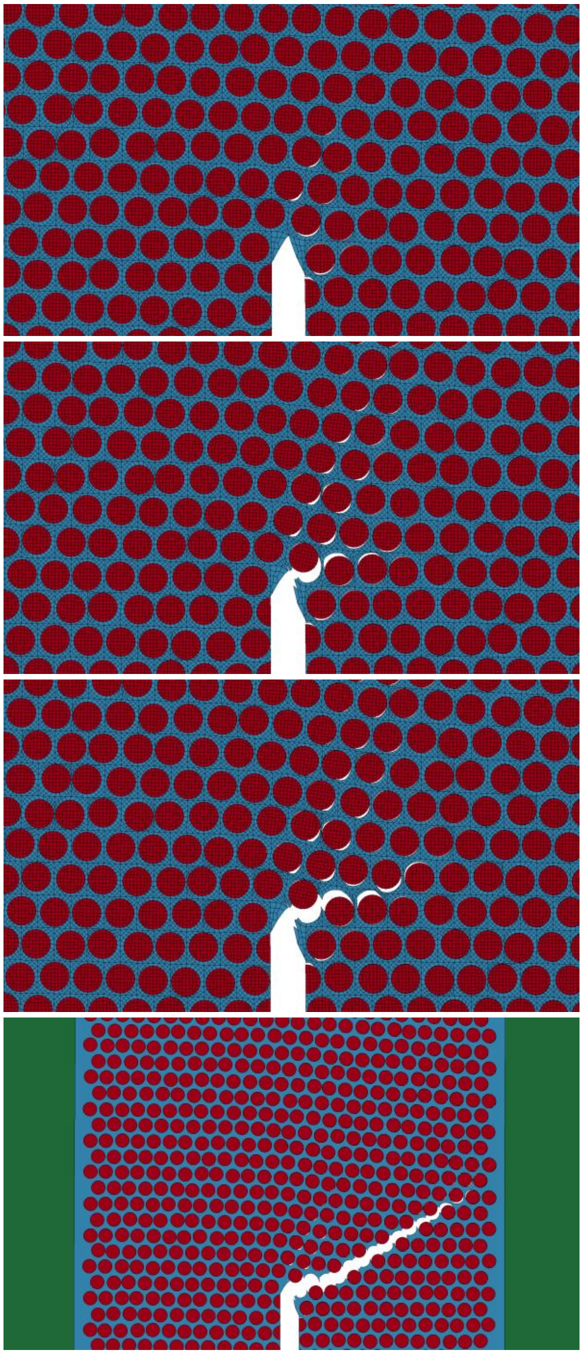

Figure 4.33: Crack growth under 0.1 m/s mode II loading in [90/90] microstructure with (a) early time initiation and (b) propagation, (c) later time propagation, and (d) crack approaching the embedded cell boundary.

a

b

c

d

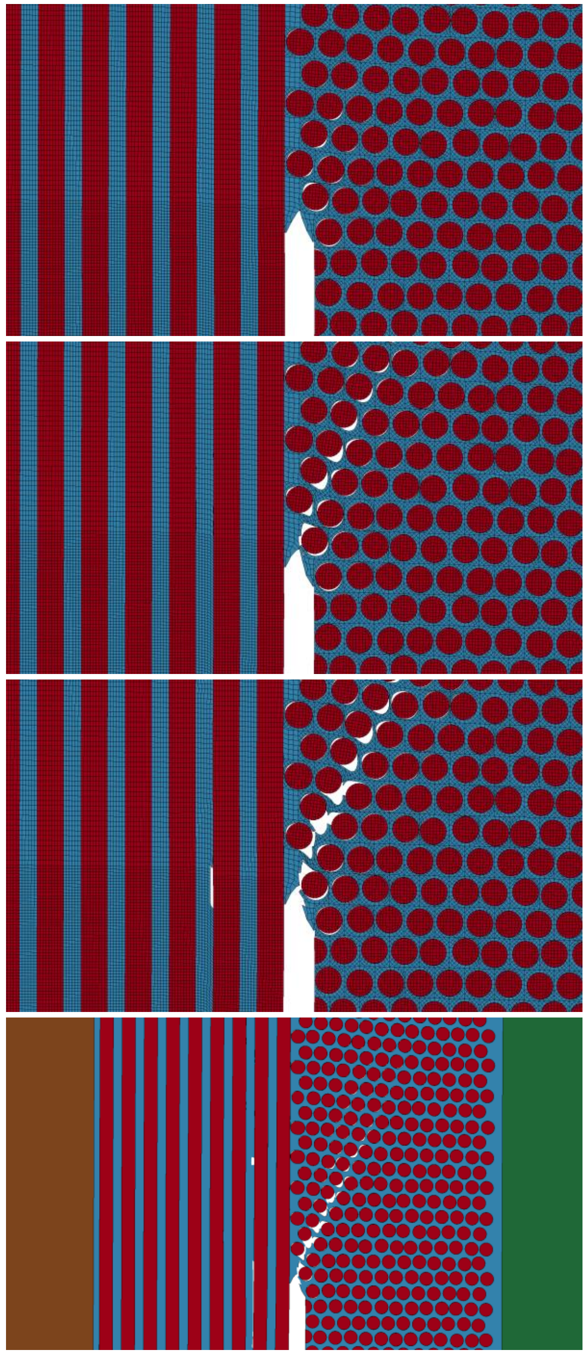

Figure 4.34: Crack growth under 10 m/s mode II loading in [0/90] microstructure with (a) early time initiation and (b) propagation, (c) later time propagation, and (d) crack approaching the embedded cell boundary.

a

b

c

d

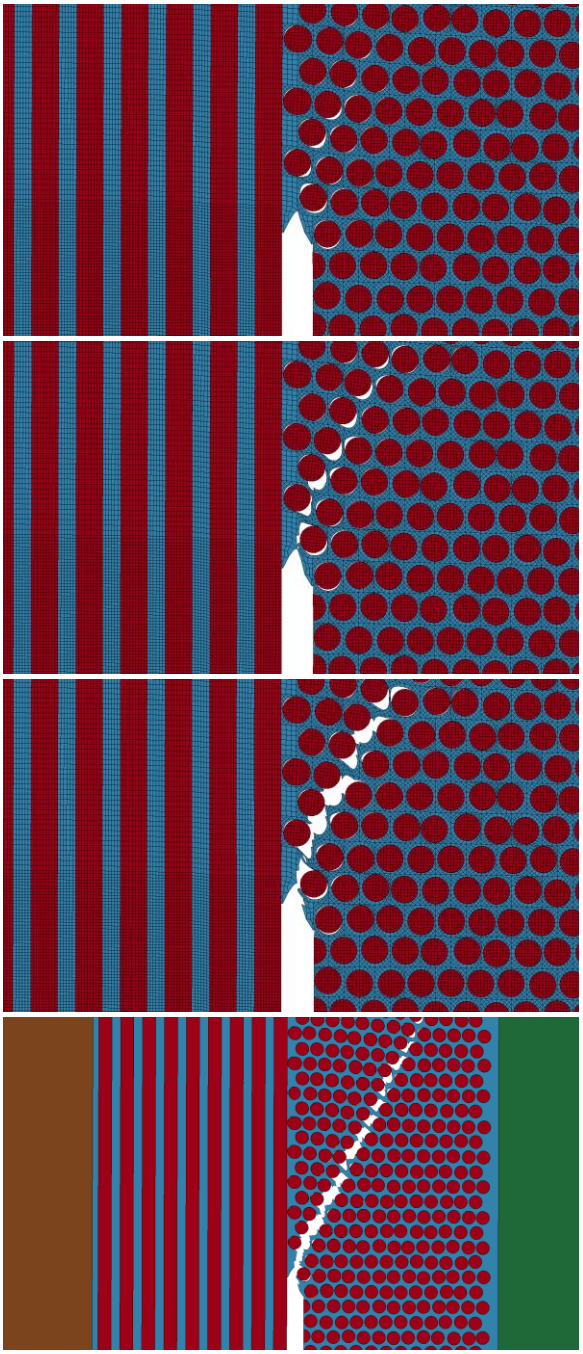

Figure 4.35: Crack growth under 1 m/s mode II loading in [0/90] microstructure with (a) early time initiation and (b) propagation, (c) later time propagation, and (d) crack approaching the embedded cell boundary.

a

b

c

d

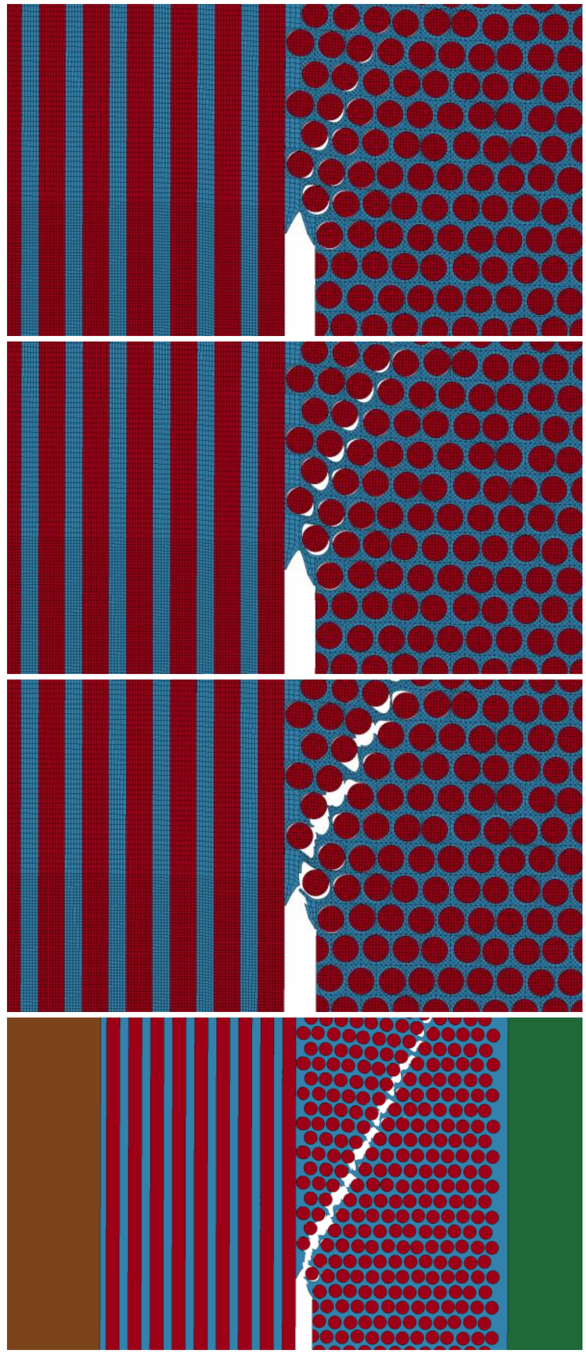

Figure 4.36: Crack growth under 0.1 m/s mode II loading in [0/90] microstructure with (a) early time initiation and (b) propagation, (c) later time propagation, and (d) crack approaching the embedded cell boundary.

4.7.3 Determining Mode II Traction-Separation Laws

As for mode I traction laws, stresses, strains, and displacements were output from the finite element models from a domain in the mesoscale elastic continuum region surrounding the microscale embedded cell. The domain begins and ends on the crack faces and is sufficiently far from the model boundary and load noses to avoid stress concentrations. The model output was then input into a MATLAB program, which computed $J(t)$ according to equations (4.5) to (4.8). Tangent crack opening displacement was used for δ_t.

The $J(t)$ and $\delta(t)$ were correlated to give $J(\delta)$. An S-shaped curve given by equation (4.14) was fit to the $J(\delta)$ data, and the traction-separation law was determined the derivative given by equation (4.15). Because the crack approached the embedded cell boundary before steady-state cracking developed, the $J(\delta)$ data does not have a knee. Effort was taken to ensure a reasonable fit to the data.

Rate-dependent J-integral data is presented in figure 4.37a for mode II [90/90] transverse cracking. The corresponding rate-dependent traction-separation laws for mode II transverse cracking is presented in figure 4.37b. Bilinear TSLs are provided in table 4.7 for each loading rate.

Rate-dependent J-integral data is shown in figure 4.38a for mode II [0/90] tow-tow delamination cracking, and the corresponding rate-dependent TSLs are in figure 4.38b. Bilinear TSLs are given in table 4.8 for mode II tow-tow delamination cracks.

Table 4.7: Rate-dependent mode II [90/90] transverse crack traction-separation laws.

	$\dot{\delta} = 10\ \mathrm{m/s}$	$\dot{\delta} = 1\ \mathrm{m/s}$	$\dot{\delta} = 0.1\ \mathrm{m/s}$
T_{II}, MPa	51.8	41.6	34.6
δ_{II}, mm	0.064	0.050	0.045
G_{IIc}, MPa-mm	1.661	0.889	0.690
E_s, MPa/mm	12958	6403	3644

Table 4.8: Rate-dependent mode II [0/90] tow-tow delamination crack traction-separation laws.

	$\dot{\delta} = 10\ \mathrm{m/s}$	$\dot{\delta} = 1\ \mathrm{m/s}$	$\dot{\delta} = 0.1\ \mathrm{m/s}$
T_{II}, MPa	249.2	220.2	212
δ_{II}, mm	0.038	0.038	0.035
G_{IIc}, MPa-mm	4.130	3.630	3.210
E_s, MPa/mm	24190	22024	21203

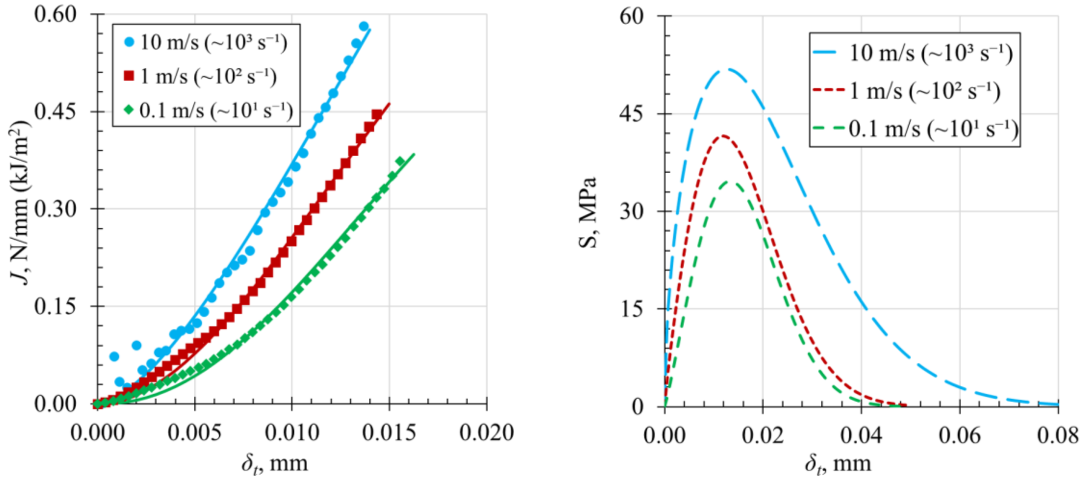

a b

Figure 4.37: (a) Transverse crack [90/90] mode II data and curve fit for J-integral as a function of normal opening displacement and loading rate. (b) Derivative of the fit to J-integral data, which is the traction-separation law for each loading rate.

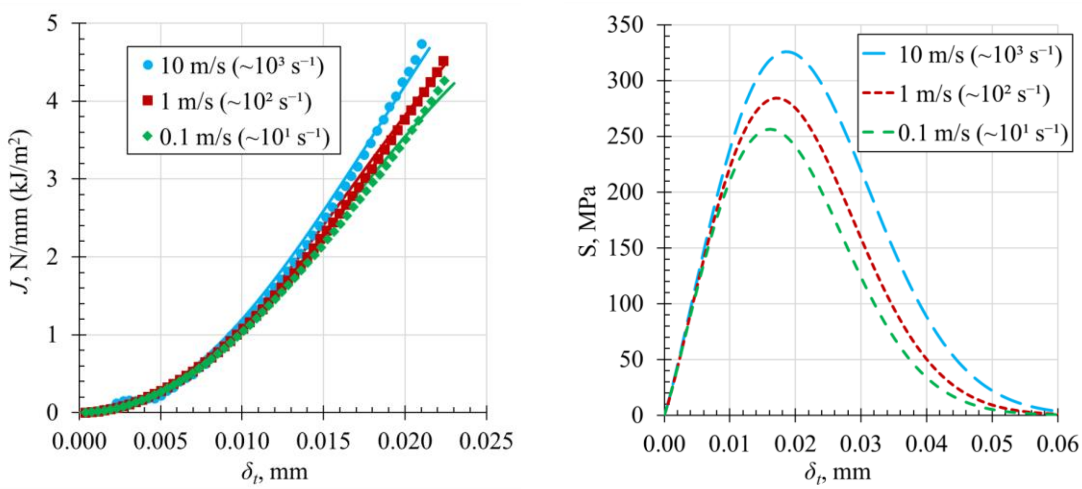

a b

Figure 4.38: (a) Tow-tow delamination crack [0/90] mode II data and curve fit for J-integral as a function of normal opening displacement and loading rate. (b) Derivative of the fit to J-integral data, which is the traction-separation law for each loading rate.

4.8 Bridging Length Scales

Using a microstructurally-resolved model embedded in a continuum, the microscale (~1 μm) was connected to the mesoscale (~1 mm). Microscale mechanics included rate-dependent matrix and fiber-matrix interface, and friction. The J-integral was used to bridge from microscale to mesoscale. Traction-separation laws were determined at the mesoscale from cracking within fiber-matrix microstructure. These mesoscale traction laws can be used to model microscale cracks as a mesoscale continuum crack using the cohesive zone model.

The bridging of length scales was studied by considering the load-displacement response of the embedded cell model compared with that of a mesoscale continuum crack. To do this, the embedded cell was replaced with cohesive interfaces in the direction of higher length scale cracking. Thus, mesoscale continuum cracking is controlled by the rate-dependent mixed-mode TSLs just determined. Only transverse cracking in mode I and II were considered for this study. Additional investigation is beyond the scope of this work and so is reserved for future work.

Bilinear traction laws were included in tables 4.5 through 4.8, and are presented graphically in figure 4.39 for convenience. The TSLs were fit to the rate-dependent cohesive model described earlier, and the parameters from this fit are included in table 4.9 for transverse cracks (i.e., [90/90] cracks). The fits for mode I and mode II transverse cracks are shown in figures 4.40a and 4.41a respectively. Examples of bilinear traction laws are extracted for various strain rates for mode I and mode II transverse cracks in figures 4.40b and 4.41b respectively.

Similarly, the TSLs were fit for tow-tow delamination cracks (i.e., [0/90] cracks) and are in table 4.10. Mode I and II fits for tow-tow delamination are shown in figures 4.42a and 4.43a and example TSLs are presented in figure 4.42b and 4.43b.

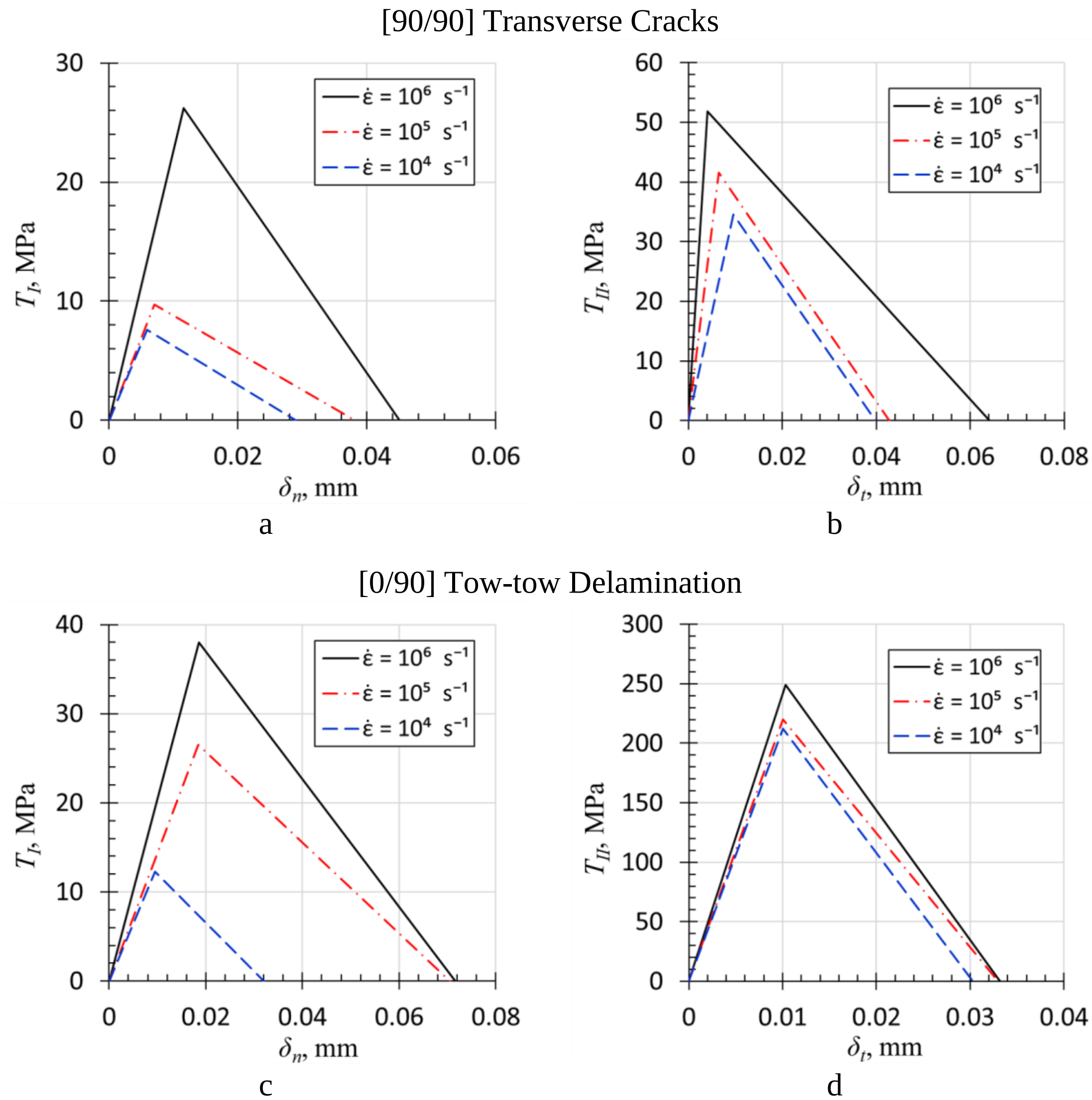

Figure 4.39: Rate-dependent mesoscale bilinear traction-separation laws for (a) mode I and (b) mode II transverse cracks and (c) mode I and (d) mode II tow-tow delamination cracks.

Table 4.9: Rate-dependent transverse crack mesoscale cohesive model parameters.

Mode I — Transverse Cracks			
T_0, MPa	4.2	G_{I_0}, MPa · μm	111
T_1, MPa	0.365	G_{I_∞}, MPa · μm	697
$\dot{\varepsilon}_{min}$, s^{-1}	450	$\dot{\varepsilon}_G$, s^{-1}	2.05×10^5
Mode II — Transverse Cracks			
S_0, MPa	31.4	G_{II_0}, MPa · μm	688
S_1, MPa	0.345	G_{II_∞}, MPa · μm	1,861
$\dot{\varepsilon}_{min}$, s^{-1}	450	$\dot{\varepsilon}_G$, s^{-1}	1.89×10^5

Table 4.10: Rate-dependent tow-tow delamination crack mesoscale cohesive model parameters.

Mode I — Tow-tow Delamination Cracks			
T_0, MPa	7.54	G_{I_0}, MPa · μm	192
T_1, MPa	0.513	G_{I_∞}, MPa · μm	1,427
$\dot{\varepsilon}_{min}$, s^{-1}	450	$\dot{\varepsilon}_G$, s^{-1}	5.28×10^4
Mode II — Tow-tow Delamination Cracks			
S_0, MPa	212	G_{II_0}, MPa · μm	3,210
S_1, MPa	1.88	G_{II_∞}, MPa · μm	4,230
$\dot{\varepsilon}_{min}$, s^{-1}	1.13×10^4	$\dot{\varepsilon}_G$, s^{-1}	9.28×10^4

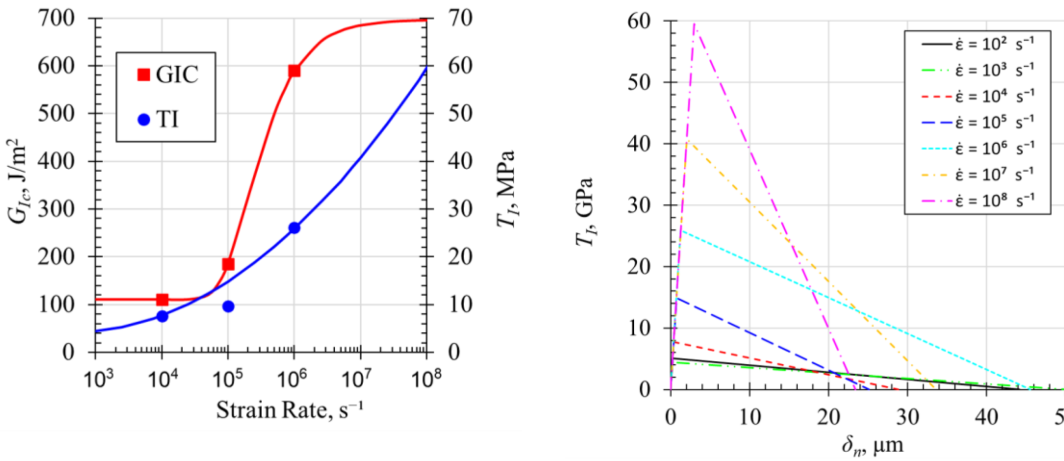

a b

Figure 4.40: Rate-dependent mode I mesoscale transverse crack [90/90] traction-separation laws. (a) Mesoscale points determined from microscale models, and rate-dependent cohesive model fit for use in mesoscale models. (b) Example bilinear traction laws from rate-dependent cohesive model for a range of strain rates, determined from model fit in (a).

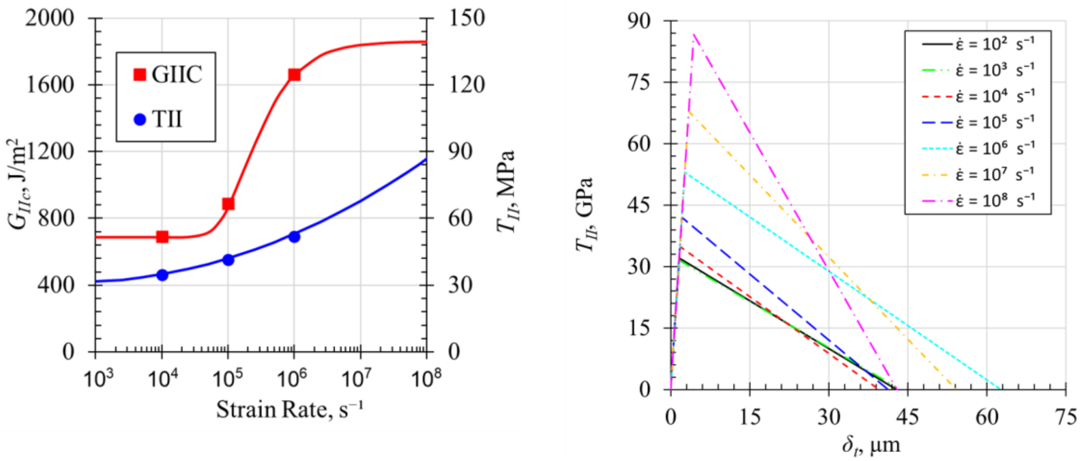

a b

Figure 4.41: Rate-dependent mode II mesoscale transverse crack [90/90] traction-separation laws. (a) Mesoscale points determined from microscale models, and rate-dependent cohesive model fit for use in mesoscale models. (b) Example bilinear traction laws from rate-dependent cohesive model for a range of strain rates, determined from model fit in (a).

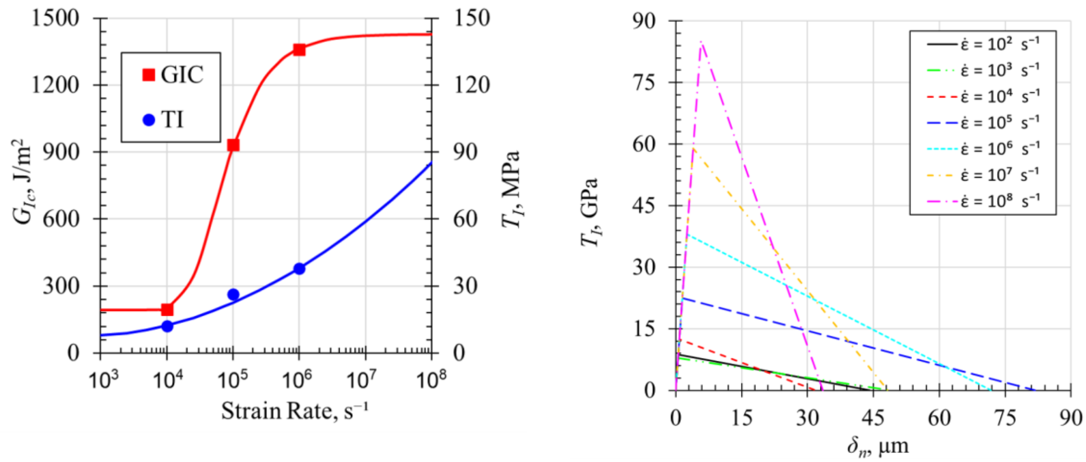

a b

Figure 4.42: Rate-dependent mode I mesoscale tow-tow delamination [0/90] traction-separation laws. (a) Mesoscale points determined from microscale models, and rate-dependent cohesive model fit for use in mesoscale models. (b) Example bilinear traction laws from rate-dependent cohesive model for a range of strain rates, determined from model fit in (a).

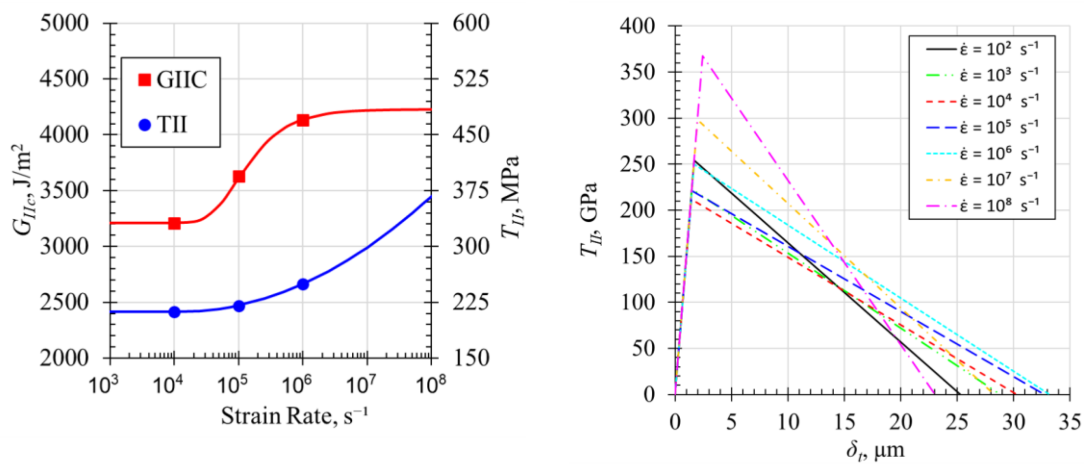

a b

Figure 4.43: Rate-dependent mode II mesoscale tow-tow delamination [0/90] traction-separation laws. (a) Mesoscale points determined from microscale models, and rate-dependent cohesive model fit for use in mesoscale models. (b) Example bilinear traction laws from rate-dependent cohesive model for a range of strain rates, determined from model fit in (a).

The mode I and II TSLs in table 4.9 and figures 4.40 and 4.41 were used to govern mesoscale continuum crack opening and the load-displacement response was compared with the load-displacement from the embedded cell model. Microscale embedded cell and mesoscale continuum mode I and mode II crack opening are compared in figures 4.44 and 4.45 respectively.

Modeling microstructurally resolved fracture as a mesoscale cohesive continuum limits the crack path, but this simplifying assumption is reasonable if the energy dissipated by fracture is adequately captured. Cohesive crack modeling is usually used for structural length scale simulations of composite fracture. For example, cohesive crack lengths range from ~10–100 mm in these references [64]–[66], [68], [69], [74]–[76], [119], [120]. However, cohesive zone modeling has found increased use in mesoscale modeling of woven composites. For example, mesoscale crack lengths range from ~1–10 mm in these references [14], [33], [52].

To the author's knowledge, the cohesive model has never been compared to microstructurally resolved cracks ranging in length from ~0.1–1 mm. The approach in the present work was to accurately model the microscale mechanisms and bridge up in length scale using the J-integral to determine mesoscale traction-separation laws. Qualitatively, this approach appears adequate for the mode I cracks in figure 4.44. However, the approach is limited by the continuum model assumption of self-similar crack growth in mode II. This limitation is seen when comparing cracks in figure 4.45. As discussed earlier, the mode II microstructural model restricts crack growth to mode I at approximately 45° relative to the loading direction. Future work should extend the microstructural region and computation time to allow additional 45° cracks to form and coalesce into a delamination crack at the boundary.

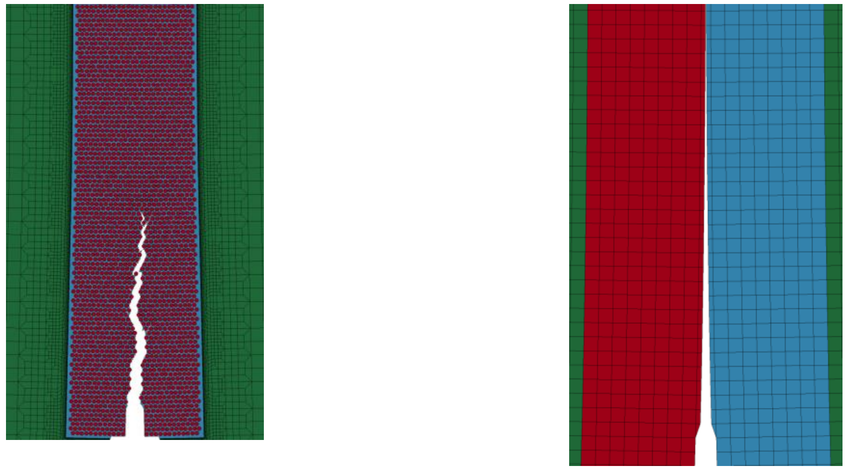

a b

Figure 4.44: Mode I opening of (a) the embedded cell microstructural model and (b) the continuum model with cohesive interfaces. Models are scaled similarly (largest element size is 30 µm in both). 10 m/s loading rate is shown.

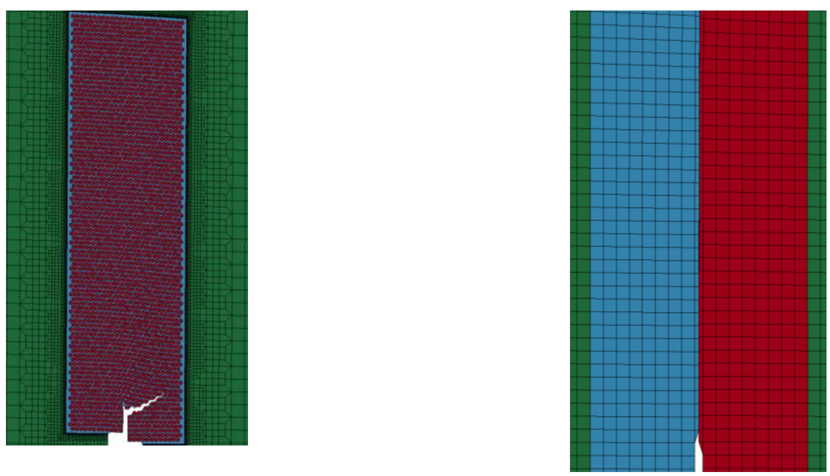

a b

Figure 4.45: Mode II shearing of (a) the embedded cell microstructural model and (b) the continuum model with cohesive interfaces. Models are scaled similarly (largest element size is 30 µm in both). 10 m/s loading rate is shown.

Mode I and II load-displacement response for the mesoscale continuum and the microscale embedded cell models are compared in figures 4.46 and 4.47, respectively. As before, the loading rates are 10 m/s, 1 m/s, and 0.1 m/s. In figure 4.46, mode I cracking initiates at around 0.02 mm under 10 m/s loading, 0.003 mm for 1 m/s, and 0.001 mm for 0.1 m/s. Cracks accelerate to apparent steady-state propagation by about 0.04 mm for 10 m/s, 0.02 mm for 1 m/s, and 0.013 mm for 0.1 m/s. Future investigation of the crack velocity is a possible extension of this model.

The lower loading rate load-deflection for the microstructural models appear typical of mode I brittle fracture, but higher rate load-deflection is more ductile. This difference is due to higher matrix yield strength and longer fiber matrix interface softening at higher loading rate. Mode I continuum model load-deflection is also initially brittle, but transitions to more ductile behavior. Continuum model ductile behavior is from continuum composite constitutive behavior and post-peak softening of the mesoscale traction laws. There are several energy dissipating mechanisms not included in the continuum model including rate-dependent constitutive behavior, microstructural strain rate variation at the crack tips, crack meandering, fiber-matrix debonding, and friction after debonding.

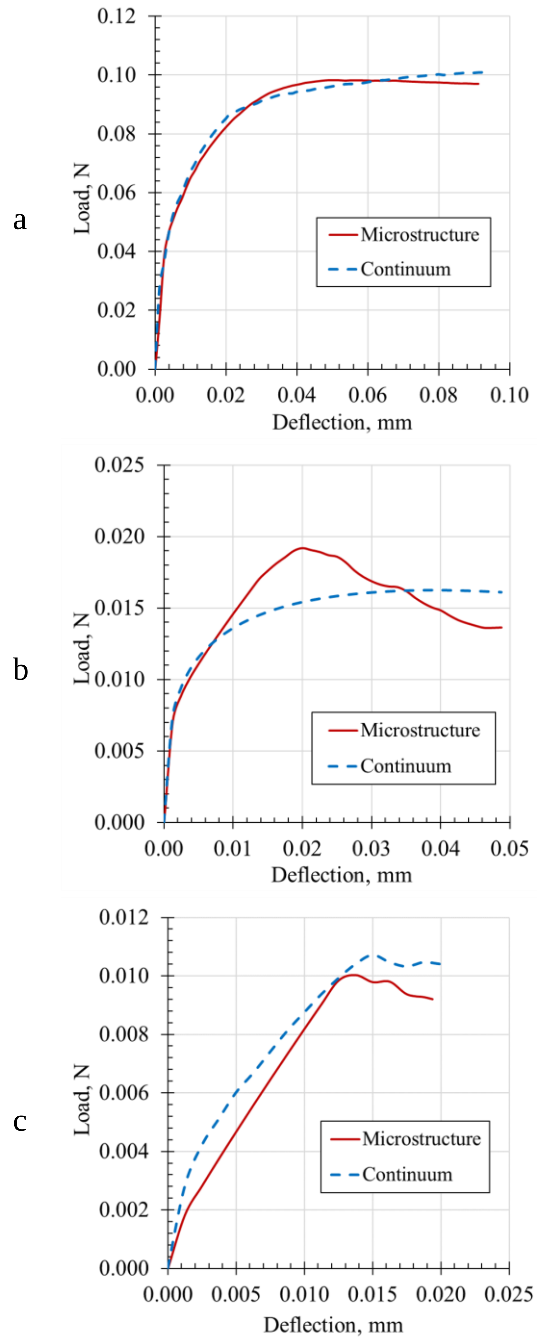

Figure 4.46: Mode I load-displacement results for microstructure and continuum models with loading rates (a) 10 m/s, (b) 1 m/s, and (c) 0.1 m/s.

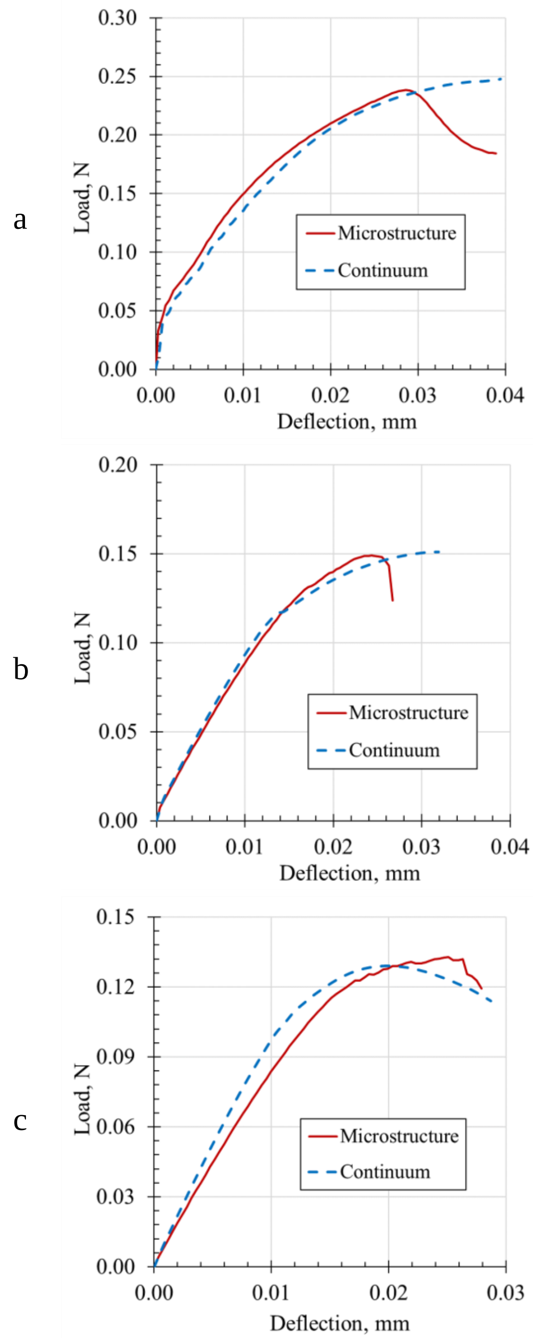

Figure 4.47: Mode II load-displacement results for microstructure and continuum models with loading rates (a) 10 m/s, (b) 1 m/s, and (c) 0.1 m/s.

There is some deviation of the 1 m/s and 0.1 m/s continuum response from the microstructure response. The microstructure model has local variations in strain rate within the FPZ, but the continuum model has constant strain rate in the FPZ. Local strain rate variations affect material responses in the microstructure FPZ due to rate-dependent matrix and fiber-matrix debonding. Thus, local strain rate variation affects energy dissipation. The 10 m/s loading rate model had fiber-matrix debonding response within the upper plateau, so the continuum and microstructure models are similar. However, the 1 m/s and 0.1 m/s models' fiber-matrix debonding response was in the transition region of the energy versus strain rate curve. Thus, material response can vary significantly with relatively small changes in strain rate. The continuum model cohesive interface strain rates were 10^7 s^{-1} for 10 m/s, 10^6 s^{-1} for 1 m/s, and 10^5 s^{-1} for 0.1 m/s, but these are constant for constant loading rate.

The mode II load-displacement responses show a smaller initial elastic region than mode I, which is typical of mode II brittle fracture. Microstructure and continuum model load-displacement responses are similar in mode II until the microstructure models show a load drop. The load drop is due to the 45° crack reaching the boundary of the embedded cell microstructure. The continuum model mode II crack propagation is self-similar, so it can only propagate along the cohesive interface and so it does not show a load drop. Eventually, the self-similar cohesive crack does interact with the end of the cohesive zone, and this causes the load to decrease eventually, but it is not a sharp drop. Overall, mode II microstructure and continuum load-displacement results are more similar than mode I. This is due to the fiber-matrix interface strain rates in the mode II microstructure model being within the upper plateau of response for 10 m/s and 1 m/s, while only the 0.1 m/s response is within the transition region.

4.9 Conclusions

In this chapter, traction-separation laws were developed to model transverse cracks and tow-tow delamination cracks in mesoscale models of plain weave composites. To develop these TSLs, a finite element model was built with microscale fiber-matrix microstructure embedded within a mesoscale continuum. The micro-to-mesoscale model included rate-dependent matrix and fiber-matrix debonding. The microstructural crack initiation and growth was examined.

Strain-rate dependent mode I and II traction-separation laws were determined using a domain J-integral to bridge from the microscale embedded cell to the mesoscale continuum. The J-integral computed the fracture energy as a function of crack opening displacement, and the derivative gave the TSL. Bilinear TSLs were derived from the micro-to-mesoscale model.

Length scale bridging was demonstrated by comparing load-deflection response of the embedded cell microstructural model with a fully continuum mesoscale cohesive crack model. The load-deflection responses were shown to be reasonably similar despite differences in strain rate and local crack evolution.

Future extensions of this work could include additional stochasticity in the microstructure. For example, an exploration of the effects of fiber size, fiber mesh resolution, larger matrix gaps between fibers, fibers touching, and introduction of defects around fibers. A wider mode II microstructure can be used to investigate the local mode I opening and coalescence into a global mode II crack. Mode I and II models could be extended to investigate crack speeds.

As discussed earlier, for dynamic impact simulations, it is important to understand the rate dependence of matrix and fiber-matrix interphase at high strain rates. The rate-dependent cohesive model used for fiber-matrix interface debonding assumes an S-shaped curve shape for strain energy release rate as a function of strain rate. This curve saturates to a constant energy beyond a given strain rate, but this maximum is based on three data points derived from microscale models. The microscale models could be loaded at higher rates to examine this plateau. Additionally, it is assumed that the traction quadratically increases with strain rate. Recent molecular dynamics (MD) simulations have shown that the traction also exhibits an S-shaped relationship with strain rate. These MD simulations could be used to investigate the input fiber-matrix interface debonding traction laws for much larger strain rates. This possibility highlights a need for a computational framework to bridge from the atomistic length scale to the microscale.

Chapter 5

THROUGH-THICKNESS IMPACT DAMAGE IN WOVEN COMPOSITES AT THE EARLIEST TIMESCALE

This chapter focuses on the earliest timescale following projectile impact. The domain of interest here is a finite RCC projectile impacting a mesoscale RVE of composite (see figure 2.2 and 2.4). The goal is to assess damage during this initial, short timescale, within the region of a single RVE. Damage includes continuum progressive damage in undulating composite tows, matrix damage, and tow-tow delamination. This study investigates the conditions for the initiation of damage, which is relevant to later timescales. Of interest is tow-tow delamination, which may initiate due to spall or deformation during this earliest timescale, and propagate during later timescales.

The approach taken is summarized by the flow chart in figure 5.1. At the earliest timescale, a longitudinal stress wave propagates through the composite thickness. The 1D analytical model of this stress wave propagation is compared with FEM predictions to validate the FEM. Validation involves a simple 1D FEM with elastic material behavior. A planar FEM of 1D wave propagation is used to investigate spallation in the absence of edge effects and without undulating plain weave composite geometry. The planar spall model considers elastic material behavior with rate-dependent interfacial debonding. Complexity is increased to a 3D FEM without edge effects but with inelastic material behavior and undulating woven composite geometry. Initially, the damage is investigated in the absence of projectile edge effects, when the projectile size equals the RVE size on the impact face. Then projectile edge effects are included, and damage is investigated under and around the projectile impact.

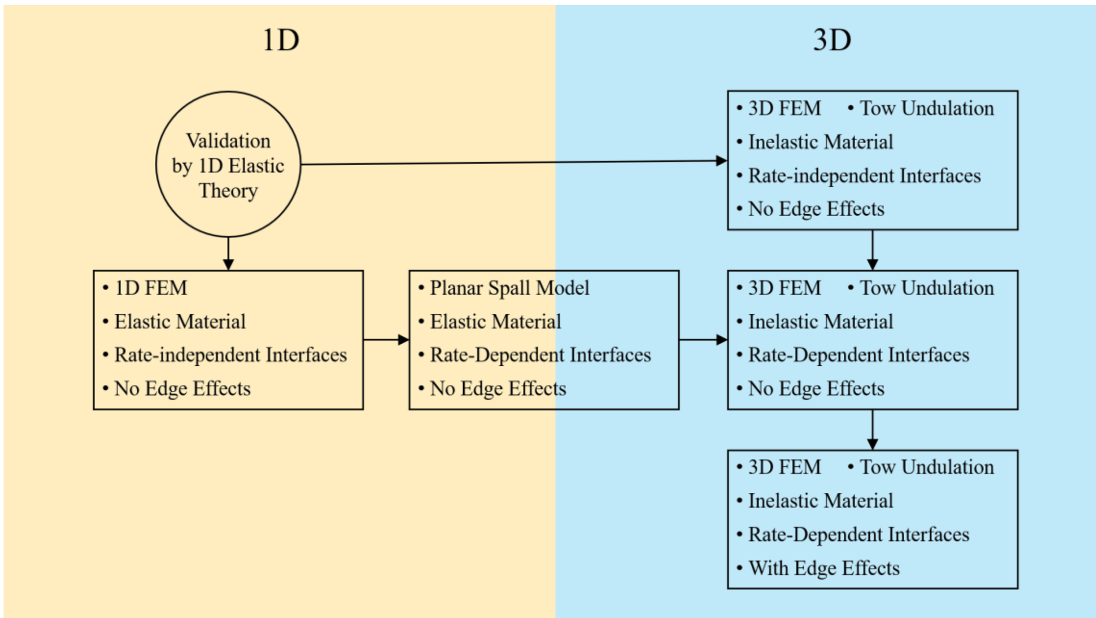

Figure 5.1: Illustration of the flow of modeling approaches taken in Chapter 5.

Naik et al. [121] discussed impact induced longitudinal stress waves and transverse deformation waves but neglected through-thickness stress waves, and they assumed transverse and longitudinal wave velocities were the same. Phoenix and Porwal showed that transverse deformation wave velocity is an order of magnitude smaller than longitudinal stress wave velocity [5]. Chocron et al. performed material characterization and mesoscale modeling in a methodology used to study impact on fabric and composites [52], [54], [122]–[124]. In this methodology, Chocron et al. validate their models with yarn impact and the transverse wave velocity according to

Smith [125], along with experiments and simulations, but neglect through-thickness waves.

Roylance studied through-thickness stress wave propagation and attenuation in 3.2 mm thick unidirectional carbon fiber epoxy composite laminates. [126] Roylance induced uniaxial strain, compressive waves by flyer plate impact, and assumed continuum composite properties for a single layer of unidirectional material. He found that woven composites and unidirectional composites have similar stress wave attenuation, but woven composites have higher spall strength. Roylance concluded that the improvement must be due to strengthening in the direction of wave propagation, which is provided by the yarn undulation leading to some fibers being partially oriented in the through-thickness direction. [126] However, the continuum assumption may not be adequate to study delamination damage between tows within a woven composite.

At the fiber length scale, Sockalingam investigated wave propagation in single fibers and in fiber bundles.[127], [128] Sockalingam studied the longitudinal wave and transverse wave propagation as well as the bending wave at the front of the transverse wave. However, the tow geometry considered was much smaller than in the present work.

Wave attenuation is enhanced in composites. Roylance cites several sources of attenuation: (1) hydrodynamic catch-up, where the unloading part of the wave catches up to and attenuates the leading part of wave; (2) geometric wave dispersion, due to wave reflections and refractions at the fiber-matrix interfaces; (3) crush-up of porosity; and (4) viscous losses due to the viscoelastic response of the matrix [126]. For wavelengths much larger than the composite thickness, the effects of dispersion on through-thickness stress waves is neglected [129]. However, considering geometric dispersion at the tow length scale (i.e., mesoscale) allows us to examine through-thickness stress wave propagation and early timescale damage. It is still assumed that the wavelength remains sufficiently large that the continuum assumption is valid for the fiber length scale (i.e., microscale).

5.1 1D Stress Wave Theory

Stress waves travel through material with a velocity equal to the speed of sound in the material. The longitudinal speed of sound, c_{L_i}, in a material, i, is given by equation (5.1), where ρ_i is the density and E_{L_i} is the longitudinal elastic modulus of the material. Wave speeds of the materials of interest in this work are presented in table 5.1.

Table 5.1: Elastic material properties for (A) unidirectional S-2 glass/epoxy composite [7], [130], [131], (B) epoxy [103], [104], and (C) steel projectile.

(A)	Composite
Density, ρ_C, $\mathrm{g/cm^3}$	1.76
Coefficient of Thermal Expansion, $10^{-6}\ \mathrm{C^{-1}}$	30.0
Elastic Modulus, GPa	
E_{11}	55.3
E_{22}	11.8
E_{33}	11.8
Wave Velocity, $\mathrm{m/s}$	
c_{11}	5,605
c_{33}	2,591
(B)	**Epoxy**
Density, ρ_M, $\mathrm{g/cm^3}$	1.14
Coefficient of Thermal Expansion, $10^{-6}\ \mathrm{C^{-1}}$	70.0
Elastic Modulus, E_M, GPa	2.48
Poisson's Ratio	0.36
Wave Velocity, c_M, $\mathrm{m/s}$	1,475
(C)	**Steel**
Density, ρ_P, $\mathrm{g/cm^3}$	7.85
Elastic Modulus, E_P, GPa	210.0
Wave Velocity, c_P, $\mathrm{m/s}$	5,172

$$c_{L_i} = \sqrt{\frac{E_{L_i}}{\rho_i}}\,, \qquad i = 1, 2, 3\ \ldots \tag{5.1}$$

When a projectile impacts a target with velocity V_I, shown schematically in figure 5.2, a longitudinal compressive stress wave of constant cross-section A travels out from the interface between projectile and target. Assuming materials remain in contact at the boundaries, then stress σ_j and particle velocity $\dot{u}_j$ are continuous across the boundary, as in equations (5.2) and (5.3). Here $j = I, R, T$ represent the incident, reflected, and transmitted portions, and $\dot{u}$ is the time derivative of displacement.

$$\sigma_I(z,t) + \sigma_R(z,t) = \sigma_T(z,t) \tag{5.2}$$

$$\dot{u}_I(z,t) + \dot{u}_R(z,t) = \dot{u}_T(z,t) \tag{5.3}$$

Momentum is also conserved across the boundary. For a segment dz, the impulse is equal to the change in momentum in equation (5.4). Then for this 1D (longitudinal) system, $\sigma = F/A$ and $m = \rho A z$ gives equation (5.5). Finally, the longitudinal speed of sound in the material is given by $c_L = dz/dt$ so that the uniaxial stress in the material is given by equation (5.6) [2].

$$F\,dt = d(m\dot{u}) \tag{5.4}$$

$$\sigma = \rho \frac{dz}{dt} \dot{u} \tag{5.5}$$

$$\sigma = \rho c_L \dot{u} \tag{5.6}$$

$$\dot{u}_I = \frac{\sigma_I}{\rho_1 c_{L_1}} \quad , \quad \dot{u}_R = \frac{\sigma_R}{\rho_1 c_{L_1}} \quad , \quad \dot{u}_T = \frac{\sigma_T}{\rho_2 c_{L_2}} \tag{5.7}$$

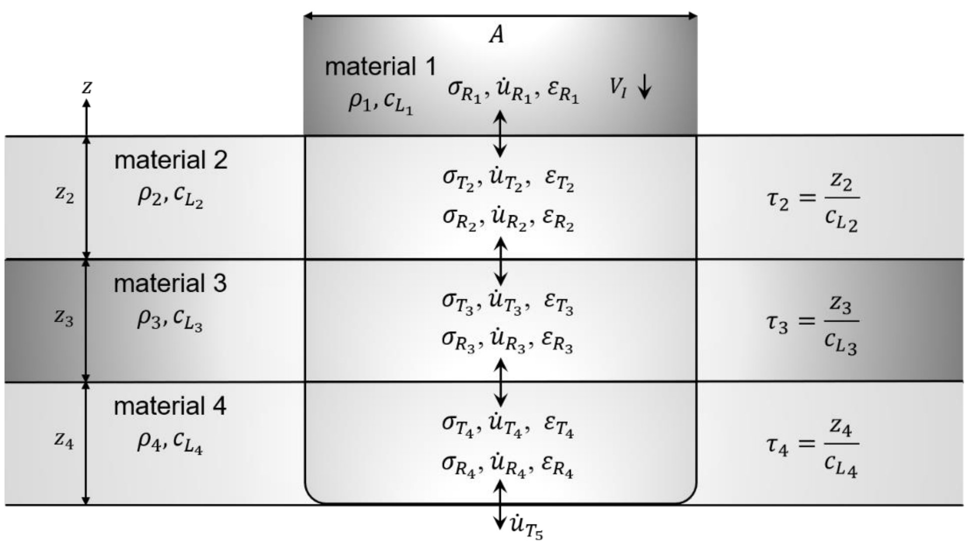

Figure 5.2: 1D wave propagation mechanics for a projectile impacting multi-layered materials.

Impedance is defined as a material's density times the sound speed in the material. If the impedance of a layer is greater than the impedance of a subsequent, neighboring layer, i.e., $\rho_i c_{L_i} > \rho_{i+1} c_{L_{i+1}}$, compressive stress will reflect as tension (i.e., sign change).

Consider the interface between the projectile, $i = 1$, and target, $i = 2$, in figure 5.2. From equation (5.6), relationships are found for incident, reflected, and transmitted portions of the stress wave, given in equation (5.7). The stress transmitted into a given layer is the same as the stress incident upon the next layer. Plugging equation (5.7) into equation (5.3) and solving the resulting equation simultaneously with equation (5.2) gives equation (5.8).

The assumption of continuity of displacement across the boundary (for constant area A, at time t) gives equation (5.9). Continuity of particle velocity gives equation (5.10). Simultaneously solving equations (5.9) and (5.10) and using equation (5.6) gives equation (5.11), which is the stress in the first layer of the target, $i = 2$, following impact by the projectile, $i = 1$, at velocity V_I. It can be shown [132] that the stress in any subsequent layer of the target, $3, 4, 5, \ldots$, is given by equations (5.11) and (5.12). Similarly, particle velocity may be found for any subsequent layer using equations (5.6), (5.11), and (5.12). Strain in any layer may be found according to $\varepsilon_i = \dot{u}_{T_i}/c_{L_i}$. Finally, the characteristic time for a stress wave to propagate across any layer is given by $\tau_i = z_i/c_{L_i}$.

$$\frac{\sigma_T}{\sigma_I} = \frac{2\rho_2 c_{L_2}}{\rho_1 c_{L_1} + \rho_2 c_{L_2}} \quad , \quad \frac{\sigma_R}{\sigma_I} = \frac{\rho_2 c_{L_2} - \rho_1 c_{L_1}}{\rho_1 c_{L_1} + \rho_2 c_{L_2}} \tag{5.8}$$

$$\rho_1 c_{L_1} \dot{u}_{I_1} = \rho_2 c_{L_2} \dot{u}_{T_2} \tag{5.9}$$

$$V_I - \dot{u}_{I_1} = \dot{u}_{T_2} \tag{5.10}$$

$$\sigma_{T_2} = \frac{\rho_2 c_{L_2} V_I}{1 + \frac{\rho_2 c_{L_2}}{\rho_1 c_{L_1}}} \tag{5.11}$$

$$\sigma_{T_k} = \frac{2\rho_k c_{L_k}}{\rho_{k-1} c_{L_{k-1}} + \rho_k c_{L_k}} \cdot \sigma_{T_{k-1}}, \quad k = 3, 4, 5, \ldots \tag{5.12}$$

5.2 Finite Element Models

5.2.1 1D Limitations

The stress according to the 1D theory was generalized here for any number of target layers. However, there are limitations that should be considered. First, equations (5.11) and (5.12) assume linear elastic response of the projectile and specimen, which is approximately correct only for low impact velocities. Second, for the response to be 1D, the projectile and target must have the same area A, or there will be edge effects, and Poisson effects must be neglected. Third, the assumptions of continuity and conservation of momentum across the boundaries must remain valid, so the 1D theory becomes invalid once fracture or delamination occurs. Finally, there are two limiting times. The characteristic time for the compressive wave to traverse the projectile is the first, so the projectile must be thick enough that the stress wave crosses the target before the projectile. Similarly, for a multi-layered analysis, once the compressive wave returns to the impact face of the first layer, undesirable reverberations begin. For these reasons, validation involves a 1D finite element model, neglecting Poisson effects, impacted at $100\ \mathrm{m/s}$, and considers early time, before any delamination may occur and before undesirable reverberations begin. Once the finite element model is shown to produce a similar response to that predicted by the 1D theory, these requirements will be relaxed and the 1D finite element model will be extended to 3D.

5.2.2 Geometry

The geometry of an RVE of a plain weave fabric composite is shown in figure 5.3.[25]–[28] Geometry and parameters were discussed in chapter 3.

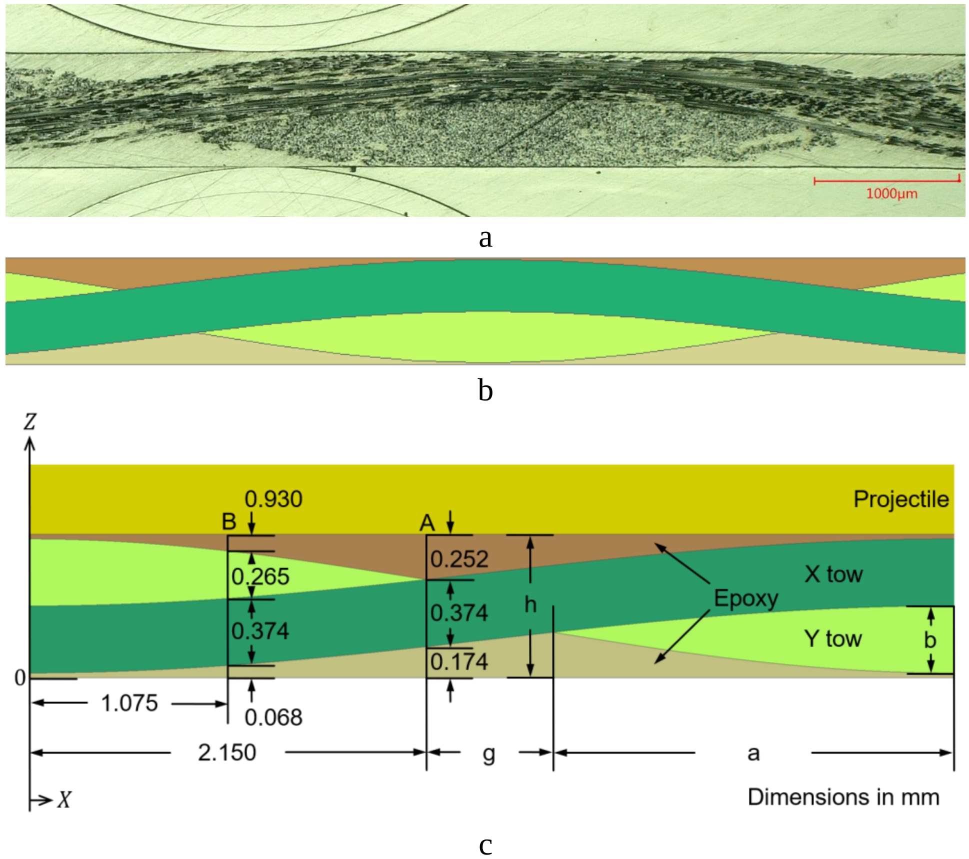

Figure 5.3: Mesoscale plain weave fabric composite architecture in (a) micrograph and (b) finite element model with (c) dimensions and parameters.

The mesoscale model violates the 1D theory for two reasons. First, thin epoxy layers will lead to wave reverberations, which cause the continuity assumption to break down. Also, interfaces with impedance mismatch cause wave reflections and sign change as described earlier. Second, the curvature of the layers violates the requirement of constant longitudinal cross-sectional area. However, it is reasonable to expect that if the model is well behaved and valid for the 1D response, then the 3D response will be well behaved and valid. Therefore, initially two lines are taken from the mesoscale model for validation by the 1D theory. These lines are indicated in figure 5.3c as A and B. Two 1D finite element models (FEMs) were developed for these two positions. These 1D FEMs are shown in figure 5.4. These 1D models have 80 elements of 0.01 mm in the through-thickness dimension by 0.02 mm in each of the lateral dimensions.

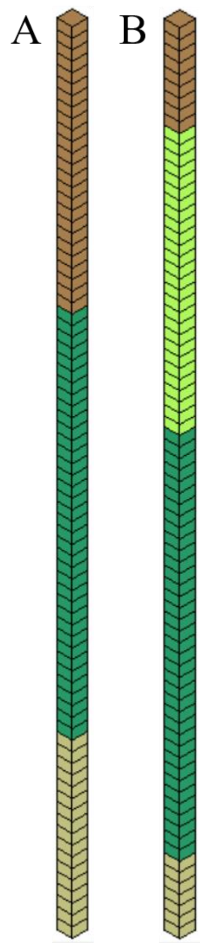

Figure 5.4: 1D finite element models for lines in the mesoscale RVE at positions A and B. Colors follow from figure 5.3, where light/dark brown are epoxy and light/dark green are composite tows.

In all models, unless otherwise indicated, the length of the projectile was 5.6 mm. The limiting time for all validation simulations was therefore $5.6 \times 10^{-3}\ \mathrm{m} \div 5172\ \mathrm{m/s} = 1.08$ μs. Validation simulations were ended before this time, before the stress wave in the projectile reached the back face of the projectile. The lateral dimensions of the projectile were the same as the target model so that there were no edge effects, which will be investigated later.

The second limiting time is when stress waves begin to reverberate within any layer of the target. Stress waves will begin to reverberate in the first layer (epoxy) of the 1D model A at a time of $2 \times 0.252 \times 10^{-3}\ \mathrm{m} \div 1475\ \mathrm{m/s} = 0.34$ μs. This time is sufficient for the stress wave to have propagated into the third layer, meaning the stress in each layer may be compared to the 1D theory without concern.

Stress waves will begin to reverberate in first layer (epoxy) of the 1D model B at a time of $2 \times 0.093 \times 10^{-3}\ \mathrm{m} \div 1475\ \mathrm{m/s} = 0.13$ μs. This time is not sufficient for the stress wave to have propagated into the third or fourth layers of 1D model B, therefore some error is expected when comparing the stress in these layers with the 1D theory.

Since the composite impedance is greater than the epoxy, stress waves will reflect at composite-epoxy interfaces and change sign (compression to tension). However, validation considers only the wave front of the compressive wave as it passes through the layers, and does not investigate wave reflections or reverberations.

5.2.3 Mesh Convergence Study

A mesh convergence study was conducted with 1D FEMs for line A in figure 5.3c. Models investigated element through-thickness sizes of 0.01 mm, 0.02 mm, 0.04 mm, 0.08 mm, and ≥ 0.16 mm (i.e., a single element through the thickness in each layer). Lateral element sizes of 0.016 mm were maintained for all models since only the through-thickness response is of interest here. To accurately model stress wave propagation, it is important that the stress wave does not cross one or more elements per time step, or the wave could be attenuated by stress averaging across elements. The speed of sound in the composite through-thickness layers is $2591\ \mathrm{m/s}$, so considering the 0.01 mm element size, a maximum time step of $\sim 10^{-9}$ s was ensured for all simulations.

Each 1D FEM was impacted at $V_I = 100\ \mathrm{m/s}$, layers were perfectly bonded (i.e., layers shared nodes at each boundary, "node merged"), and elastic response was modeled and compared with the 1D theory. The stress and particle velocity produced in each of the three layers by the stress wave propagation were determined. The percent error was calculated as $Error\ (\%) = 100 \times \left|\frac{1D\ Theory\ Result - 1D\ FEM\ Result}{1D\ Theory\ Result}\right|$. This error was averaged for each of the six data points (discussed later) for each of the five mesh size models. The results of the mesh convergence study are plotted in figure 5.5. Note that the results for the coarsest mesh, 0.16 mm element model, are not shown since they are far off the chart ($> 90\%$ error). The results in figure 5.5 show convergence to about 2% average error as element size decreases, so a through-thickness element size of about 0.01 mm was used for all subsequent simulations (3,335,084 elements). Smaller elements were not investigated as they could decrease the time step and thereby increase the computational cost of the simulations. Due to the short time scale of interest ($\sim 1\ \mu$s), simulations with 0.01 mm element thickness were not overly computationally expensive, so this element size is acceptable.

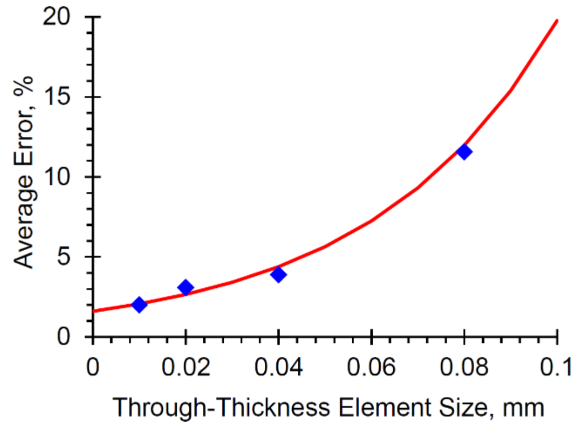

Figure 5.5: Results of the mesh convergence study on 1D models.

5.2.4 Additional Model Details

Semi-infinite boundary conditions were used on four sides in 1D simulations. Symmetry boundary conditions were used on two faces of the one-quarter symmetry 3D model, and semi-infinite boundary conditions were used on the remaining two faces. Hence, stress waves do not reflect at model boundaries (only at material interfaces). The top of the projectile and bottom of the target were free, and contact was set between projectile and target. These boundary conditions are summarized in figure 5.8.

Single integration point hexahedral elements were used in all simulations. Stress is computed by LS-DYNA at the integration point at the element center and particle velocity is computed at the nodes. To compare with the 1D theory at a given time, the model elements interrogated for stress and model nodes are interrogated for velocity. Thus, some error is expected when comparing the stress and particle velocity with the 1D theory, which does not consider discretized geometry.

To eliminate the possibility of Poisson effects, the 1D model simulations set all Poisson's ratios to zero. In all models, the fiber tows were treated as a unidirectional continuum composite material. In the 3D mesoscale model, the material properties were oriented to follow the undulation of the tows. Taking stiffness for example, E_{11} follows the tow undulation along the length, E_{22} across the width, and E_{33} through the thickness. In the 1D model simulations, the through-thickness properties were important for comparison with the 1D theory, and material properties were oriented along the 1D lines indicated in figure 5.3c (i.e., A and B). In reality, the through-thickness properties will have some orientation bias, but assuming no bias in 1D FEMs facilitates comparison with the 1D theory in which bias is not possible.

Simulations were conducted using LS-DYNA [133]. Figure 5.1 illustrates the flow of simulations from 1D validation through 3D damage investigations. Elastic material properties and models were described earlier. Inelastic, rate-dependent material properties for all models were taken from the literature as follows. Unidirectional S-2 glass, DER353 epoxy composite materials were modeled with MAT_162 (MAT_COMPOSITE_MSC_DMG) [7], [21], [134]–[136]. Layers of DER353 epoxy were modeled with the rate-dependent, tabular DER353 epoxy data using MAT_24 (MAT_PIECEWISE_LINEAR_PLASTICITY). Rate-dependent, stress-strain response of the DER353 epoxy may be found in these references [103], [104]. A rate-dependent cohesive zone modeling approach for delamination [106] used tiebreak contact (option 13) in LS-DYNA (CONTACT_AUTOMATIC_ONE_WAY_SURFACE_TO_SURFACE_TIEBREAK). Material model parameters are included in table 5.1 and table 5.2, and cohesive model parameters are discussed later. The MAT_162 composite material model is discussed in Appendix A and in the LS-DYNA manual [133].

Table 5.2: Composite material model parameters for MAT_162. [7], [21], [134]–[136], used in 3D models investigating damage.

E_{11}, GPa	E_{22}, GPa	E_{33}, GPa	ν_{21}	ν_{31}	ν_{32}	G_{12}, GPa	G_{23}, GPa	G_{31}, GPa
55.3	11.8	11.8	0.05	0.05	0.45	4.3	3.7	4.3
ρ, g/cm^3	X_{1T}, MPa	X_{1C}, MPa	X_{2T}, MPa	X_{2C}, MPa	X_{3T}, MPa	S_{FC}, MPa	S_{FS}, MPa	S_{12}, MPa
1.76	1380	770	45	137	45	850	250	76
S_{23}, MPa	S_{31}, MPa	SFFC	PHIC	E_LIMIT	S_DELM	OMGMX	ECRSH	EEXPN
38	76	0.1	10	0.2	1.2	0.999	0.005	2
AM1	AM2	AM3	AM4	C_{rate1}	C_{rate2}	C_{rate3}	C_{rate4}	
100	10	1.0	0.1	0.03	0	0.03	0.03	

5.3 Model Validation

For an impact velocity of $V_I = 100\ \mathrm{m/s}$, the particle velocity, $\dot{u}$, and stress, σ, according to the generalized 1D theory in equations (5.6), (5.11) and (5.12) were computed for each layer of 1D finite element models A and B and compared with the simulation results. As the wave front passed through elements or nodes in each layer, these elements/nodes were interrogated and the output from at least 3 elements/nodes was averaged to determine stress or particle velocity at the wave front. As discussed, validation simulations considered elastic material behavior only since the 1D theory can only consider elastic behavior.

Since the tiebreak cohesive approach will be used in the 3D models to investigate delamination, tiebreak contact is introduced between layers in the 1D model to ensure it does not introduce any numerical error. Simulations were conducted with interlayer nodes merged (contact *cannot* be broken) and with interlayer cohesion (tied contact *can* be broken, but validation simulations are stopped before any separation occurs). Note that the zero-thickness cohesive approach in tiebreak contact does not have integration points, but constitutive behavior involves traction-separation rather than stress-strain.

The results for 1D model A are provided in table 5.3. The results for 1D model B are provided in table 5.4. In both tables, the time, τ, at which the stress wave will have crossed each layer, is provided. The stress wave propagation in the 1D models is illustrated by figures 5.6 for model A and 5.9 for model B. Later in time, the wave reverberations become difficult to track, as seen in figure 5.9 after 0.42 μs.

Table 5.3: Comparison of results from 1D theory and 1D FEM for line A. Impact velocity 100 m/s. (Model uses elastic material behavior with node-merged or rate-independent cohesive zones.)

Layer	Thick, mm	τ, μs	1D Theory $\dot{u}$, m/s	Node-Merged		Cohesive Zones		1D Thry σ, MPa	Node-Merged		Cohesive Zones	
				1D FEM $\dot{u}$, m/s	Err, %	1D FEM $\dot{u}$, m/s	Err, %		1D FEM σ, MPa	Err, %	1D FEM σ, MPa	Err, %
Epoxy	0.252	0.18	96.0	95.8	0.2	96.0	0.01	161.5	164.0	1.6	164.0	1.6
Comp.	0.374	0.32	51.8	53.5	3.3	53.5	3.3	235.9	238.8	1.2	238.8	1.2
Epoxy	0.174	0.43	75.6	77.3	2.2	77.3	2.1	127.2	131.6	3.5	131.6	3.5

Table 5.4: Comparison of results from 1D theory and 1D FEM for line B. Impact velocity 100 m/s. (Model uses elastic material behavior with node-merged or rate-independent cohesive zones.)

Layer	Thick, mm	τ, μs	1D Thry $\dot{u}$, m/s	Node-Merged		Cohesive Zones		1D Thry σ, MPa	Node-Merged		Cohesive Zones	
				1D FEM $\dot{u}$, m/s	Err, %	1D FEM $\dot{u}$, m/s	Err, %		1D FEM σ, MPa	Err, %	1D FEM σ, MPa	Err, %
Epoxy	0.093	0.06	96.0	96.0	0.01	96.0	0.02	161.5	163.9	1.5	163.9	1.5
Comp.	0.265	0.17	51.8	53.2	2.7	53.0	2.4	235.9	238.5	1.1	238.4	1.1
Comp.	0.374	0.31	51.8	53.3	2.9	53.2	2.8	235.9	238.9	1.3	238.6	1.2
Epoxy	0.068	0.36	75.6	77.3	2.2	77.0	1.8	127.2	127.5	0.2	127.6	0.3

The percent error was again calculated as $Err\ (\%) = 100 \times \left|\frac{1D\ Theory\ Result - 1D\ FEM\ Result}{1D\ Theory\ Result}\right|$. The results show very little error for the 1D finite element models compared with the 1D theory. Error is generally less than about 3%. As discussed earlier, sources of discrepancy can include wave reverberations at later time and computation of stress at integration points at the center of elements rather than nodes.

Recall that these validation simulations do not continue to the point of decohesion. Extension to 3D and investigation of delamination cracking requires appropriate cohesive traction-separation laws, which were determined in Chapter 4.

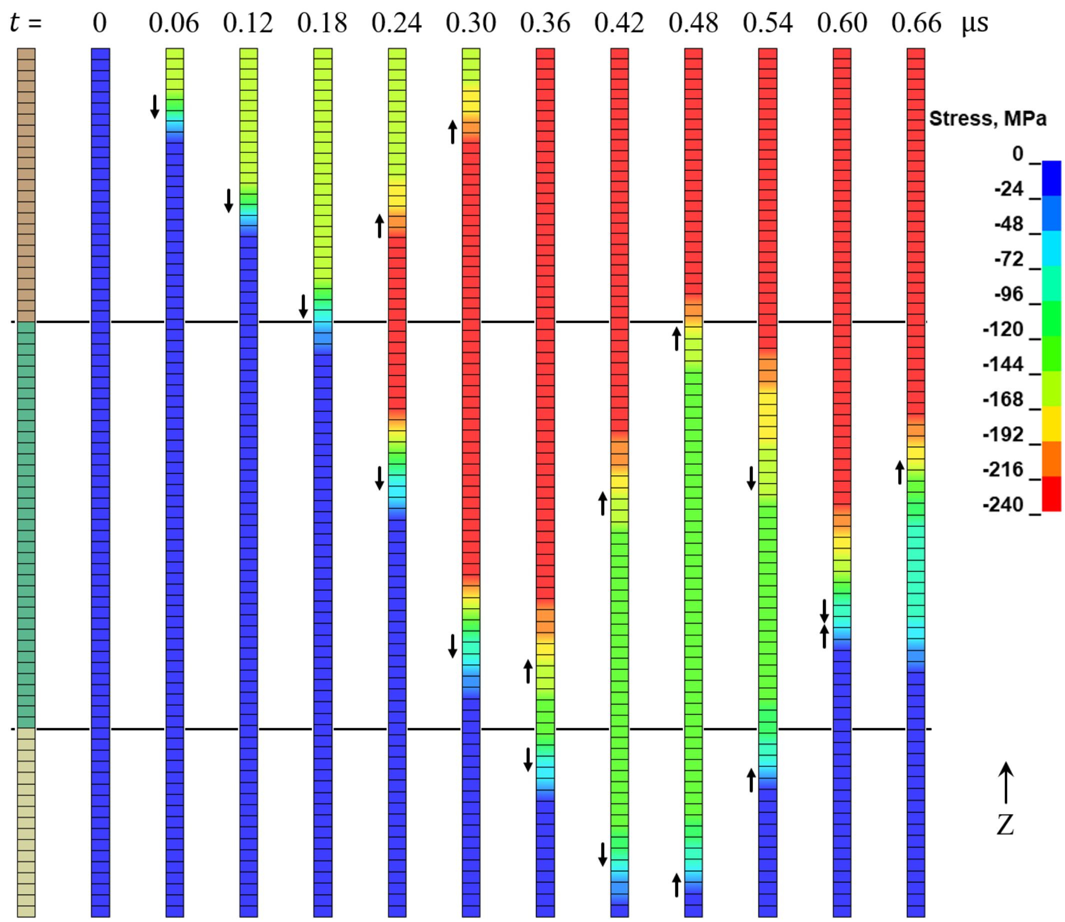

Figure 5.6: Elastic stress wave propagation in 1D finite element model over time for location A.

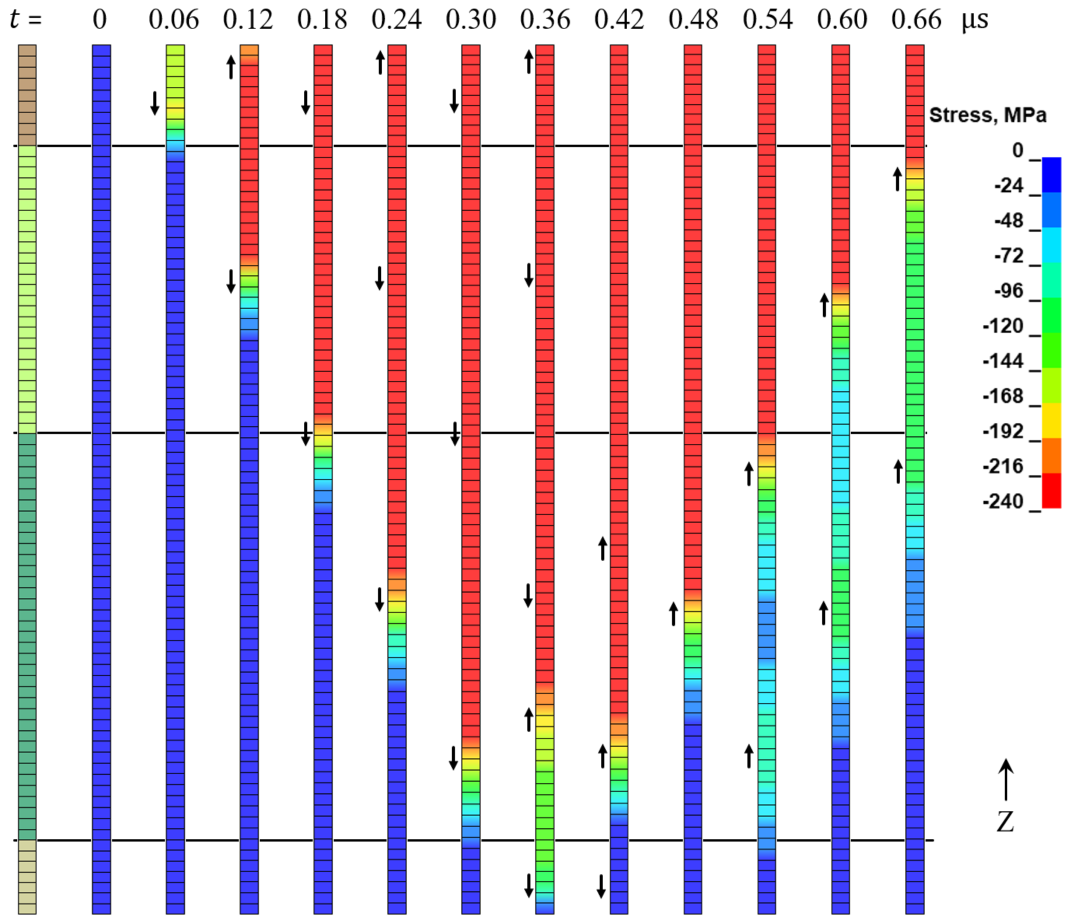

Figure 5.7: Elastic stress wave propagation in 1D finite element model over time for location B.

5.4 Results and Discussion

5.4.1 Comparing 3D Model to 1D Theory

The through-thickness stress wave modeling approach was validated by demonstrating that the 1D finite element model responses match the 1D theory with very little error. To investigate early timescale tow-tow delamination cracking and damage in a woven composite, we must relax the requirements described earlier for the 1D theory comparison. Namely, we enable non-linear, inelastic, and strain-rate dependent material behavior [103], [104], interfacial cohesive failure [106], [137], and we consider a realistic projectile [7] and sufficient time for stress wave propagation and the initiation of the deformation cone wave [5], [7], [138]. Two 3D models are shown in figure 5.8.

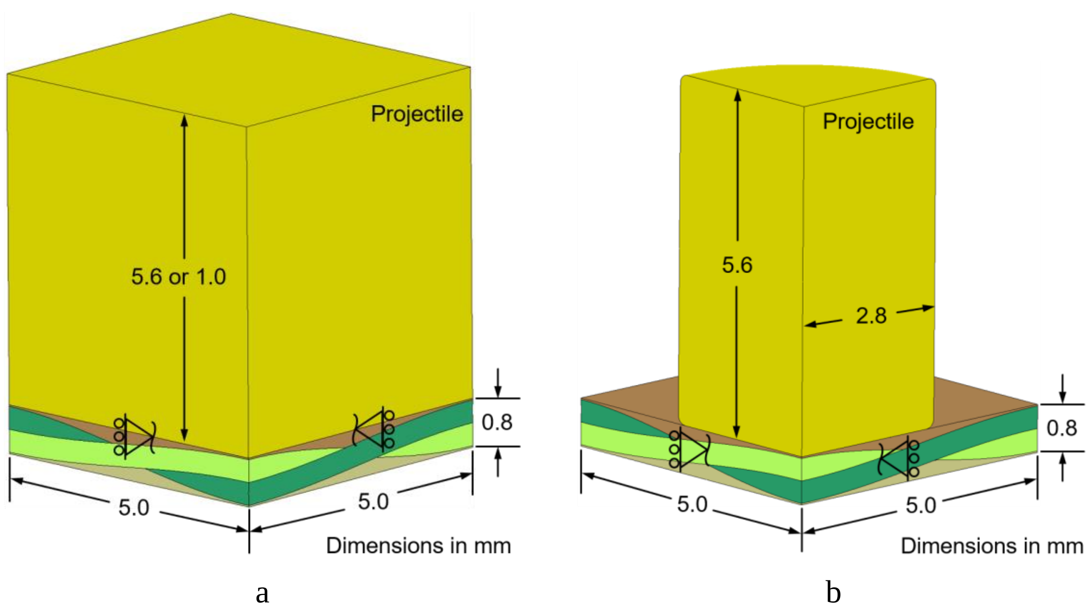

Figure 5.8: One-quarter symmetry, mesoscale finite element models of plain weave composite impacted by (a) projectile of the same length and width as the target and by a (b) right circular cylindrical projectile.

The first model considered, figure 5.8a, included a projectile that matched the target face size. This model produces a roughly planar stress wave across the target, illustrated by figure 5.9, and is used to investigate spall-induced delamination without any projectile-edge effects. Note that, to illustrate the through-thickness stress wave propagation in a plain weave unit cell, the model shown in figure 5.9 used elastic material properties with zero Poisson's ratio and node-merged interfaces, but the results reported in this section consider the progressive damage material model (MAT_162). Figure 5.10 illustrates through-thickness stress wave propagation in the model from figure 5.8b, which is used to investigate delamination with projectile-edge effects. The attenuating effects of geometry and disparate impedance, described earlier, are clear in figure 5.9 and figure 5.10. To be clear, the modeling in figures 5.9 and 5.10 are only to illustrate elastic wave propagation in the mesoscale geometry under two projectiles. In figures 5.9 and 5.10, there is no damage, no spall, and the elastic stresses are similar to the 1D elastic stresses in tables 5.3 and 5.4 and figures 5.6 and 5.7.

Now considering inelastic material behavior, the particle velocity is determined along lines A and B from figure 5.3, but now using the 3D models in figure 5.8. Now we use the inelastic, progressive damage material properties and cohesive interfaces described earlier. Note that the lines A and B are sufficiently far from the projectile edge (figure 5.8b) so that particle velocity results are the same for both models in figure 5.8. As before, two interfacial conditions are considered: node-merged (unbreakable interface) and cohesive zones (breakable interface). The particle velocities are compared to the 1D theory predictions from equations (5.6), (5.11), and

(5.12). Table 5.5 provides this comparison for line A, and table 5.6 provides this comparison for line B. As expected, the inclusion of 3D geometry, inelastic material behavior, and cohesive interfaces all increase difference to the 1D theory. Despite this, the 3D finite element model results are very close to the 1D theory, and these results provide confidence in the model predictions in the following sections. This is because of the assumption of linear elastic behavior, which is approximately true for this low impact velocity of 100 m/s. Later investigations consider impact velocities nearer to and above the ballistic limit velocity.

Table 5.5: Comparison of particle velocity, $\dot{u}$, 3D FEM results to 1D theory along line A. (Model uses progressive damage material behavior with node-merged or rate-independent cohesive zones.)

Layer	Thickness, mm	τ, μs	1D Theory $\dot{u}$ m/s	Node-Merged		Cohesive Zones	
				3D FEM $\dot{u}$, m/s	Difference, %	3D FEM $\dot{u}$, m/s	Difference, %
Epoxy	0.252	0.18	96.0	96.1	0.1	95.9	0.1
Composite	0.374	0.32	51.8	54.7	5.8	56.3	8.9
Epoxy	0.174	0.43	75.6	79.2	4.8	80.8	6.9

Table 5.6: Comparison of particle velocity, $\dot{u}$, 3D FEM results to 1D theory along line B. (Model uses progressive damage material behavior with node-merged or rate-independent cohesive zones.)

Layer	Thickness, mm	τ, μs	1D Theory $\dot{u}$ m/s	Node-Merged		Cohesive Zones	
				3D FEM $\dot{u}$, m/s	Difference, %	3D FEM $\dot{u}$, m/s	Difference, %
Epoxy	0.093	0.06	96.0	96.2	0.2	96.7	0.7
Composite	0.265	0.17	51.8	53.5	3.5	55.4	7.2
Composite	0.374	0.31	51.8	53.6	3.7	54.4	5.2
Epoxy	0.068	0.36	75.6	78.9	4.4	76.7	1.5

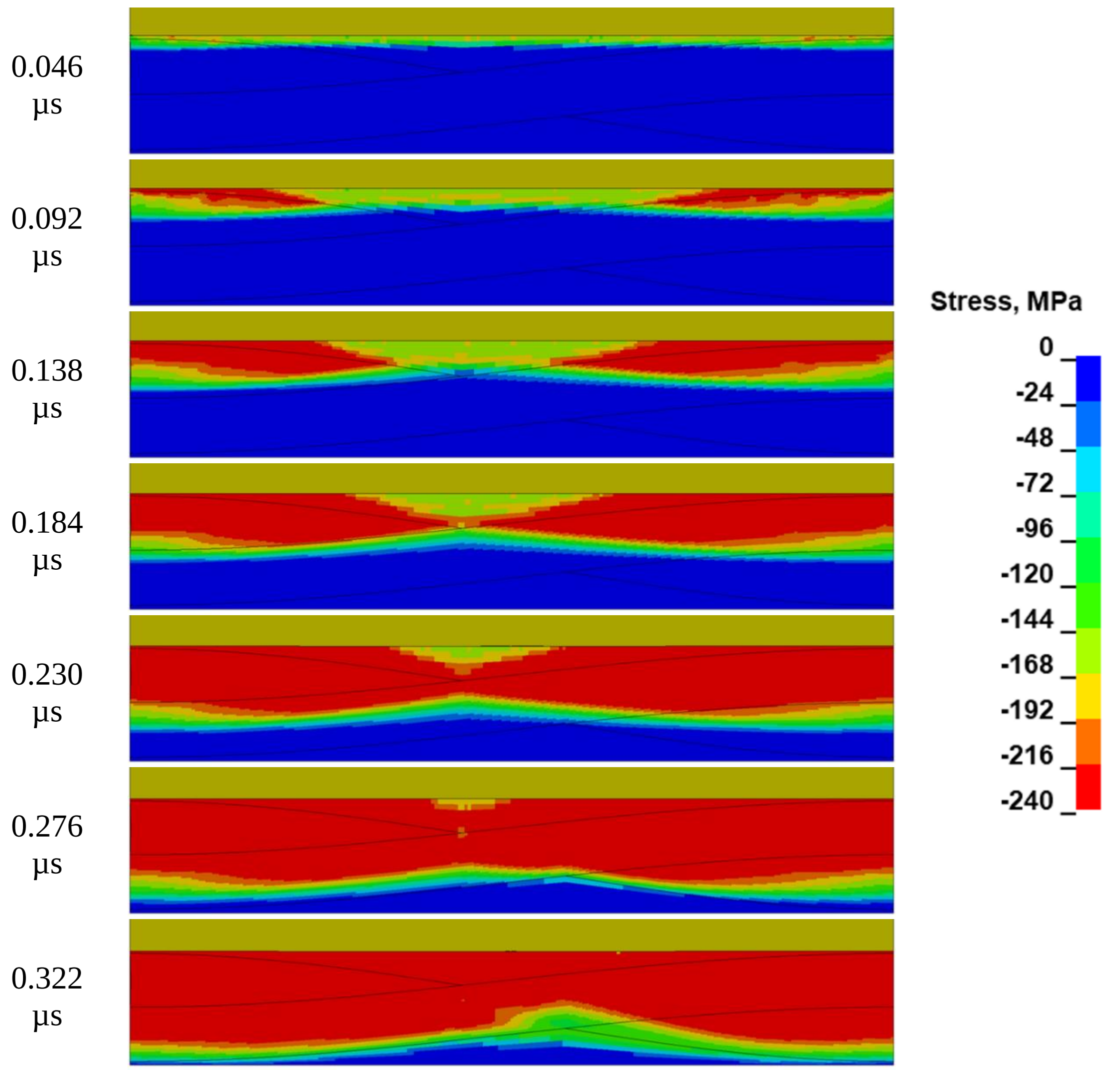

Figure 5.9: Through-thickness stress wave propagation in a unit cell of plain weave glass/epoxy composite impacted by a projectile of the same in-plane size. Impact velocity 100 m/s. Material properties are elastic, internal interfaces cannot separate, and in-plane boundary conditions are semi-infinite. Stress shown is in the through-thickness direction, and negative sign indicates compression.

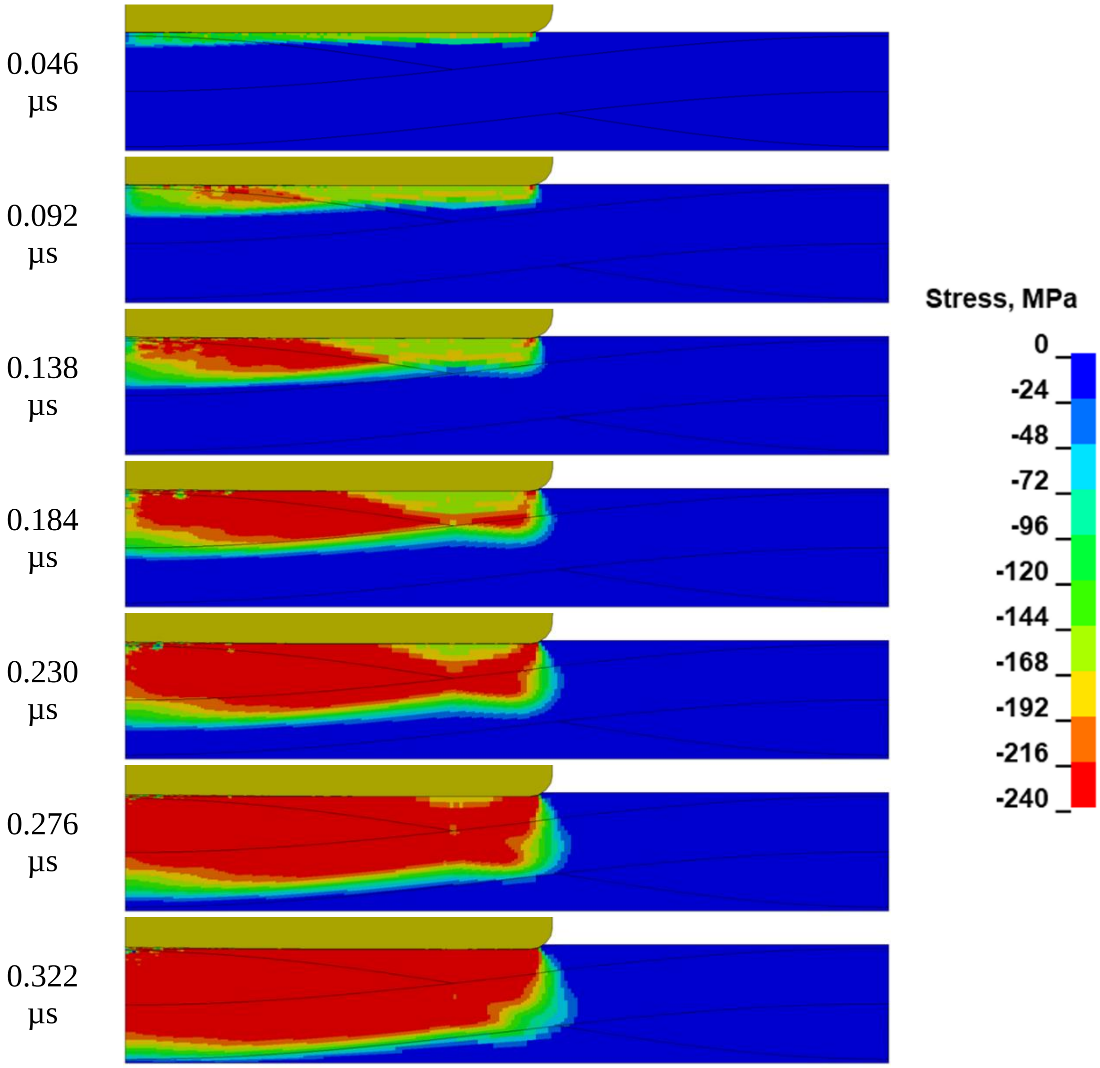

Figure 5.10: Through-thickness stress wave propagation in a unit cell of plain weave glass/epoxy composite impacted a 5.6 mm diameter right circular cylindrical projectile of the same in-plane size. Impact velocity 100 m/s. Material properties are elastic, internal interfaces cannot separate, and in-plane boundary conditions are semi-infinite. Stress shown is in the through-thickness direction, and negative sign indicates compression.

5.4.2 Damage Modes

In this section, we investigate the damage that develops under the projectile and around the projectile perimeter during this earliest timescale stage of impact. This section is concerned with the damage in the continuum composite tows (rate-dependent, progressive damage material model, MAT_162) and in the matrix (rate-dependent, elastic-plastic model, MAT_024). This damage includes matrix yielding, compression in layers, shear in layers, transverse tension (transverse cracking in a continuum sense), and crushing and shear under the projectile. Cohesive tow-tow delamination behavior is included here, but is discussed in the next section. This section focuses on continuum damage within matrix and composite tows. Further discussion of the continuum damage modes can be found in Appendix A and these references [21], [136]. Rate effects are included (see table 5.2 and Appendix A). This damage increases with increasing impact velocity. From the experiments [9], the ballistic limit velocity was identified as 188 m/s for an impact over primary tows, as shown in figure 5.8b. Therefore, this model was used to investigate early timescale (< 2 μs) response to impact velocities from 10 m/s to 250 m/s. Velocities beyond 250 m/s were not considered here since the highly refined finite elements in this model, with its very short length and time scales, begin to suffer from significant element distortion and numerical instability for higher velocities.

In this section, the entire RVE is considered (i.e., no longer considering only lines A and B). Contour plots of the various damage modes identified the locations of maximum damage in the continuum tows and matrix. From these locations, elements were selected from under the projectile and from an annulus outside the projectile perimeter. Figure 5.11 illustrates these regions of interest. These elements were interrogated for each impact velocity to determine the maximum values of each damage mode as a function of impact velocity. Thus, the stress/strain values discussed in this section represent the local maximum values, not the stress/strain in the bulk material.

Maximum damage values were determined in primary and secondary composite tows and in the epoxy matrix. The onset of yield in the epoxy for high-strain rate compressive loading is 0.14 strain [103], [104].

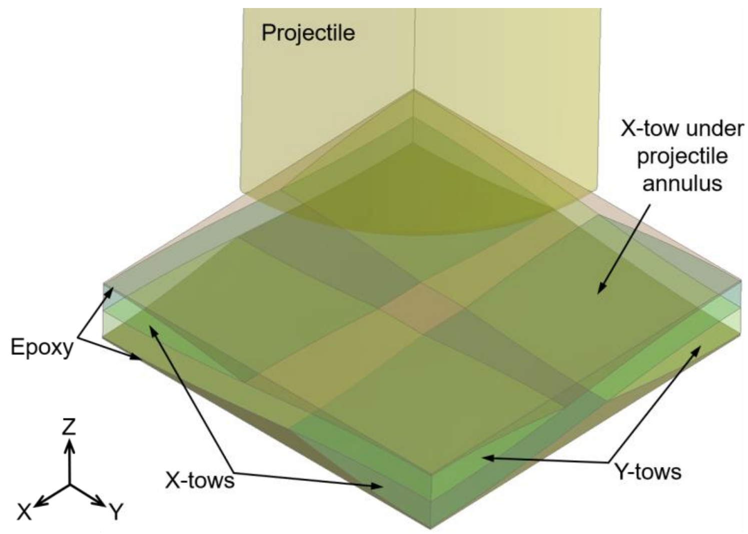

Figure 5.11: Regions of interest in the study of maximum damage modes occurring during the earliest timescale following impact of a projectile on a woven composite target. These regions include epoxy and primary and secondary X- and Y-tows directly under the projectile and in an annulus surrounding the projectile.

The effective strain, ε_{eff}, in the epoxy is given by equation (5.13), where ε_{ij} indicate the components of strain (see figure 5.11). The maximum effective strain in

$$\varepsilon_{eff} = \sqrt{\frac{2}{3}(\varepsilon_{XX}^2 + \varepsilon_{YY}^2 + \varepsilon_{ZZ}^2) + \frac{1}{3}(\varepsilon_{XY}^2 + \varepsilon_{YZ}^2 + \varepsilon_{ZX}^2)} \qquad (5.13)$$

epoxy is plotted in figure 5.12 as a function of impact velocity. The yield strain is shown in figure 5.13 as a dashed line. Maximum strain occurs under the projectile. The strain increases with increasing impact velocity during this early timescale (i.e., < 2 μs). Strain is expected to continue increasing after this timescale as the projectile plastically deforms the target. However, in this short timescale, strain does not reach sufficient level to yield the epoxy for these velocities. Effective strain appears to be saturating to yield with increasing impact velocity.

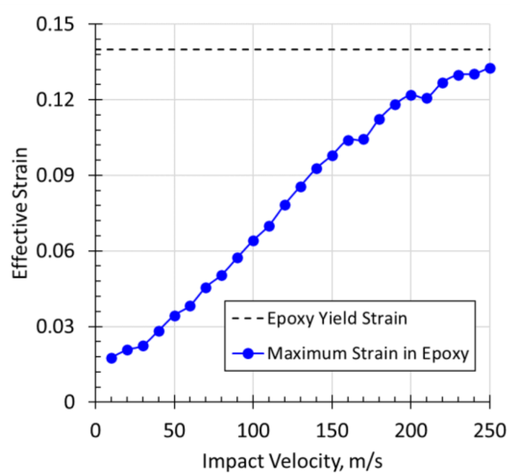

Figure 5.12: Maximum effective strain in epoxy (< 2 μs).

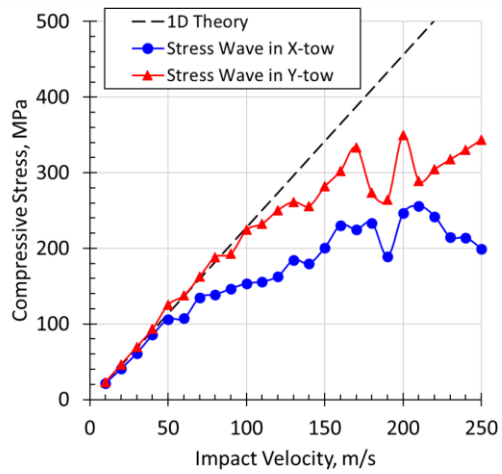

Figure 5.13: Initial compressive stress pulse in primary tows compared with elastic 1D theory (< 0.33 μs).

As discussed earlier, projectile impact sends a longitudinal stress wave through the composite thickness. Consider the initial stress wave propagating through the target for < 0.33 μs. Up to the elastic limit, the 1D theory can be used to estimate the compressive stress as a function of velocity according to $\sigma = \rho c \dot{u}$ (where ρ and c are material density and sound speed respectively, and $\dot{u}$ is the particle velocity). Early in time, compressive stress is induced in the tows as the stress wave propagates (before reverberation), and this is plotted along with the 1D theory (i.e., $\sigma = \rho c \dot{u}$) in figure 5.13. Note that absolute values are used for all stresses in this section. The stress in the composite tows matches well the linear elastic behavior up to about 50 m/s in the X-tow and about 100 m/s in the Y-tow. As impact velocity increases, stiffness loss reduces the sound speed leading to dispersion. As with strain in epoxy, stress is approaching a maximum with increasing impact velocity, and appears to saturate after the ballistic limit velocity.

Later in time ($0.33 \leq t \leq 2$ μs), target deformation increases and compressive stress increases beyond the initial compressive stress wave. This section shows that, in general, the composite tows do not fail directly under or next to the projectile impact location for impact velocities below or somewhat above the ballistic limit velocity. Strengths are shown as constant, but would be somewhat greater for high-rate loading and would increase with increasing impact velocity. However, the constant strength lines are informative by showing, in general, the composite is not failed until the impact velocity greatly exceeds the ballistic limit, when the damage and failure localize to the projectile impact location. The maximum fiber-direction compressive stress in primary tows (under projectile) is plotted in figure 5.14a, along with the fiber-direction compressive strength. The fiber direction compressive strength, X_{1C} is 770 MPa, which is equivalent to X-direction in X-tows and Y-direction compression in Y-tows. Transverse to the fiber direction, the compressive stress in X- and Y-tows are plotted in figure 5.14b, along with the transverse compressive strength, X_{2C}, which is 137 MPa. Through-thickness compression of primary tows is due to the motion of the projectile, and transverse and fiber-direction compressive stresses under the projectile are due to Poisson expansion. The maximum through-thickness compressive stress in primary tows is plotted in figure 5.15. This stress is compared with the punch-crush strength of the composite, S_{FC}, which is 850 MPa. Shear components of punch crush stress in the primary tows are not shown because they are very small (maximum of 19 MPa) relative to the punch crush strength.

Considering figure 5.14, compressive stress in primary tows approaches a maximum and saturates after the ballistic limit velocity. Note that strengths are shown as constant for illustration purposes, but are rate-dependent so will increase. The fiber-direction compressive stress is much less than the strength, but the transverse compressive stress exceeds the material strength. The fiber-direction compressive stress reaches a maximum at about the same velocity that the transverse compressive stress exceeds the material strength (~60 m/s). The through-thickness compressive stress (figure 5.15a) also saturates after the ballistic limit velocity. Although the failure stresses are not necessarily exceeded, material damage is accumulating, the material is losing stiffness and its ability to reduce the projectile momentum decreases with increasing impact velocity up to the ballistic limit. In figure 5.15b, the punch shear stress in the primary tows is much less than the punch shear strength. For thin composites, penetration resistance is dominated by primary tow tension and in-plane shear spreading of this tension to secondary tows.

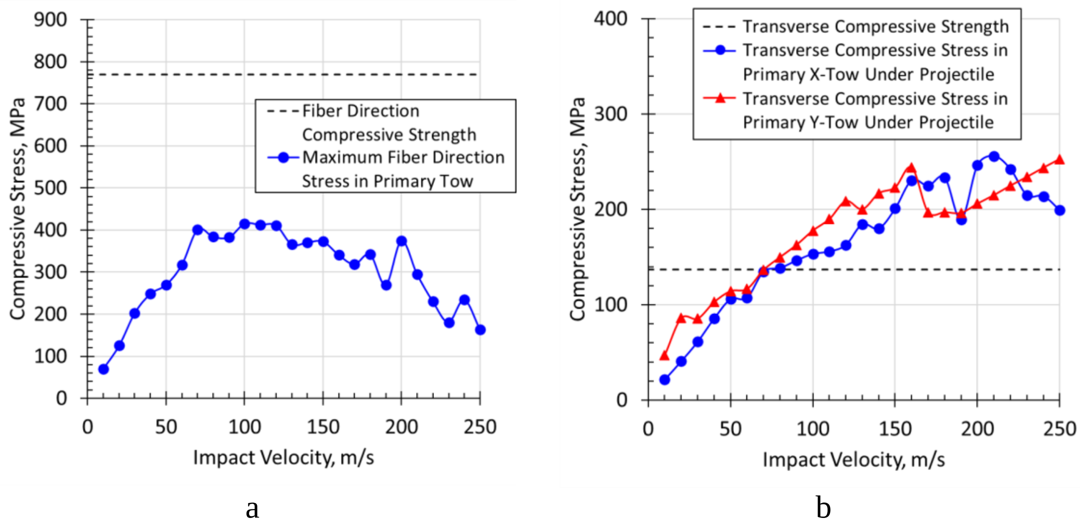

Figure 5.14: Maximum compressive stress in primary tows in (a) fiber direction and (b) transverse to the fiber direction.

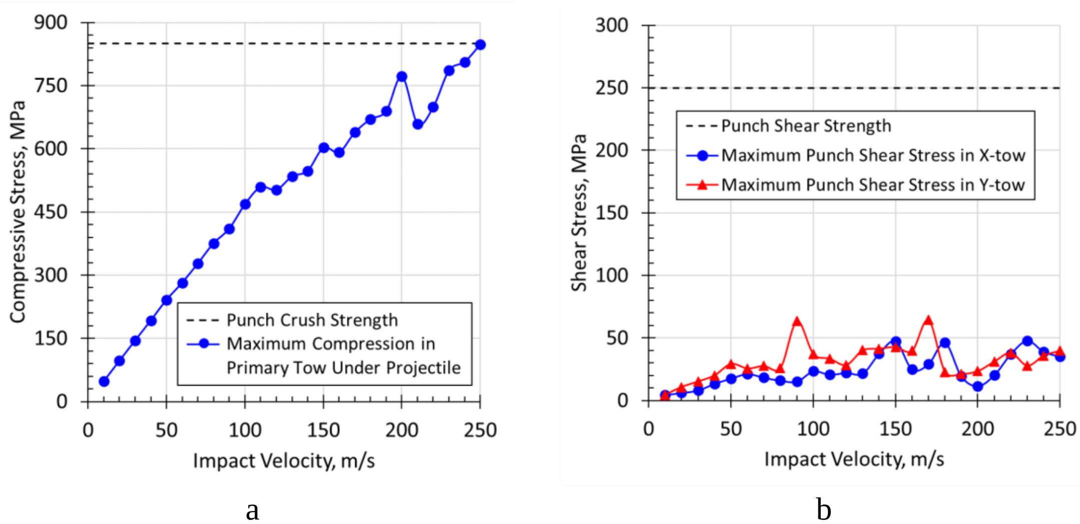

Figure 5.15: (a) Maximum through-thickness compressive stress on primary tows under the projectile compared with punch crush strength of the composite. (b) Maximum shear stress in primary tows in the annulus surrounding the projectile compared with punch shear strength of the composite.

All components of shear stress in X- and Y-tows were less than the respective shear strengths, so to save space, only the maximum shear stress values are shown in figure 5.16a. The maximum primary tow tensile stress is plotted in figure 5.16b, and compared with the fiber-direction tensile strength, X_{1T}, which is 1380 MPa. Ultimately, failure of the target occurs during later time scales than considered here. For impact velocities far beyond the ballistic limit, damage localizes to the impact site and the projectile perforates. For impact velocities near the ballistic limit, the damage spreads as tows stretch in tension, but it takes more time for the tows to straighten and load to failure. However, transverse cracks can occur at early timescales under relatively small transverse tensile stresses in secondary tows. The maximum transverse tensile stress in the secondary tows is plotted in figure 5.17, and compared with the transverse tensile strength, X_{2T}, which is 45 MPa. Transverse tensile stress quickly saturates to the transverse tensile strength for impact velocities exceeding about 100 m/s. For lower impact velocities, damage accumulates and transverse cracks are expected, but the number of transverse cracks per tow is expected to saturate for velocities above 100 m/s [10].

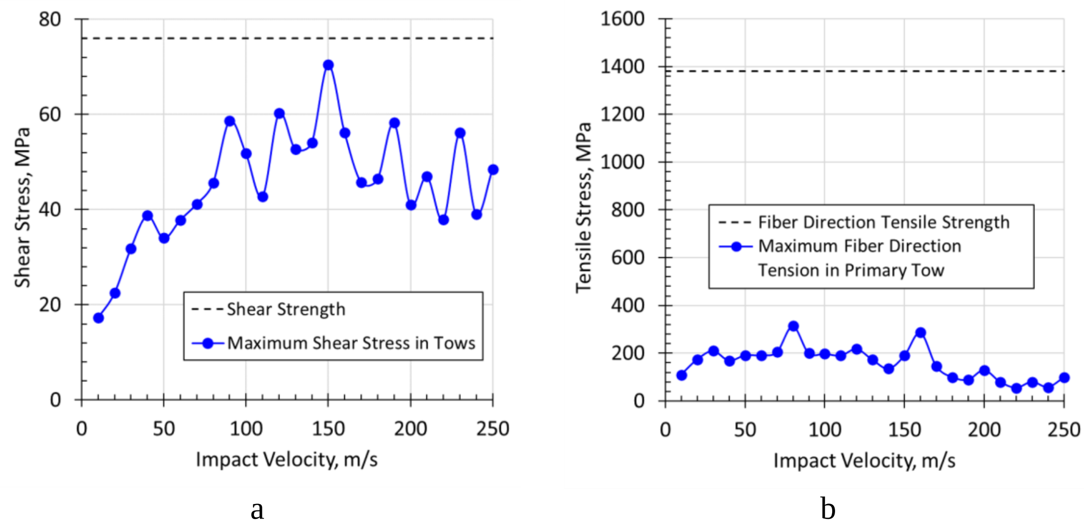

Figure 5.16: (a) Maximum of all components of shear stress in tows compared with shear strength of the composite. (b) Maximum primary tow tension compared with the fiber direction tensile strength of the composite.

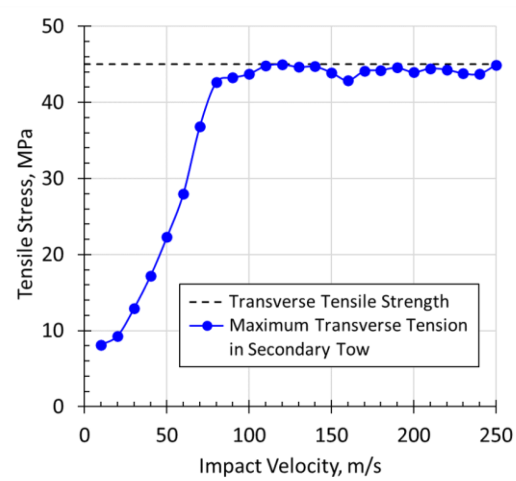

Figure 5.17: Maximum tension transverse to the fiber direction within secondary tows next to projectile, which implies transverse cracking when the applied tension reaches the transverse tensile strength.

5.4.3 Tensile Release Waves and Tow-Tow Delamination in Mesoscale Geometry

The effects of geometry and progressive damage on dispersion and attenuation of the stress waves inhibit tensile spall for the projectile height and layer thickness considered. By adjusting the height of the projectile in figure 5.8a to 1.0 mm, tensile stress waves can be made to meet at the tow-tow interface near line B (though this section considers the entire RVE). Compressive stress waves reflect off projectile top free surface and target bottom free surface, become tensile, then propagate through the target to meet at the interface. The 1.0 mm projectile height was determined from material sound speed and thicknesses based on elastic wave propagation.

Figure 5.18a shows the mesoscale target model impacted by this projectile at 100 m/s, and the through-thickness stress state when tensile stress is induced on the tow-tow interface. Figure 5.18a involves elastic composite and matrix response, but the interface is modeled as rate-dependent, cohesive as described earlier (see table 4.10 and figures 4.42 and 4.43). From figure 4.42, for strain rates from 10^2 to 10^8 s^{-1}, tensile tractions of about 10 to 85 GPa initiate delamination and mode I separations of about 30 to 80 μm result in cohesive failure (for scale, target thickness is ~800 μm).

Figure 5.18b includes the inelastic, progressive damage composite (e.g., table 5.2) and inelastic matrix (see §4.3.2.3) material models described earlier. With elastic material behavior, the tensile release waves intersect producing tensile stress on the interface, and 100 m/s impact velocity produces a maximum tensile stress of about 67 MPa. Conversely, the inelastic model suffers from severe wave attenuation (due to the progressive damage accumulation) so that little or no tension is produced at the tow-tow interface. The maximum separation produced at line B in the elastic model with these conditions is 4 μm, but zero separation is produced in the inelastic model. It was shown in the previous section that damage under 100 m/s impact is not sufficient to fail the material (and this 1 mm thick projectile now has less mass than in the previous section). However, damage accumulates and reduces the transversely isotropic material stiffness components (see Appendix A), which changes the speed of sound in the material and leads to wave dispersion and attenuation. Different finite elements have varying amounts of stiffness reduction, which leads to wave dispersion. Stress wave energy is reduced by damage accumulation, which with dispersion leads to wave attenuation. These effects are demonstrated by comparing figure 5.18a (elastic) to 5.18b (inelastic). In figure 5.18b (simulation time 0.6 μs), the compressive stress wave has passed through the target, reflected off the free faces, but much of the energy has been attenuated so that minimal tensile stress is produced within the composite or at the interfaces. The reduction in wave speed from stiffness loss due to damage also affects the average wave speed in a continuum sense, which means what is left of the tensile waves do not cross at the interface.

Inelasticity and progressive damage cause wave dispersion as the stiffness of the material is degraded by damage accumulation, the stress wave spreads and attenuates, so ensuring release waves with sufficient amplitude intersect at the tow-tow interface becomes impossible in a mesoscale model. In real material, geometric dispersion is further enhanced by fiber-matrix microstructure, which, when taken with the model results, indicate that tow-tow delamination does not initiate near the projectile impact location due to tensile spall for velocities below the ballistic limit. Experimental observations show tow-tow delamination for impact velocities below the ballistic limit (see figure 2.9a and b), but these occur away from the projectile impact location. Tow-tow delamination away from the impact location is due to tensile elongation of the primary tows, which is investigated in the next chapter.

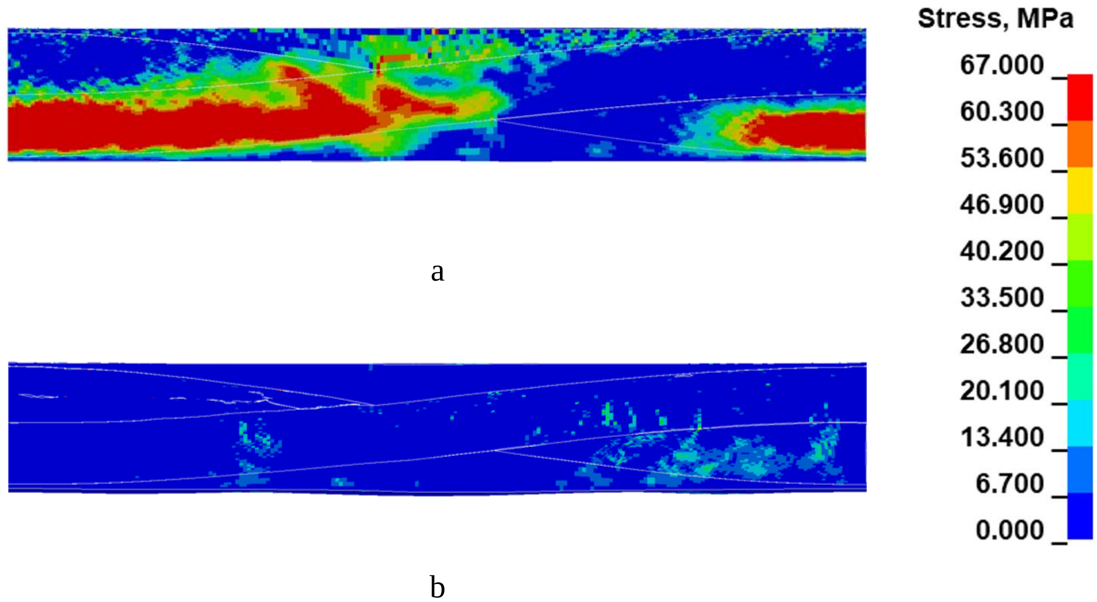

Figure 5.18: Impact on composite by 1.0 mm thick projectile (same impact area as composite), designed to produce release wave intersection at tow-tow interface at the time snapshot shown. Through-thickness tensile stress contour plots shown for model with (a) elastic and (b) inelastic progressive damage material models. Compressive (negative) stress is present but not shown (i.e., stress is not zero). Simulation time is 0.6 μs.

5.4.4 Tensile Release Waves and Tow-Tow Delamination in Idealized Geometry

The previous section adjusted the projectile thickness to try to induce tensile spall at the tow-tow interface, but it was found that spall was inhibited by dispersion and attenuation, which were due to geometry and material damage and stiffness degradation. This section investigates if tow-tow delamination can be produced by tensile spall under ideal conditions for impact velocities that are greater than the ballistic limit. Ideal means flat geometry (no tow undulation) and elastic composite properties (no damage or stiffness degradation). This section considers arbitrary layer thicknesses designed to ensure planar tensile stress wave interaction at the delamination plane (i.e., not related to lines A or B).

The single-layer ballistic impact experiments that motivated this study were conducted at velocities in the range 104–472 m/s, so here we consider 100–500 m/s impact velocities. A plate impact model is used to eliminate the geometric irregularities of the plain weave model and ensure a planar longitudinal stress wave. This plate impact model considers only elastic material behavior so that progressive damage and softening does not cause wave dispersion. The model length and width are 5.0 mm as in previous models. The steel impactor is 0.2 mm thick, the top (0°) composite layer is 0.2 mm thick, and the bottom (90°) composite layer is 0.1 mm thick. Steel wave velocity is 5,172 m/s and composite through-thickness wave velocity is 2,591 m/s (see table 5.1), so tensile release waves meet at the interface between 0° and 90° composite layers (i.e., $2 \times \frac{0.0002\ \mathrm{m}}{5172\ \mathrm{m/s}} + \frac{0.0002\ \mathrm{m}}{2591\ \mathrm{m/s}}$ on the top side of the interface $\approx \frac{0.0002\ \mathrm{m}}{2591\ \mathrm{m/s}} + 2 \times \frac{0.0001\ \mathrm{m}}{2591\ \mathrm{m/s}}$ on the bottom side of the interface). Besides ensuring tensile loading at the interface, these layer thicknesses were chosen for computational efficiency. The elements in the model are the same size as used previously, 0.01 mm thick by 0.02 mm in other dimensions (3,125,000 elements).

These dimensions ensure interaction of two release waves at the layer interface. While the plain weave model uses unidirectional continuum composite material properties following tow undulation, here the unidirectional properties of the first layer are oriented to the X-axis and those of the second layer are oriented to the Y-axis (i.e., [0/90]). Otherwise, all constitutive models and properties are as described previously (see table 4.10 and figures 4.42 and 4.43 for rate-dependent cohesive interface properties, table 5.2 includes elastic composite tow properties).

The projectile impacted the composite target with velocities of 100, 200, 300, 400, and 500 m/s. The deformation and spall gap produced by the 500 m/s impact velocity is shown in figure 5.19. Velocities greater than 500 m/s cause significant element distortion and numerical instability, so are not considered.

The free surface velocity was determined as a function of time and impact velocity, and is plotted in figure 5.20a. An impact at 500 m/s was simulated on a target with the [0/90] delamination plane removed so that no delamination could occur (i.e., node-merged). The free surface velocity for this condition ("no spall") is plotted in figure 5.20b along with the baseline 500 m/s impact ("spall"). The free surface particle velocity returns to zero when spall is suppressed.

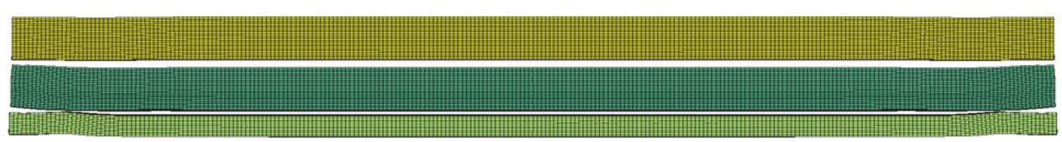

Figure 5.19: Plate impact model with projectile (yellow, top), 0° composite layer (dark green, middle), and 90° composite layer (light green, bottom). Deformation is produced by 500 m/s impact velocity at time 0.32 μs.

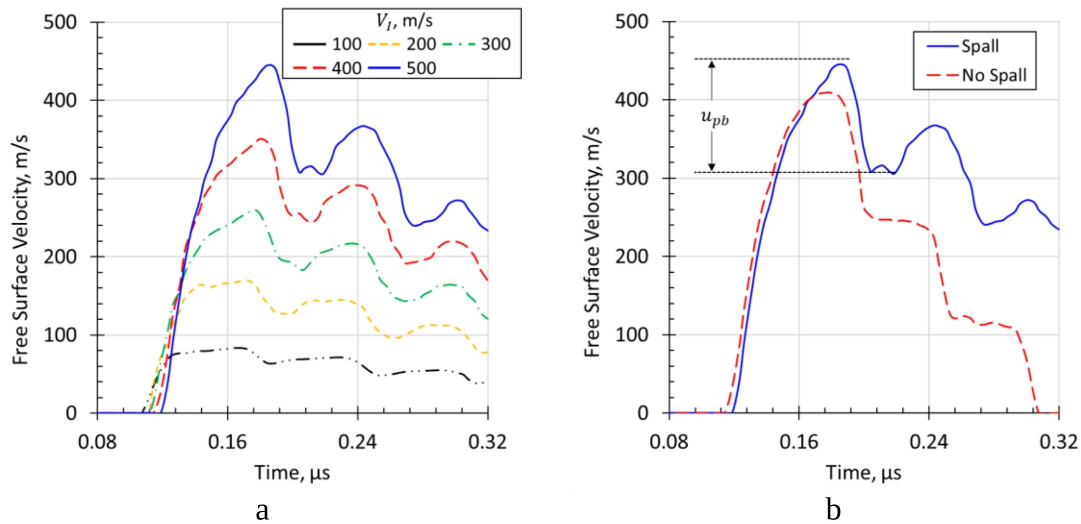

Figure 5.20: (a) Plate impact model study of free surface velocity vs. time as a function of impact velocity. (b) 500 m/s impact velocity with baseline model, "spall," and with no delamination possible between [0/90] layers, "no spall." Pullback velocity, u_{pb}, is indicated.

It can be seen in figure 5.20a that the maximum free surface velocity increases with increasing impact velocity. After the maximum, there is a reduction in velocity known as pullback, which is indicative of spall. The free surface velocity-time curves have been used to estimate spall stress for metals [139], concrete [140] and geomaterials [141], and delamination in composites [142]. The pullback velocity, u_{pb}, is indicated in figure 5.20b. The pullback velocity can be used to estimate the stress at the interface as $\sigma^* = \frac{1}{2}\rho c u_{pb}$ [139]. This linear approximation assumes the spalled material behaves elastically, and the through-thickness impedances match between the two composite layers. The approximated interfacial stresses, σ^*, are included in table 5.7 for the impact velocities investigated. The stress at the interface can also be determined from finite elements. The average through-thickness stress was determined from several elements near the model horizontal center on either side of the interface between 0° and 90° layers. This stress is included in table 5.7 as σ^{FE}. The linear stress approximation matches the finite element prediction reasonably well.

The spall gap between 0° and 90° layers is plotted in figure 5.21a. The spall gap was measured as a function of time from the relative displacement of nodes on both sides of the gap. Nodes were selected at the center of the model to avoid any edge effects. Over time, the gap approximately achieves a plateau, and this plateau was determined as the average of the oscillations, which is plotted as horizontal lines in figure 5.21a. These plateaus are taken as the maximum separation, δ^*, of the two layers and are included in table 5.7. After this time, the gap does not increase since the velocity of the two layers is the same aside from slight oscillations due to wave reverberations. Similar to the spall gap, the average relative velocity of the gap, $\bar{V}^*$, was determined. Recall that the interface is modeled as strain-rate dependent. The average interface strain rate is estimated from the gap opening velocity, $\bar{V}^*$, and the maximum gap separation, δ^*, which is taken as constant when $\bar{V}^* \rightarrow 0$ (i.e., when 0° and 90° layers move together at the same velocity). Then strain rate in the gap is estimated as $\bar{\dot{\varepsilon}}^* = \bar{V}^*/\delta^*$. The strain rate in the gap is approximately $7 \times 10^6\ \mathrm{s}^{-1}$ for all impact velocities.

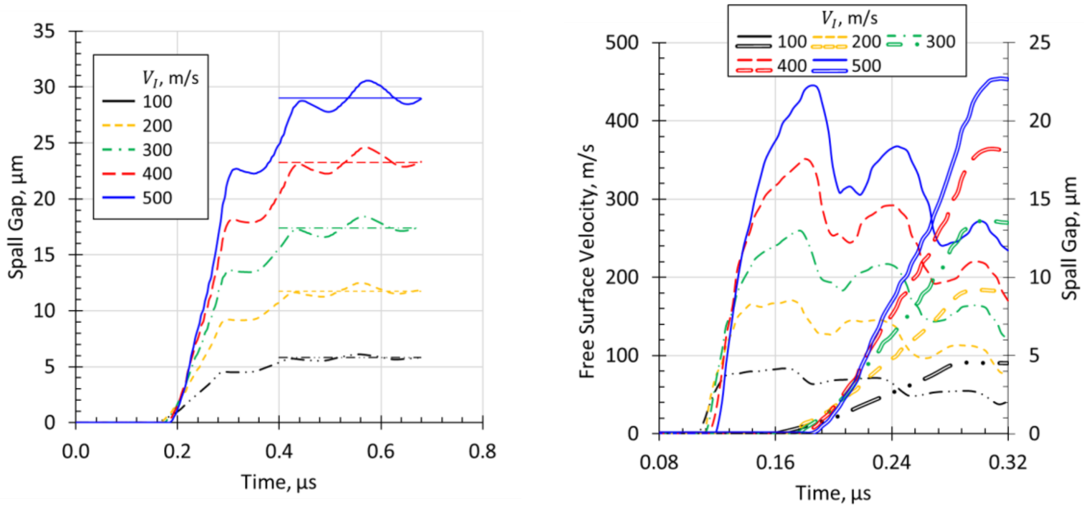

a b

Figure 5.21: (a) Spall gap produced between 0° and 90° unidirectional composite layers for each impact velocity. Horizontal lines indicate average of oscillations. (b) Spall gap (hollow lines) overlayed on free surface velocity (c.f., figure 5.20a) showing spall initiates at the first drop in free surface velocity.

Table 5.7: Results of elastic plate impact spall investigation. (Elastic material behavior with rate-dependent cohesive interface.)

Impact Velocity	Pullback Velocity	Interface Stress		Maximum Separation	Spall Gap Velocity	Spall Gap Strain Rate
V_I, m/s	u_{pb}, m/s	σ^*, MPa	σ^{FE}, MPa	δ^*, µm	$\bar{V}^*$, m/s	$\bar{\dot{\varepsilon}}^*, s^{-1}$
100	20	45	46	6	44	7.3×10^6
200	43	99	98	12	83	6.9×10^6
300	76	173	194	17	130	7.6×10^6
400	107	244	254	23	171	7.4×10^6
500	139	316	301	29	215	7.4×10^6

In figure 5.21b, the spall gap from figure 5.21a was overlayed onto the free surface velocity from figure 5.20a. figure 5.21b shows that the spall separation begins at the first free surface velocity drop, though it takes two more wave reverberations to reach the maximum gap. Equations 4.9 and 4.10 and the constants in table 4.10 and the interfacial strain rate (7E6 s^{-1}) can be used to determine the cohesive traction-separation law governing mode I opening (see [106]). Assuming a triangular cohesive law shape, the peak traction is 59 MPa, energy release rate is 1416 MPa-μm, and maximum separation is 48 μm. The separation is not sufficient for cracking to occur, under these conditions and velocities investigated. This implies that tensile spall is not expected to cause tow-tow delamination cracks under the projectile for these conditions investigated. This makes sense in light of the earlier investigation, which showed that the material under the projectile will suffer significant crush damage. However, tow-tow delamination cracks away from the projectile contribute to the evolution of primary tow tension and punch shear damage around the projectile, which results after wave reverberation, late in this earliest timescale, as the deformation wave initiates.

5.4.5 Deformation and Tow-Tow Delamination at the Projectile Perimeter

The previous two sections investigated if tow-tow delamination results from through-thickness stress wave propagation under the projectile. This section investigates if tow-tow delamination results from deformation at the perimeter of the projectile during short timescales. This section uses the RVE model, RCC projectile, rate-dependent cohesive interface, rate-dependent elastic-plastic matrix, and rate-dependent, progressive damage (inelastic) composite.

For impact velocity beyond the ballistic limit velocity, target damage under the projectile is dominated by material crushing. Target perforation damage around the projectile is dominated by large deformation due to momentum transfer. A cone in isotropic materials or pyramid in plain woven composites forms with large deformation that leads to transverse cracks and tow-tow delamination cracks near the projectile annulus and further away in primary and nearby secondary tows. This section uses the impact model in figure 5.8b with inelastic, rate-dependent material and interface models and properties. Impact velocities studied are 100 m/s and 250 m/s (below and above the ballistic limit velocity, respectively).

In addition to the through-thickness damage discussed earlier (both under and at the perimeter of the projectile), the perimeter is subjected to shear deformation. Large deformation results in the build-up of inplane fiber tension in the primary tows. These two deformation modes result in mode II loading of the tow-tow interface as well as in-plane transverse tension, which can cause transverse cracks discussed in chapters 2 and 4.

Impact at 100 m/s is shown in figure 5.22. The state of deformation is shown at the end time of the simulation, 1.8 μs. The dimensions of the opening tow-tow delamination crack are shown. The maximum separation at this time is 32 μm in mode I and 18 μm in mode II.

Impact at 250 m/s is shown in figure 5.23, also at 1.8 μs. For 250 m/s impact velocity, the maximum separation is 34 μm in mode I and 40 μm in mode II. The 250 m/s impact causes significant crushing damage to the tows under the projectile.

Incremental nodal velocity divided by incremental opening data at these locations gives a measure of the strain rates at the interface, which are approximately 10^7 s^{-1} (mode I) and 10^6 s^{-1} (mode II). Assuming triangular cohesive traction-separation laws, mode I cohesive zone propagates after 48 μm and mode II after 33 μm. Assuming quadratic relationship, separation of $\sqrt{48^2 + 33^2} = 58$ μm mixed-mode separation is needed for tow-tow delamination cracking at these strain rates. Under 100 m/s, mixed-mode separation is 37 μm, and under 250 m/s, mixed-mode separation is 52 μm, which indicates tow-tow delamination is not expected to initiate at the perimeter of the projectile during the first 1.8 μs of time for these impact velocities.

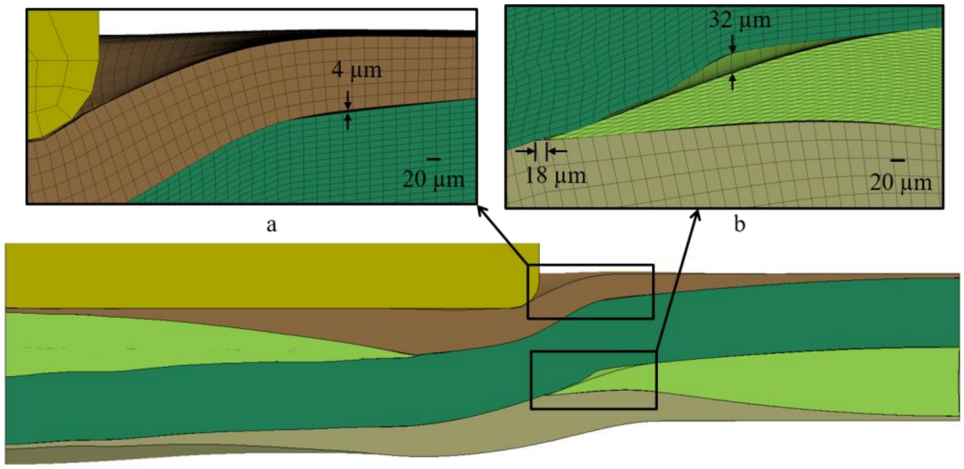

Figure 5.22: 100 m/s impact velocity post-impact, deformed target material and locations of maximum tow-tow and tow-matrix separations. Simulation time is 1.8 µs.

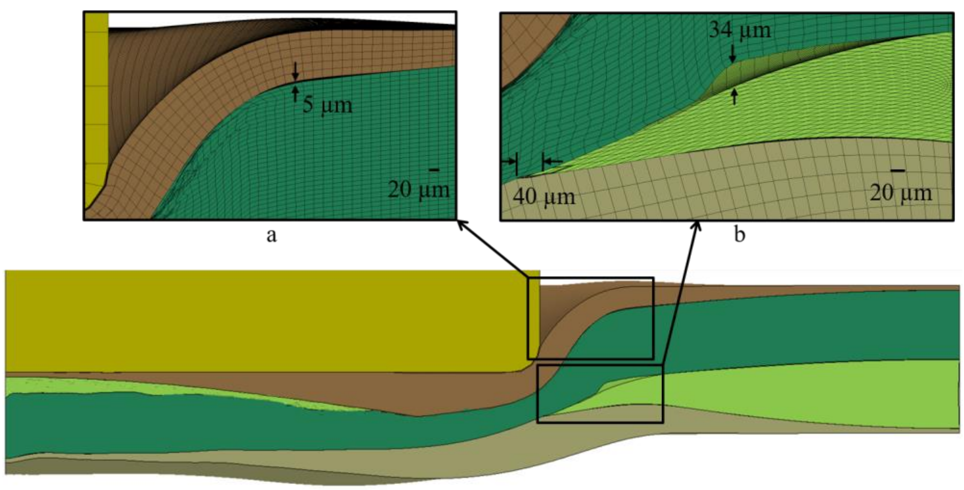

Figure 5.23: 250 m/s impact velocity, post-impact deformed target material and locations of maximum tow-tow and tow-matrix separations. Simulation time is 1.8 µs.

Investigation of the influence of transverse cracks on tow-tow delamination cracks is saved for future work. Transverse cracks initiate under tensile loading transverse to the fiber direction, and they propagate through the tow thickness until they reach a boundary, typically an orthogonal tow. At a boundary with an orthogonal tow, the crack may turn and propagate along the interface, becoming a tow-tow delamination crack. The present study investigates the effects of through-thickness stress waves on nucleating tow-tow delamination cracks, and so loading is dominated by through-thickness compressive stress rather than transverse tension. Although the model with a projectile size smaller than the target will produce transverse tension in primary tows outside of the impact zone, the in-plane size of the model is not sufficient for a deformation cone to fully develop. Also, the present work considers a very short time scale (~0–1.8 μs), but a well-formed deformation cone requires a longer time scale. Hence, in-plane tension and shear become more important than through-thickness loading at longer length and time scales than are considered in the present work.

5.5 Conclusions

Ballistic impact experiments typically investigate the end-state of target damage with little diagnostic evaluation of the evolution of target damage over time. Numerical studies typically focus on deformation and damage occurring over longer timescales during which the projectile is perforating the target. The present study concentrated on the earliest timescale (~0–1.8 μs) involved in composite impact, and investigated the question of how damage effected in this timescale affects later timescales. The results of this work indicate that, in a continuum sense, the degradation of material will affect damage evolution in later timescales. Damage such as transverse cracks and tow-tow delamination cracks propagate over longer a timescale. Damage initiated during the earliest timescale continues to evolve over time so that the immediate effect on global damage is minimal, but the cumulative effects begin at initial projectile contact and contribute to eventual target perforation.

Under the projectile, damage is dominated by through-thickness compression and crushing and damage suppresses tow-tow delamination. At the perimeter of the projectile, damage is dominated by punch shear and the development of in-plane tension. Stress wave propagation causes stiffness degradation and adds with punch shear and in-plane tension to cause mixed-mode loading of the interface, which can cause tow-tow delamination and transverse cracking away from the projectile perimeter. Transverse cracks can propagate through the tow thickness and turn at the orthogonal tow and grow as tow-tow delamination cracks. At longer timescales, the magnitude of in-plane tension increases and becomes a dominant source of tow-tow delamination and transverse cracking.

For thick composites, it is likely that geometric dispersion and material degradation will cause attenuation so delamination cracking due to stress waves is not expected to be a significant factor in material response. Rather, the crushing under the projectile (punch crush, transverse compression) and large deformation around it (punch shear, transverse cracks) drive the damage evolution beginning during the earliest timescale and evolving over longer timescales.

Additionally, in this work we generalized the one-dimensional (1D), longitudinal stress wave propagation theory so that the stress and particle velocity could be determined for any number of elastic layers. We used this generalized 1D theory to validate our modeling approach, and showed that our 1D model matches the theory with less than 3% error and our 3D model matches the 1D theory with less than 9% error. Our models also matched the linear spall stress theory very well.

Future work should include transverse cracks (modeled with cohesive zones or another method), and consider much longer length and time scales to investigate the effects of a fully developed deformation wave.

Chapter 6

BALLISTIC IMPACT EXPERIMENTS AND MESOSCALE MODELING OF A SINGLE-LAYER PLAIN WEAVE COMPOSITE

Ballistic perforation of single-layer plain weave glass/epoxy composites involves a number of damage mechanisms. The earliest timescale was investigated in the previous chapter. It was shown that damage occurs under and around the projectile during early time. In later timescales, primary tows are loaded in tension as a transverse deformation wave grows. Tension spreads to secondary tows through in-plane shear. Tow-tow delamination cracking and tow pullout lead to tow elongation. With sufficient impact velocity, the projectile shears through primary tows and perforates the target. Figure 6.1 illustrates the flow of the dissertation, culminating in the present chapter.

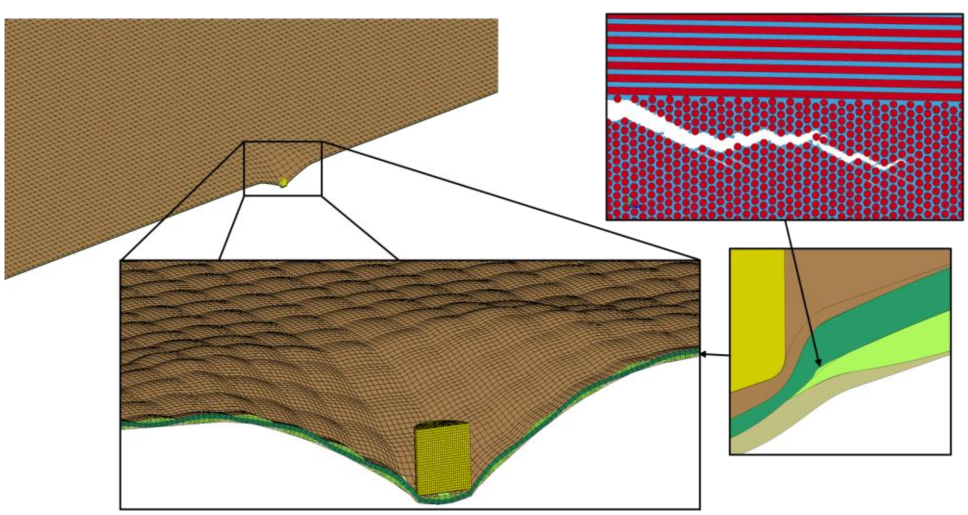

Figure 6.1: Illustration of the flow of the dissertation informing the present chapter.

The focus of this chapter is on that longer timescale deformation and damage and related energy absorption. The mesoscale modeling approach discussed in Chapters 2 and 3 is used here, enhanced with tow-tow delamination traction-separation laws developed in Chapter 4. The early timescale damage investigated in Chapter 5 involved an RVE with highly refined mesh, which is not practical for a full-scale impact model. The full-scale model used in the current chapter is refined as much as practical, as discussed in Chapters 2 and 3. Damage during the earliest timescale investigated in Chapter 5 accumulated within the first 2E-6 seconds. The RVE model used in Chapter 5 had a timestep of ~3E-10 seconds, and the full-scale model used in the present chapter has a similar timestep of ~5E-10 seconds. With this timestep and four elements through each tow thickness, the through-thickness stress wave is coarsely resolved. Considering the tow thickness, ~0.4 mm, elements are ~0.1 mm, the through-thickness wave speed is 2591 m/s, so the wave will travel ~0.001 mm per time step. The damage occurring during that earliest timescale is still accumulated in the full-scale model, but at a lower resolution. However, it was shown in Chapter 5 that the damage in the vicinity of the projectile generally does not approach failure strength until velocities much greater than the ballistic limit velocity. Exceptions are matrix yield, transverse cracking, and fiber crush. These failure strengths will still be exceeded at a lower resolution. Similarly, compressive damage under the projectile and tension and shear near the projectile perimeter are also included in the full-scale model. As in the RVE model, these damage modes are included with the rate-dependent progressive damage composite constitutive model (MAT_162). During longer timescales, tow tension and shear, tow-tow delamination, and tow elongation, pullout, and frictional sliding are the dominant mechanisms near the ballistic limit.

Continuum models were shown in Chapters 2 and 3 to be inadequate for predicting ballistic limit velocity because they lack damage mechanisms that occur at the mesoscale. Continuum models do not include rate-dependent matrix deformation and damage, tow-tow delamination, and tow straightening, elongation, and frictional sliding. Mesoscale models including plain weave architecture and tow-tow delamination were shown to improve ballistic limit velocity prediction.

Modeling tow-tow delamination with the cohesive zone model requires a traction-separation law. An embedded cell model was used in Chapter 4 to determine the traction-separation law. This TSL was used in Chapter 5 in an RVE model to investigate damage at the earliest timescale following impact.

The development of a predictive finite element model including important damage mechanisms can be used in a materials-by-design framework to partition energy and identify mechanisms that could be optimized for increased penetration resistance.

In this chapter, the tow-tow delamination TSL is used in a mesoscale model of single-layer ballistic perforation. The model is validated against new ballistic perforation experiments. The validated model is then used to partition energy dissipation and conduct a parametric study for improving penetration resistance.

6.1 Single-layer Perforation Experiments, Part II

6.1.1 Materials and Fabrication

Single-layer panels were made using two processes. Vacuum-assisted resin transfer molding (VARTM) was used same as in the previous perforation experiments. Additionally, a wet layup (WL) process was used to conserve resin. As before, plain weave S-2 glass fabric (5 × 5 tows/inch (2 × 2 tows/cm) areal density 24 oz/yd^2 (744 g/m^2), AGY 463-AA-250, 30 ends) was infused with epoxy matrix. For these experiments the matrix used was a commercially available modified bisphenol A/F epoxy, DER 353 (Dow Epoxy Resin, Olin Corporation), which was cured with PACM-20 (bis p-aminocyclohexyl methane, PACM-20, Air Products and Chemicals, Inc.) at a stoichiometric ratio of 100:28. DER 353 resin and PACM hardener were mixed and degassed at room temperature.

Both processes infused a 1.27 × 1.27 m (4.2 × 4.2 ft) single-layer sheet of plain weave S-2 glass fabric. The VARTM process infused under a vacuum and cured under vacuum for 2 hours at 80°C then for 2 hours at 150°C. The WL process involved manually pouring 1000 g of resin onto the center of the fabric sheet, then infusing the resin into the fabric with a squeegee. After that, the WL material was vacuum bagged and cured same as the VARTM material. After cure, 0.6 × 0.6 m (2 × 2 ft) ballistic specimens were cut from the panels using a water jet.

The average thickness of the VARTM test specimens was 0.905 mm and the average thickness of the WL test specimens was 0.860 mm. The two processes resulted in test specimens that were nearly identical in architecture, fiber volume fraction, and density.

6.1.2 Perforation Experiments

Ballistic impact experiments used a steel 17-grain (1.1 g), 0.22 caliber fragment simulating projectile (FSP) to perforate the targets. Projectile diameter was 5.5 mm and height 6.3 mm. As discussed previously, the projectile diameter and tow width are both about 5 mm in dimension, so impact generally occurs on one or two primary tows in the 0° and 90° directions.[9]

The projectile was shot from a two-stage helium gas gun with a smooth bore 0.227 caliber barrel. The experimental setup is shown schematically in figure 6.2.

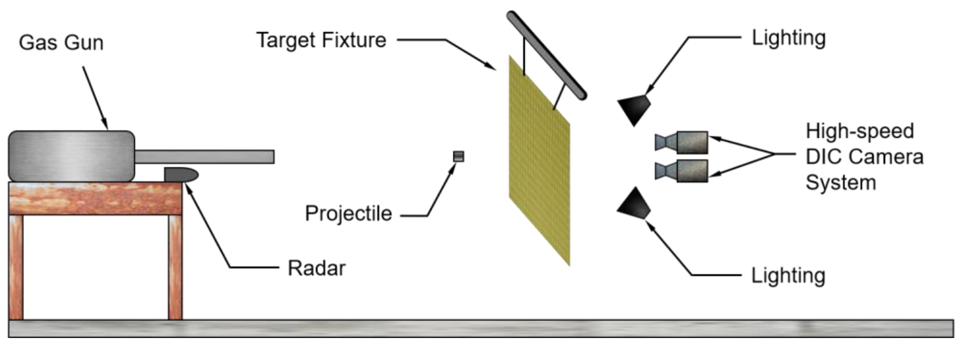

Figure 6.2: Schematic of test setup.

To limit the effects of boundary conditions [50], specimens were hung from two points along the top of the panel. Therefore, the specimens had essentially free boundary conditions. Because the specimen is large, 0.6 m square, and has free boundary conditions, and considering the axial sound speed in the material, perforation will occur before the radial stress wave reaches the boundary, which occurs around 55 μs.

For shots that perforated the target, residual velocity was measured by high-speed video. The experimental results are provided in table 6.1. The ballistic limit velocity, V_{50}, was determined in accordance with MIL-STD-662F. This standard procedure averages the three lowest velocity complete perforations (CP) and the three highest velocity partial perforations (PP). The V_{50} was found to be 154 m/s.

Table 6.1: Impact experiment results.

Shot Number	Process	Impact Velocity, m/s	Residual Velocity, m/s	Penetration Type
1	VARTM	351	315	CP
2	VARTM	156	0	PP
3	VARTM	214	144	CP
4	VARTM	185	91	CP
5	VARTM	162	0	PP
6	VARTM	175	143	CP
7	VARTM	167	86	CP
8	WL	151	0	PP
9	WL	175	70	CP
10	WL	164	0	PP
11	WL	166	90	CP
12	WL	164	0	PP
13	WL	163	116	CP
14	WL	179	57	CP
22	VARTM	163	87	CP
23	VARTM	151	70	CP
24	VARTM	135	85	CP
25	WL	134	0	PP
26	WL	147	42	CP

6.2 Mesoscale Modeling

The mesoscale model RVE of plain weave glass/epoxy composite was created by the same method as described in Chapter 3. The RVE is shown in figure 6.3. The RVE dimensions were based on experimental observations, and are a = 5 mm, b = 0.42 mm, g = 0.56 mm, and h = 0.86 mm. The RVE thickness of 0.860 mm matched the VARTM experimental specimens' average thickness. The RVE was tiled in space to create a 0.6 m by 0.6 m panel, to match the experiments. Boundary conditions were free, as in the experiments.

The fully 3D mesoscale model is quite large with 3600 RVEs making 8.5 million finite elements. As discussed in Chapter 3, the mesh is at the maximum level of refinement that is practical. Impact simulations required 36-120 hours on 72 processors, depending on the impact velocity considered. For example, low velocity rebounding solutions required more time than very high velocity perforations.

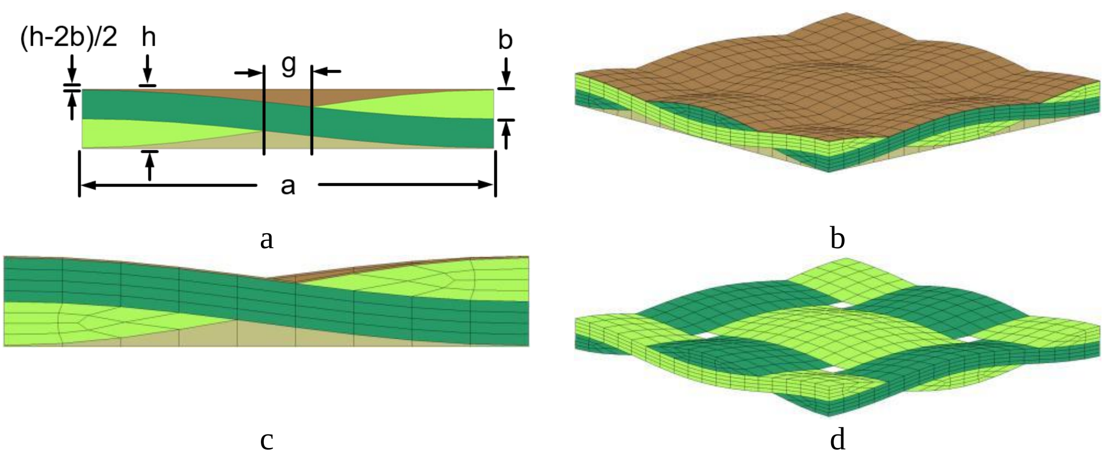

Figure 6.3: Plain weave mesoscale RVE. (a) Unit cell with dimensions. (b) Full RVE with matrix (brown) and composite (green). (c) Side view of RVE showing top surface of matrix matching tow undulation. (d) RVE without matrix showing warp and weft tows.

Material models used were the same as previously described. The projectile was modeled as elastic steel (see table 4.3). The matrix was modeled with rate-dependent plasticity and rate-dependent erosion. Matrix again used the tabular model *MAT_PIECEWISE_LINEAR_PLASTICITY (MAT_24). Matrix stress-strain response and erosion was as described in Chapter 4. Unidirectional composite tows included material properties aligned to the tow undulation to follow the fiber direction, which was described in Chapter 3 (see tables 3.2, 4.4, and A.3). The unidirectional composite model, *MAT_COMPOSITE_DMG_MSC (MAT_162), is discussed in Appendix A.

Tow-tow delamination was modeled with tied contact option 13 (e.g., MAT_240 or *MAT_COHESIVE_MIXED_MODE_ELASTOPLASTIC_RATE). This approach was previously discussed in Chapter 4 for modeling rate-dependent fiber-matrix interfacial debonding. The traction-separation laws governing this model for rate-dependent tow-tow delamination was determined in Chapter 4 and used in Chapter 5. The parameters for the model are in table 4.10 and are illustrated in figures 4.42 and 4.43.

It was discussed previously that continuum models lack mesoscale architecture and damage modes and so generally have more error when predicting the ballistic limit velocity. Energy dissipating damage mechanisms that occur at the mesoscale include primary tow tension, shear, rate-dependent matrix behavior, and inter-tow delamination and friction. For comparison with the mesoscale model, a continuum model was made with the same dimensions as the targets, 0.6 m by 0.6 m by 0.860 mm, and using MAT_162 effective plain weave properties in Appendix A.

6.3 Results and Discussion

Numerical simulations were conducted of the steel FSP impacting the mesoscale and continuum models of the composite target. The range of velocities simulated was 140 m/s to 400 m/s. The mesoscale model is hereafter referred to as "baseline" when using the reference constitutive and cohesive properties as previously discussed.

The results of the continuum and mesoscale simulations are plotted along with the experimental data in figure 6.4. Recall that the experimental ballistic limit velocity is V_{50} = 154 m/s. Mesoscale and continuum model simulations were run with impact velocities from 140 m/s to 170 m/s to determine the model predictions of ballistic limit velocity. The continuum model ballistic limit velocity was found to be V_{BL}^{Cont} = 144 m/s. The mesoscale model ballistic limit velocity was found to be V_{BL}^{Meso} = 153 m/s. Therefore, the continuum model prediction has 6% error while the mesoscale model has 1% error in the prediction of ballistic limit.

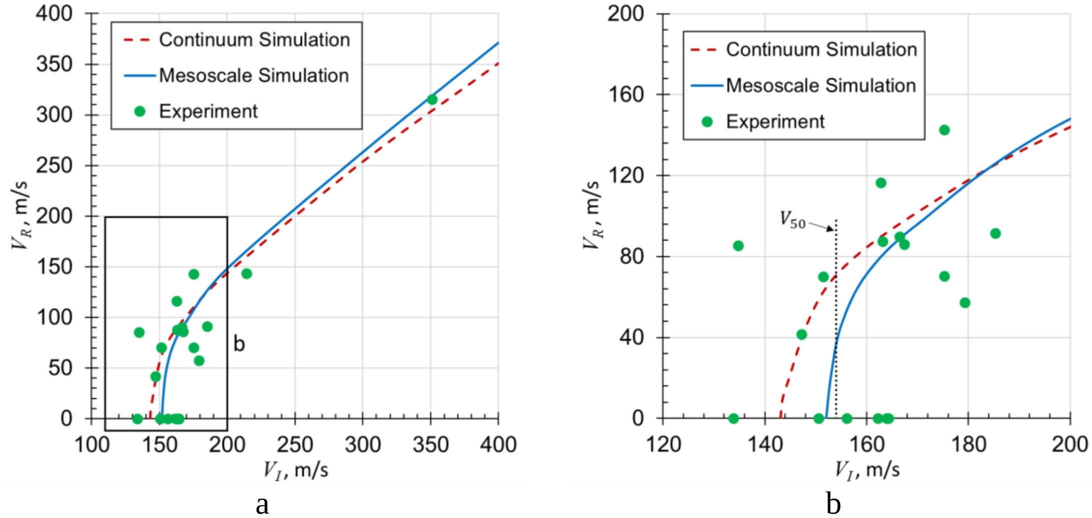

Figure 6.4: Mesoscale and continuum model results versus experimental residual velocity, V_R, results as a function of impact velocity, V_I, with V_{50} = 154 m/s. (a) Box marked b is enlarged in (b).

6.3.1 Mesoscale Damage Mechanisms

During impact of a projectile on a woven composite target, momentum transfers from the projectile to the composite. Matrix deformation and cracking, tension and shear in tows, and tow-tow delamination and friction all contribute to energy dissipation. Tensile loading that is transverse to the tow fiber direction causes matrix cracking. Tow-tow delamination occurs principally between primary tows and secondary tows since the primary tows are stretched in tension, elongate, and delaminate from the orthogonal secondary tows.

A post-test, backlit image of a damaged plain weave composite is shown in figure 6.5a. Tow-tow delamination can be seen to be concentrated on primary tows. This was also shown in Chapter 2. Delamination and pullout of the primary tows extends the time of momentum transfer, increases the angle of the transverse deformation cone that forms, and increases primary tow tensile elongation and frictional sliding. Thus, additional energy dissipation occurs due to this deformation as the mesoscale damage modes extend away from the projectile.[8] Tow-tow delamination reduces tow constraint, and it has been shown that friction is more effective at absorbing energy when the tows are less constrained.[51]

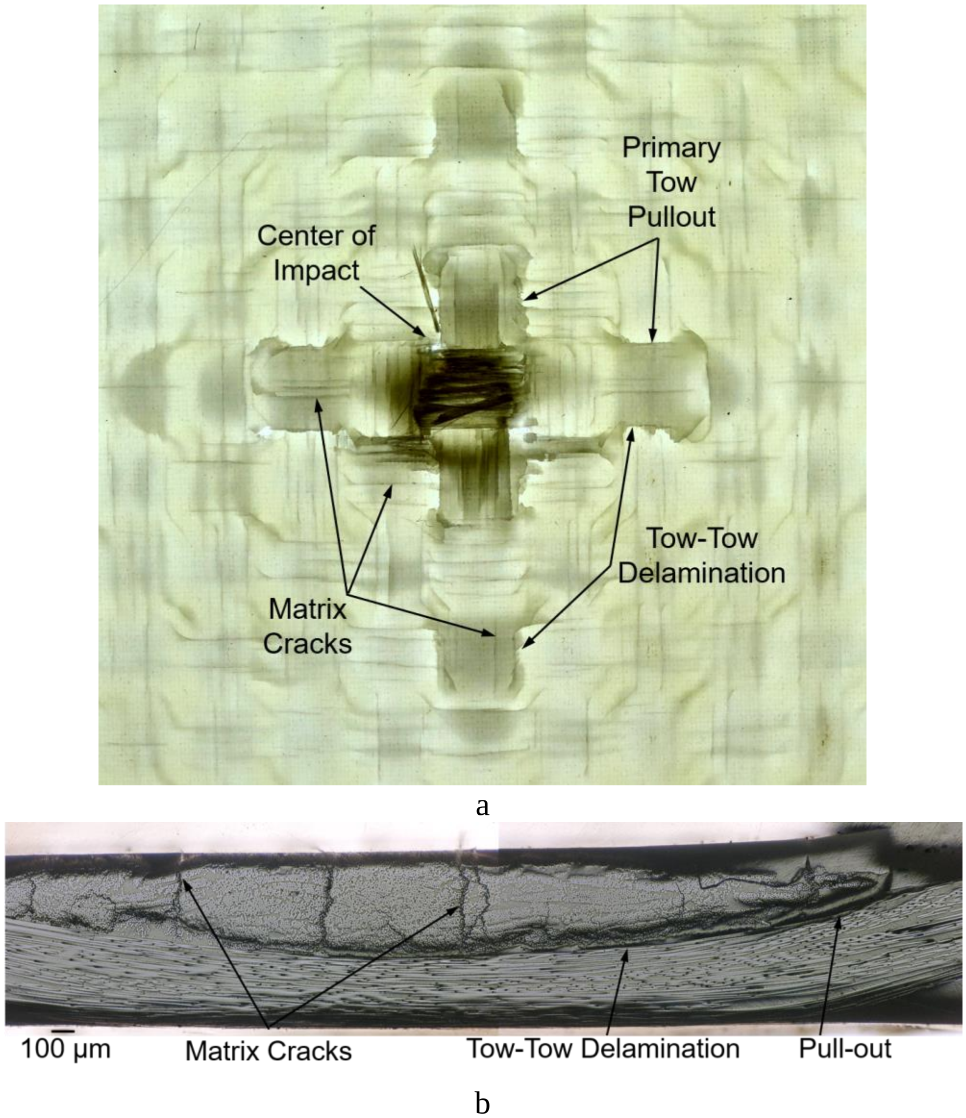

Figure 6.5: (a) High-resolution image of backlit post-test single-layer plain weave composite impact experiment with V_I = 153 m/s. Impact face is shown. (b) Micrograph of cross section through damaged orthogonal tows.

Maximum extent of tow-tow delamination, tow pullout, and frictional sliding is only observed for impact velocities near the ballistic limit. Impact velocities well below the ballistic limit have momentum transfer, matrix cracking, tensile tow elongation, and transverse deflection energy absorption mechanisms.[8], [50] Some momentum is stored by the target as elastic energy and returned to the projectile causing the projectile to rebound. For impact velocities well above the ballistic limit, the projectile punches and shears through the target. Tows fail in tension and shear before they have time to delaminate and pull out, so transverse deflection is reduced, and damage becomes localized around the projectile impact location.[8], [50] Damage localization is demonstrated by the damage quantification studies discussed in Chapter 2. In those previous single-layer impact experiments, it was shown that matrix cracking and tow-tow delamination are maximum near the ballistic limit but decrease with increasing impact velocity.[8]

The composite impact shown in figure 6.5 can be described by two phases. Results from the 153 m/s impact of the FSP on the mesoscale model is shown in figure 6.6. Figure 6.6 is a plot of projectile velocity over time as the projectile impacts the target. First, projectile velocity reduction is dominated by momentum transfer (figure 6.6-I). Tension-shear and matrix cracking dissipate energy, matrix cracks and tow elongation permit transverse deflection to increase, and primary tows delaminate from secondary tows. The second phase begins after tow-tow delamination releases the primary tows from being constrained to secondary tows (figure 6.6-II). During this phase, primary tow tension, pullout and friction dissipate energy. Eventually, the primary tows fail under tension, crushing, and shear and the projectile perforates or rebounds (figure 6.6-III).

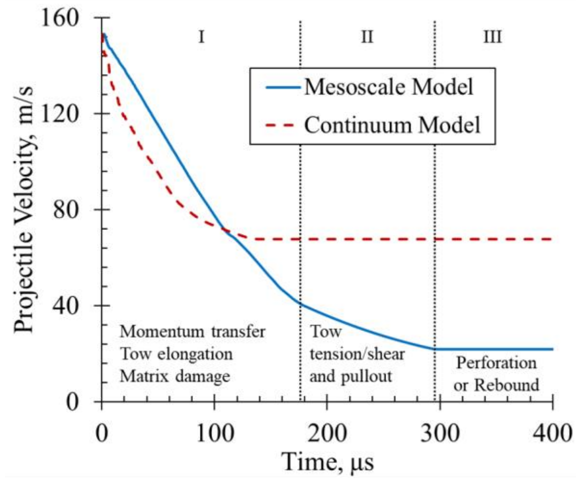

Figure 6.6: Velocity-time curve for 153 m/s projectile impact on mesoscale and continuum models.

Nilakanten et al.[41] observed a similar two-phase velocity-time response was for ballistic perforation of fabric. Fabric (without matrix) has a more compliant first phase because fabric composites (with matrix) have more in-plane shear and bending stiffness. Fabric also has a more extensive second phase since tow pullout is less constrained during impact out to the boundaries. The continuum model velocity-time response in figure 6.6 does not show these penetration phases because it does not include discrete tow response. Also, the continuum model predicts much larger residual velocity than the mesoscale model; the continuum model predicts less energy dissipation because it neglects mesoscale energy dissipation mechanisms.

Figure 6.7 shows the continuum model transverse deflection over time. Figure 6.8 shows the mesoscale model transverse deflection over time. It can be seen by comparing these two figures that the mesoscale model includes more realistic deformation. The mesoscale model transverse deformation cone has a steeper angle and wider extent than that of the continuum model. This result suggests that the mesoscale model can better predict back face deflection, though such an investigation is proposed for future work. Tow straightening, tow elongation, and tow-tow delamination are seen in the mesoscale model deformation in figure 6.8 but not in the continuum model in figure 6.7. Since the mesoscale model includes more realistic deformation modes, it aids in understanding the energy absorption mechanisms and can provide a framework for materials-by-design approach to improving ballistic limit.

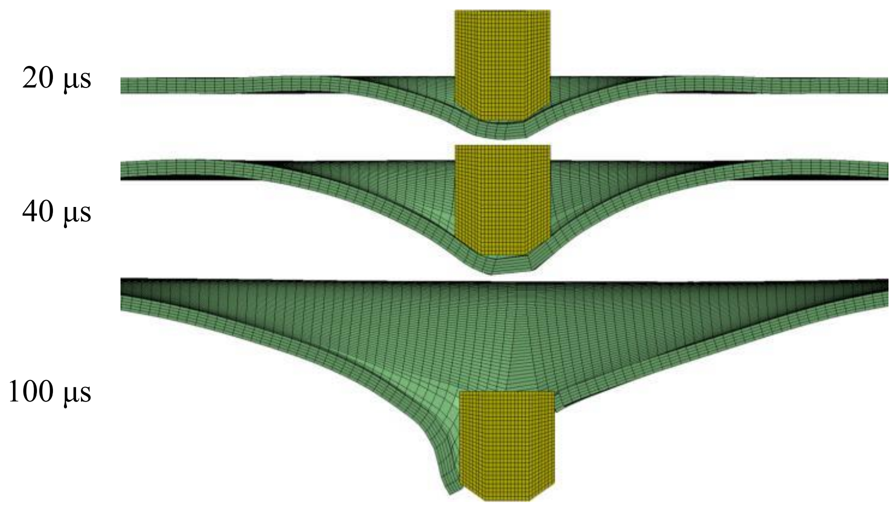

Figure 6.7: Continuum model deformation response under 153 m/s projectile impact. Residual velocity is 68 m/s.

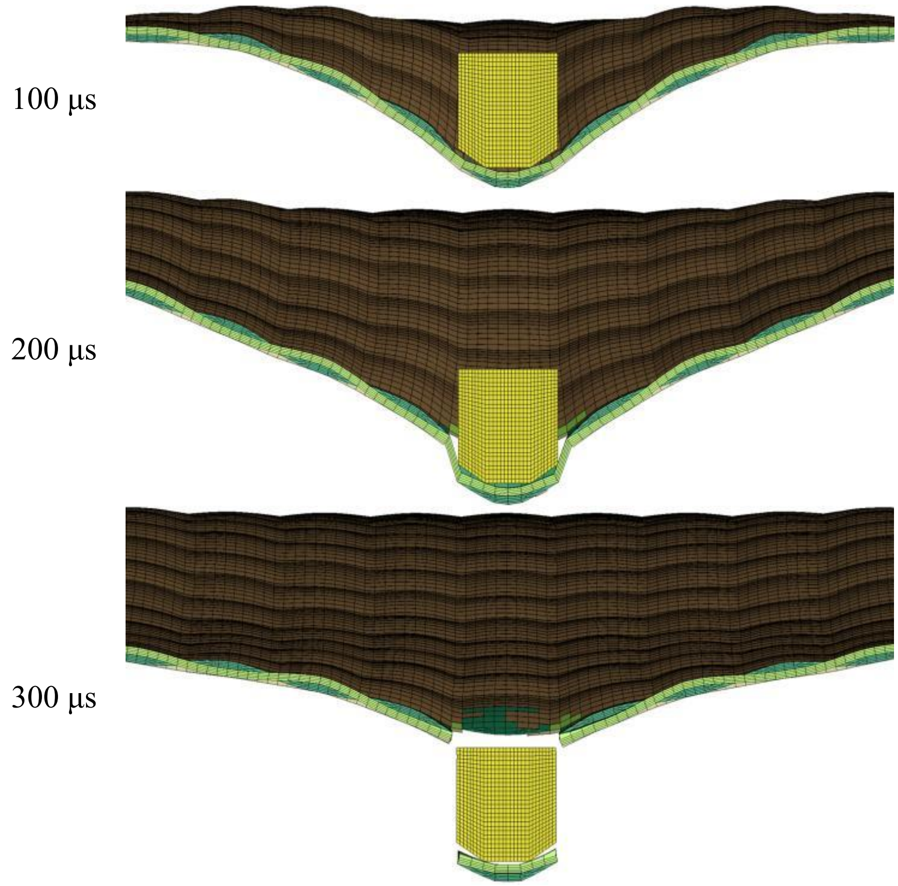

Figure 6.8: Mesoscale model deformation response under 153 m/s projectile impact. Residual velocity is 22 m/s.

6.3.2 Energy Dissipation

The mesoscale model includes rate-dependent matrix plasticity and failure, rate-dependent composite tow behavior, rate-dependent tow-tow delamination, and friction. Tow-tow delamination is coupled with composite tow tension, shear, progressive damage, and failure, so it is difficult to quantify the energy dissipation contribution of tow-tow delamination. However, composite fabric and matrix can be modeled separately to estimate energy dissipation. After interfaces delaminate, Coulomb friction between surfaces is modeled with coefficient, μ = 0.5 [51], [108], and friction can be removed by setting the coefficient to zero. Recall that composite fabric has the properties of unidirectional composite following tow undulation, so it is not the same as modeling fabric (without matrix), which has less shear and bending stiffness as just noted.

The minimum velocity for the projectile to perforate the mesoscale model target is 153 m/s, so this initial velocity and the full 3D, 0.6×0.6 m model is used for the following analyses. The velocity-time results for this impact velocity are included in figure 6.9 and denoted as Baseline. Kinetic energy is given by $KE = \frac{1}{2} m_P V^2$ where projectile mass, m_P, is 1.1 g so that initial kinetic energy from $V_I = 153\ \mathrm{m/s}$ is 12.9 J. The Baseline configuration perforates with residual velocity $V_R = 22\ \mathrm{m/s}$, so 12.6 J is transferred. A series of simulations are conducted to estimate the energy absorption by various mechanisms by individual layers (matrix only, composite fabric only) and in combination (matrix and composite fabric). In this series, the composite fabric was modeled assuming the tow-tow interfaces are not bonded and frictionless. This boundary condition ensures there is no energy dissipation from tow-tow delamination but does include effects of tow undulation and straightening and other weaving interactions. Comparing the total energy absorption to the baseline allows us to estimate the amount of energy absorbed by debonding and sliding of the interfaces.

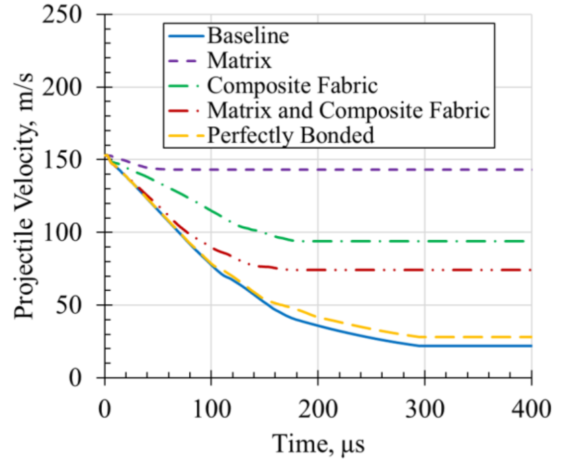

Figure 6.9: Velocity-time curves for 153 m/s projectile impact on the mesoscale model investigating energy dissipating mechanisms. Baseline includes all mechanisms (fabric, matrix, tow-tow delamination, and friction). Matrix, Composite Fabric, and Matrix and Composite Fabric models have sliding-interfaces and no friction. Perfectly Bonded model includes fabric and matrix, but interfaces cannot delaminate (no sliding, no friction).

Perforation of the matrix only was simulated, and the projectile velocity-time results are shown in figure 6.9. The projectile residual velocity after matrix perforation was 143 m/s, which indicates 1.6 J or 13% of the dissipated energy was absorbed by the matrix. Results for perforation of the composite fabric only are included in figure 6.9. Residual velocity was 94 m/s, indicating 8.0 J or 63% of energy was dissipated by perforation of the composite fabric. Perforation of matrix and composite fabric together predicts the residual velocity was 74 m/s or 9.9 J dissipated, which means 0.3 J or 2% of energy was dissipated by interactions between composite fabric and matrix. Adding these up, 79% of the dissipated energy was by tension, shear, progressive damage, and failure of the composite fabric and matrix plasticity and failure. The remaining 21% of impact energy is dissipated by energy absorbed from tow-tow delamination (i.e., debonding governed by the traction laws determined in Chapter 4), friction of the sliding interfaces ($\mu = 0.5$) between the debonding tows, any coupling with tow pullout, elongation, or other deformation and damage processes, and by elastic energy in the target dissipated by vibration, mass damping, sound wave generation. This is an approximate approach to energy partitioning, but it points to opportunities for enhancing performance.

6.3.3 Parametric Study

The model results presented in figure 6.9 under 153 m/s projectile impact shows that the Baseline mesoscale model absorbs the most energy resulting in the lowest residual velocity and includes all deformation modes including local tow-tow delamination as shown in figure 6.5. Results for perfect bonding between tows results in more localized deformation, less energy absorption and an increase in residual velocity. This localized deformation is very similar to the continuum models presented above where tow-tow delamination is ignored. In contrast, the composite fabric plus matrix results where tows are not bonded together and there was no frictional dissipation from tow sliding included (i.e., a free-sliding, frictionless interface) also absorbs less energy and has a higher residual velocity even though tow constraint is reduced. This suggests that an optimal level of tow-tow interaction may lead to maximum energy absorption.

To gain insight into this interaction, we model the composite fabric deformation with minimal constraint by tow-tow delamination (no bonding condition is modeled with near zero peak traction stress in the cohesive separation laws) which enhances tow pullout and elongation and sliding where friction can dissipate additional energy (i.e., a frictional-sliding interface, *with* friction between tows). This scenario is shown in figure 6.10a where the model includes friction ($\mu = 0.5$). Tow tension, shear, and pullout (phase II in figure 6.6a) is extended until the projectile reaches zero velocity. Then elastic energy stored in the composite is returned to the projectile as momentum, which rebounds with 20 m/s velocity in the opposite direction. Other intermediate levels of friction will provide residual velocities between the bounds ($0 > \mu > 0.5$) presented in figure 6.9. This represents a significant improvement in energy absorption compared to the baseline. Energy dissipated by tow tension, shear, and frictional sliding is limited by the tow-tow bonding, which constrains tow displacement and deformation. Without that constraint, additional energy is absorbed and the projectile rebounds, as shown in figure 6.10. To achieve this improvement, a weak interface between tows with an optimal level of frictional sliding is desired. In addition, higher levels of friction may suppress tow sliding and reduce energy absorption by localizing deformation resulting in an increase in residual velocity. This optimization study is an excellent topic for future work. Improvement in performance is most relevant near the ballistic limit velocity where tow elongation and tow pullout are maximum. As impact velocity increases and damage becomes more localized, tow elongation and pullout does not have time to occur before the projectile shears through the tows.

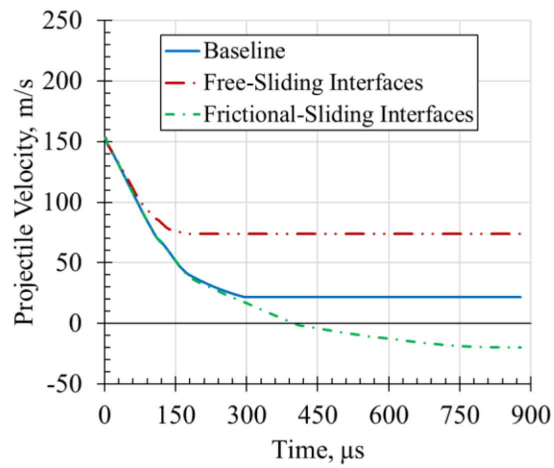

Figure 6.10: Velocity-time curve for 153 m/s projectile impact on mesoscale model investigating the effects of free-sliding, frictionless vs. frictional-sliding tow-tow interfaces ($\mu = 0.5$). Baseline includes progressive debonding and friction using input properties from Chapter 4.

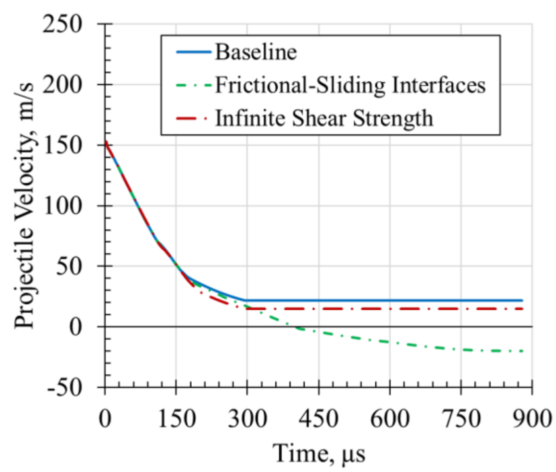

Figure 6.11: Velocity-time curve for 153 m/s projectile impact on mesoscale model investigating the effect of suppressing shear failure (i.e., infinite shear strength means S_{12}, S_{23}, S_{31} = 10^{20} MPa).

One can also use the mesoscale model to study the benefits of improved fiber properties. Ultimately, with sufficient impact velocity, the woven fabric composite fails in tension and shear and the projectile perforates. Increasing shear strength of the composite tows to an effectively infinite value (i.e., from Table 3, $S_{12}, S_{23}, S_{31} = 10^{20}$ MPa) forces primary tows to fail in tension. Figure 6.11 shows the velocity-time curve for 153 m/s impact with infinite shear strength in tows. The momentum-dominated phase is extended, and the residual velocity is decreased slightly (15 m/s) compared with the baseline (22 m/s). This result illustrates that tow tension is the dominant failure mechanism, because suppressing shear failure makes little difference. Improving the strength of fiber tows in tension or shear can increase penetration resistance. One approach is to increase the fiber volume fraction within the tow (e.g., from 50% to 65%). Improvements in matrix behavior can also increase penetration resistance. The mesoscale model developed in this study can be used as a materials design framework to optimize ballistic performance.

6.4 Conclusions

The goal of this work was to develop an accurate, plain weave composite, mesoscale model to investigate ballistic impact energy dissipation and identify important damage mechanisms in a materials-by-design framework. Continuum models with a good database of properties are adequate for modeling impact velocities greater than the ballistic limit velocity. But mesoscale models provide improved predictive capability for impacts near the ballistic limit velocity. We demonstrated that a mesoscale model with realistic geometry, rate-dependent material constitutive behavior, and including important damage mechanisms is able to more accurately predict ballistic limit velocity than a continuum model. We conducted ballistic impact experiments on a single-layer plain weave glass/epoxy composite, and the data was used to validate the mesoscale model. Compared with the experimental ballistic limit velocity, we found that the continuum model predicts the limit velocity with 6% error while the mesoscale model predicts it with 1% error. The mesoscale model includes deformation and damage mechanisms not included in the continuum model. These mechanisms include primary tow tension, rate-dependent matrix behavior, tow-tow delamination, tow pullout and frictional sliding.

We observed two phases of penetration near the ballistic limit velocity. Energy dissipation in the first phase is dominated by momentum transfer, matrix damage, and tow-tow delamination. The second phase is dominated by tow tension and pullout. Modeling constituent materials at the meso-length scale can approximate the energy absorption contribution of each phase, though coupled mechanisms such as material interaction are not included. The mesoscale model indicates that matrix plastic deformation and damage dissipate about 13% of impact energy, composite fabric deformation and damage about 63%, and the remaining energy is absorbed by coupled mechanisms such as tow-tow delamination cracking, tow-matrix cracking, tow pullout and frictional sliding.

It is understood that increasing the strength of fibers can improve ballistic penetration resistance. Fabric without matrix has a lower penetration resistance than fabric with matrix. This is because the matrix spreads load between fibers within tows and between woven tows. Matrix also restricts lateral movement of tows so that projectiles cannot push tows out of the way as easily. However, the matrix also restricts axial movement of tows, which inhibits tensile tow pullout. If by processing or materials selection, one could facilitate tow pullout, tensile elongation, and frictional sliding, these mechanisms enable the composite to dissipate more energy.

Mesoscale models provide additional opportunities for investigating materials by design with more accurate and meaningful deformation at lower length scales. Perforation residual velocity can be reduced by increasing tow sliding, which increases the time the projectile is in contact with the target, and related energy dissipation. Mesoscale models enable investigation of the deformation mechanisms to reduce residual velocity or back face deflection. In a materials-by-design framework, mesoscale models can be used to introduce different matrix materials with improved properties, higher fiber volume fractions within tows, or better fibers for improved tensile strength, and studying energy absorbed. Such studies are proposed as topics for future work. However, providing guidelines for enhanced ballistic performance must be concurrently developed with material processing techniques to realize these improvements.

Chapter 7

CONCLUDING REMARKS

7.1 Summary of Conclusions

Plain weave glass/epoxy composites have found multi-purpose use in light military vehicles, serving as both structural and protection materials. Understanding the response of these materials to ballistic impact is an important aspect of this multi-purpose use. This work has sought to provide new understanding of the evolution of ballistic impact damage in space and time. The length scales considered included microscale (1-10 μm), mesoscale (1-10 mm), and macroscale (>1 cm), and dynamic timescales (1-1000 μs). Improvements in understanding were pursued through the development of multi-scale models for the investigation of damage evolution in these length and timescales. These multi-scale models also provide a framework for studies in materials-by-design optimization of penetration resistance.

Two series of ballistic impact experiments were conducted for this work. The first involved a 0.22 caliber right circular cylindrical projectile impacting 0.3 m by 0.3 m single-layer clamped composite. A state-of-the-art continuum model of these experiments was shown to produce reasonable results when comparing the experimental and numerical residual velocity, V_R, as a function of impact velocity, V_I, but it was clear that there was room for improvement. A mesoscale model of the experiments was developed and shown to produce improved prediction of the experimental V_I–V_R. This improvement was due to the inclusion of the mesoscale architecture, which uses unidirectional material properties aligned with the undulation of the tows, rather than effective plain weave properties as used in the continuum model. For these experiments, the ballistic limit velocity, V_{BL}, was found to be about 175 m/s. The continuum model underpredicts V_{BL} because it treats the in-layer properties as an effective weave but the tow-direction tensile strength and stiffness are lower than unidirectional composite properties. The mesoscale model better predicts V_{BL} with unidirectional composite properties oriented to follow the undulation of interwoven tows, but the mesoscale model still underpredicts V_{BL}. There are additional energy dissipation mechanisms that were not being modeled.

Post-test inspection of damaged composites identified and quantified mesoscale damage modes including transverse matrix cracking and tow-tow delamination. These damage modes were shown to be maximum when impact velocity was near V_{BL}. This is because back face deflection is also maximum, but as velocity increases well beyond V_{BL}, damage localizes around the projectile and punch-shear perforation becomes more dominant. Tow-tow delamination was identified as a significant mesoscale damage mode that was not being modeled. Penetration is governed by in-plane tension, and tow-tow delamination facilitates fiber tension in plain weave composites. Without tow-tow delamination, damage becomes more localized leading to early failure. Addition of this damage mode to the mesoscale model improved V_{BL} prediction. However, the properties used to model this damage were guessed at based on the literature. This indicated that a new method was needed for determining these properties more accurately.

Modeling tow-tow delamination using the cohesive zone model requires knowledge of the rate-dependent traction-separation response of the cracking. With no currently available experimental methods to determine this information, lower length scale modeling was considered. Models were developed with a microscale region of fiber-matrix microstructure embedded within a mesoscale continuum. These models were loaded in mode I and mode II, and the crack energy was determined by the J-integral method. The J-integral data as a function of crack opening was fit with an S-shaped curve and that curve fit was differentiated to determine the traction-separation response. In this way, the microscale cracking was bridged to mesoscale traction-separation law using the J-integral method. Length scale bridging was demonstrated by showing that the load-displacement response of the embedded cell model of microscale cracking was similar to that of a mesoscale model using the traction-separation law to model the crack.

To study the damage evolution at the earliest timescale after projectile impact, a mesoscale model of a plain weave RVE was developed with extremely fine mesh resolution. The model was used to investigate through-thickness stress wave propagation and early-time transverse deformation wave development, and their effect on damage and tow-tow delamination. Study of the damage under and around the projectile as a function of impact velocity revealed the effect of impact velocity from below to above V_{BL}. Damage including matrix failure, punch-crush, and transverse cracking all increase to a maximum for impact velocities exceeding V_{BL}. Transverse cracking is expected for impact velocities as low as about 80 m/s. It was found that transverse cracks and tow-tow delamination cracks initiate during this earliest timescale (<1.8 μs), but propagation evolves over longer timescales (2-1000 μs). At later times, punch-crush and punch-shear become dominant damage modes under and around the projectile.

A much larger mesoscale model was used to explore the damage evolution further away from the projectile, which occurs over longer timescales. A second series of ballistic impact experiments were conducted. These experiments involved a 0.22 caliber fragment simulating projectile impacting 0.6 m by 0.6 m targets with free boundary conditions, to avoid boundary effects related to radial stress wave propagation. The full scale of the experiments was modeled using the mesoscale modeling approach developed in this work. The experimental V_I–V_R data was used to validate the mesoscale model. The model showed good correlation with V_I–V_R and good capability for predicting the experimental V_{BL}, which was found to be 154 m/s. The mesoscale model predicted V_{BL} with 1% error while the continuum model predicted it with 6% error.

The validated mesoscale model was used to partition energy absorption and study damage evolution. It was found that the matrix deformation and failure absorbs about 13% of impact energy, and composite fabric deformation and failure dissipates about 63% of impact energy. The remaining energy is dissipated by coupled mechanisms including tow-tow delamination cracking, tow-matrix cracking, tow-pullout, and frictional sliding, as well as longer-time elastic dissipation (vibration, etc.). Investigation of the damage evolution at the mesoscale revealed that tow-tow delamination reduces constraint on primary tows, enabling additional energy dissipation by tow-pullout, tow-tensile elongation and frictional sliding. This damage evolution is relevant to impact velocities near V_{BL} where tow tensile response dominates. For impact velocities much greater than V_{BL}, damage localizes and punch-crush and punch-shear dominates projectile perforation.

7.2 Future Work

The mesoscale modeling approach developed in this work was used to investigate impact-induced damage evolution over several length scales and a broad timescale. This work provided new insights and understanding of this damage evolution. The models developed in this work can be used in a materials-by-design approach to optimizing the penetration resistance of woven composites.

7.2.1 Improving Model Fidelity

Models are just that. Generally, they are simplified representations of real materials, real geometry, or real phenomena. There is always a need to improve model fidelity, and as computing power increases and diagnostic capabilities progress, models can be made more realistic.

The models developed in the present work made several simplifying assumptions and idealizations. New models could be developed to relax these simplifications or add additional realistic complexity. Examples and extensions of the models are discussed in the following.

Additional stochasticity or real fiber distributions could be added to the fiber-matrix microstructure models. This is an active area of current research (e.g., [100], [101]). Microscopy shows that real fibers have a range of diameters, but a single diameter is often assumed. A distribution of diameters could be used. Also, in real composites, fibers may be touching, which creates a stress concentration between fibers and a likely location for microcracking. The finite element method suffers from very thin elements, which can drive the timestep down and cause simulations to require extremely long wall clock times to complete. Alternatives should be sought that allow for fibers to touch in models. Also, future work could introduce defects to the fiber-matrix interface in a microstructural model.

The microscale embedded cell models in this work, and others like it, typically have a narrow microstructural region because typically only mode I fracture is modeled. The present work was the first to use the method for investigating mode II opening, but this study demonstrated the need for expanding the lateral size of the embedded cell microstructure. New and improved models could be used to investigate various aspects of microstructural crack evolution including crack speeds and mode II opening locally in mode I.

The mesoscale models developed in this work used idealized RVE geometry. The RVE made idealizing assumptions about the tow cross sectional geometry, interstitial gaps between tows, and the resin-rich regions. The idealized RVE was based on mesostructural investigations, which revealed average tow geometry, so the RVEs used in the present work are reasonable. But improvement can be made that would introduce stochastic tow geometry.

It is assumed that the properties are the same throughout all tows, but in reality, the properties depend on the distribution of fibers within the tow. For example, some tows may have higher tensile strength, some may have lower. There has been some investigation of the effects of tow strength on ballistic perforation of fabrics.[143] Such work could be done for fabric composites.

Transverse matrix cracks are another mesoscale damage mode, but they were not included in the present work. These cracks are not expected to dissipate much energy, and this is supported by the investigation in chapter 5, which indicates transverse cracks appear for impact velocities much lower than V_{BL}. Also, there is typically a very large number of these cracks near V_{BL}.[8] Because of the location, frequency, and large number of these cracks, modeling them can be difficult in practice and computationally expensive. However, this is still an area of active research, but generally only for quasi-static loading and within RVEs or single tows (e.g., [30], [101]). To the author's knowledge, transverse cracks have not been modeled in dynamic impact on large composites. Future mesoscale models of impact could incorporate transverse cracks using cohesive zones and the TSLs derived in the present work.

Finally, the projectile impact was assumed to be rigid with flat-nosed impact by generally cylindrical projectiles. Rather than modeling as rigid elastic, projectiles may need to be simulated with a flow stress model such as Johnson-Cook. This is particularly important for thick composite penetration, where projectile deformation can be expected. But this is much less important in thin perforation where projectile deformation will not be significant. Also, in real impact, projectile yaw is an important source of stochasticity in V_I–V_R response. Additionally, projectile nose shape has significant influence on perforation resistance. Sharp-nosed projectiles typically perforate with higher residual velocity than blunt-nosed projectiles, all else being equal. Future work could use mesoscale models to investigate the effects of various projectile nose shapes and impact orientations.

7.2.2 Lower Length Scale Model Inputs

One of the key ingredients to the microscale embedded cell modeling approach was rate-dependent traction-separation law inputs for fiber-matrix interface debonding. The inputs used in the present work were determined experimentally from a microdroplet of resin cured on a single fiber. The load-displacement response of pushing the microdoplet along the length of the fiber was used to determine the microscale TSL inputs. However, such experiments require specialized equipment, are costly and time consuming, and determining higher-rate properties may not be possible. Research is currently being done to derive TSLs directly from atomistic models of fiber, matrix, and interphase.[144], [145]

Atomistic models of fiber-matrix debonding are free of defects, and predict traction-separation laws for the nanometer length scale. These TSLs, for example, predict peak tractions in the GPa range, and maximum separations in the nanometer range. Such TSLs are not appropriate for microscale models of fiber-matrix debonding where peak tractions are on the order of tens of MPa and maximum separations are on the order of μm. It is proposed that new models are needed to bridge length scales from the nanometer to the micrometer length scale. Such models could apply TSLs derived from molecular dynamics (MD) simulations to idealized continuum models of the fiber-matrix interface. Then by adding defects to the MD interfacial properties, the appropriate TSL for higher length scale fiber-matrix debonding could be derived from lower length scale MD calculations.

Development of such models to bridge from the atomistic length scale to the microscale would be an important piece of the full materials-by-design approach. With such models, new fiber or matrix materials, new fiber-matrix sizing chemistry, or new interfacial geometries could be explored at the MD length scale. Traction-separation laws could be derived at the MD scale, then bridged up to the microscale. The microscale embedded cell model described in the present work could be used to derive the TSLs for use in mesoscale models of impact. Then the mesoscale modeling approach could be used to evaluate the ballistic performance of these new materials.

7.2.3 Extension of the Mesoscale Modeling Approach to Multi-layered Composite Impact

The single-layer mesoscale model developed in this work has been used to gain new understanding of ballistic perforation and energy dissipation mechanisms in plain woven composites. However, practical application of the mesoscale model to real-world problems involves extending the model to multiple composite layers.

Penetration and perforation experiments of single-layer composites were conducted and discussed in previous chapters. Multiple-layer composite impact experiments are beyond the scope of the present work. There is limited data available in the literature for multi-layered impact experiments on plain weave glass/epoxy composites.

Haque (Gama) and Gillespie [136] conducted experiments on 22-layer S-2 glass, SC-15 epoxy composites. In this section, these data are used to evaluate the mesoscale model for multiple-layer composite impact simulations. Delamination between layers is a penetration mechanism important in multi-layer impact, but not found in single-layer perforation. Cohesive tiebreak contact is included in mesoscale models between tows and between tows and matrix, but real cracks do not occur within matrix between layers (i.e., on the top of the RVE in figure 7.1) so epoxy layers are node-merged. However, while delamination is present in the multi-layer model, study of this delamination is reserved for future work.

7.2.3.1 Modeling the Experiments

The Haque and Gillespie experiments were conducted on S-2 glass, SC-15 epoxy composite plates of 178 mm by 178 mm by 13.2 mm. Plates were impacted by a steel right circular cylinder (RCC) of 13.8 g, 12.7 mm diameter, and 14.0 mm height. The RCC from previous models was scaled to the correct dimensions. As discussed previously, the RCC has filleted edges to reduce stress concentration at the projectile annulus, and because the experimental RCCs are also filleted. The RCC volume is 1.773E-6 m^3 so to ensure correct mass, the steel density was set to a realistic value of 7.785 g/cm^3.

Boundary conditions were clamped such that a circular hole of 101.6 mm diameter was within the clamped boundaries.[136] Therefore, the model is 101.6 mm square. Boundary conditions were applied by fully constraining the nodes of the two outermost elements of the 3D model perimeter. Square shape was chosen for simplicity and ease of boundary condition application since the hexahedral mesh was made square on the RVE surfaces, as shown in figure 7.1. The mesh was designed to be able to tile the RVE in space both horizontally and vertically for building up large models.

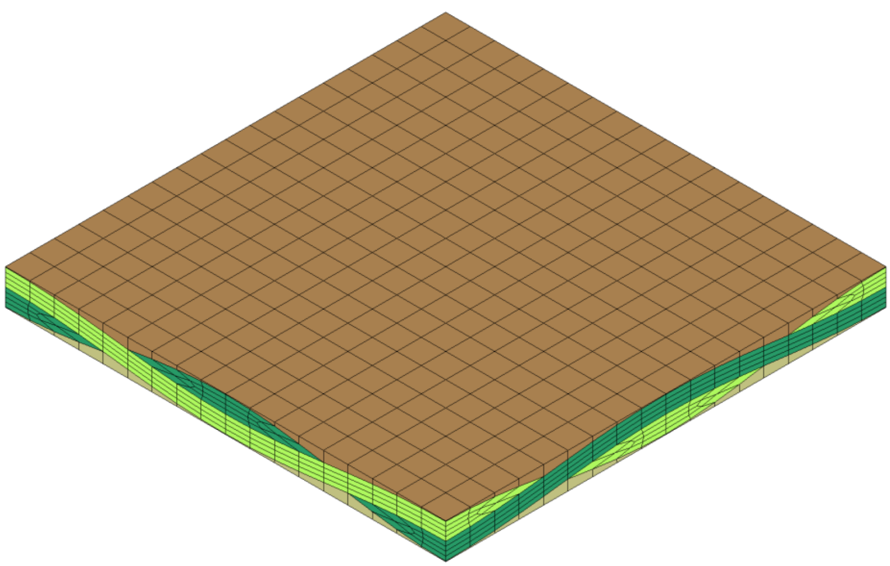

Figure 7.1: Repeating volume element used to build large scale, multi-layer plain weave composite models.

Model parameters for composite tows and epoxy matrix were the same as used to simulate the single-layer perforation experiments. Penetration through epoxy and tows is modeled by element erosion. The rate-dependent matrix erosion was discussed in Chapters 3 and 4 and used in Chapters 5 and 6. Rate-dependent composite tow behavior was discussed in Chapters 2 and 3 and Appendix A, and was used in Chapters 5 and 6. Under tension, composite elements are eroded if tensile failure is predicted in the element through accumulation of progressive damage, and if the axial tensile erosion strain in the element exceeds e_{limit} (e.g., 4.5 in Table A.3). Under compression, composite elements are eroded if the relative volume of a failed element is less than e_{crush} (i.e., if the element is compressed to 0.1% of its original volume, see Table A.3). If the composite element should expand under loading, it would be eroded if its relative volume exceeded 450% of its original volume (i.e., e_{expn} in Table A.3).

Cohesive tiebreak contact is modeled tow-tow and tow-matrix using the same mode I and mode II traction laws for tow-tow delamination in the single-layer model, which were determined in Chapter 4 for tow-tow delamination. Due to stress concentration from fibers within the matrix, cracking between tows and matrix is expected to propagate through fibers along the interface. Although unlikely, real cracks could jump through the epoxy layer to other fiber tows, but this is not modeled. A postmortem microscopic investigation of such delamination cracks in multi-layer composites is needed and proposed for future work.

Two models were built to investigate mesostructure. The first is a perfectly stacked mesostructure, shown in figure 7.2, and the second is a perfectly nested mesostructure, shown in figure 7.3. These two models bound the range of possible mesostructures. In real composites, made by stacking layers of plain weave fabric and infusing with resin, there will be some combination of stacking and nesting. While the fabric layers may be ordered such as in the stacked model, compression by vacuum bagging will lead to some amount of nesting within the stacked structure.

The models have about 5.5 million elements with considerable complexity of cohesive tiebreak contact. Depending on impact velocity and tow nesting, the models run for 1-5 days on 144 cores. The nested model generally requires longer solution times for similar impact velocities compared with the stacked model.

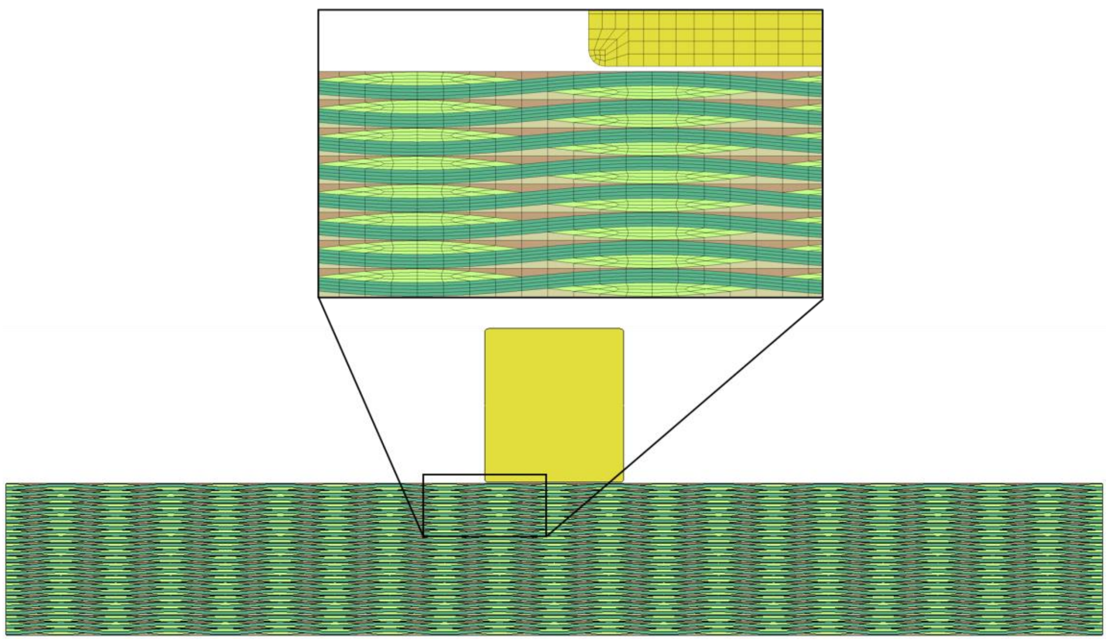

Figure 7.2: Stacked plain weave glass/epoxy composite impact model with 22 layers arranged with tows stacked vertically overtop of one another.

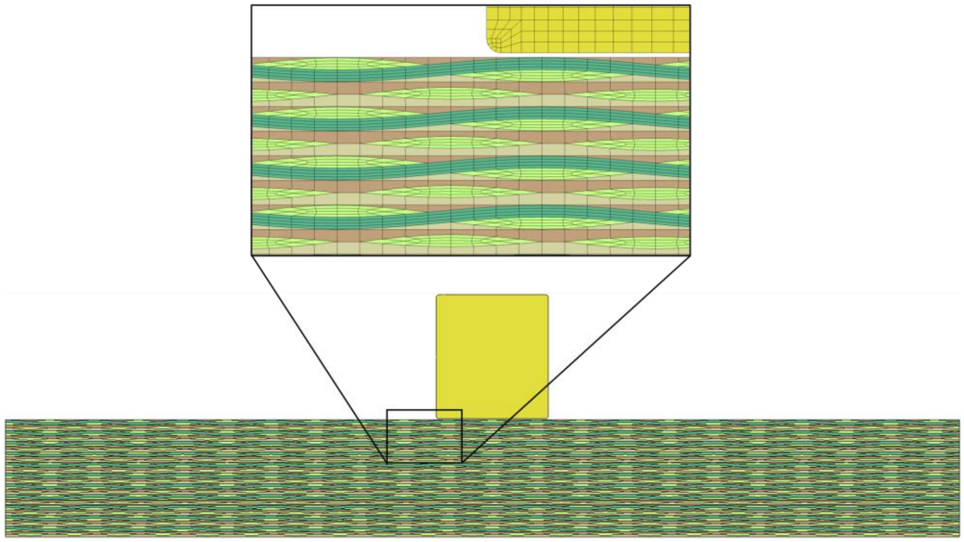

Figure 7.3: Nested plain weave glass/epoxy composite impact model with 22 layers arranged with tows in alternating stacks offset by a half-tow width.

7.2.3.2 Results and Discussion

Impact velocities simulated followed the ballistic experiments from the reference, which ranged from 365 to 1100 m/s.[136] Figure 7.4 compares the simulation results to the experimental data. Stacked refers to the model in figure 7.2 and nested refers to the model in figure 7.3.

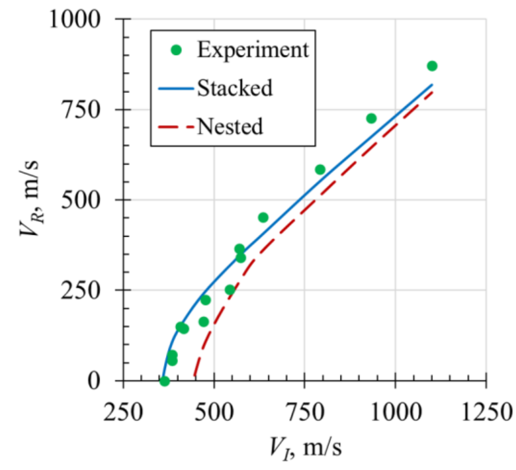

Figure 7.4: Residual velocity, V_R, as a function of impact velocity, V_I, results of 22-layer simulations compared with experiment. [136] Two different models are included, stacked and nested.

For impact velocities below about 600 m/s, the stacked and nested models seem to bound the experimental data. Overall, and particularly for impact velocities near the ballistic limit, the stacked model is a better match to the experimental data than the nested. Below about 600 m/s, the stacked model slightly overpredicts the residual velocity while the nested model underpredicts. This is because the stacked model has alternating vertical (parallel to projectile impact) planes of high areal density where fiber tows are stacked and low areal density where interstitial matrix regions are stacked. The nested model has a more constant areal density through the thickness since the layers are staggered. Thus, the nested model has a much stronger resistance to penetration than the stacked model. Real composites have a mesostructure somewhere between fully stacked and fully nested, so the two models bound the experimental data.

This investigation considered V_I–V_R only. Experimental results show considerable delamination between layers. However, while delamination is present, it was not investigated in the present work. Study of damage and delamination is suggested for future work. Additionally, comparison of the mesoscale model to predictions by a continuum model with interlaminar delamination is also proposed for future work.

7.2.3.3 Summary and Future Work

The single-layer mesoscale modeling approach was extended to multi-layered models of plain weave glass/epoxy composite. Experimental results from the literature were simulated for impact velocities from 365 to 1100 m/s. The numerical V_I–V_R results are similar to the experimental data. Future work is needed to investigate depth of penetration, delamination, and compare mesoscale model results to results predicted by continuum models with interlaminar delamination and erosion.

Two mesostructures were modeled. In the stacked mesostructure, tows were stacked vertically relative to composite thickness. In the nested mesostructure, alternating layers of tows were offset by a half-tow width. These two mesostructures bound the problem, and realistic mesostructure is expected to be somewhere in between these extremes. Investigation of the mesostructure of real multi-layered composites is needed, and could be done using optical microscopy and micro computed tomography (μ-CT). Optical microscopy is recommended to investigate a large number of representative volumes to produce a statistical picture of the stochastic mesostructure. Optical microscopy is good for larger scale views of the mesostructure and for producing a statistical picture of the mesostructure, but lacks fine detail. Then μ-CT is useful to provide a picture of the finer detail of mesostructures, since μ-CT is not practical for larger volumes and so may not be as useful to produce a statistical picture. The mesoscale modeling approach could then be used to produce more realistic mesostructural models for multi-layer penetration and perforation simulations.

Penetration of multi-layer woven composites is known to develop significant interlaminar delamination. A microscopic or μ-CT study of delamination cracking at the microscale is needed to guide the modeling of delamination, to qualify the delamination crack paths. The matrix material may need to be modeled as more brittle, while the present model has ascribed plasticity to the matrix based on experimental data. Modeling delamination with cohesive zones has initially used the traction-separation laws derived from the microscale embedded cell models for tow-tow delamination. However, it is possible that interlaminar delamination follows a different set of cohesive behaviors. New models could use the J-integral approach to compute interlaminar delamination traction-separation laws. Additionally, new numerical model post-processing techniques or applications are needed for visualizing cohesive separation in the very large models (with millions of elements and hundreds of possible locations for tow-tow delamination and tow-matrix decohesion) proposed by this work.

Finally, the materials-by-design approach can be applied from the lower length scale models to the single-layer to the multi-layer mesoscale models. Such a multi-scale materials-by-design approach is needed for developing new materials with enhanced resistance to penetration.

REFERENCES

1. W. M. Lai, D. Rubin, and E. Krempl, *Introduction to Continuum Mechanics*, 2nd ed. New York, NY: Pergamon Press, 1978.

2. M. A. Meyers, *Dynamic Behavior of Materials*. New York: John Wiley & Sons, Inc., 1994.

3. K. S. Pandya, M. D. Kulkarni, A. Warman, and N. K. Naik, "Simulation of stress wave attenuation in plain weave fabric composites during in-plane ballistic impact," *Composite Structures*, 2017.

4. B. Parga-Landa, S. Vlegels, F. Hernández-Olivares, and S. D. Clark, "Analytical simulation of stress wave propagation in composite materials," *Composite Structures*, 1999.

5. S. Leigh Phoenix and P. K. Porwal, "A new membrane model for the ballistic impact response and V50 performance of multi-ply fibrous systems," *International Journal of Solids and Structures*, vol. 40, no. 24, pp. 6723–6765, 2003.

6. N. K. Naik, P. Shrirao, and B. C. K. Reddy, "Ballistic impact behaviour of woven fabric composites: Formulation," *International Journal of Impact Engineering*, vol. 32, no. 9, pp. 1521–1552, 2006.

7. C. S. Meyer, B. Z. (Gama. Haque, D. J. O'Brien, N. Getinet, J. H. Yu, E. Bonyi, K. Aslan, and J. W. Gillespie, "Mesoscale ballistic damage mechanisms of a single-layer woven glass/epoxy composite," *International Journal of Impact Engineering*, vol. 113, no. August 2017, pp. 118–131, 2018.

8. E. Bonyi, C. S. Meyer, B. Kioko, O. Adesina, C. Lansiquot, Z. Onuk, D. J. O'Brien, B. Z. Haque, J. W. Gillespie Jr., and K. Aslan, "Assessment and quantification of ballistic impact damage of a single-layer woven fabric composite," *International Journal of Damage Mechanics*, vol. 28, no. 2, pp. 249–269, 2019.

9. C. S. Meyer, B. Z. (Gama. Haque, D. J. O'Brien, N. Getinet, J. H. Yu, E. Bonyi, K. Aslan, and J. W. Gillespie Jr., "Mesoscale ballistic damage mechanisms of a single-layer woven glass/epoxy composite," *International*

Journal of Impact Engineering, vol. 113, no. August 2017, pp. 118–131, 2018.

10. E. Bonyi, C. S. Meyer, B. Kioko, O. Adesina, C. Lansiquot, Z. Onuk, D. J. O'Brien, B. Z. Haque, J. W. Gillespie, and K. Aslan, "Assessment and quantification of ballistic impact damage of a single-layer woven fabric composite," *International Journal of Damage Mechanics*, vol. 28, no. 2, pp. 249–269, 2019.

11. P. Cunniff, "Decoupled response of textile body armor," in *Proceedings of the 18th International Symposium on Ballistics*, 1999.

12. S. V. Lomov, D. S. Ivanov, I. Verpoest, M. Zako, T. Kurashiki, H. Nakai, J. Molimard, and A. Vautrin, "Full-field strain measurements for validation of meso-FE analysis of textile composites," *Composites Part A: Applied Science and Manufacturing*, vol. 39, no. 8, pp. 1218–1231, 2008.

13. R. L. Karkkainen and B. McWilliams, "Dynamic micromechanical modeling of textile composites with cohesive interface failure," *Journal of Composite Materials*, vol. 46, no. 18, pp. 2203–2218, 2012.

14. R. L. Karkkainen, "Dynamic micromechanical modeling of textile composite strength under impact and multi-axial loading," *Composites Part B: Engineering*, vol. 83, pp. 27–35, 2015.

15. J. P. Lambert and G. H. Jonas, "Towards standardization in terminal ballistics testing: velocity representation. BRL-R-1852," Aberdeen Proving Ground, MD, 1976.

16. E. Bonyi, B. Kioko, C. S. Meyer, O. Adesina, T. Obafemi-Babatunde, J. Guy, D. J. O'Brien, B. Z. Haque, J. W. Gillespie Jr., and K. Aslan, "Toward automated identification and quantification of meso-scale damage modes in plain weave glass/epoxy composite laminates," *International Journal of Damage Mechanics*, vol. 29, no. 5, pp. 831–848, 2020.

17. C. S. Meyer, E. Bonyi, K. Drake, T. Obafemi-Babatunde, A. Daodu, D. Ajifa, A. Bigio, J. Taylor, B. Z. Haque, D. J. O'Brien, J. W. Gillespie Jr., and K. Aslan, "Automated detection and quantification of transverse cracks on woven composites," *Journal of Reinforced Plastics and Composites*, 2021.

18. A. J. Carpenter, S. Chocron, and C. E. Anderson, "Bridging the scales: Continuum-based material constitutive modeling of mechanical and ballistic test data from composites and fabrics," *International Journal of Impact Engineering*, vol. 120, no. January, pp. 31–45, 2018.

19. B. A. Gama and J. W. Gillespie, "Finite element modeling of impact, damage evolution and penetration of thick-section composites," *International Journal of Impact Engineering*, vol. 38, no. 4, pp. 181–197, 2011.

20. J. O. Hallquist, *LS-DYNA® Keyword User's Manual*, vol. I. Livermore, CA: Livermore Software Technology Corporation, 2016.

21. C. F. Yen, "A ballistic material model for continuous-fiber reinforced composites," *International Journal of Impact Engineering*, vol. 46, pp. 11–22, 2012.

22. M. Olave, A. Vanaerschot, S. V. Lomov, and D. Vandepitte, "Internal Geometry Variability of Two Woven Composites and Related Variability of the Stiffness," *Polymer Composites*, vol. 33, no. 8, pp. 1335–1350, 2012.

23. A. Doitrand, C. Fagiano, F. X. Irisarri, and M. Hirsekorn, "Comparison between voxel and consistent meso-scale models of woven composites," *Composites Part A: Applied Science and Manufacturing*, vol. 73, pp. 143–154, 2015.

24. T. D. Blacker, S. J. Owen, M. L. Staten, W. R. Quadros, B. Hanks, B. W. Clark, R. J. Meyers, C. Ernst, K. Merkley, R. Morris, C. McBride, C. Stimpson, M. Plooster, and S. Showman, "CUBIT Geometry and Mesh Generation Toolkit 15.2 User Documentation," Sandia National Lab., Albuquerque, NM, SAND2016-6850R, 2016.

25. C. T. Key and C. Scott Alexander, "Experimental Testing and Numerical Modeling of Ballistic Impact on S-2 Glass/SC15 Composites," *Journal of Dynamic Behavior of Materials*, vol. 4, no. 3, pp. 373–386, 2018.

26. C. T. Key and C. S. Alexander, "Numerical and experimental evaluations of a glass-epoxy composite material under high velocity oblique impacts," *International Journal of Impact Engineering*, vol. 137, no. November 2019, p. 103443, 2020.

27. M. Ito and T. W. Chou, "An analytical and experimental study of strength and failure behavior of plain weave composites," *Journal of Composite Materials*, vol. 32, no. 1, pp. 2–30, 1998.

28. E. J. Barbero, P. Lonetti, and K. K. Sikkil, "Finite element continuum damage modeling of plain weave reinforced composites," *Composites Part B: Engineering*, vol. 37, no. 2–3, pp. 137–147, 2005.

29. A. Doitrand, C. Fagiano, V. Chiaruttini, F. H. Leroy, A. Mavel, and M.

Hirsekorn, “Experimental characterization and numerical modeling of damage at the mesoscopic scale of woven polymer matrix composites under quasi-static tensile loading,” *Composites Science and Technology*, vol. 119, pp. 1–11, 2015.

30. A. Doitrand, C. Fagiano, F. Hild, V. Chiaruttini, A. Mavel, and M. Hirsekorn, “Mesoscale analysis of damage growth in woven composites,” *Composites Part A: Applied Science and Manufacturing*, vol. 96, pp. 77–88, 2017.

31. A. Doitrand, C. Fagiano, N. Carrère, V. Chiaruttini, and M. Hirsekorn, “Damage onset modeling in woven composites based on a coupled stress and energy criterion,” *Engineering Fracture Mechanics*, vol. 169, pp. 189–200, 2017.

32. B. A. Bednarcyk, B. Stier, J. W. Simon, S. Reese, and E. J. Pineda, “Meso- and micro-scale modeling of damage in plain weave composites,” *Composite Structures*, vol. 121, pp. 258–270, 2015.

33. J. W. Simon, D. Höwer, B. Stier, and S. Reese, “Meso-mechanically motivated modeling of layered fiber reinforced composites accounting for delamination,” *Composite Structures*, vol. 122, pp. 477–487, 2015.

34. X. Tang and J. D. Whitcomb, “Progressive failure behaviors of 2D woven composites,” *Journal of Composite Materials*, vol. 37, no. 14, pp. 1239–1259, 2003.

35. B. Stier, J. W. Simon, and S. Reese, “Comparing experimental results to a numerical meso-scale approach for woven fiber reinforced plastics,” *Composite Structures*, vol. 122, pp. 553–560, 2015.

36. S. Daggumati, E. Voet, W. Van Paepegem, J. Degrieck, J. Xu, S. V. Lomov, and I. Verpoest, “Local strain in a 5-harness satin weave composite under static tension: Part I - Experimental analysis,” *Composites Science and Technology*, vol. 71, no. 8, pp. 1171–1179, 2011.

37. S. D. Green, M. Y. Matveev, A. C. Long, D. Ivanov, and S. R. Hallett, “Mechanical modelling of 3D woven composites considering realistic unit cell geometry,” *Composite Structures*, vol. 118, no. 1, pp. 284–293, 2014.

38. C. Zhang, N. Li, W. Wang, W. K. Binienda, and H. Fang, “Progressive damage simulation of triaxially braided composite using a 3D meso-scale finite element model,” *Composite Structures*, vol. 125, pp. 104–116, 2015.

39. M. P. Rao, G. Nilakantan, M. Keefe, B. M. Powers, and T. A. Bogetti, “Global/local modeling of ballistic impact onto woven fabrics,” *Journal of*

Composite Materials, vol. 43, no. 5, pp. 445–467, 2009.

40. G. Nilakantan, M. Keefe, T. A. Bogetti, R. Adkinson, and J. W. Gillespie Jr., "On the finite element analysis of woven fabric impact using multiscale modeling techniques," *International Journal of Solids and Structures*, vol. 47, no. 17, pp. 2300–2315, 2010.

41. G. Nilakantan and J. W. Gillespie, "Ballistic impact modeling of woven fabrics considering yarn strength, friction, projectile impact location, and fabric boundary condition effects," *Composite Structures*, vol. 94, no. 12, pp. 3624–3634, 2012.

42. F. Pascal, O. Dorival, P. Navarro, S. Marguet, and J. F. Ferrero, "Impact damage prediction in thin woven composite laminates – Part I: Modeling strategy and validation," *Composite Structures*, vol. 190, pp. 32–42, 2018.

43. M. Schwab, M. Todt, and H. E. Pettermann, "A multiscale approach for modelling impact on woven composites under consideration of the fabric topology," *Journal of Composite Materials*, vol. 52, no. 21, pp. 2859–2874, 2018.

44. E. M. Parsons, T. Weerasooriya, S. Sarva, and S. Socrate, "Impact of woven fabric: Experiments and mesostructure-based continuum-level simulations," *Journal of the Mechanics and Physics of Solids*, vol. 58, no. 11, pp. 1995–2021, 2010.

45. M. Grujicic, W. C. Bell, G. Arakere, T. He, X. Xie, and B. A. Cheeseman, "Development of a meso-scale material model for ballistic fabric and its use in flexible-armor protection systems," *Journal of Materials Engineering and Performance*, vol. 19, no. 1, pp. 22–39, 2010.

46. X. Jia, Z. Huang, X. Zu, X. Gu, and Q. Xiao, "Effect of mesoscale and multiscale modeling on the performance of kevlar woven fabric subjected to ballistic impact: A numerical study," *Applied Composite Materials*, vol. 20, no. 6, pp. 1195–1214, 2013.

47. P. Tran, T. Ngo, E. C. Yang, P. Mendis, and W. Humphries, "Effects of architecture on ballistic resistance of textile fabrics: Numerical study," *International Journal of Damage Mechanics*, vol. 23, no. 3, pp. 359–376, 2014.

48. C. C. Yang, T. Ngo, and P. Tran, "Influences of weaving architectures on the impact resistance of multi-layer fabrics," *Materials and Design*, vol. 85, pp. 282–295, 2015.

49. X. L. Gao and K. Li, “Damaged mosaic laminate model of woven fabric composites with transverse yarn cracking and interface debonding,” *Composites Science and Technology*, vol. 62, no. 14, pp. 1821–1834, 2002.

50. B. A. Cheeseman and T. A. Bogetti, “Ballistic impact into fabric and compliant composite laminates,” *Composite Structures*, vol. 61, no. 1–2, pp. 161–173, 2003.

51. Y. Duan, M. Keefe, T. A. Bogetti, and B. A. Cheeseman, “Modeling the role of friction during ballistic impact of a high-strength plain-weave fabric,” *Composite Structures*, vol. 68, no. 3, pp. 331–337, 2005.

52. A. J. Carpenter, S. Chocron, and C. E. Anderson, “Mesoscale modeling of S-2 Glass/SC-15 epoxy composites: Plain-weave architecture,” *Journal of Composite Materials*, vol. 50, no. 5, pp. 685–700, 2016.

53. A. J. Carpenter, C. E. Anderson, and S. Chocron, “Mesoscale simulations of high-velocity impact on plain-weave and 3-D weave S-2 glass targets,” *Procedia Engineering*, vol. 103, pp. 60–67, 2015.

54. S. Chocron, A. J. Carpenter, N. L. Scott, R. P. Bigger, and K. Warren, “Impact on carbon fiber composite: Ballistic tests, material tests, and computer simulations,” *International Journal of Impact Engineering*, 2019.

55. B. Z. (Gama) Haque, “A Progressive Composite Damage Model for Unidirectional and Woven Fabric Composites,” Materials Sciences Corporation and University of Delaware Center for Composite Materials, MAT_162 User Manual, 2017.

56. M. Pankow, A. M. Waas, C. F. Yen, and S. Ghiorse, “Modeling the response, strength and degradation of 3D woven composites subjected to high rate loading,” *Composite Structures*, vol. 94, no. 5, pp. 1590–1604, 2012.

57. B. Justusson, J. Yu, A. Chen, and C. Yen, “Mechanical Testing of 3D Fabric Composites and Their Matrix Material SC-15,” no. November, 2012.

58. G. R. Cowper and P. S. Symonds, “Strain-Hardening and Strain-Rate Effects in the Impact Loading of Cantilever Beams,” Office of Naval Research, NR-064-406, 1957.

59. LSTC, *LS-DYNA: Keyword User’s Manual: Material Models*, vol. II. 2016.

60. R. Talreja, “Multi-scale modeling in damage mechanics of composite materials,” *Journal of Materials Science*, vol. 41, no. 20, pp. 6800–6812, 2006.

61. T. L. Anderson, *Fracture Mechanics Fundamentals and Applications*, 3rd ed. Taylor & Francis, 2005.

62. D. S. Dugdale, “Yielding of steel sheets containing slits,” *Journal of the Mechanics and Physics of Solids*, vol. 8, no. 2, pp. 100–104, 1953.

63. G. N. Barenblatt, “Mathematical theory of equilibrium cracks,” *Advances in Applied Mechanics*, vol. 7, no. 1, pp. 55–129, 1962.

64. P. P. Camanho, C. G. Dávila, and M. F. De Moura, “Numerical Simulation of Mixed-mode Progressive Delamination in Composite Materials,” *Journal of Composite Materials*, vol. 37, no. 16, pp. 1415–1438, 2003.

65. S. Li, M. D. Thouless, A. M. Waas, J. A. Schroeder, and P. D. Zavattieri, “Use of a cohesive-zone model to analyze the fracture of a fiber-reinforced polymer-matrix composite,” *Composites Science and Technology*, vol. 65, no. 3–4, pp. 537–549, 2005.

66. A. Turon, C. G. Dávila, P. P. Camanho, and J. Costa, “An engineering solution for mesh size effects in the simulation of delamination using cohesive zone models,” *Engineering Fracture Mechanics*, vol. 74, no. 10, pp. 1665–1682, 2007.

67. M. Loikkanen, G. Praveen, and D. Powell, “Simulation of Ballistic Impact on Composite Panels,” in *10th International LS-DYNA Users Conference*, 2008, pp. 1–12.

68. P. W. Harper and S. R. Hallett, “Cohesive zone length in numerical simulations of composite delamination,” *Engineering Fracture Mechanics*, vol. 75, no. 16, pp. 4774–4792, 2008.

69. C. Bouvet, B. Castanié, M. Bizeul, and J. J. Barrau, “Low velocity impact modelling in laminate composite panels with discrete interface elements,” *International Journal of Solids and Structures*, vol. 46, no. 14–15, pp. 2809–2821, 2009.

70. F. Dogan, H. Hadavinia, T. Donchev, and P. S. Bhonge, “Delamination of impacted composite structures by cohesive zone interface elements and tiebreak contact,” *Central European Journal of Engineering*, vol. 2, no. 4, pp. 612–626, 2012.

71. V. A. Phadnis, K. S. Pandya, N. K. Naik, A. Roy, and V. V. Silberschmidt, “Ballistic impact behaviour of woven fabric composite: Finite element analysis and experiments,” *Journal of Physics: Conference Series*, vol. 451, no. 1, 2013.

72. S. A. Muflahi, G. Mohamed, and S. R. Hallett, “Investigation of Delamination Modeling Capabilities for Thin Composite Structures in LS-DYNA®,” in *13th International LS-DYNA Users Conference*, 2014, pp. 1–13.

73. J. Pernas-Sánchez, J. A. Artero-Guerrero, J. Zahr Viñuela, D. Varas, and J. López-Puente, “Numerical analysis of high velocity impacts on unidirectional laminates,” *Composite Structures*, vol. 107, pp. 629–634, 2014.

74. A. Cornec, I. Scheider, and K. H. Schwalbe, “On the practical application of the cohesive model,” *Engineering Fracture Mechanics*, vol. 70, no. 14, pp. 1963–1987, 2003.

75. M. R. Wisnom, “Modelling discrete failures in composites with interface elements,” *Composites Part A: Applied Science and Manufacturing*, vol. 41, no. 7, pp. 795–805, 2010.

76. K. Park and G. H. Paulino, “Cohesive zone models: A critical review of traction-separation relationships across fracture surfaces,” *Applied Mechanics Reviews*, vol. 64, no. 6, 2011.

77. S. Abrate, J. F. Ferrero, and P. Navarro, “Cohesive zone models and impact damage predictions for composite structures,” *Meccanica*, vol. 50, no. 10, pp. 2587–2620, 2015.

78. A. Needleman, “Some issues in cohesive surface modeling,” *Procedia IUTAM*, vol. 10, pp. 221–246, 2014.

79. V. Tvergaard and J. W. Hutchinson, “The relation between crack growth resistance and fracture process parameters in elastic-plastic solids,” *Journal of the Mechanics and Physics of Solids*, vol. 40, pp. 1377–1392, 1992.

80. R. D. S. G. Campilho, M. D. Banea, J. A. B. P. Neto, and L. F. M. Da Silva, “Modelling adhesive joints with cohesive zone models: Effect of the cohesive law shape of the adhesive layer,” *International Journal of Adhesion and Adhesives*, vol. 44, pp. 48–56, 2013.

81. L. M. Fernández-Cañadas, I. Iváñez, and S. Sanchez-Saez, “Influence of the cohesive law shape on the composite adhesively-bonded patch repair behaviour,” *Composites Part B: Engineering*, vol. 91, pp. 414–421, 2016.

82. J. Xue and K. Kirane, “Effect of the Shape of the Softening Damage Law on the Predicted Fracturing Behavior of Composites,” in *Proceedings of the 35th Technical Conference of the American Society for Composites2*.

83. K. D. Papoulia, C. H. Sam, and S. A. Vavasis, “Time continuity in cohesive finite element modeling,” *International Journal for Numerical Methods in Engineering*, vol. 58, no. 5, pp. 679–701, 2003.

84. K. L. Nielsen and J. W. Hutchinson, “Cohesive traction-separation laws for tearing of ductile metal plates,” *International Journal of Impact Engineering*, vol. 48, pp. 15–23, 2012.

85. S. C. Chowdhury, R. Prosser, T. W. Sirk, R. M. Elder, and J. W. Gillespie, “Glass fiber-epoxy interactions in the presence of silane: A molecular dynamics study,” *Applied Surface Science*, vol. 542, no. December 2020, p. 148738, 2021.

86. V. C. Li, C. M. Chan, and C. K. Y. Leung, “Experimental determination of the tension-softening relations for cementitious composites,” *Cement and Concrete Research*, vol. 17, no. 3, pp. 441–452, 1987.

87. J.R.Rice, “A Path Independent Integral and the Approximate Analysis of Strain Concentration by Notches and Cracks,” *Journal of Applied Mechanics*, vol. 35, no. 2, p. 379, 1968.

88. C. F. Shih, B. Moran, and T. Nakammura, “Energy Release Rate Along a Three-Dimensional Crack Front in a Thermally Stressed Body,” *International Journal of Fracture*, vol. 30, pp. 79–102, 1986.

89. B. Moran and C. F. Shih, “A General Treatment of Crack Tip Contour Integrals,” *International Journal of Fracture*, vol. 35, pp. 295–310, 1987.

90. A. T. Zehnder, *Fracture Mechanics*. Springer Nature, 2012.

91. P. Lindström, A. Jonsson, A. Jernberg, and E. Østby, “Non-linear fracture mechanics in LS-DYNA and LS-PrePost,” in *10th European LS-DYNA Conference*, 2015.

92. C. Sarrado, A. Turon, J. Renart, and I. Urresti, “Assessment of energy dissipation during mixed-mode delamination growth using cohesive zone models,” *Composites Part A: Applied Science and Manufacturing*, vol. 43, no. 11, pp. 2128–2136, 2012.

93. W. Brocks and I. Scheider, “Reliable J-values: Numerical aspects of the path-dependence of the J-integral in incremental plasticity,” *Materialprüfung*, vol. 45, no. 6, pp. 264–275, 2003.

94. W. Brocks, *Plasticity and Fracture*, vol. 244. 2018.

95. I. Scheider, “Micromechanical based derivation of traction-separation laws for cohesive model simulations,” *Procedia Engineering*, vol. 1, no. 1, pp. 17–21, 2009.

96. L. P. Canal, C. González, J. Segurado, and J. LLorca, “Intraply fracture of fiber-reinforced composites: Microscopic mechanisms and modeling,” *Composites Science and Technology*, vol. 72, no. 11, pp. 1223–1232, 2012.

97. D. M. Montenegro, L. P. Canal, J. Botsis, M. Zogg, A. R. Studart, and K. Wegener, “On the validity of the J-integral as a measure of the transverse intralaminar fracture energy of glass fiber-reinforced polyurethanes with nonlinear material behavior,” *International Journal of Solids and Structures*, vol. 139–140, pp. 15–28, 2018.

98. Y. Zhu, K. M. Liechti, and K. Ravi-Chandar, “Direct extraction of rate-dependent traction-separation laws for polyurea/steel interfaces,” *International Journal of Solids and Structures*, vol. 46, no. 1, pp. 31–51, 2009.

99. Y. Liu, F. P. van der Meer, L. J. Sluys, and L. Ke, “Modeling of dynamic mode I crack growth in glass fiber-reinforced polymer composites: Fracture energy and failure mechanism,” *Engineering Fracture Mechanics*, p. 107522, 2021.

100. R. Sepasdar, A. Karpatne, and M. Shakiba, “A Data-Driven Approach to Full-Field Damage and Failure Pattern Prediction in Microstructure-Dependent Composites using Deep Learning,” *Submitted for publication*, 2021.

101. R. Sepasdar and M. Shakiba, “Micromechanical Study of Multiple Transverse Cracking in Cross-Ply Fiber-Reinforced Composite Laminates,” *Submitted for publication*, 2021.

102. A. Ortega, P. Maimí, E. V. González, and L. Ripoll, “Compact tension specimen for orthotropic materials,” *Composites Part A: Applied Science and Manufacturing*, vol. 63, pp. 85–93, 2014.

103. S. Tamrakar, R. Ganesh, S. Sockalingam, B. Z. Haque, and J. W. Gillespie Jr., “Experimental Investigation of Strain Rate and Temperature Dependent Response of an Epoxy Resin Undergoing Large Deformation,” *Journal of Dynamic Behavior of Materials*, vol. 4, no. 1, pp. 114–128, 2018.

104. S. Tamrakar, R. Ganesh, S. Sockalingam, B. Z. Haque, and J. W. Gillespie Jr., “Strain rate-dependent large deformation inelastic behavior of an epoxy resin,” *Journal of Composite Materials*, vol. 54, no. 1, pp. 71–87, 2020.

105. S. Marzi, O. Hesebeck, M. Brede, and F. Kleiner, “A Rate-Dependent, Elasto-

Plastic Cohesive Zone Mixed-Mode Model for Crash Analysis of Adhesively Bonded Joints,” *7th European LS-Dyna Conference*, 2009.

106. S. Marzi, O. Hesebeck, M. Brede, and F. Kleiner, “A Rate-Dependent Cohesive Zone Model for Adhesively Bonded Joints Loaded in Mode I,” *Journal of Adhesion Science and Technology*, vol. 23, no. 6, pp. 881–898, 2009.

107. S. Sockalingam, M. Dey, J. W. Gillespie Jr., and M. Keefe, “Finite element analysis of the microdroplet test method using cohesive zone model of the fiber/matrix interface,” *Composites Part A: Applied Science and Manufacturing*, vol. 56, pp. 239–247, 2014.

108. S. Tamrakar, R. Ganesh, S. Sockalingam, and J. W. Gillespie, “Rate dependent mode II traction separation law for S-2 glass/epoxy interface using a microdroplet test method,” *Composites Part A: Applied Science and Manufacturing*, vol. 124, no. June, 2019.

109. S. Ogihara and J. Koyanagi, “Investigation of combined stress state failure criterion for glass fiber/epoxy interface by the cruciform specimen method,” *Composites Science and Technology*, vol. 70, no. 1, pp. 143–150, 2010.

110. ASTM E1820-06, “Standard Test Method for Measurement of Fracture Toughness,” *Annual Book of ASTM Standard*, no. August, pp. 1–65, 2006.

111. A. Bergan, C. Dávila, F. Leone, J. Awerbuch, and T. M. Tan, “A Mode I cohesive law characterization procedure for through-the-thickness crack propagation in composite laminates,” *Composites Part B: Engineering*, vol. 94, pp. 338–349, 2016.

112. H. Wafai, A. Yudhanto, G. Lubineau, R. Yaldiz, and N. Verghese, “An experimental approach that assesses in-situ micro-scale damage mechanisms and fracture toughness in thermoplastic laminates under out-of-plane loading,” *Composite Structures*, vol. 207, no. September 2018, pp. 546–559, 2019.

113. Z. C. Xia and J. W. Hutchinson, “Mode II fracture toughness of a brittle adhesive layer,” *International Journal of Solids and Structures*, vol. 31, no. 8, pp. 1133–1148, 1994.

114. W. L. Bradley, “Relationship of Matrix Toughness to Interlaminar Fracture Toughness,” in *Composite Material Series Volume 6: Application of Fracture Mechanics to Composite Materials*, K. Friedrich, Ed. Amsterdam: Elsevier Science Publishers B.V., 1989, pp. 159–187.

115. M. Hibbs and W. Bradley, “Correlations Between Micromechanical Failure

Processes and the Delamination Toughness of Graphite/Epoxy Systems," *Fractography of Modern Engineering Materials: Composites and Metals, ASTM STP 948*, pp. 68–97, 1987.

116. C. Corleto and W. Bradley, "Mode II Delamination Fracture Toughness of Unidirectional Graphite/Epoxy Composites," *Composite Materials: Fatigue and Fracture, ASTM STP 1012*, vol. 2, pp. 201–221, 1989.

117. W. M. Jordan and W. L. Bradley, "Micromechanisms of Fracture in Toughened Graphite-Epoxy Laminates.," *Toughened Composites, ASTM STP 937*, pp. 95–114, 1987.

118. B. Smith and R. Grove, "Determination of Crack Propagation Directions in Graphite/Epoxy Structures," *Fractography of Modern Engineering Materials: Composites and Metals, ASTM STP 948*, pp. 154–173, 1987.

119. S. T. Pinho, L. Iannucci, and P. Robinson, "Formulation and implementation of decohesion elements in an explicit finite element code," *Composites Part A: Applied Science and Manufacturing*, vol. 37, no. 5, pp. 778–789, 2006.

120. T. E. Tay, G. Liu, V. B. C. Tan, X. S. Sun, and D. C. Pham, "Progressive failure analysis of composites," *Journal of Composite Materials*, vol. 42, no. 18, pp. 1921–1966, 2008.

121. N. K. Naik, P. Shrirao, and B. C. K. Reddy, "Ballistic impact behaviour of woven fabric composites: Formulation," *International Journal of Impact Engineering*, 2006.

122. S. Chocron, E. Figueroa, N. King, T. Kirchdoerfer, A. E. Nicholls, E. Sagebiel, C. Weiss, and C. J. Freitas, "Modeling and validation of full fabric targets under ballistic impact," *Composites Science and Technology*, vol. 70, no. 13, pp. 2012–2022, 2010.

123. S. Chocron, T. Kirchdoerfer, N. King, and C. J. Freitas, "Modeling of fabric impact with high speed imaging and nickel-chromium wires validation," *Journal of Applied Mechanics, Transactions ASME*, vol. 78, no. 5, pp. 1–13, 2011.

124. S. Chocron, C. E. Anderson, and A. E. Nicholls, "Response of 3-D and Plain-Weave S-2 Glass Composites in Out-of-Plane Tension and Shear," *Experimental Mechanics*, vol. 53, no. 6, pp. 989–1000, 2013.

125. J. C. Smith, F. L. Mccrackin, and H. F. Schiefer, "Stress-Strain Relationships in Yarns Subjected to Rapid Impact Loading:Part V: Wave Propagation in Long

Textile Yarns Impacted Transversely," *Textile Research Journal*, vol. 28, no. 4, pp. 288–302, 1958.

126. D. Roylance, "Stress Wave Damage in Graphite/Epoxy Laminates," *Journal of Composite Materials*, vol. 14, no. 2. pp. 111–119, 1980.

127. S. Sockalingam, J. W. Gillespie Jr., and M. Keefe, "Dynamic modeling of Kevlar KM2 single fiber subjected to transverse impact," *International Journal of Solids and Structures*, vol. 67–68, pp. 297–310, 2015.

128. S. Sockalingam, J. W. Gillespie Jr., and M. Keefe, "On the transverse compression response of Kevlar KM2 using fiber-level finite element model," *International Journal of Solids and Structures*, vol. 51, no. 13, pp. 2504–2517, 2014.

129. F. C. Moon, "A Critical Survey of Wave Propagation and Impact in Composite Materials," NASA Lewis Research Center, NASA CR-121226, 1973.

130. B. Z. Haque, J. L. Harrington, and J. W. Gillespie Jr., "Multi-hit ballistic impact on S-2 glass/SC15 thick-section composites: Finite element analyses," *Journal of Strain Analysis for Engineering Design*, vol. 47, no. 7, pp. 495–512, 2012.

131. B. Z. Haque and J. W. Gillespie Jr., "A combined theoretical-semiempirical penetration model of ballistic penetration of thick section composites," *Journal of Thermoplastic Composite Materials*, vol. 25, no. 5, pp. 631–659, 2012.

132. C. S. Meyer, B. Z. (Gama) Haque, D. J. O'Brien, and J. W. Gillespie Jr., "Mesoscale and Continuum Models of Wave Propagation in a Woven Composite," in *Proceedings of the American Society for Composites 34th Technical Conference*, 2019.

133. LSTC, *LS-DYNA Keyowrd User's Manual Volume I*, vol. I. 2016.

134. B. Z. (Gama) Haque, *A PROGRESSIVE COMPOSITE DAMAGE MODEL FOR UNIDIRECTIONAL AND WOVEN FABRIC COMPOSITES*. Newark, DE: Materials Sciences Corporation (MSC) & University of Delaware Center for Composite Materials (UD-CCM), 2017.

135. J. R. Xiao, B. A. Gama, and J. W. Gillespie Jr., "Progressive damage and delamination in plain weave S-2 glass/SC-15 composites under quasi-static punch-shear loading," *Composite Structures*, vol. 78, no. 2, pp. 182–196, 2007.

136. B. A. Gama and J. W. Gillespie Jr., "Finite element modeling of impact, damage evolution and penetration of thick-section composites," *International*

Journal of Impact Engineering, vol. 38, no. 4, pp. 181–197, 2011.

137. C. S. Meyer, B. Z. Haque, and J. W. Gillespie Jr., "Bridging Length Scales from Micro to Mesoscale through Rate-dependent Traction-separation Law Predictions," *Composites Part B: Engineering*, 2021.

138. B. (Gama) Haque and J. Gillespie Jr., "A combined theoretical–semiempirical penetration model of ballistic penetration of thick section composites," *Journal of Thermoplastic Composite Materials*, vol. 25, no. 5, pp. 631–659, 2012.

139. S. Novikov, I. Divnov, and A. Ivanov, "The study of fracture of steel, aluminum, and copper under explosive loading," *Phys Metals Metal Science (USSR)*, vol. 21, pp. 608–615, 1966.

140. B. Erzar and P. Forquin, "An Experimental Method to Determine the Tensile Strength of Concrete at High Rates of Strain," *Experimental Mechanics*, vol. 50, no. 7, pp. 941–955, 2010.

141. W. Heard, B. Song, B. Williams, B. Martin, P. Sparks, and X. Nie, "Dynamic Tensile Experimental Techniques for Geomaterials: A Comprehensive Review," *Journal of Dynamic Behavior of Materials*, vol. 4, no. 1, pp. 74–94, 2018.

142. T. Lässig, F. Bagusat, S. Pfändler, M. Gulde, D. Heunoske, J. Osterholz, W. Stein, H. Nahme, and M. May, "Investigations on the spall and delamination behavior of UHMWPE composites," *Composite Structures*, vol. 182, no. July, pp. 590–597, 2017.

143. G. Nilakantan, "Experimentally validated predictive finite element modeling of the V0-V100 probabilistic penetration response of a Kevlar fabric against a spherical projectile," *International Journal of Protective Structures*, vol. 9, no. 4, pp. 504–524, 2018.

144. S. C. Chowdhury, E. A. Wise, R. Ganesh, and J. W. Gillespie, "Effects of surface crack on the mechanical properties of Silica: A molecular dynamics simulation study," *Engineering Fracture Mechanics*, vol. 207, no. December 2018, pp. 99–108, 2019.

145. S. C. Chowdhury, R. Prosser, T. W. Sirk, R. M. Elder, and J. W. Gillespie Jr., "Glass fiber-epoxy interactions in the presence of silane: A molecular dynamics study," *Applied Surface Science*, vol. 542, 2021.

146. A. Matzenmiller, J. Lubliner, and R. L. Taylor, "A constitutive model for anisotropic damage in fiber-composites," *Mechanics of Materials*, vol. 20, no.

2, pp. 125–152, 1995.

147. J. Van Hoof, M. J. Woeswick, P. V. Straznicky, M. Bolduc, and S. Tylko, "Simulation of ballistic impact response of composite helmets," in *Proceedings of the 5th International LS-DYNA Users Conference*, 1998.

148. Z. Hashin, "Failure criteria for unidirectional fiber composites," *Journal of Applied Mechanics*, vol. 47, pp. 329–334, 1980.

Appendix A

PROGRESSIVE DAMAGE COMPOSITE MODEL

The constitutive model by Yen [21] and employed by Haque and Gillespie [19] is implemented in LS-DYNA [20] as MAT_162, and is used to simulate both unidirectional and woven fabric composites. [55] This model uses the continuum damage mechanics (CDM) approach presented by Matzenmiller et al. [146] This CDM approach models unidirectional composite lamina with a two-dimensional plane-stress state. The model also includes maximum strain failure criteria due to tension, punch-shear, and crush, which was first proposed by Van Hoof et al. [147] Yen extends these approaches by including rate-dependency, response to a three-dimensional stress field, and application to woven composites. Rate-dependency is necessary for modeling composite behavior under high-strain rate, high-pressure loading conditions such as impact. The following is a brief overview of this material model, which is used in the present work.

Damage initiation and progressive failure are expressed in terms of ply-level engineering strains for each layer of unidirectional or fabric composite. These strains are written as $\varepsilon_x, \varepsilon_y, \varepsilon_z, \varepsilon_{xy}, \varepsilon_{yz}, \varepsilon_{zx}$. For unidirectional composites, x, y, z indicate the fiber, in-plane transverse, and out-of-plane directions respectively. For fabric composites, x, y, z indicate in-plane fill, in-plane warp, and out-of-plane or through-thickness directions respectively. The elastic moduli associated with these strains are $E_x, E_y, E_z, G_{xy}, G_{yz}, G_{zx}$.

A.1 Unidirectional Composite Damage Model

This model generalizes the Hashin [148] fiber failure criteria for a unidirectional lamina. Failure can occur in fiber mode, which is relative to the fiber direction and involves uniaxial tension and transverse shear (A.1), uniaxial compression (A.2), or transverse compression (A.3).

$$f_1 - r_1^2 = \left(\frac{E_x\langle\varepsilon_x\rangle}{S_{xT}}\right)^2 + \frac{G_{xy}^2\varepsilon_{xy}^2 + G_{xz}^2\varepsilon_{xz}^2}{S_{FS}^2} - r_1^2 = 0 \tag{A.1}$$

$$\begin{gathered} f_2 - r_2^2 = \left(\frac{E_x\langle\varepsilon'_x\rangle}{S_{xC}}\right)^2 - r_2^2 = 0, \\ \varepsilon'_x = \max\left\{-\varepsilon_x - \langle-\varepsilon_y\rangle\frac{E_y}{E_x}, -\varepsilon_x - \langle-\varepsilon_z\rangle\frac{E_z}{E_x}\right\} \end{gathered} \tag{A.2}$$

$$f_3 - r_3^2 = \left(\frac{E_y\langle-\varepsilon_y\rangle}{S_{FC}}\right)^2 + \left(\frac{E_z\langle-\varepsilon_z\rangle}{S_{FC}}\right)^2 - r_3^2 = 0 \tag{A.3}$$

where $\langle\rangle$ are Macaulay brackets, S_{xT} is axial tensile strength, S_{xC} is axial compressive strength, S_{FS} is fiber-shear layer strength, and S_{FC} is fiber-crush layer strength. Damage threshold is given by $r_j, j = 1, 2, 3$, which equal 1 for damage-free material, before damage initiation. Damage threshold values are updated as damage accumulates in the associated damage modes (i.e., uniaxial tension and transverse shear, uniaxial compression, or transverse compression). Transverse compression is sometimes called crush, S_{FS} is called punch-shear strength, and S_{FC} is called punch-crush strength.

Failure can also occur in matrix mode, which is on planes parallel to the fiber direction, perpendicular (A.4) or parallel to the lamina planes, which is delamination (A.5).

$$f_4 - r_4^2 = \left\{\left(\frac{E_y\langle\varepsilon_y\rangle}{S_{yT}}\right)^2 + \left[\frac{G_{yz}\varepsilon_{yz}}{S_{yz0} + S_{ySR}}\right]^2 + \left[\frac{G_{xy}\varepsilon_{xy}}{S_{xy0} + S_{ySR}}\right]^2\right\} - r_4^2 = 0 \tag{A.4}$$

$$f_5 - r_5^2 = S^2\left\{\left(\frac{E_z\langle\varepsilon_z\rangle}{S_{zT}}\right)^2 + \left[\frac{G_{yz}\varepsilon_{yz}}{S_{yz0} + S_{zSR}}\right]^2 + \left[\frac{G_{xz}\varepsilon_{xz}}{S_{xy0} + S_{zSR}}\right]^2\right\} - r_5^2 = 0 \tag{A.5}$$

where S_{yT} and S_{zT} are transverse tensile strengths in y and z directions respectively (for $\varepsilon_y > 0$ or $\varepsilon_z > 0$), and S_{xy0}, S_{yz0}, and S_{xz0} are quasi-static shear strengths. For $\varepsilon_y > 0$ or $\varepsilon_z > 0$, that is, under compressive transverse strain, the damaged surface is closed (i.e., the faces of matrix cracks are in contact) and shear strengths are assumed to depend on the associated compressive normal strains (ε_y or ε_z) similar to the Mohr-Coulomb theory. These shear strengths are given by (A.6) and (A.7).

$$S_{ySR} = E_y \tan\varphi\langle-\varepsilon_y\rangle \tag{A.6}$$

$$S_{zSR} = E_z \tan\varphi\langle-\varepsilon_z\rangle \tag{A.7}$$

where φ is the Coulomb friction angle. Damage thresholds $r_j, j = 4, 5$ are equal to 1 before damage imitates, and these are updated as damage accumulates in the associated damage modes (i.e., perpendicular matrix damage and delamination). The

S is a scale factor, intended to provide better correlation of delamination area with experiment.

A.2 Fabric Composite Damage Model

Similar to unidirectional composite, the Hashin [148] failure criteria are generalized to calculate the fiber damage in terms of strain components for a plain weave composite layer. Fill and warp fiber tension and shear damage are given by (A.8) and (A.9).

$$f_6 - r_6^2 = \left(\frac{E_x\langle\varepsilon_x\rangle}{S_{xT}}\right)^2 + \left(\frac{G_{xz}\varepsilon_{xz}}{S_{xFS}}\right)^2 - r_6^2 = 0 \tag{A.8}$$

$$f_7 - r_7^2 = \left(\frac{E_y\langle\varepsilon_y\rangle}{S_{yT}}\right)^2 + \left(\frac{G_{yz}\varepsilon_{yz}}{S_{yFS}}\right)^2 - r_7^2 = 0 \tag{A.9}$$

where S_{xT} and S_{yT} are axial tensile strengths in the fill and warp directions, S_{xFS} and S_{yFS} are layer shear strengths. These layer shear strengths are from fiber shear failure in fill (x) and warp (y) directions, and apply when the associated strains (ε_x or ε_y) are positive (tensile).

When strains ε_x and ε_y are negative (compressive), the in-plane compressive damage in fill and warp directions are given by the maximum strain criterion (A.10) and (A.11).

$$f_8 - r_8^2 = \left(\frac{E_x\langle\varepsilon'_x\rangle}{S_{xC}}\right)^2 - r_8^2 = 0, \qquad \varepsilon'_x = -\varepsilon_x - \langle-\varepsilon_z\rangle\frac{E_z}{E_x} \tag{A.10}$$

$$f_9 - r_9^2 = \left(\frac{E_y\langle\varepsilon_y'\rangle}{S_{yC}}\right)^2 - r_9^2 = 0, \qquad \varepsilon_y' = -\varepsilon_y - \langle-\varepsilon_z\rangle\frac{E_z}{E_y} \tag{A.11}$$

where S_{xC} and S_{yC} are axial compressive strengths in fill and warp directions.

Crush damage is given by (A.12) and results from through-thickness compressive pressure.

$$f_{10} - r_{10}^2 = \left(\frac{E_z\langle-\varepsilon_z\rangle}{S_{FC}}\right)^2 - r_{10}^2 = 0 \tag{A.12}$$

where S_{FC} is fiber crush strength (punch-crush).

Plain weave composite layers can be damaged by in-plane shear stress without fiber failure. In-plane matrix damage is given by (A.13).

$$f_{11} - r_{11}^2 = \left(\frac{G_{xy}\varepsilon_{xy}}{S_{xy}}\right)^2 - r_{11}^2 = 0 \tag{A.13}$$

where S_{xy} is layer shear strength.

The final failure mode results from the quadratic interaction between thickness strains, which is primarily a through-thickness matrix failure mode and is given by (A.14).

$$f_{12} - r_{12}^2 = S^2\left\{\left(\frac{E_z\langle\varepsilon_z\rangle}{S_{zT}}\right)^2 + \left[\frac{G_{yz}\varepsilon_{yz}}{S_{yz0} + S_{zSR}}\right]^2 + \left[\frac{G_{xz}\varepsilon_{xz}}{S_{xz0} + S_{zSR}}\right]^2\right\} - r_{12}^2 = 0 \tag{A.14}$$

where S_{zT} is through-thickness tensile strength, S_{yz0} and S_{xz0} are shear strengths for tensile strain ε_z. The damage surface resulting from (A.14) is parallel to the composite layer plane. For compressive through-thickness strain ($\varepsilon_z < 0$), the damaged interface (delamination) is closed, and the damage strengths depend on the compressive normal strain ε_z similar to Mohr-Coulomb, given by (A.15).

$$S_{zSR} = E_z \tan\varphi\langle -\varepsilon_z \rangle \tag{A.15}$$

where φ is the Coulomb friction angle and S is a scale factor to provide better correlation of delamination area with experiment.

Again, damage thresholds $r_j, j = 6, 7, 8, 9, 10, 11, 12$ are equal to 1 before damage initiation.

A.3 Progressive Damage

Damage leads to a reduction in stiffness. Progressive stiffness degradation is governed by six damage variables ϖ_j where $j = 1, \ldots, 6$. These six variables correspond to the six moduli, $E_x, E_y, E_z, G_{xy}, G_{yz}, G_{zx}$. Then the compliance matrix $[S^*]$ is given by (A.16).

$$[S^*] = \begin{bmatrix} \frac{1}{(1-\varpi_1)E_x} & -\frac{\nu_{yx}}{E_y} & -\frac{\nu_{zx}}{E_z} & 0 & 0 & 0 \\ -\frac{\nu_{xy}}{E_x} & \frac{1}{(1-\varpi_2)E_y} & -\frac{\nu_{zy}}{E_z} & 0 & 0 & 0 \\ -\frac{\nu_{xz}}{E_x} & -\frac{\nu_{yz}}{E_y} & \frac{1}{(1-\varpi_3)E_Z} & 0 & 0 & 0 \\ 0 & 0 & 0 & \frac{1}{(1-\varpi_4)G_{xy}} & 0 & 0 \\ 0 & 0 & 0 & 0 & \frac{1}{(1-\varpi_5)G_{yz}} & 0 \\ 0 & 0 & 0 & 0 & 0 & \frac{1}{(1-\varpi_6)G_{zx}} \end{bmatrix} \tag{A.16}$$

Then the stiffness matrix $[C]$ is given by inverting the compliance matrix, $[C] = [S^*]^{-1}$.

Progressive damage evolution is given by the rate of damage growth in (A.17).

$$\dot{\varpi}_j = \sum_i \dot{\phi}_i q_{ji} \tag{A.17}$$

where scalar functions, $\dot{\phi}_i$ $(i = 1, \ldots, 12)$ define the growth rate of each damage mode i. The binary vector-valued functions q_{ji} $(j = 1, \ldots, 6, i = 1, \ldots, 12)$ give coupling between a given damage variable, ϖ_j, and a given damage mode, f_i.

The damage criteria in equations (A.1) to (A.5) or (A.8) to (A.14) give damage surfaces in strain space. Damage growth $\dot{\phi}_i > 0$ happens if the strain path crosses the updated damage surface $f_i^2 - r_i^2 = 0$ and if the associated strain-vector increment has a non-zero component in the direction of the damage surface outward normal. That is, when $\sum_k \left(\frac{\partial f_i}{\partial \varepsilon_k}\right) \dot{\varepsilon}_k > 0$ where $k = 1, \ldots, 6$ indicates the six components of the strain vector. When combined with the damage growth function $\gamma_i(\varepsilon_k, \varpi_j)$, damage growth rate is given by (A.18) and (A.19).

$$\dot{\phi}_i = \sum_k \gamma_i \frac{\partial f_i}{\partial \varepsilon_k} \varepsilon_k \tag{A.18}$$

$$\gamma_i = \frac{1}{2}(1 - \phi_i) f_i^{\frac{m_j}{2} - 1} \tag{A.19}$$

where $\sum_k \left(\frac{\partial f_i}{\partial \varepsilon_k}\right) \dot{\varepsilon}_k = \dot{f}_i$ so that for the quadratic functions in equations (A.1) to (A.5) or (A.8) to (A.14),

$$\dot{\phi}_i = \frac{1}{2}(1-\phi_i) f_i^{\frac{m_i}{2}-1} \dot{f}_i \tag{A.20}$$

where ϕ_i is the scalar damage function associated with the i^{th} failure mode, and m_i are material softening constants.

The scalar damage function, ϕ_i, is obtained by integrating equation (A.20) and is given by (A.21).

$$\phi_i = 1 - \exp\left(\frac{1}{m_i}\left(1 - r_i^{m_i}\right)\right) \tag{A.21}$$

The damage coupling is given by matrix q_{ij} for unidirectional (A.22) and fabric (A.23) composites.

$$q_{ij}^{uni} = \begin{bmatrix} 1 & 1 & 1 & 0 & 0 \\ 0 & 0 & 1 & 1 & 0 \\ 0 & 0 & 1 & 0 & 1 \\ 1 & 1 & 1 & 1 & 0 \\ 0 & 0 & 1 & 1 & 1 \\ 1 & 1 & 1 & 0 & 1 \end{bmatrix} \tag{A.22}$$

$$q_{ij}^{fabric} = \begin{bmatrix} 1 & 0 & 1 & 0 & 1 & 0 & 0 \\ 0 & 1 & 0 & 1 & 1 & 0 & 0 \\ 0 & 0 & 0 & 0 & 1 & 0 & 1 \\ 1 & 1 & 1 & 1 & 1 & 1 & 0 \\ 0 & 1 & 0 & 1 & 1 & 0 & 1 \\ 1 & 0 & 1 & 0 & 1 & 0 & 1 \end{bmatrix} \tag{A.23}$$

From damage coupling (A.22) or (A.23) and the damage function (A.21), damage variables ϖ_j are determined for each failure mode i as (A.24).

$$\varpi_j = 1 - \exp\left(\frac{1}{m_i}\left(1 - r_i^{m_i}\right)\right), \qquad r_i \geq 1 \tag{A.24}$$

Damage thresholds r_i have an initial value of 1 and are continuously increasing functions with increasing damage. Initially, the associated damage variable ϖ_j has a value of zero. Hence there is an initial elastic region in strain space, which is bounded by the damage functions. After the linear elastic region, behavior is nonlinear. Loading the material causes progressive damage growth, and as damage thresholds increase, damage variables increase, and damage accumulates as stiffness loss.

A.4 Strain Rate Dependent Strength and Stiffness

The strain-rate dependent strengths are given by (A.25), where $\{S_0\}$ are quasi-static strength values and $\{S\}$ are updated strength values, depending on the average local strain rate of a finite element. The strain rate dependent moduli are given by (A.26), where $\{E_0\}$ are quasi-static moduli values and $\{E\}$ are updated moduli values, depending on the local strain rate of a finite element. The reference strain rate is typically chosen as $\dot{\varepsilon}_0 = 1\ \mathrm{s}^{-1}$.

$$\{S\} = \{S_0\}\left(1 + C_{rate1} \ln\left(\frac{\{\dot{\varepsilon}\}}{\dot{\varepsilon}_0}\right)\right) \tag{A.25}$$

where $\{S\} = \{S_{xT}, S_{xC}, S_{yT}, S_{yC}, S_{FC}, S_{FS}\}$, $\{\dot{\varepsilon}\} = \left\{\dot{\varepsilon}_x, \dot{\varepsilon}_y, \dot{\varepsilon}_z, \dot{\varepsilon}_{xy}, \dot{\varepsilon}_{yz}, \dot{\varepsilon}_{zx}\right\}$, and C_{rate1} is a rate parameter.

$$\{E\} = \{E_0\}\left(1 + \{C_{rate}\}\ln\left(\frac{\{\dot{\varepsilon}\}}{\dot{\varepsilon}_0}\right)\right) \tag{A.26}$$

where $\{E\} = \{E_x, E_y, E_z, G_{xy}, G_{yz}, G_{zx}\}$ and $\{C_{rate}\} = \{C_{rate2}, C_{rate2}, C_{rate4}, C_{rate3}, C_{rate3}, C_{rate3}\}$ and C_{rate2}, C_{rate3}, and C_{rate4} are rate parameters.

A.5 Nomenclature

Haque and Gillespie [19] provide a discussion of the parameters for this model, along with a list of nomenclature, which is summarized in table A.1.

Table A.1: Nomenclature of the progressive damage composite model.

Elastic Modulus	E_{11}, GPa	E_{22}, GPa	E_{33}, GPa	
Poisson's Ratio	ν_{21}	ν_{31}	ν_{32}	
Shear Modulus	G_{12}, GPa	G_{23}, GPa	G_{31}, GPa	
Tensile Strength	X_{1T}, MPa	X_{2T}, MPa	X_{3T}, MPa	
Compressive Strength	X_{1C}, MPa		X_{2C}, MPa	
Shear Strength	S_{12}, MPa	S_{23}, MPa	S_{31}, MPa	
Fiber Mode Strength	Punch-Crush Strength S_{FC}, MPa		Punch-Shear Strength S_{FS}, MPa	
Erosion Criteria	Axial Erosion Strain e_{Limit}	Expansion Erosion e_{Expn}	Compression Erosion e_{Crush}	
Rate Effects	C_{rate1} for X_{1T}, X_{1C}, X_{2T}, X_{2C}, S_{FC}, S_{FS}	C_{rate2} for E_{11}, E_{22}	C_{rate3} for G_{12}, G_{23}, G_{31}	C_{rate4} for E_{33}
Softening Parameters	Fiber damage in x-direction m_1	Fiber damage in y-direction m_2	Fiber crush and punch shear m_3	Matrix cracking and delamination m_4
Scale Factors	Residual confined strength under compression S_{FFC}		Delamination S_{Delam}	
Other Parameters	Coulomb friction angle φ	Density ρ	Maximum modulus reduction ω_{max}	

A.6 Continuum Model Properties

Parameters used in continuum modeling of plain weave glass/epoxy composites are included in table A.2.

Table A.2: Continuum effective plain weave parameters for glass/epoxy composite models.

<table>
<tr><td>Elastic Modulus</td><td colspan="2">E_{11}, GPa
27.5</td><td colspan="2">E_{22}, GPa
27.5</td><td colspan="2">E_{33}, GPa
11.8</td></tr>
<tr><td>Poisson’s Ratio</td><td colspan="2">ν_{21}
0.11</td><td colspan="2">ν_{31}
0.18</td><td colspan="2">ν_{32}
0.18</td></tr>
<tr><td>Shear Modulus</td><td colspan="2">G_{12}, GPa
4.1</td><td colspan="2">G_{23}, GPa
3.0</td><td colspan="2">G_{31}, GPa
3.0</td></tr>
<tr><td>Tensile Strength</td><td colspan="2">X_{1T}, MPa
854</td><td colspan="2">X_{2T}, MPa
854</td><td colspan="2">X_{3T}, MPa
82</td></tr>
<tr><td>Compressive Strength</td><td colspan="2">X_{1C}, MPa
412</td><td colspan="2">X_{2C}, MPa
412</td><td colspan="2"></td></tr>
<tr><td>Shear Strength</td><td colspan="2">S_{12}, MPa
106</td><td colspan="2">S_{23}, MPa
82</td><td colspan="2">S_{31}, MPa
82</td></tr>
<tr><td>Fiber Mode Strength</td><td colspan="2">S_{FC}, MPa
1202</td><td colspan="2">S_{FS}, MPa
424</td><td colspan="2"></td></tr>
<tr><td>Erosion Criteria</td><td colspan="2">Axial Erosion Strain
4.5</td><td colspan="2">Expansion Erosion
4.5</td><td colspan="2">Compression Erosion
0.001</td></tr>
<tr><td>Rate Effects</td><td>X_{1T}, X_{1C}, X_{2T}, X_{2C}, S_{FC}, S_{FS}
0.02</td><td colspan="2">E_{11}, E_{22}
0.02</td><td colspan="2">G_{12}, G_{23}, G_{31}
0.02</td><td>E_{33}
0.02</td></tr>
</table>

A.7 Mesoscale Model Properties

Parameters used in mesoscale modeling of plain weave glass/epoxy composites are included in table A.3.

Table A.3: Unidirectional parameters for mesoscale models of plain weave glass/epoxy composite.

<table>
<tr><td rowspan="2">Elastic Modulus</td><td colspan="2">E_{11}, GPa</td><td>E_{22}, GPa</td><td>E_{33}, GPa</td></tr>
<tr><td colspan="2">55.3</td><td>11.8</td><td>11.8</td></tr>
<tr><td rowspan="2">Poisson's Ratio</td><td colspan="2">ν_{21}</td><td>ν_{31}</td><td>ν_{32}</td></tr>
<tr><td colspan="2">0.05</td><td>0.05</td><td>0.45</td></tr>
<tr><td rowspan="2">Shear Modulus</td><td colspan="2">G_{12}, GPa</td><td>G_{23}, GPa</td><td>G_{31}, GPa</td></tr>
<tr><td colspan="2">4.3</td><td>3.7</td><td>4.3</td></tr>
<tr><td rowspan="2">Tensile Strength</td><td colspan="2">X_{1T}, MPa</td><td>X_{2T}, MPa</td><td>X_{3T}, MPa</td></tr>
<tr><td colspan="2">1380</td><td>45</td><td>45</td></tr>
<tr><td rowspan="2">Compressive Strength</td><td colspan="2">X_{1C}, MPa</td><td>X_{2C}, MPa</td><td></td></tr>
<tr><td colspan="2">770</td><td>137</td><td></td></tr>
<tr><td rowspan="2">Shear Strength</td><td colspan="2">S_{12}, MPa</td><td>S_{23}, MPa</td><td>S_{31}, MPa</td></tr>
<tr><td colspan="2">76</td><td>38</td><td>76</td></tr>
<tr><td rowspan="2">Fiber Mode Strength</td><td colspan="2">S_{FC}, MPa</td><td>S_{FS}, MPa</td><td></td></tr>
<tr><td colspan="2">850</td><td>250</td><td></td></tr>
<tr><td rowspan="2">Erosion Criteria</td><td colspan="2">Axial Erosion Strain</td><td>Expansion Erosion</td><td>Compression Erosion</td></tr>
<tr><td colspan="2">4.5</td><td>4.5</td><td>0.001</td></tr>
<tr><td rowspan="2">Rate Effects</td><td>X_{1T}, X_{1C}, X_{2T}, X_{2C}, S_{FC}, S_{FS}</td><td>E_{11}, E_{22}</td><td>G_{12}, G_{23}, G_{31}</td><td>E_{33}</td></tr>
<tr><td>0.02</td><td>0.02</td><td>0.02</td><td>0.02</td></tr>
</table>

Appendix B

DERIVATION AND COMPUTATION OF THE ENERGY DOMAIN J-INTEGRAL

B.1 Energy Domain Integral

The energy release rate, J, for a cracked, nonlinear elastic material is defined as the energy dissipated, $-d\Pi$, per unit increase in crack area, dA

$$J = -\frac{d\Pi}{dA} \tag{B.1}$$

Rice [87] showed that J can be written as a path-independent integral where, for an arbitrary counterclockwise path around the crack tip, J is given by

$$J = \int_{\Gamma} \left(\mathcal{W} n_1 - T_i \frac{\partial u_i}{\partial x_1} \right) d\Gamma \tag{B.2}$$

where $\mathcal{W}$ is the strain energy density, n_1 is the x_1 component of the unit vector normal to Γ, T_i are the components of the traction vector, u_i are the components of the displacement vector, and $d\Gamma$ is a length increment along the contour Γ in figure B.1a. The strain energy density (or, stress work, which includes material constitutive behavior [61]) is defined as

$$\mathcal{W} = \int_0^{\varepsilon_{ij}} \sigma_{ij} d\varepsilon_{ij} \tag{B.3}$$

where σ_{ij} is the stress tensor and ε_{ij} is the strain tensor. Traction is a stress vector acting at a given point on the contour and is given by

$$T_i = \sigma_{ij} n_j \tag{B.4}$$

where n_j are the components of the unit vector normal to the contour Γ [61].

Contour integration is not practical in finite element analysis, but integration over an area domain is. Shih et al. [88], [89] developed the energy domain integral, which is used as the basis for numerical computation of the J-integral. The domain integral is applicable to quasi-static and dynamic problems, elastic, plastic and viscoplastic material behavior, mechanical and thermal loading conditions, is readily and efficiently numerically implemented, and is relatively insensitive to mesh size for domains defined far from the crack tip [61]. Quadrilateral or hexahedral elements are important for ensuring a smooth, regular, concentric integration domain.

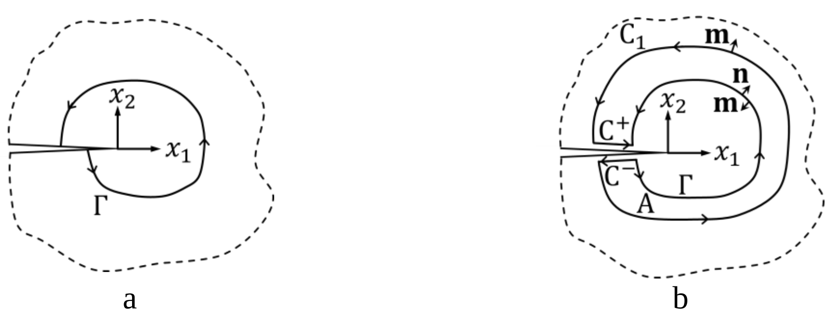

Figure B.1: Schematic of (a) contour J-integral and (b) area J-integral (energy domain integral).

Consider a closed contour C with the outward normal unit vector **m** in figure B.1b. The closed contour C is composed of segments such that $C = C_1 + C^- + C^+ - \Gamma$, and the area enclosed by C is A. For a crack growing in the x_1 direction, and for an arbitrary contour Γ that begins and ends on the crack line and has outward normal **n**, equation (B.2) is true. Define any sufficiently smooth function $\tilde{q}(x_1, x_2)$ such that $\tilde{q} = 1$ on Γ and $\tilde{q} = 0$ on C_1. Replace **n** with $-\mathbf{m}$ on Γ and recall that $\tilde{q} = 0$ on C_1, then equation (B.2) becomes

$$J = -\oint_C \left(Wm_1 - \sigma_{ij} m_j \frac{\partial u_i}{\partial x_1}\right) \tilde{q}\, \mathrm{d}C - \int_{C^+ + C^-} \sigma_{ij} m_j \frac{\partial u_i}{\partial x_1} \tilde{q}\, \mathrm{d}C \qquad \text{(B.5)}$$

Note that on crack faces (assumed to be closed, not exaggerated as in figure B.1) $\mathbf{m} = \pm m_2 \boldsymbol{e}_2$ such that $\int_{C^+ + C^-} \sigma_{ij} m_j \frac{\partial u_i}{\partial x_1} \tilde{q}\, \mathrm{d}C = 0$. Then applying the divergence theorem, equation (B.5) becomes

$$J = \int_A \left(\frac{\partial}{\partial x_j} \left(\sigma_{ij} \frac{\partial u_i}{\partial x_1} \tilde{q} \right) - \frac{\partial (\mathcal{W} \tilde{q})}{\partial x_1} \right) dA \qquad \text{(B.6)}$$

Differentiating and since $\partial \sigma_{ij} / \partial x_j = 0$, equation (B.6) becomes

$$J = \int_A \left(\sigma_{ij} \frac{\partial^2 u_i}{\partial x_j \partial x_1} \tilde{q} + \sigma_{ij} \frac{\partial u_i}{\partial x_1} \frac{\partial \tilde{q}}{\partial x_j} - \frac{\partial \mathcal{W}}{\partial x_1} \tilde{q} - \mathcal{W} \frac{\partial \tilde{q}}{\partial x_1} \right) dA \qquad \text{(B.7)}$$

Finally, noting that $\partial \mathcal{W} / \partial x_1 = \sigma_{ij}\, \partial^2 u_i / \partial x_j \partial x_1$ so 1st and 3rd terms cancel, we have the energy domain integral [90]

$$J = \int_A \left(\sigma_{ij} \frac{\partial u_i}{\partial x_1} \frac{\partial \tilde{q}}{\partial x_j} - \mathcal{W} \frac{\partial \tilde{q}}{\partial x_1} \right) dA \tag{B.8}$$

B.2 Computing the J-integral

Consider a plain strain finite element model (FEM) with a domain of elements surrounding the crack tip, as shown schematically in figure B.2a. In-plane stress, strain, and displacement are output from the FEM for each element, k, in the domain, over time, t. These data are read into a MATLAB (or similar) script, that computes the J-integral as a function of time, $J(t)$, according to

$$J^k(t) = \int_{A^k} \left(\sigma_{ij}^k \frac{\partial u_i^k}{\partial x_1} \frac{\partial \tilde{q}^k}{\partial x_j} - \mathcal{W}^k \frac{\partial \tilde{q}^k}{\partial x_1} \right) dA^k \tag{B.9}$$

where, for each element k, A^k is the in-plane area, σ_{ij}^k are the stresses at the integration point, u_i^k are the displacements averaged from the nodes, $\mathcal{W}^k$ are the strain energy densities (implicitly including constitutive behavior such as rate dependence) computed from stresses (at centroidal integration points) and strains (averaged from the nodes) from equation (B.3), and $\tilde{q}^k$ is a function where $\tilde{q}^k = 1$ at the nodes closest to the crack tip and $\tilde{q}^k = 0$ at the nodes furthest from the crack tip for each element. Crack opening displacement as a function of time, $\delta(t)$, is output from the FEM and correlated with $J(t)$.

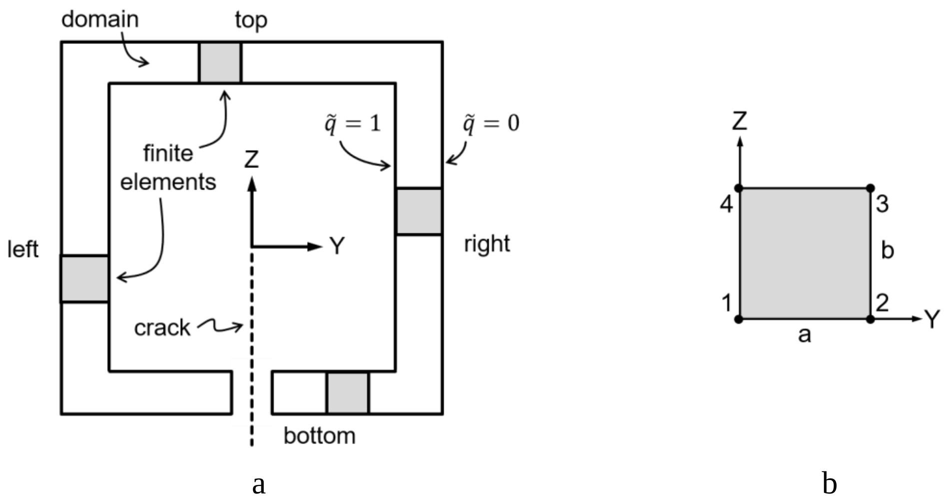

Figure B.2: Schematic of (a) J-integral domain and (b) finite element in the domain.

The energy domain integral requires definition of the function $\tilde{q}$. It is convenient to define $\tilde{q}$ as the FEM shape functions that interpolate displacement. Then $\tilde{q}$ is

$$\tilde{q} = \sum_{i=1}^{n} N_i \tilde{q}_i \tag{B.10}$$

where N_i are shape functions and $\tilde{q}_i$ are the values of $\tilde{q}$ at nodes $i = 1, \dots, n$ (i.e., $\tilde{q} = 1$ on the inner nodes relative to the crack tip and $\tilde{q} = 0$ on the outer nodes relative to the crack tip). Then J may be calculated by equation (B.9) over any annular domain of k elements surrounding the crack tip. For example, square elements may be modeled (i.e., 3D solid elements under plain strain conditions), and then the shape functions are given by

$$
\begin{aligned}
N_1 &= \frac{1}{ab}(Y - Y_2)(Z - Z_4);\ N_2 = -\frac{1}{ab}(Y - Y_1)(Z - Z_3); \\
N_3 &= \frac{1}{ab}(Y - Y_4)(Z - Z_2);\ N_4 = -\frac{1}{ab}(Y - Y_3)(Z - Z_1)
\end{aligned}
\tag{B.11}
$$

where a is the Y-dimension of the element, b is the Z-dimension of the element, and nodes are given counterclockwise by $n = 1, 2, 3, 4$, as shown in figure B.2b. Then the J-integral is given by equations (B.3), (B.4), (B.9), (B.10), and (B.11).